SLAC-229
UC-34d
(T/E/A)

SLAC LINEAR COLLIDER

CONCEPTUAL DESIGN REPORT

Stanford Linear Accelerator Center
Stanford University, Stanford, California

This is a reprint of the original SLAC Linear Collider Conceptual Design Report. Readers should be cautioned that this report has not been updated to reflect the many design details that have changed since the report was written.

SLAC Report No. 229
June 1980

Prepared for the Department of Energy
under contract number DE-AC03-76SF00515

Printed in the United States of America. Available from the National Technical Information Service, U.S. Department of Commerce, 5285 Port Royal Road, Springfield, VA 22161. Price: Printed Copy A09; Microfiche A01.

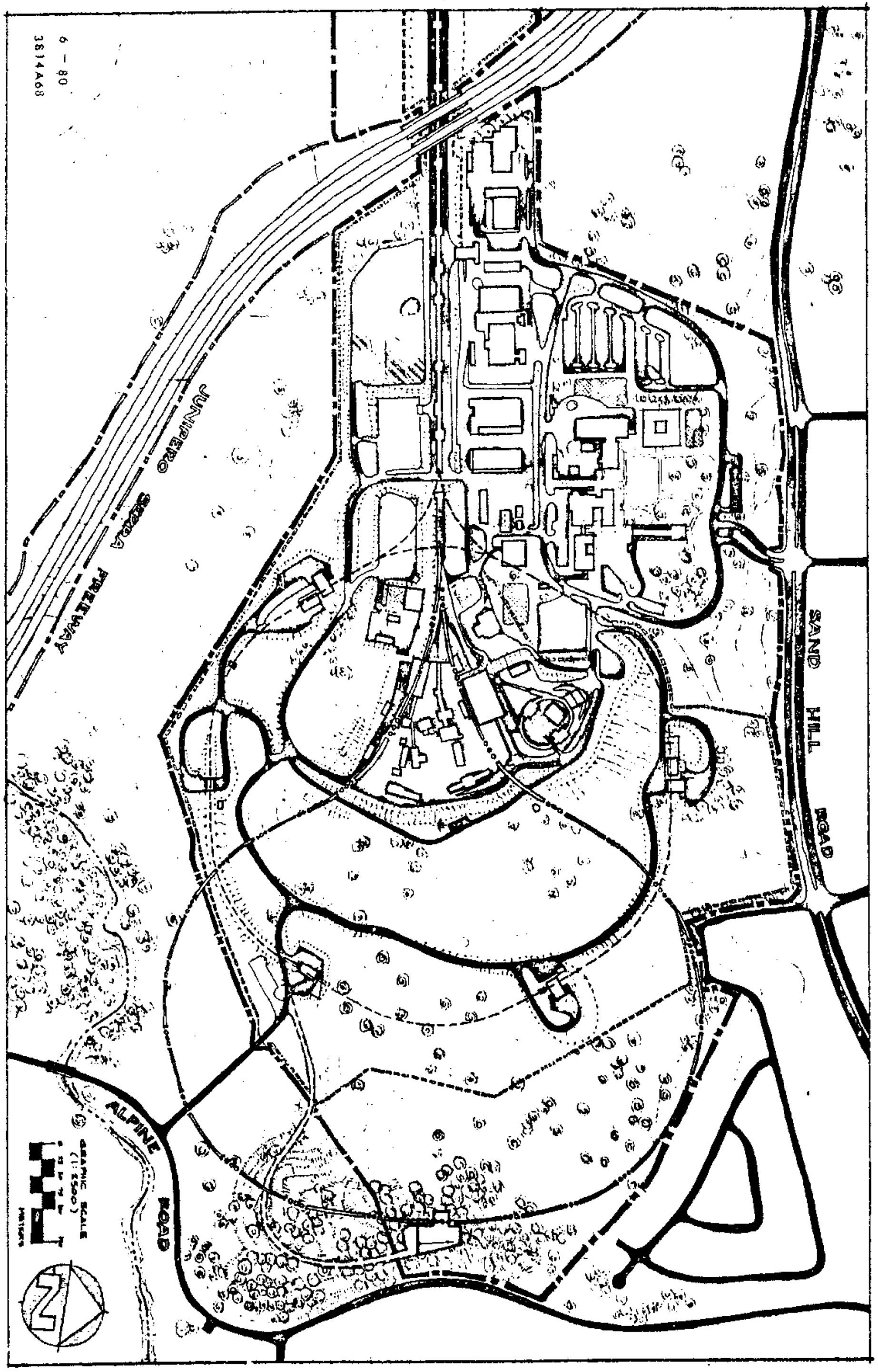

Location of the Linear Collider at SLAC

TABLE OF CONTENTS

APPENDICES:

LIST OF FIGURES

LIST OF TABLES

I. INTRODUCTION

A. The Rationale for Linear Colliders

The progress of particle physics has always been intimately connected with the progress of accelerator technology. The past decade has seen the coming to maturity of the electron-positron colliding-beam storage-ring technique, and the machines built to exploit this technique have yielded most of what we have learned about the properties of new quarks, mesons, leptons, jets, etc. The physics arguments for continuing to higher energy in electron-positron colliding beams are compelling. However, the storage rings are becoming evermore costly. While it is clear that higher energies in electron-positron storage rings are technically possible, it is not clear that they are fiscally feasible.

The SLAC Linear Collider (SLC) proposed here has two main goals. One is to serve as the pioneer machine in a new technique to achieve high-energy electron-positron collisions at lower cost per GeV than the storage-ring technique used until now. The other is to increase the center-of-mass energy available in the electron-positron system to one above that required to investigate the unification of the weak and electromagnetic interactions that we now expect to become manifest at approximately 90 GeV in the center-of-mass.

The SLC is a variant of a new class of accelerators called Linear Colliders. The true Linear Collider would use two linear accelerators aimed at each other to accelerate intense bunches of electrons and positrons. The beams would be focused to micron sizes and would collide between the two linacs. The particles would then be disposed of and not used again. These Linear Colliders could tolerate extremely high current densities at the collision point compared to those tolerable in storage rings. Further, because these machines would not store particles in a ring of magnets as do the storage rings, they would not require large amounts of RF power to make up for the synchrotron radiation energy losses that occur in storage rings. These two factors combine to give different scaling laws of size and cost vs energy for the two types of machines, and it is these different scaling laws which promise lower cost per unit energy for very high energy Linear Colliders compared to storage rings.

The highest energy electron-positron storage rings now in existence are the PEP project at Stanford and the PETRA project at Hamburg, West Germany. These two machines each cost around 80 million dollars (without experimental apparatus) for a center-of-mass energy of approximately 35 GeV. A much larger storage ring is being designed by CERN physicists and engineers to achieve a maximum center-of-mass energy of 160 GeV with conventional RF, and 240 GeV with superconducting RF when the latter technique becomes practical. The version with conventional RF is estimated to cost approximately 1000 million Swiss Francs (1979 value SF) plus personnel costs. The detailed design studies of the CERN group agree with the scaling law, derived on general grounds, which shows that the cost of e^+e^- storage rings scales roughly as the square of the center-of-mass energy. This scaling law arises because of the rapid increase in RF voltage necessary to make up for synchrotron-radiation losses in the circular ring of magnets; and it forces the storage-ring designer, in order to minimize the total cost of the project, to choose a radius and, hence, a cost for the machine which increases roughly as the square of the energy.

In contrast to storage rings, the true Linear Collider would not have to cope with synchrotron radiation. Hence, the length and the cost of an accelerator required to drive a linear colliding-beam system scale as the first power of the energy. Thus, at some energy a first-power scaling law will result in a less costly device than a quadratic scaling law.

The Collider proposed here does have a ring of magnets to guide the linac bunches to the collision point. At energies below roughly 70 GeV per beam, the synchrotron radiation emitted in these magnets has a negligible effect on the total power required to operate the facility, while allowing the facility to be based on a single linac rather than on two linacs.

The proposed SLC project will not only lead to a better understanding of the physics world thorugh the experiments to be done using it, but it will also pioneer a new accelerator technology which promises to reduce the cost of future generations of electron-positron machines.

B. Brief Description of the Project

The SLC is designed to operate at energies up to 100 GeV in the center-of-mass system with a luminosity at 100 GeV of $10^{30}\ cm^{-2}sec^{-1}$. The project can be increased in energy at a later time to 140 GeV in the center-of-mass, should that become desirable.

The main components of the project are the SLED II conversion of the SLAC linac; a transport system from the end of the linac to a small-aperture magnet ring; the magnet ring itself; a special focusing system near the interaction point; the necessary housing; an experimental hall and staging area; a high-power positron-production target; a positron booster; a transport system from the positron target at the two-thirds point of the linac back to the injection end of the linac; a new high-peak-current electron gun; two small storage rings to reduce the emittances of the electron and positron beams by radiation damping; pulse compressors to reduce the length of the bunches in the storage ring before injection into the linac; and the necessary instrumentation and control systems for both the linac and the Collider system. A schematic of the complete system is shown in Fig. 1, and Table 1 summarizes the important parameters.

Since the Collider is a new kind of machine, a typical operation cycle is described below. This cycle begins just before the pulsing of the linac. The electron and positron damping rings each contain two bunches of 5×10^{10} particles at an energy of about 1.2 GeV. One of the positron bunches is extracted from the damping ring, passes through a pulse compressor which reduces the bunch length from the centimeter typical of the storage ring to the millimeter required for the linac, and is then injected into the linac. Both electron bunches are extracted from the electron damping ring, pass through an independent pulse compressor, and are injected into the linac behind the positron bunch. The typical spacing between bunches is about 15 meters in the linac.

The three bunches are then accelerated down the linac. At the two-thirds point, the trailing electron bunch is extracted from the linac with a pulsed magnet and is directed onto a positron-production target. The positron bunch and the leading electron bunch continue to the end of the linac, where they reach an energy of 50 GeV.

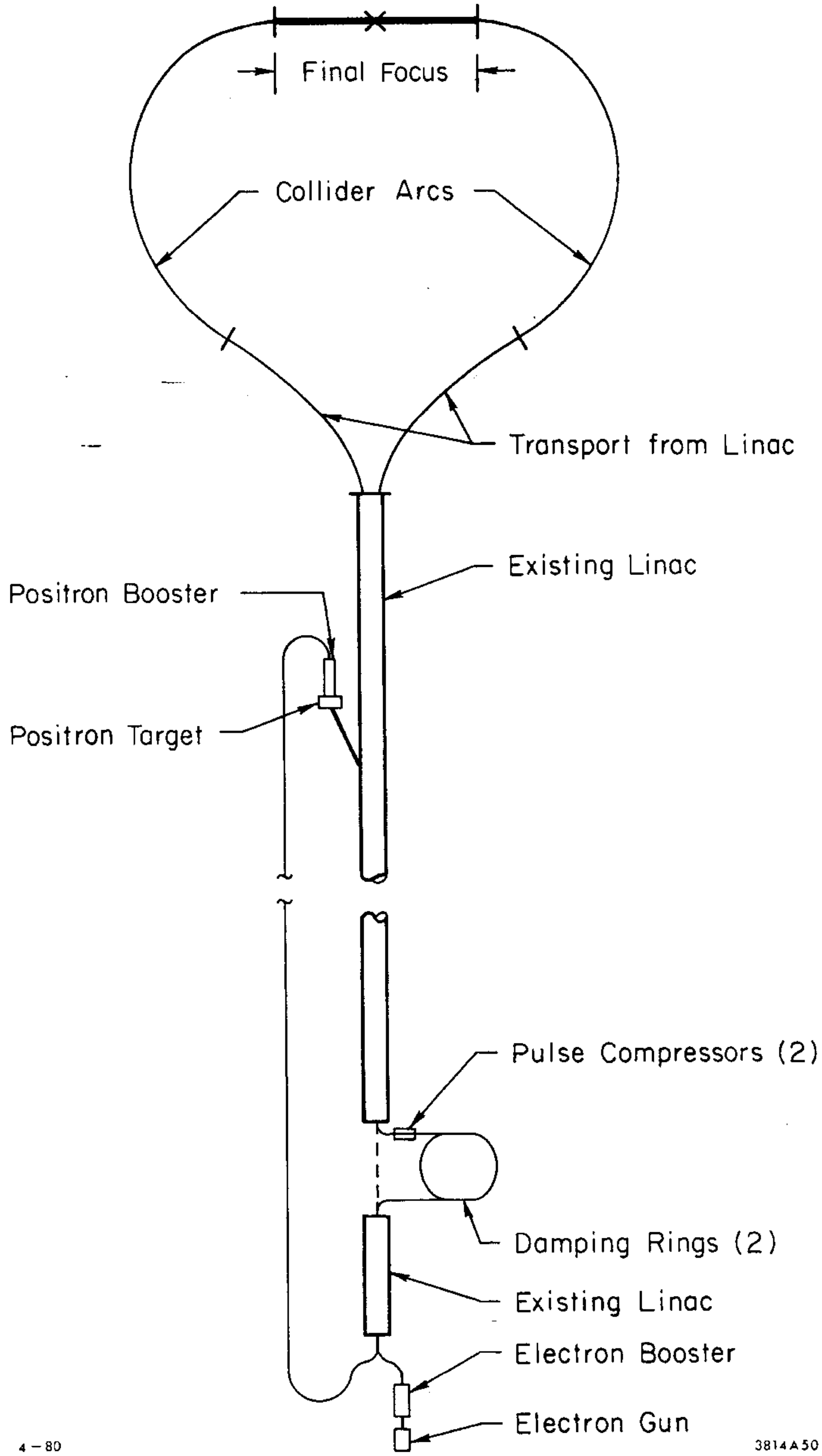

Fig. 1. General layout of the SLAC Linear Collider.

TABLE 1

Parameters of the SLC at 50 GeV

A. Interaction Point	
Luminosity	10^{30} cm^{-2}sec^{-1}
Invariant Emittance ($\sigma_x \sigma'_x \gamma$)	3×10^{-5} rad-m
Repetition Rate	180 Hz
Beam Size ($\sigma_x = \sigma_y$)	2 microns
Equivalent Beta Function	1 cm
B. Collider Arcs	
Average Radius	300 m
Focusing Structure	AG
Cell Length	5 m
Betatron Phase Shift per Cell	110°
Full Magnet Aperture (x;y)	10; 8 mm
Vacuum Requirement	$< 10^{-2}$ Torr
C. Linac	
Accelerating Gradient	17 MeV/m
Focusing System Phase Shift	360° per 100 m
Number of Particles/ Bunch	5×10^{10}
Final Energy Spread	± 1/2 %
Bunch Length (σ_z)	1 mm
D. Damping Rings	
Energy	1.21 GeV
Number of Bunches	2
Damping Time (Transverse)	2.9 ms
Betatron Tune (x;y)	7.1; 3.1
Circumference	34 m
Aperture (x;y)	±5; ±6 mm
Bend Field	19.7 kg

At the end of the linac, the two opposite-charge bunches are separated by a DC magnet, pass through a transport system which matches the focusing of the linac to that of the main Collider ring, and then begin to travel around the ring in opposite directions. The Collider ring is composed of small-aperture magnets with very strong alternating-gradient focusing, which is required to hold down emittance growth in the Collider arcs. After emerging from the arcs, the bunches pass through an achromatic matching and focusing section which focuses the beams to a very small size at the collision point.

The positrons produced by the "scavenger" electron bunch that was extracted at the two-thirds point of the linac pass through a focusing system at the positron source, a 200 MeV linear accelerator booster, a 180° bend, and an evacuated transport pipe located in the existing linac tunnel. This brings the positron bunches back to the beginning of the linac. At this point, the positron bunch passes through another 180° bend and is boosted to an energy of 1.2 GeV in the first sector of the existing linac and is then injected into the damping ring.

Because the emittance of the positron beam is very much larger than that required for Collider operation, a positron bunch must remain in the damping ring for approximately four radiation damping times, which corresponds to twice the time interval between linac pulses. Thus the positron bunch to be used in the next linac cycle is the one that is still stored in the damping ring from the previous cycle.

Electrons for Collider operation are produced from a special gun equipped with a subharmonic buncher and located at the beginning of the linac. Two bunches of electrons are produced, are boosted to 200 MeV in a dedicated section of linac, and are then injected into the same section of linac used to boost the positron bunch to 1.2 GeV. At the end of this section the 1.2 GeV electrons are injected into their own damping ring. The electron bunches at the time of injection into their damping ring have an emittance somewhat larger than required for Collider operation but considerably smaller than the emittance of the positron bunch and thus need only be damped for two damping times or one interpulse period. The entire cycle repeats 180 times per second.

The SLC project is estimated to cost $63 million (March 1980 prices) and to require a construction period of three years.

Section II of this report gives detailed descriptions of the various components and systems of the project. In Section III, an analysis is made of the novel background problems that will be encountered in experiments using the Collider, and the scale of detector systems required for experiments is studied in order to determine the appropriate size of the experimental halls. Section IV describes the project's conventional facilities. Section V gives the estimated budget and construction schedule for the project. Finally, a series of Appendices is included which discuss in detail some of the new accelerator physics issues that are involved in Collider design.

C. Physics Potential

During the past decade, while electron-positron colliding-beam experiments were illuminating particle properties, the fixed-target machines were making great strides in measurements of the weak interaction. A new manifestation of the weak interaction, the neutral current, was discovered, and both the electromagnetic and weak structure-functions of the proton were measured.

From all of this experimental work, a new theoretical picture has emerged which interprets both the weak and electromagnetic forces as different manifestations of ONE basic force. This unifying concept is known as gauge theory, the simplest form of which is the "standard model" of Weinberg and Salam. All of the variants of gauge theory have one or more heavy particles which interact with the electron-positron system in the same basic way as does the ordinary massless photon. It is the interaction of this heavy gauge particle (Z^o) and its charged companions that is responsible for the properties of what is called the weak interaction. Gauge theories have had so much success in explaining apparently unrelated facts that they are generally believed to be correct.

The SLC is designed to have a total energy large enough to produce these neutral gauge particles. When the energy of the colliding beams matches the mass of the Z^o (about 90 GeV), thousands of Z^o will be produced per day. The decay of these Z^o's into quarks, leptons, and perhaps other more exotic particles, will give a vast amount of information about a broad spectrum of basic physics questions ranging from the number of elementary building blocks which make up our world, to the possible relation of the strong interaction to the weak and the electromagnetic, to the conditions in the early universe when it was only a few seconds old. These physics opportunities are discussed in detail in Section III.

The gauge particles may be discovered by other machines which come into operation earlier than this project (the antiproton-proton collider at CERN, for example), but experiments on these other machines can give only a small fraction of the basic information to be obtained from an electron-positron machine.

There is always the possibility that the present picture is wrong: that there are no heavy gauge particles. This would force a fundamental change in our thinking about the ways of nature, and the data obtained with the SLC would point toward a better road.

D. Compatibility with other SLAC Operations

The operation of the SLAC linac in the era of the Collider must be compatible with other programs at SLAC that will use the linac. It is difficult to project a detailed laboratory program for the second half of the 1980's, but present plans would call for operation of the PEP and SPEAR storage rings, test beams in the research area for the development of new detectors and apparatus, and fixed-target experiments that would probably require the high-energy and high-intensity beams available from the upgraded linac.

When the linac is set up for Collider operation, the focusing system along the machine is capable of delivering beams at the end of the accelerator with any energy greater than about 20 GeV. The storage rings require both electron and positron beams at energies ranging from 2 to 17 GeV, and are therefore not compatible with Collider operation on a pulse-to-pulse interlaced basis without the addition of an expensive pulsed-focusing system capable of changing focusing in less than 5 ms. Since the storage rings only require the use of the linac for a few minutes per hour for refilling, an alternative system would dedicate the linac to the storage rings for those few minutes. This requires only that the quadrupoles on the linac be capable of being reset to their new values in a few seconds. Since this procedure results in a very much less costly system than the interlaced pulse-to-pulse system, we shall adopt it for storage-ring filling. The positron intensity from the new source required for the Collider will be much greater than that available at present, and the filling times of the storage rings will be correspondingly reduced.

Test beams for apparatus development require only low intensities. These beams can be generated as secondary beams from targets struck by the primary Collider beam. The existing pulsed-magnet system is capable of diverting pulses as required from the Collider to a secondary-beam target.

The potential demand for high-energy, high-intensity beams for fixed-target experiments some five years hence is not clear at this time. There is no problem in delivering the two electron bunches that will be used in a Collider cycle to the end of the accelerator, and then diverting these bunches down the existing beam lines. This mode of operation will give 10^{11} electrons per pulse (150 KW at 50 GeV, 180 pps). Should longer duty cycle beams be required, we have included in the Collider design a provision for pulsed magnets at the take-off point from the linac to the damping rings. These pulsed magnets allow the damping system to be bypassed, and thus any beam with energy greater than 20 GeV can be generated and interlaced with the Collider beams, up to the full pulse length of SLED II (approximately 200 nsec).

We estimate that storage-ring operation and test-beam operation will require about 10% of the linac pulses. This does not seriously impact the Collider luminosity. A major fixed-target experiment would, however, compete for the available electrons, and the scheduling of such experiments would be a matter of physics priorities.

II. GENERAL DESCRIPTION

A. 50 GeV Beams From the SLAC Linac

1. Present Linac Capability and Upgrading for SLC

As this report is being written, the SLAC linac is capable of producing 1.6 μsec electron beam pulses with a maximum energy of 23.8 GeV. This energy is obtained with a complement of about 240 klystrons, each supplying 2.5 μsec RF pulses to a 12.5 m girder supporting four 3.05 m constant-gradient accelerator sections. The present klystron population contains a mixture of older tubes with nominal peak powers of 20 and 30 MW, and newer tubes of 38 MW. The average is about 25 MW, which yields approximately 100 MeV per station in accordance with the simple expression $E_{MeV} = 20\sqrt{P_{MW}}$. When SLED I is used, this energy can be increased by a factor of 1.4 to a maximum of about 33.3 GeV. By comparison, the upgrading program necessary to meet the SLC specifications is summarized in Table 2:

TABLE 2

Linac Upgrading Program for SLC

	1980	SLC
Average peak power per klystron	25 MW	38 MW
Number of "standard" in-line girders	238	236
Energy per girder without SLED	100 MeV	123 MeV
Maximum energy without SLED	23.8 GeV	29 GeV
Energy per girder with SLED I	140 MeV	
Maximum energy with SLED I	33.3 GeV	
Energy per girder with SLED II		220 MeV
Maximum energy with SLED II		51.6 GeV
RF pulse length	2.5 μsec	5.0 μsec
Maximum repetition rate	360 pps	180 pps
AC power	≃ 28 MW	≃ 28 MW

As shown, attainment of the SLC specifications will require the installation of SLED II and an increase in average peak klystron power from 25 to 38 MW. It is expected that this increase in klystron power will take place through simple attrition of the older tubes and replacement of some tubes by newer ones. In addition, the linac will have to undergo a number of other improvements and modifications. These include:

(a) Layout changes to allow incorporation of SLC components while at the same time presserving conventional SLAC operation including fixed-target, SPEAR and PEP beams.

(b) An upgraded beam-guidance system with new quadrupoles, steering dipoles and beam-position monitors independently sensitive to the three bunches (e^+, e^- and e_s^-).

(c) Improved alignment using the existing laser-alignment system.

(d) Improved overall instrumentation and control.

These various topics will now be discussed in some detail.

2. Layout Modifications

The principal modifications in linac layout will take place in the injector, Sectors 1 and 2 and Sectors 19 and 20. Figure 2 illustrates the major changes schematically. The SLC special injector will be located upstream of the regular SLAC off-axis guns in a room with separate access and shielding. A prototype of this injector will be installed in the summer of 1980. (Details of this system are described in Section II.G.) The beam from this injector will consist of two e^- bunches, the e^- bunch destined for the Collider, and the e_s^- "scavenger" bunch that will be used to produce positrons. Both bunches will have an energy of about 40 MeV and will receive further acceleration up to 200 MeV by passing through the regular injector and Stations 1-A, B and C, which are powered by individual klystrons and are not equipped with SLED systems. At this point, the two e^- bunches meet with the e^+ bunch returning from the positron source, and through a DC combiner magnet they are injected into the accelerator at girder 1-2. From here on, all stations can work in the SLED II mode.

At the end of Sector 1, where the beams have reached an energy of 1.2 GeV, the e^-e^+ bunches are again separated by a DC splitter magnet and transported to their damping rings, where they spend, respectively, one or two interpulse periods (5.6 or 11.2 msec). They are then ejected from the two rings, compressed, and by means of another DC combiner magnet reinjected into Sector 2 of the linac. Note that for this purpose a 15-m

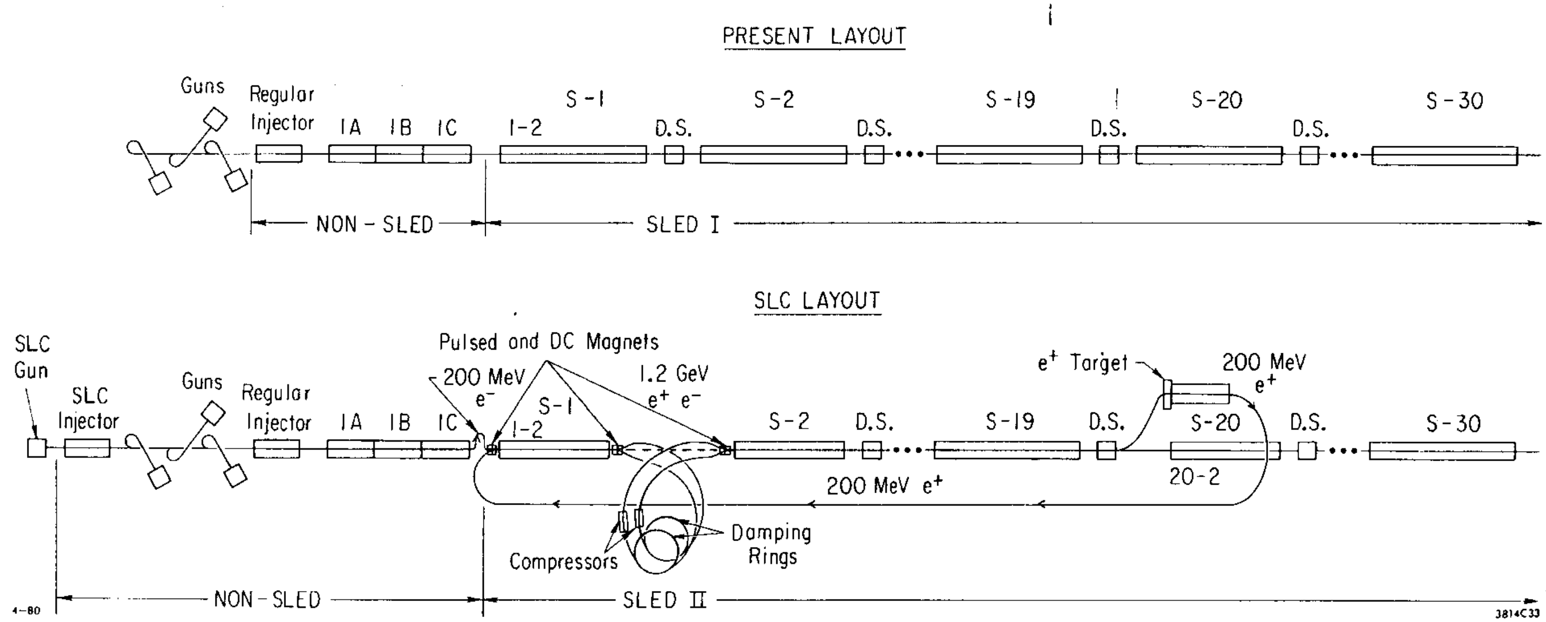

Fig. 2. Schematic of the linac modifications planned for the SLC.

length of standard accelerator must be removed to make room for the extraction and reinjection systems. (For details, see Section II.F.) With SLED II, the gain from here on is uniformly 220 MeV per girder.

The e^-e^+ bunches are now on their way to their ultimate 50 GeV destination, whereas the e_s^- scavenger bunch travels only to the end of Sector 19, where it is deflected into the positron-source area. It is at this location that another 15 m of standard accelerator length must be removed and the positron bunch is generated, focused, accelerated to 200 MeV, and bent backwards to be returned to its reinjection point at girder 1-2. (For details of the positron-production system, see Section II.E.) Note that the trip of the scavenger e_s^- bunch from the injector to the positron source and the return of the e^+ bunch to Sector 1 is about 4 km long and thus takes about 13 μsec. For this reason, the injector and Sector 1 will be triggered 13 μsec after the rest of the accelerator.

3. SLED II

The principle and operation of SLED have been described in several published documents[1-4] and will not be presented here in any detail. The SLED I parameters were summarized in the left-hand column of Table 2. SLED I installation is now complete, and operation of the linear accelerator in the SLED I mode for physics experiments has already begun. SLED II is simply an extension of SLED I in which the RF pulse length is doubled from 2.5 to 5 μsec, thereby giving the storage cavities more time to charge up; this yields higher effective power, and the energy gain is increased from 1.4 to approximately 1.8. SLED II overall performance was summarized in the right-hand column of Table 2. A theoretical curve of energy gain vs time during the pulse is shown in Fig. 3. This curve has been verified experimentally on several accelerator sections.

The physical modifications required to go from SLED I to SLED II involve only the high-power modulators and the pulse transformers which must produce the high-voltage pulses (270 kV, 5 μsec) for the 38 MW klystrons. The SLED cavities remain the same: TE_{015} mode, $Q_o = 10^5$, coupling coefficient $\beta = 5$. The parallel pulse-forming network (PFN) arrangement in the present modulators is replaced by a series arrangement

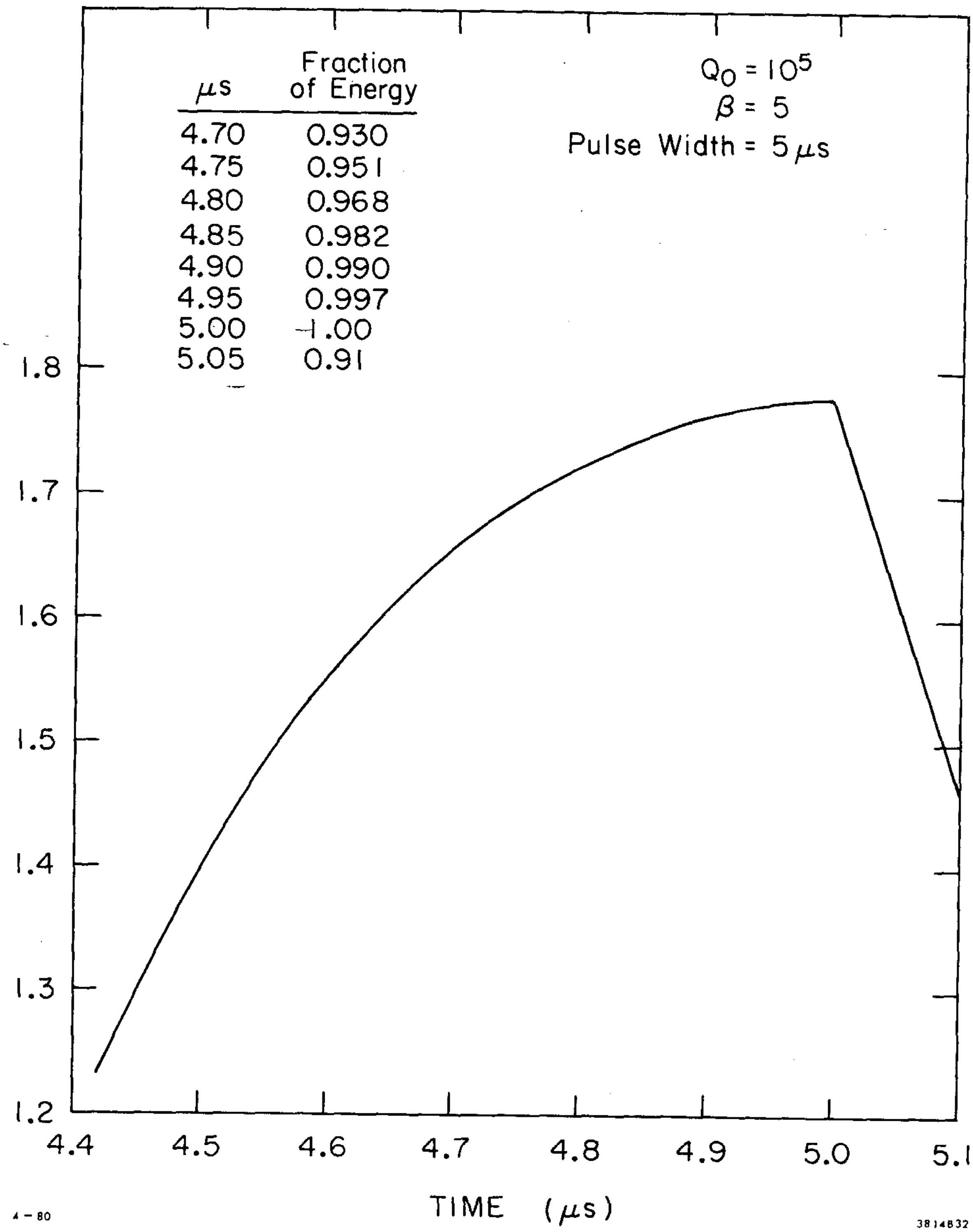

Fig. 3. SLED II energy gain vs time during the RF pulse.

for SLED II. A switch is provided half-way through the PFN that can be used to shorten the pulse length back from 5 to 2.5 μsec and thus to restore present operation. The pulse transformer size is increased to provide the added inductance for the longer pulse. This in turn leads to an increase in the size of the pulse transformer tanks under the klystrons. For installation of SLED II, these will be brought back to the shop, one by one, for proper substitution of the tanks.

As mentioned above, the SLED II principle has been tested successfully on a number of experimental stations. Up to a voltage of 258 kV, corresponding to a peak power of ≈34 MW, the operation of these experimental stations has been essentially routine. Above 258 kV, it has been found that the recycling rate (normally about 1 recycle per hour) of the klystron-modulator system due to various types of faults (overcurrent, overvoltage, reflected power, vacuum) can increase by a factor of 10-50 depending on exact conditions. To correct this situation, two programs are presently underway. One is to improve the klystron gun design to decrease the risk of arcing which leads to overcurrent faults. The second is to make a careful statistical study of the eight klystrons (in Sector 9 of the accelerator) which are presently being converted to SLED II operation. Special diagnostic and data-acquisition equipment is being installed to study the causes of increased fault rates and to indicate possible remedial changes in the klystron-modulator protection interlocks.

The maximum energy reachable with SLED II and the available complement of klystrons and accelerator girders is 51.6 GeV. In practice, the energy will be a few percent lower because:

(a) The three bunches will ride about 50-100 nsec apart from each other and will not all be at the top of the SLED II curve (see Fig. 3).

(b) A few spare klystrons will always be kept in reserve for smooth operation.

(c) The bunches will have to ride ahead of the RF wave crest in order to compensate for the effects of beam loading within each bunch from wake fields. The latter problem is discussed in a separate note.[5] An example for a 5×10^{10}, 24° truncated gaussian bunch with a σ of 4° centered 15° ahead of crest (i.e., with the head of the bunch at $\theta_o = 27^\circ$)

is shown in Fig. 4. Most of the charge is contained within 400 MeV or a $\Delta E/E$ of 0.8%. Note the comparison with a 5×10^8, identical gaussian bunch riding at the same angle but with insufficient charge to produce energy compression.

In order to make up for these energy decreases, it will be possible to add a few klystrons, modulators and SLED cavities by "doubling-up" on a few stations. The energy gained per girder by doubling-up is about 90 MeV.

4. Upgraded Beam-Guidance System

The design value of the beam emittance at the end of the SLAC linac is 3×10^{-10} radian-meters at 50 GeV or 1.5 (keV/c) cm. If there were no risk of emittance growth from the damping ring-compressor through the end of the linac, the present linac focusing system would probably be adequate. The present system consists of DC singlets every 12.5 m from Sectors 1 through 6, pulsed singlets every 12.5 m from Sectors 7 through 10, and pulsed doublets (28 m spacing) every 100 m from Sectors 11 through 30. The betatron wavelength is about 130 m in the first ten sectors and 400 m beyond that point. This focusing system was designed to allow multiple interlaced beam operation up to 30 GeV (SLED I) and to control multibunch beam breakup for pulses up to 200 mA and 200 nsec. Successful operation at these levels has now been verified experimentally.

The focusing system for the SLC has to be strengthened considerably above these levels because the beta-function must be minimized in order to control single-bunch beam breakup caused by the excitation of transversely deflecting wake fields when the bunches wander off-axis. Stronger focusing is planned, as well as steering and position detection at each quadrupole, in order to control the effects of all transversely acting fields. These include (a) the wake fields produced by the bunches themselves, (b) the stray DC fields produced by quadrupole misalignments which deflect the electrons and positrons in opposite directions, and (c) the RF fields from accelerator misalignments and coupler effects which deflect the electrons and positrons in the same direction.

The lattice that has been chosen and the criteria that led to its design are described in detail in Appendix A. It is a 25-m-cell FODO

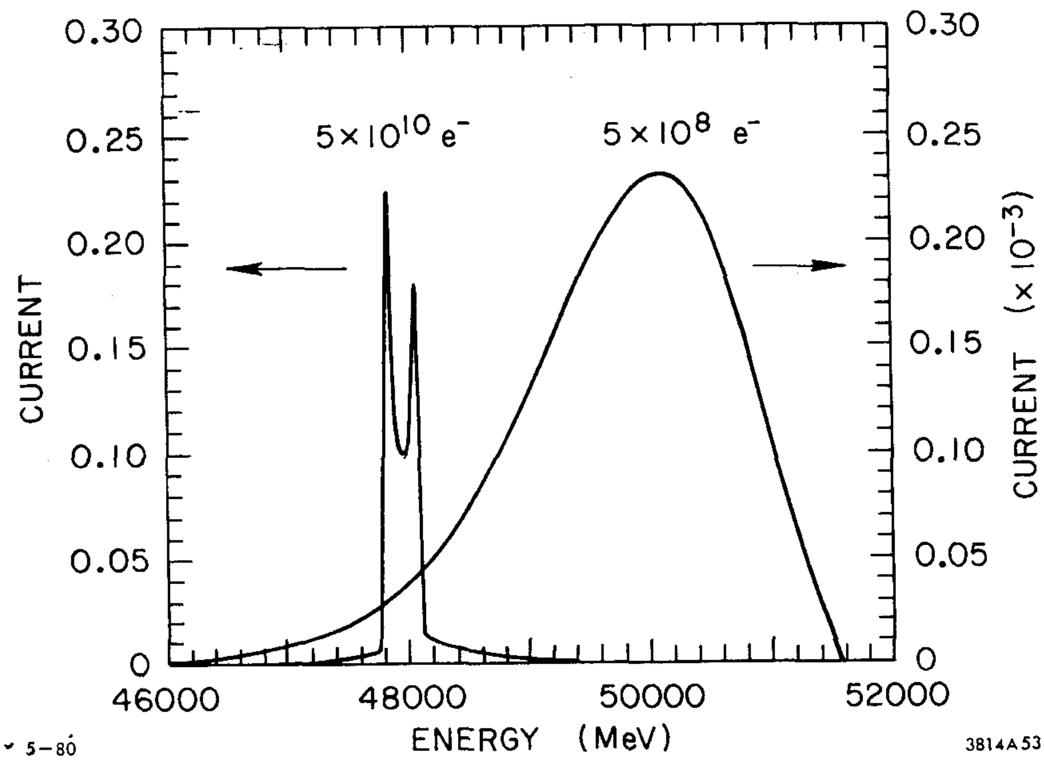

Fig. 4. Energy spread for two truncated Gaussian bunches ($\sigma = 4^o$, total length = 24^o) both riding with head at $\theta_o = 27^o$ ahead of crest. Note the difference between the right and left vertical scales.

array, with a quadrupole singlet at the end of each accelerator girder and a doublet at the end of each sector where there is a 3-m drift section, i.e., a total of 9 quadrupoles per sector. In order to obtain the required stability, the array will use only DC quadrupoles; most of the present pulsed quadrupoles will have to be removed. The existing steering dipoles and microwave position monitors, which are located in the drift sections every 100 m, will probably remain in place for use with conventional multibunch beams. For SLC operation, each of the 270 quadrupoles will carry four extra trim-windings for vertical and horizontal steering, and each will contain (within the vacuum chamber) an x-y strip-line position monitor for separate e^+, e^- and e_s^- position detection. A sketch of the assembly is shown in Fig. 5, and the design specifications for the quadrupole are given in Table 3. The maximum integrated gradient-length of about 107 kilogauss will make it possible to maintain a 90^o betatron phase advance per cell up to 25 GeV (Sector 15) then gradually tapering down to 42^o per cell at 50 GeV (Sector 30).

TABLE 3

Linac DC Quadrupole Specifications

Maximum gradient-length product	107 KG
Maximum gradient	9.9 KG/cm
Maximum pole-tip field	12.8 KG
Aperture radius	1.29 cm
Magnet length	14 cm
Maximum current	220 amps
Maximum voltage	17.5 volts
Maximum power consumption	3.85 KW
Maximum current density	1544 A/cm^2
Water cooling flow	1.57 gpm
Magnet weight	115 lbs
Number of main turns per pole	36
Number of trim turns per pole (for steering and alignment)	40 at 10 amps

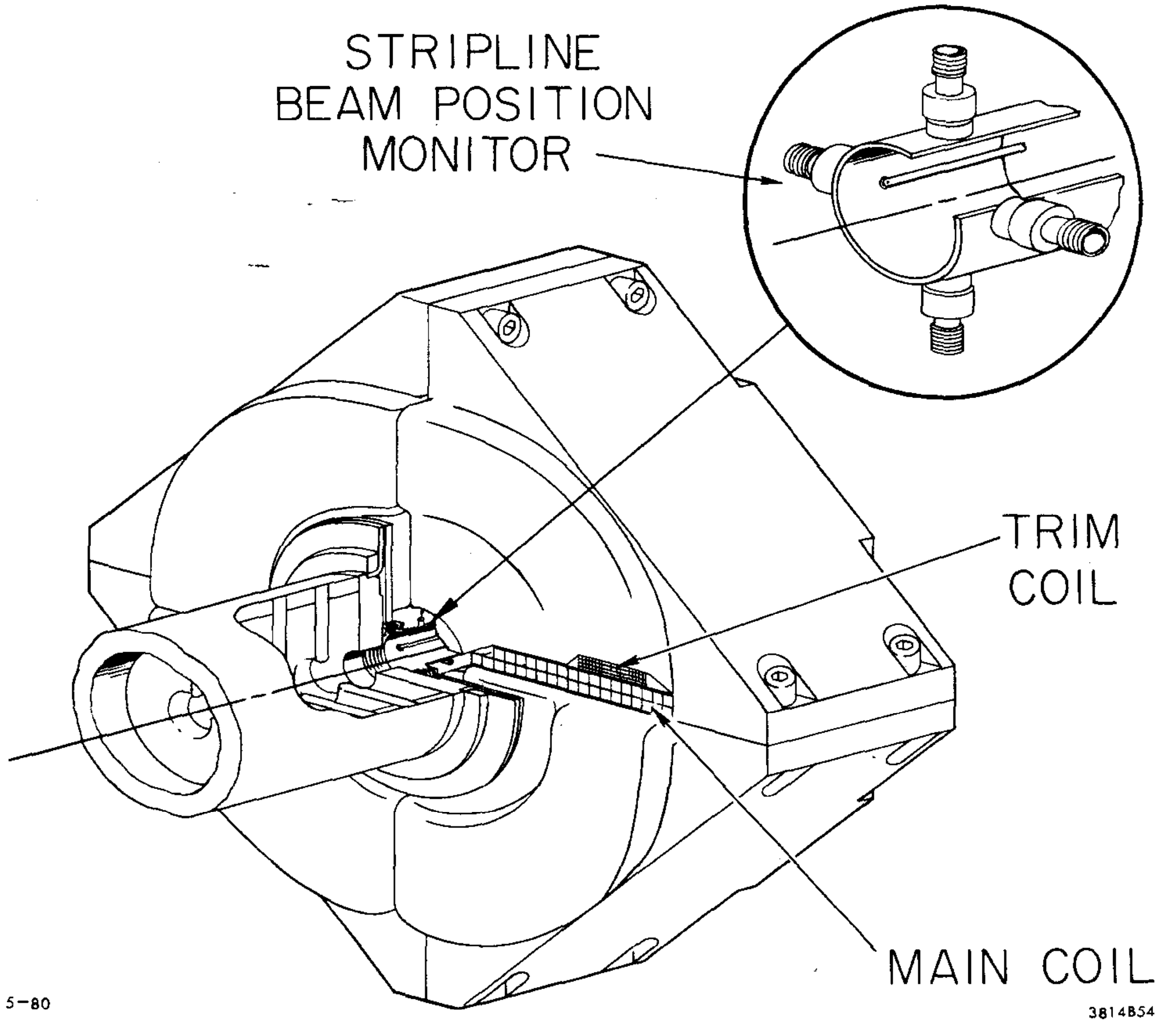

Fig. 5. Linac DC quadrupole assembly.

Prototypes of the quadrupole, steering dipoles and strip-line position monitors are presently being built and will be tested in several locations along the accelerator, in particular in Sector 1, in conjunction with early injector tests. The position monitors will be self-jigging in relation to the adjacent accelerator sections so as to keep them centered with respect to these accelerator sections to within 25 μm ($\simeq$ 1/1000 of an inch).

In parallel with these efforts, a plan is being developed to make full use of the capabilities of the laser alignment system of the accelerator. By design, this system is believed to be capable of 25 μm alignment reproducibility, with absolute rms errors of about 100 μm. In recent years it has rarely been used to these tolerances, which have simply not been needed to satisfy accelerator operation (alignment to 250 μm has generally been sufficient).

B. The Transport System

The purpose of this system is to carry the two beams emerging from the linac through the switchyard and research areas to the Collider arcs. This should be done in a manner that minimizes costs and the disruption of existing SLAC experimental facilities. Figure 6 shows the general scheme that has been chosen to achieve this end.

The starting point (suitably matched) is located in the central (C) beam line just after Dump D-2. The beams are horizontally split by a DC magnet and follow the paths indicated on the figure by the heavy lines. Bending radii are always in excess of 300 meters and, as can be seen, the paths avoid the heavy structural members of the beam switchyard housing. Most of the tunneling (in compacted dirt fill) will be done from the east end. What little material has to be removed through the switchyard is "road base" gravel, which can be carried out on mucking cars mounted on existing shielding-car rails.

The north beam line will be pitched downward so that by the time it emerges into the research yard it will below grade, entering an existing utility tunnel parallel to End Station A. The line then runs in a cut-and-cover tunnel, crosses the yard, and enters the shielding berm near Beam Dump East. The south line is pitched down to emerge from the

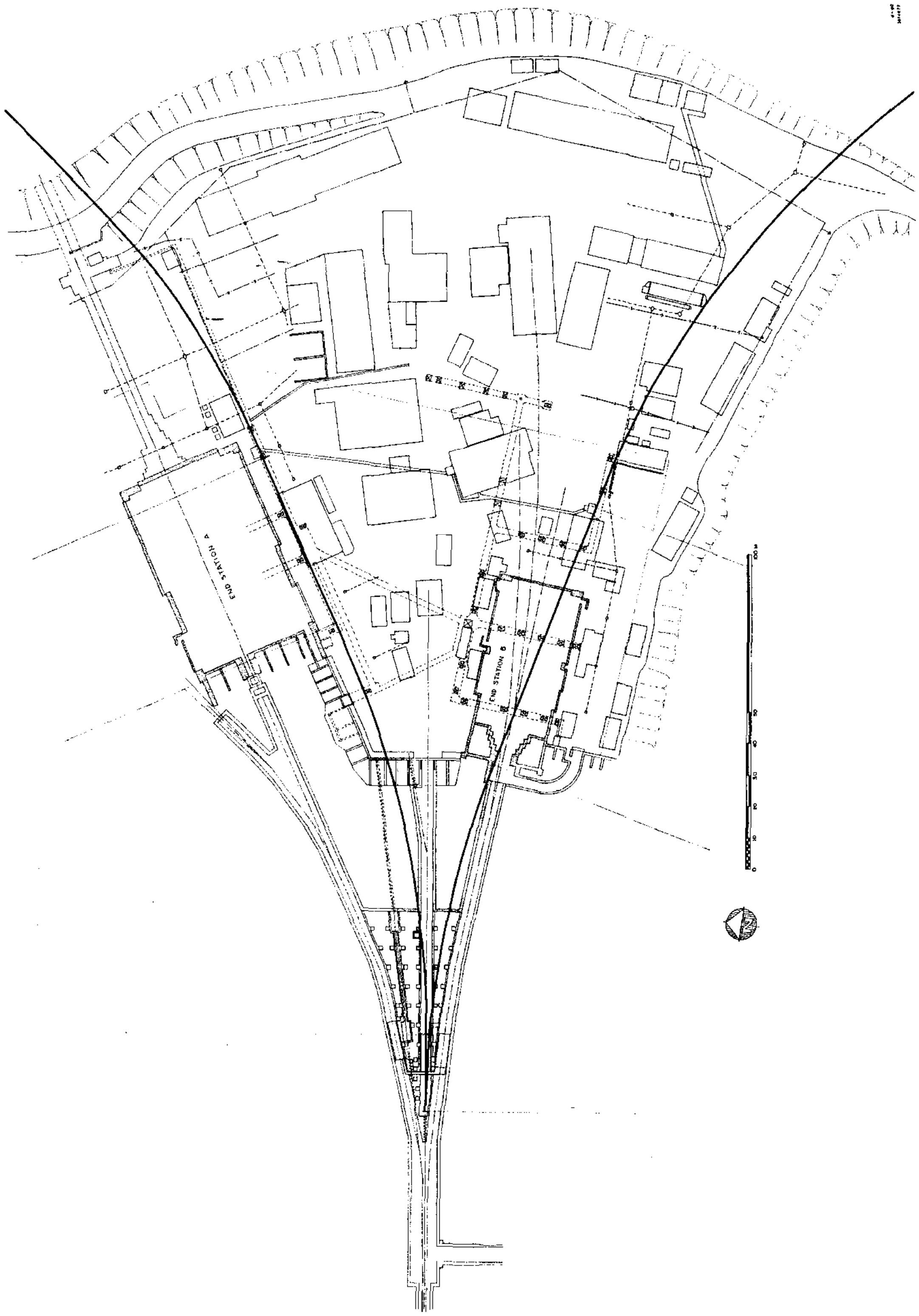

Fig. 6. Transport of SLC beams through the Beam Switchyard.

switchyard at floor level in End Station B near the B target room. Penetrating the floor of ESB, it follows a cut-and-cover tunnel crossing the research yard and then into the south Collider arc. It is estimated that down-time in the switchyard proper can be held to less than 6 months. Since the PEP injection tunnels branch off far upstream of the construction activity, it is possible with proper shielding and modifications of the personnel protection system to maintain PEP operations during most of the construction period.

Should it become desirable to bring a particle beam down the C line in the future, this will be accomplished by a pulsed "anti-splitter" in one leg of the Collider channels. In this way, the critical steering required for Collider operation is disturbed only by the remanent field of the pulsed magnet. This almost-zero remanent field can be much more easily stabilized than the pulsed field itself.

With the exception of the splitter magnet and a few matching quads in straight sections, the magnets in the new switchyard tunnels will be identical to those used in the Collider arcs, because the average radius of curvature has been chosen to be the same as that of the arcs.

C. The Collider Lattice

1. General

It is the function of the magnet lattice in the Collider arcs to bend the high-energy e^+ and e^- beams from the SLAC accelerator in such a manner that they will collide head-on with as little dilution of phase space and loss of energy as possible. Quantum effects in the synchrotron-radiation energy-loss mechanism, coupled with the finite amplitude (β) and dispersion (η) functions of the lattice, will cause some emittance growth. (See Appendix B.) For a given gradient in an alternating-gradient structure, the growth $\Delta\varepsilon$ is roughly proportional to L_m^3/ρ^4, where L_m is the length of a single focusing (F) or defocusing (D) magnet, and ρ is the bending radius.[6] This speaks for a lattice of large radius containing many short high-gradient magnets of small aperture. In the adopted design, capable of transporting beams of energy up to 70 GeV with acceptable dilution, ρ is approximately a site-limited 300 meters, and the maximum guide field B_0 is 8 KG, with a gradient not in excess of

$g = 10$ KG/cm. The tune of an equivalent circular machine would be around $\nu \simeq 100$, with an average $\bar{\beta} \simeq 3$ m. For phase advances between 90^o and 130^o per FD cell, the magnets are typically around 2 meters in length.

2. Magnet Profile

The first published article on strong focusing[7] contains the design concepts of a magnet having the above required characteristics. A suitable magnet cross section is shown in Fig. 7. The distance between the position of the equilibrium orbit and the neutral pole is $K = B_o/g = 8$ KG/10 KG/cm = 0.8 cm. Studies[8] with the program POISSON show that a good field region of ±5 mm is obtainable. Such a region is entirely adequate to contain the miniscule beam size $\sigma_x \simeq \sigma_y \simeq .03$ mm, with additional room for initial orbit distortions of several millimeters. The profile finally chosen will be shaped to produce a mild sextupole term to cancel chromatic effects in the arcs. An analysis of capital construction costs in relation to operating power costs indicates the use of aluminum as a conductor material and a generous coil window. Some parameters of the arc magnets, including the reverse-bend transport system magnets, which are of identical design, are shown in Table 4. Saturation properties are shown in Figs. 8 and 9.

3. Construction

(a) General

A circumference-filling factor of about 95% is made possible by threading 4 magnet cores on common coil conductors and "refrigeration tubing" vacuum chamber to form modules, as shown in Fig. 10. Only a few centimeters remain between core blocks, enough for miniature position-monitor stations. To facilitate installation by minimizing work in the narrow tunnel, it is proposed that each 10-meter-long module be completely assembled, to some extent aligned, and contain the complement of services, cabling, pumps, instrumentation, etc., necessary for operation. All that should be required in the tunnel is to roll in prefabricated modules, mount the girder, interconnect the busses, cabling harness and vacuum, and perform final alignment.

The Collider arc tunnels, for site-related reasons, are not in a horizontal plane. To simplify the resulting survey problems, each arc

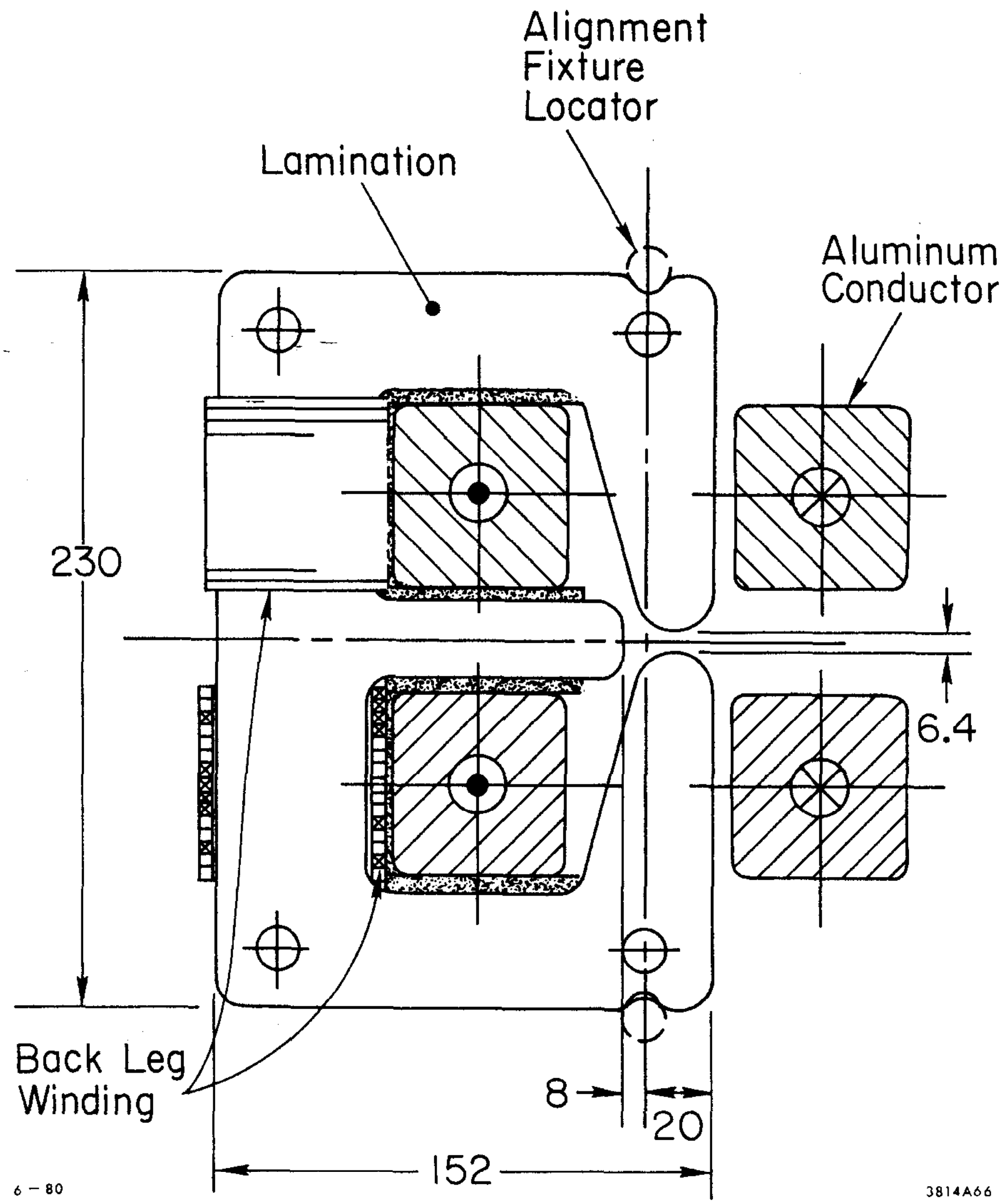

Fig. 7. Cross section of the SLC arc magnets. Dimensions are in millimeters.

TABLE 4

SLC Main Ring Bend Magnet Parameters at 50 GeV

		Type A	Type B
Magnet designation		6AG2400	6AG1600
Number of magnets		635	635
Field @ 50 GeV	(KG)	5.7	5.7
Field integral @ 50 GeV	(KGm)	13.68	9.12
Gap height	(mm)	6.4	6.4
Width of good field	(mm)	10	10
Core length	(mm)	2394	1594
Core weight	(lbs)	1034	689
Lamination width	(mm)	152	152
Lamination height	(mm)	230	230
Amp-turns/pole		3830	3830
Turns/pole		1	1
Conductor cross section	(mm)	52.3 × 57.1	
Conductor area	(mm^2)	2733	2733
Cooling hole diameter	(mm)	17.8	17.8
Current	(amps)	3830	3830
Resistance @ 40°C	(mohms)	0.1	0.07
Power	(KW)	1.66	1.10
Voltage	(V)	0.383	0.295
Current density	(A/mm^2)	1.4	1.4
Coil weight	(lbs)	158	105
Number of water circuits		4	4
Water flow rate/magnet	(gpm)	0.3	0.2
Temperature rise	(°C)	20	20
Water flow velocity	(ft/sec)	0.2/ckt	0.2/ckt

Note: Trim steering 4% of main, with 15 turns/pole, 10 ga. sq. copper.

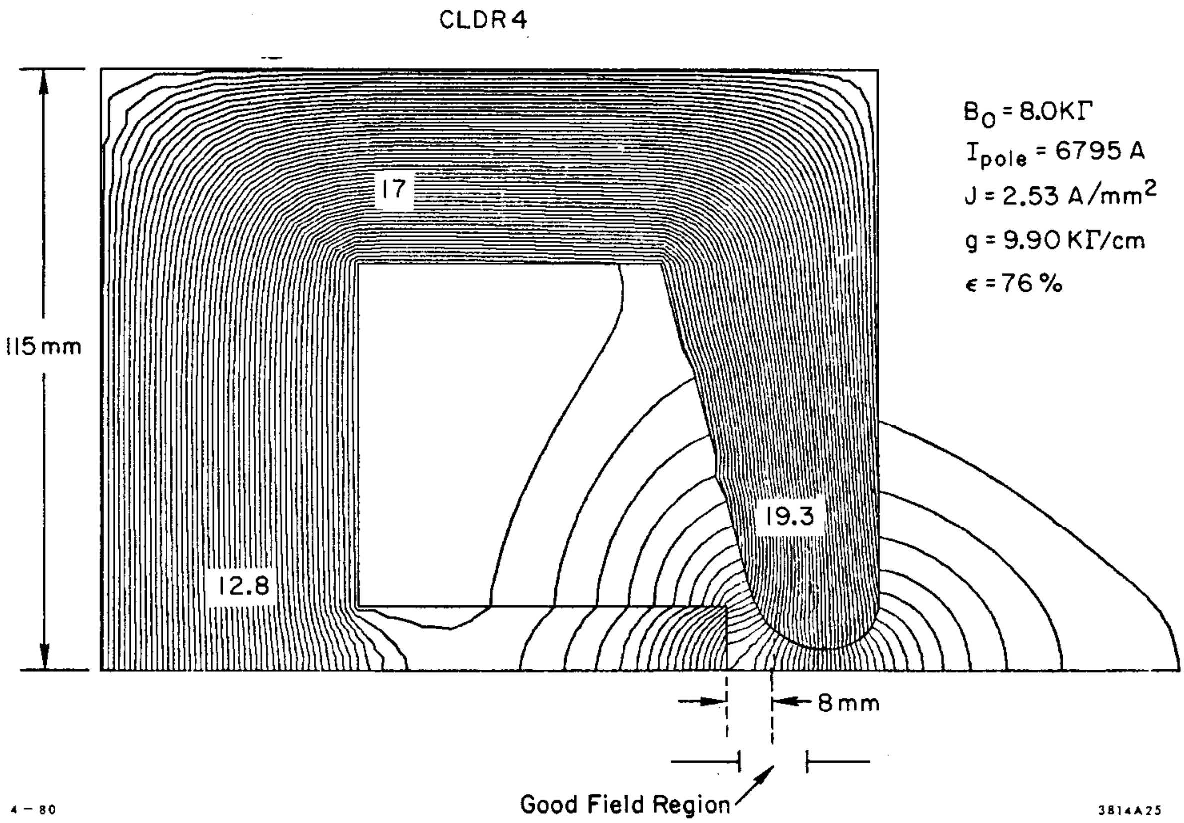

Fig. 8. Field distribution in the SLC arc magnets.

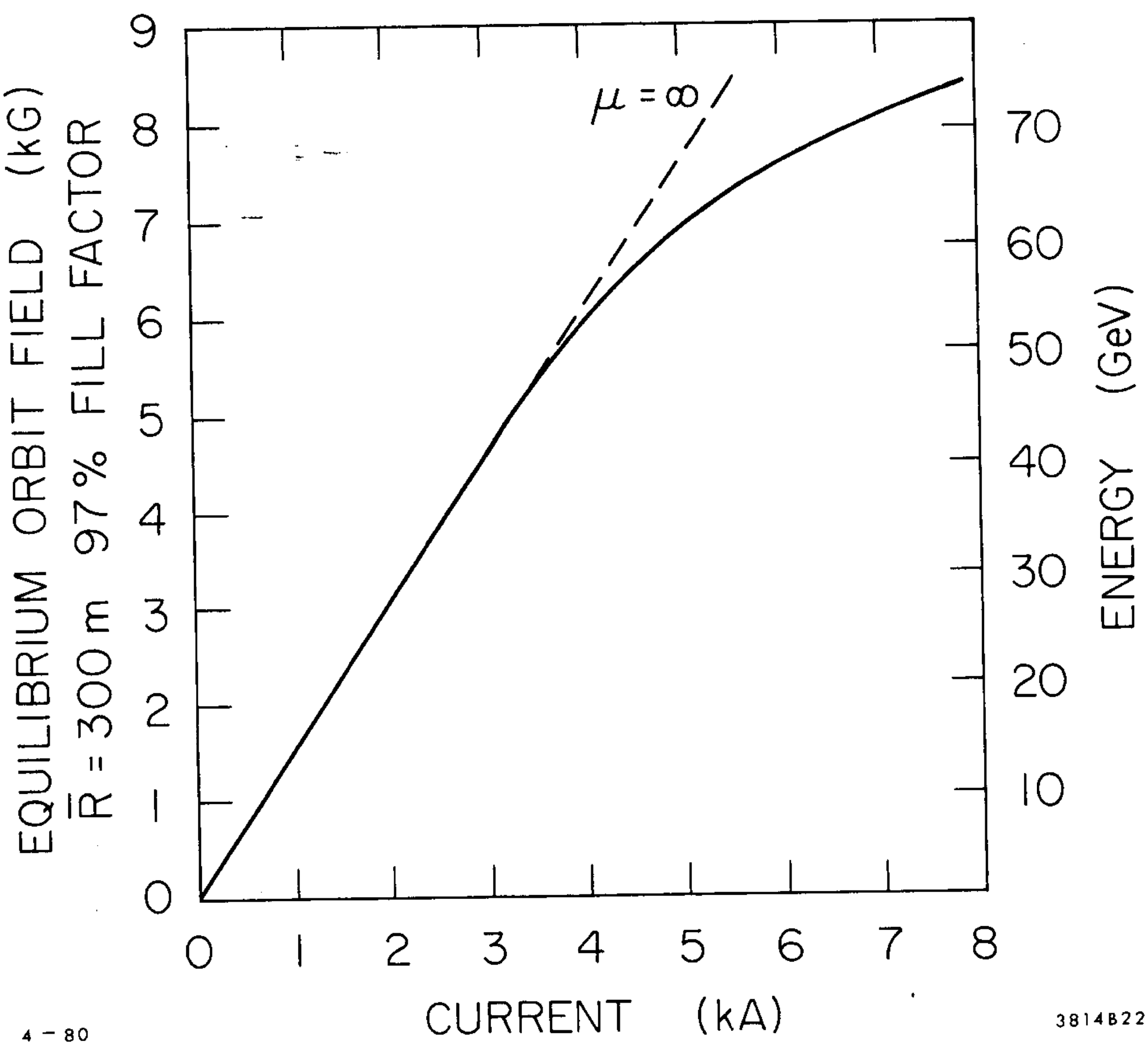

Fig. 9. Excitation curve for the SLC arc magnets.

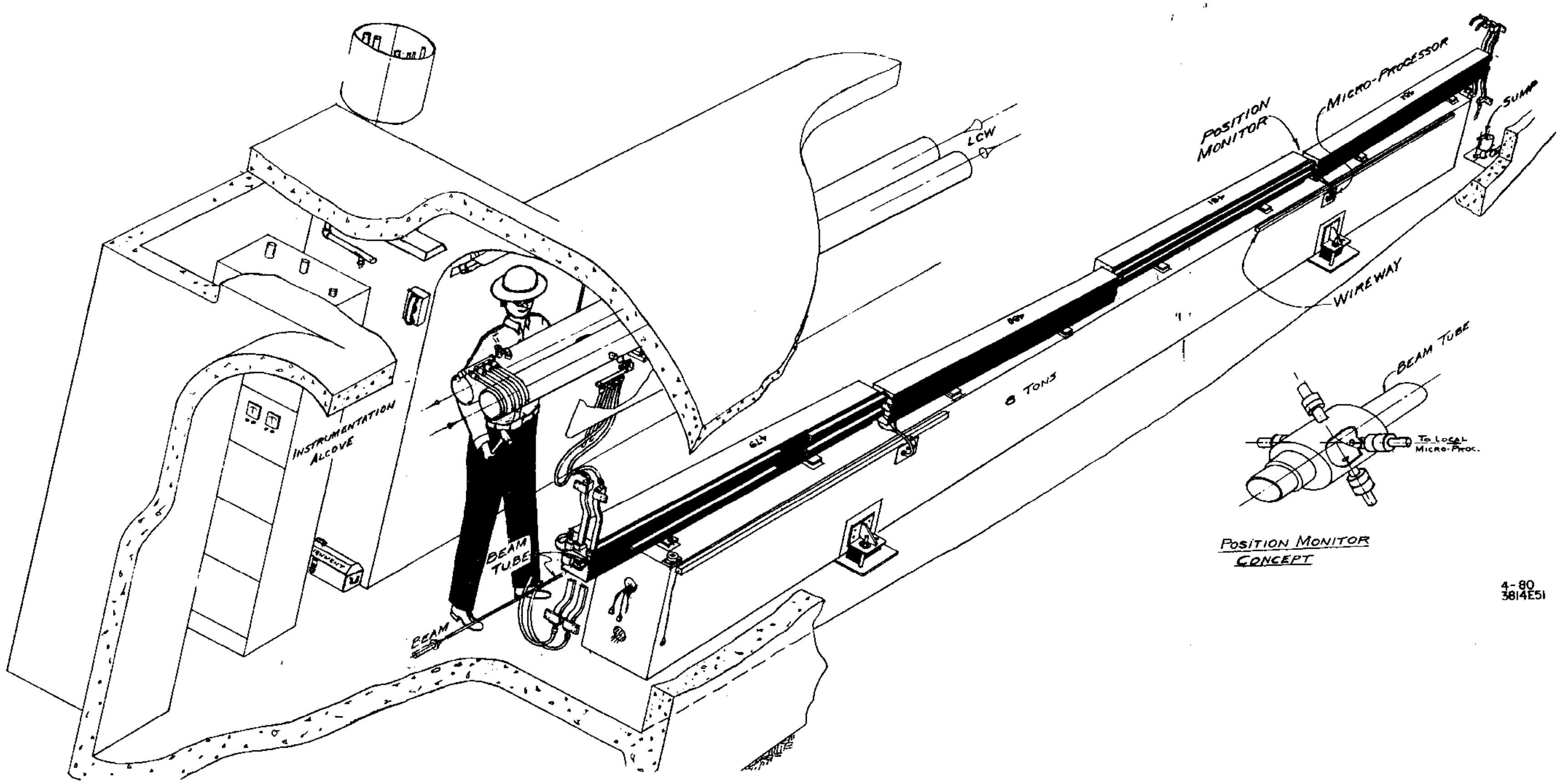

Fig. 10. General layout of the components in the SLC arc tunnel.

is segmented into three planes, one down, one level, and one up. The grades are less than 10%. The connection between planes will be accomplished by turning the standard arc magnet through 90° on selected modules. If the phase shift per vertical bend is appropriately chosen, the problem of matching the vertical η function is eliminated.

(b) Core and coil fabrication

Small-aperture, high-gradient magnets require relatively accurate pole contours. The laminations of which the cores are made will be produced using a precision process called "fine-blanking," invented in Switzerland and available in the U.S. only during the last ten years. With this process, the steel is literally extruded by a punch-die set that has almost zero clearance. Tolerances on the parts of .0005 inch are possible with material thickness up to 1/2 inch. Moreover, "partial penetration" pins in the die make possible dimples and holes by which each part is accurately registered in the stacking process. It is proposed to use ordinary low-carbon 1010 steel about 3/16-inch thick and to achieve magnet-to-magnet field uniformity by randomizing the over one-half million laminations that will comprise the transport arcs. The arc magnet system is approximately 2.5 kilometers in length. Precision pins, fitted into the end lamination, will align adjacent magnets to better than 0.1 mm. Long-range girder alignment can be performed using survey techniques similar to that of the PEP laser alignment system, which is capable of 0.2 mm resolution.

Four separate solid extruded aluminum water-cooled conductors form the coil. The water channel is designed for low velocity (~0.2 ft/sec/ckt and ~3 ft/sec in the 8-inch header) to minimize vibration. All magnets are run in series by a common power supply regulated to .01%, which is supplemented by a low-power servo amplifier to improve regulation by another factor of 2.

(c) Steering Elements

Each magnet has two 15-turn back-leg windings. When these windings are connected to aid each other, they produce a 4% $\Delta B/B$ horizontal trim at 50 GeV, or three times the variation in B_o expected to be caused by magnet-to-magnet misalignment. When connected to buck, vertical steering results. Since over 1200 magnets are involved, new concepts in trim power-supply control are called for. Computer-controlled D-to-A packages delivering 10 amps at 5 volts are envisioned. They are fed from instrument alcoves distributed around the arcs to reduce the cost of bussing. Position monitors are provided in each two-magnet cell. With these elements, in conjunction with a sophisticated orbit-correction program, the position of the beam will be held to within acceptable rms deviations with respect to the design orbit to prevent beam dilution. (See Appendix B.)

4. Ground Motion

Since the invention of strong focusing, it has been recognized that severe tolerances are placed on the position of magnetic elements. We have assumed above that a steady-state correction system will be effective in steering the beams around the transport arcs at the fractional millimeter level. In order to collide beams successfully at the interaction point at the micron level, however, a dynamic position feedback system is called for. If this system derives its positional information from a previous pulse, its bandwidth is limited by the sampling theorem.[9] Suppose the Collider operates at 180 pps. Then the upper limit of the band is 30 Hz. One must examine, therefore, whether disturbances occur around and above this frequency of sufficient amplitude to be injurious to the attainment of good luminosity. This has been done. Ground motion in the PEP tunnel and near the boundaries of the Collider site has been measured[10] in the frequency range of 0.1 to 100 Hz over a period of several days. These studies lead to the following conclusions.

(a) Ground motions arising from natural causes, earth tides, earthquakes, microseismic noise due to storm action, etc., have either steady-state amplitudes above 2 Hz that are negligible compared to the 0.2 micron rms tolerances[11] required, or else they occur very infrequently. Below 2 Hz, the wavelengths of the disturbances are larger than the Collider site and, therefore, not of importance in relative magnet motion. In addition, the feedback system can cope with them.

(b) Careful design of buildings and structures is indicated to suppress the effects of steady-state noise generated by pumps, ventilation fans, transformers, compressors, and the like.

(c) Of the other cultural (i.e., manmade) disturbances, the most commonly found were peak disturbances (amplitudes in the few-micron range, lasting seconds) associated with traffic. Fortunately, the worst daytime event rates are a few tens per hour, low enough to be acceptable. During the night the frequency is typically less than one event per hour.

D. Final Focusing System

1. General

The purpose of the final focusing system is to demagnify the beam size from the Collider arcs to a size suitable for beam collisions, and also to correct for the chromatic depth-of-focus caused by the finite momentum spread in the beam. This is accomplished in a system 114-meters long, using practical magnet strengths, with four half-wave magnetic-otpical transformers. The overall system is shown in Fig. 11. The first two transformers match the mono-energetic beta-functions in the arc lattice to an interaction-point (IP) beta-function of 1 cm. The last two transformers are used to make the chromatic corrections. They are identical but placed in mirror symmetry. Contained within each of the last two transformers are two sextupoles, one for the x plane and one for the y plane, which correct the chromatic aberrations causing the depth-of-focus problem. Dipoles are inserted (one at the end of the arc lattice, one between transformers 1 and 2, and one between transformers 3 and 4) so as to introduce an appropriate eta-function into the system which makes the chromatic correction possible. The dipole strengths are chosen so as to minimize the higher order optical aberrations at the interaction point. The beta-function at the position of the dipoles is chosen so as to restrict the emittance growth caused by synchrotron radiation to an acceptable value.

2. Focal Spot Size

Figure 12 is a scatter plot of 3000 rays traced through the system using a special program which takes into account higher order geometric and chromatic terms to all orders (see Appendix C). The input transverse phase spaces assumed are gaussian with $\sigma_x = \sigma_y = 0.0367$ mm, $\sigma'_x = \sigma'_y = 0.00825$ mr. Energy spread is a flat distribution with $\Delta E/E = \pm 0.5\%$.

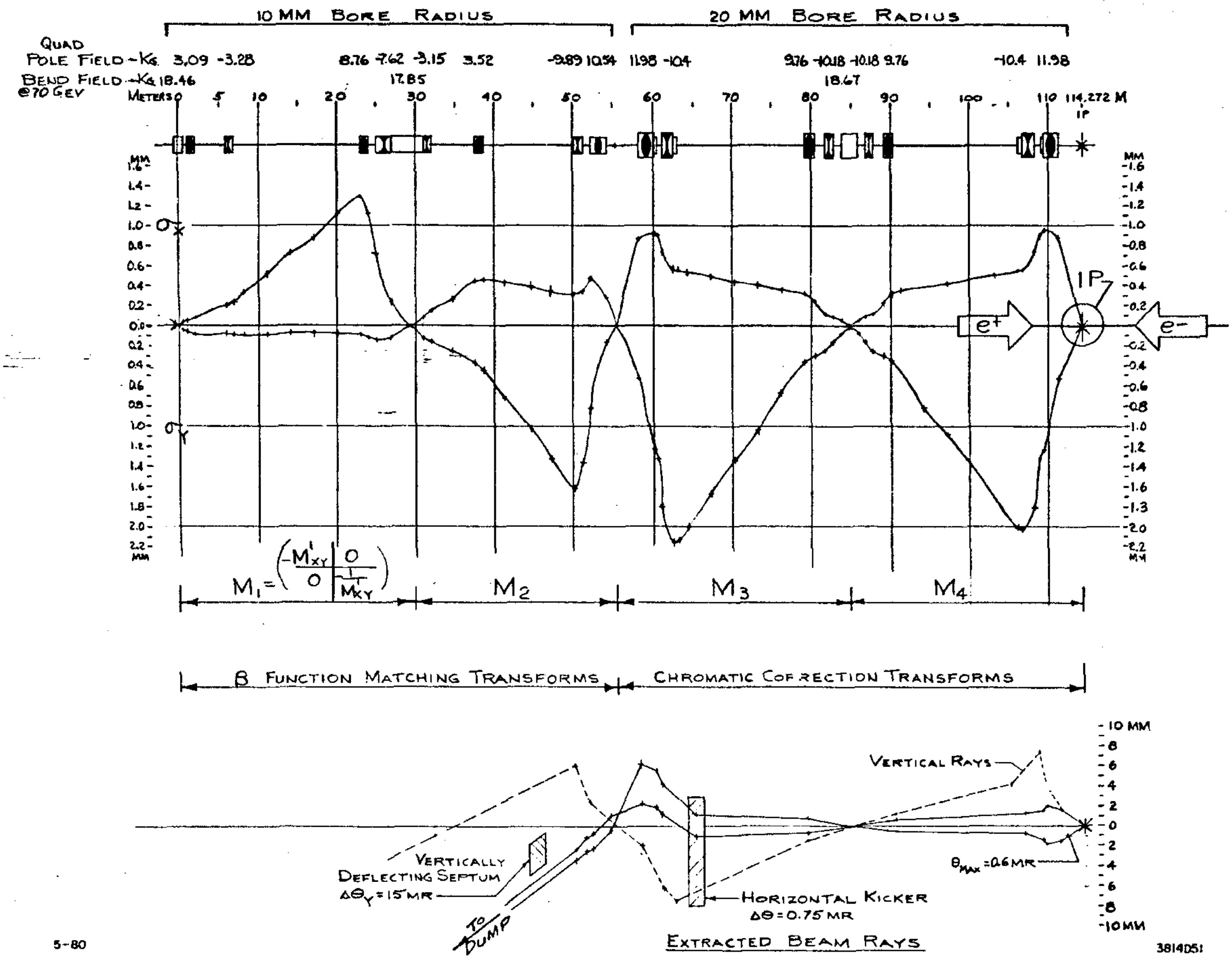

Fig. 11. Schematic representation of the final focusing system.

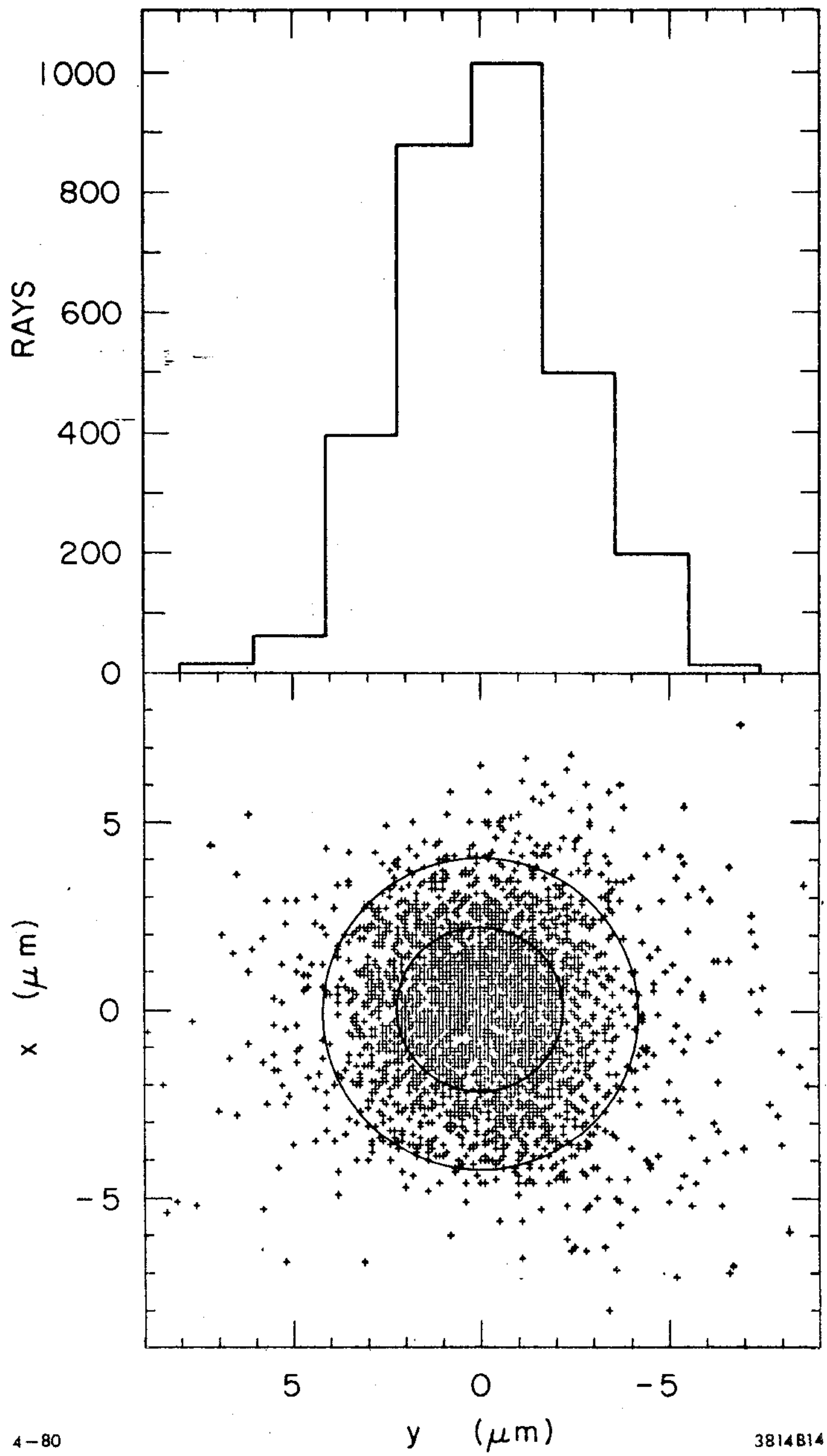

Fig. 12. A scatter plot of 3000 rays traced through the final focusing system. The inner and outer circles enclose, respectively, 50% and 90% of the charge.

The output distributions will not be pure gaussian in form due to the effects of the high-order terms. For this reason circles containing fractions of the beam's population are shown. The projected Δx, Δy distributions show "equivalent" rms widths of $\sigma_x \simeq \sigma_y \simeq 2.1$ microns, $\sigma'_x \simeq \sigma'_y \simeq 0.14$ mr.

3. Aperture Requirements

As can be seen in Fig. 11, the aperture of the magnets in this system need not be very large for the incoming beam. However, after beams strike each other, the "disruption" of the collision will magnify the output angles[12] as well as cause energy losses by the "Beamstrahlung" process.[13] For the parameters listed above, the maximum disrupted beam angles are of the order $\theta_{xmax} \simeq \theta_{ymax} \simeq 0.6$ mr. In order to ensure that background is not created by the spent particles before they are extracted and disposed of, the transport system's aperture has been chosen to be 4 cm. As shown in Fig. 11, the 4-cm diameter provides a safety factor of over two. With such an aperture, pole-tip field strengths remain below 12 KG in the larger quadrupoles at 70 GeV. The design of these high-gradient, small-aperture lenses, which traditionally run with high current densities, is being carefully optimized with power consumption in mind. Parameters are shown in Table 5.

TABLE 5

Final Focus Quadrupole Parameters at 70 GeV

	Max. Field (T)**	Effect. Length (m)	Bore Diam. (m)	Turns	Ampere Turns	Power /Mag. (KW)	No. Reqd.	Weight (lbs)
Q1*,Q8	0.958	2.5	0.04	7	8977	55.9	4	1760
Q2 ,Q7	0.958	1.627	0.04	7	8977	36.4	4	1150
Q3 ,Q6	0.958	1.019	0.04	7	8977	22.8	4	720
Q4 ,Q5	0.958	1.063	0.04	7	8977	23.8	4	750
Q9 ,Q13	0.844	2.5	0.02	3	3950	25.0	4	760
Q10,Q14	0.844	1.18	0.02	3	3950	11.8	4	340
Q11,Q15	0.316	1.11	0.02	3	1480	1.56	4	340
Q12,Q16	0.316	1.0	0.02	3	1480	1.40	4	310

* See also Section D.4.

** $\int g \cdot d\ell$ products have been maintained but lengths have been increased in order to reduce maximum pole-tip fields.

4. Permanent-Magnet Quadrupoles

The desire of the experimenters for as large a magnet-free interaction region (say ±10 meters) and the ability to correct the chromatic aberrations in a reasonable length cannot be reconciled. The ends of the last quadrupoles have had to be located ±3 m from the interaction point. This may place the last lens <u>inside</u> the axial magnetic field of the detector. This can be done by employing a new type of quadrupole[14] made of a special rare-earth cobalt permanent-magnet material ($SmCO_5$). The trick is that this very anisotropic material has both its parallel and transverse permeabilities very close to <u>unity</u>. A B-H curve is shown in Fig. 13. For this reason neither the detector nor the quadrupole fields should affect each other. The design and field plot of a 16-section permanent-magnet quad is shown in Fig. 14. Lenses of this type, having excellent field harmonics, have been constructed.[15] When subjected to axial fields up to 12.4 KG (the maximum field capability of the test setup), the results have borne out the theoretical expectations mentioned above. To reduce costs (the material itself is relatively expensive), studies are currently underway to design lenses of rectangular cross section, and in this way to minimize material by more closely conforming to the aperture requirements. It remains to find an easy way to vary the field strength smoothly when the energy of the collider is changed. One method to vary the strength, already suggested, is by axially rotating the core blocks relative to each other.

An additional advantage this type of lens provides is that it is physically small and has no current leads, and thus gives the experimenter vital space in the forward direction for small-angle apparatus.

5. Extraction

It is important to dispose of the disrupted beams cleanly for background and radiation-damage considerations. Each beam running at 70 GeV, 180 pps, and 5×10^{10} particles per pulse will deposit $\simeq$ 100 kilowatts. One pulse contains 560 joules. After collision and before re-entering the arcs, each beam will be extracted by a kicker-septum arrangement, bent vertically downward, partially refocused, and sent into a dump approximately 160 meters from the interaction point (see Fig. 11).

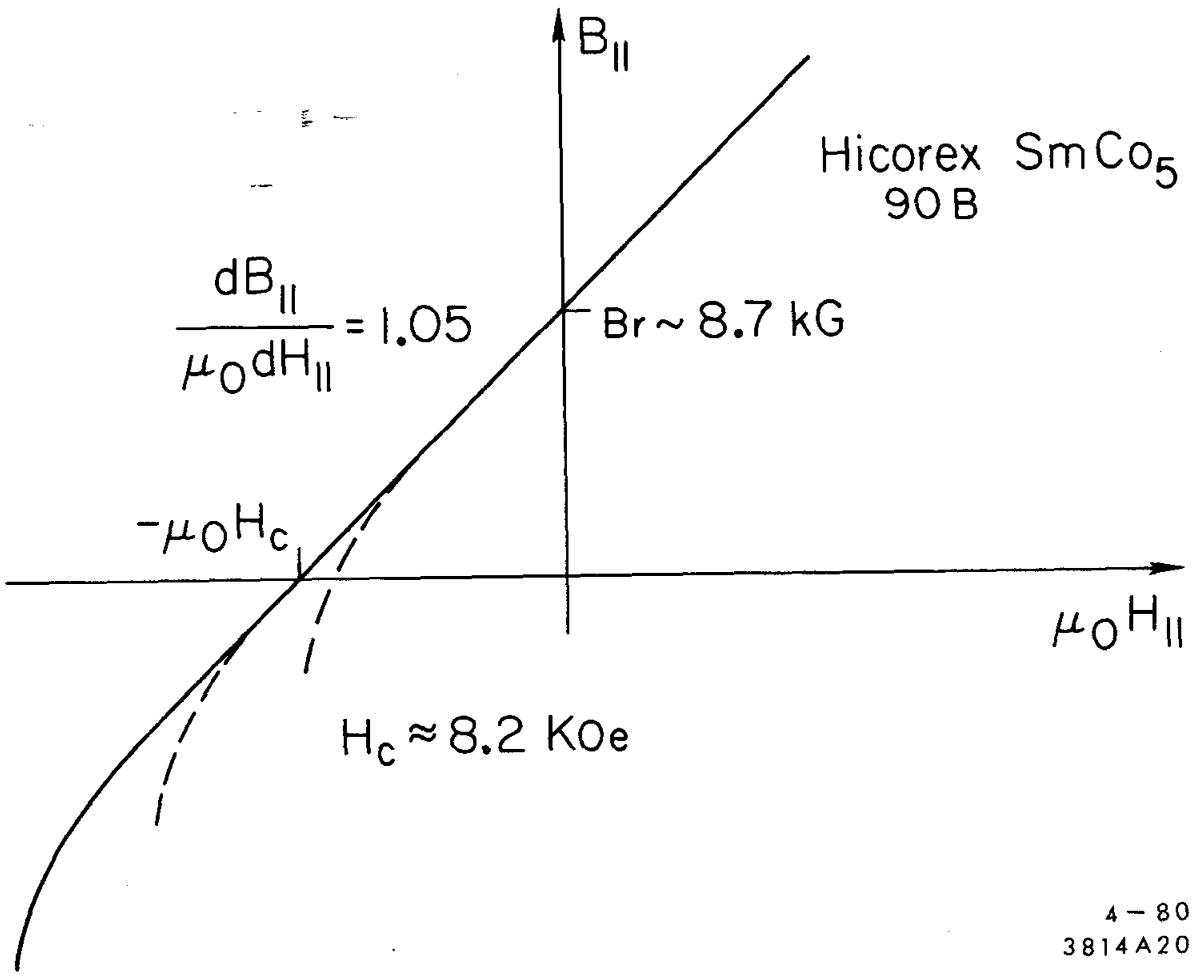

Fig. 13. B-H curve for the $SmCo_5$ permanent-magnet quadrupoles.

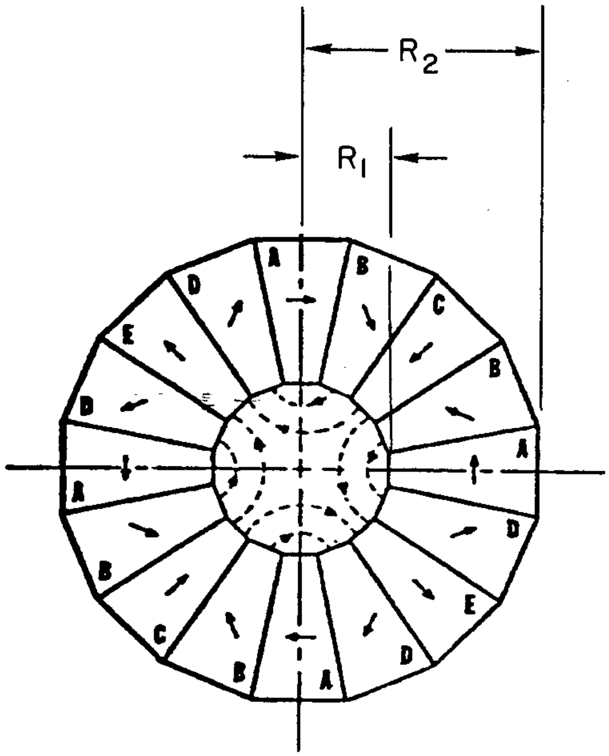

$$\frac{R_1}{R_2} = 1 - \frac{B_{\text{poletip}}}{2B_r \times 0.937}$$

For $B_{pt} = 10\,\text{kG}$

$B_r = 8.5$

$$\frac{R_2}{R_1} = 2.70$$

Schematic of 16 Piece Segmented REC
Quadrupole with 5 Easy Axis Orientations

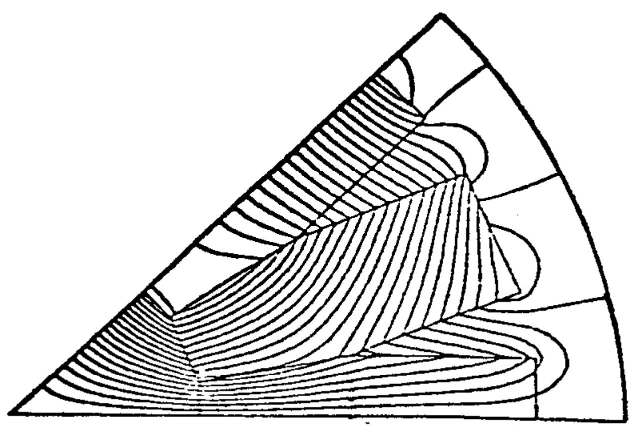

Flux Plot of 16 Piece Segmented REC
Quadrupole with 5 Easy Axis Orientations

4–80
3814A24

Fig. 14. Design and field plot of the $SmCo_5$ quadrupoles.

Sufficient earth and iron shielding is provided downstream of the dump to stop high-energy muons. The dump itself, following well-proven SLAC practice, will be a vessel containing small metal spheres through which water is forced under pressure. The radioactive water loop is completely self-contained, cooled through a heat exchanger, and provided with a catalytic hydrogen recombiner to eliminate the problems of gas generation. The dump is located in a small vault under the arc tunnels, but the pumps and ancillary equipment are to be housed in a more readily accessible area where they can be serviced.

E. Positron Production

In order to optimize the Collider luminosity, the positron source is required to produce sufficient numbers of positrons to saturate the intensity capability of the linac. Since the intensity of the scavenger pulse is subject to the same linac capability, the source is required to have a yield of at least one positron out for each incident electron. This requirement implies more than an order-of-magnitude improvement over the existing source which, at 7 GeV incident electron energy, normally has a yield of 7% but under optimum conditions has been tuned to 15%. The needed improvement will result from (a) increasing the incident electron energy to 33 GeV, and (b) using a collection system with a larger admittance.

1. Yield Calculations

It is important to determine where gains in positron yield can be made and what the limits are due to the nature of the electromagnetic cascade. Yields have been calculated for various beam energies and target materials using the EGS program,[16] and some of the results are shown in Fig. 15. The following conclusions can be drawn from these studies: (a) Materials with large atomic number are more efficient. For example, tungsten gives twice the yield of copper under the same conditions at their shower maxima. (b) Denser materials localize the shower to a smaller region. This results in a smaller emittance and hence better collection efficiency, but it also produces higher physical stress and pulse temperature rise. (c) Positrons are produced preferentially in the 2-20 MeV energy range. The collection system must

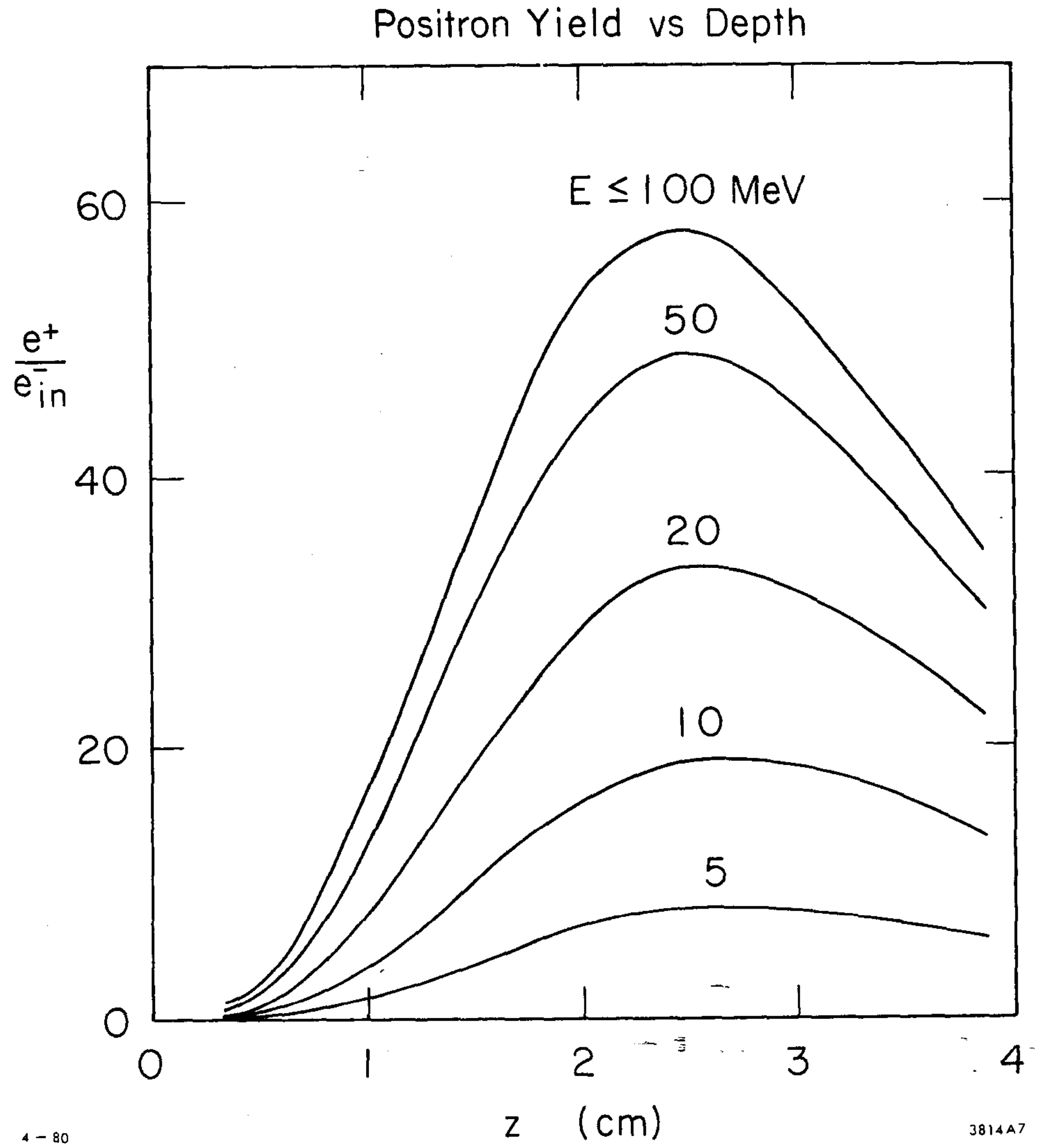

Fig. 15. Positron yield vs depth. The longitudinal distribution of positrons in a tungsten target per incident 33 GeV electron is shown for maximum positron energies of 5, 10, 20, 50 and 100 MeV.

be sufficiently wide-band to work over this range. (d) In dense materials, the positrons come from a small spot, typically 0.5 mm radius, but with large angles, typically $\pm 20^{\circ}$. (e) The yield is nearly proportional to the incident electron energy. (f) The number of positrons produced is more than sufficient, provided they can be captured and accelerated as desired. Using the parameters for the collection optics of the existing SLAC source, we calculate a yield of 15%, in good agreement with the measured yield. The intended factor of 3 increase in admittance in each transverse plane of the collecting optics, and the higher incident electron energy, result in a total calculated yield of 480%.

The overall positron-production system is shown in Fig. 16, and component parameters are summarized in Table 6. A single bunch of electrons (the scavenger pulse) is extracted from the linac at the 2/3 point by means of a fast kicker magnet and a pair of septum magnets. The extracted electron beam is focused to the desired beam spot size at the target. Target pulse-heating is expected to require beam sizes no smaller than $\sigma = 0.4$ mm (standard deviation). Positrons are collected and accelerated up to 200 MeV in a 50-ft length of linac accelerator section. They are then transported back to the beginning of the linac for further acceleration to 1.2 GeV, whereupon they are sent to the damper ring. Achieving the desired number of positrons depends on the efficiency of the collection system, which must work with a large-phase-space beam. The collection optimization is constrained by the minimum allowable beam size as determined by target strength.

2. Target

The most promising target material is a composite of tungsten with approximately 26% rhenium. It has a high melting point (3100°C), very high strength (approximately 190,000 psi yield), and reasonable ductility and thermal conductivity. Results from the EGS Monte Carlo calculations are shown in Fig. 17. For gaussian beam sizes of 0.4 and 0.8 mm, the pulse temperature rise is 480°C and 200°C, respectively. The resulting compressive thermal stress is 140,000 and 60,000 psi. This instantaneously applied stress causes a thermal shock wave to form, traveling at 4.5×10^{3} m/sec. The shock wave produces tensile stresses which are less

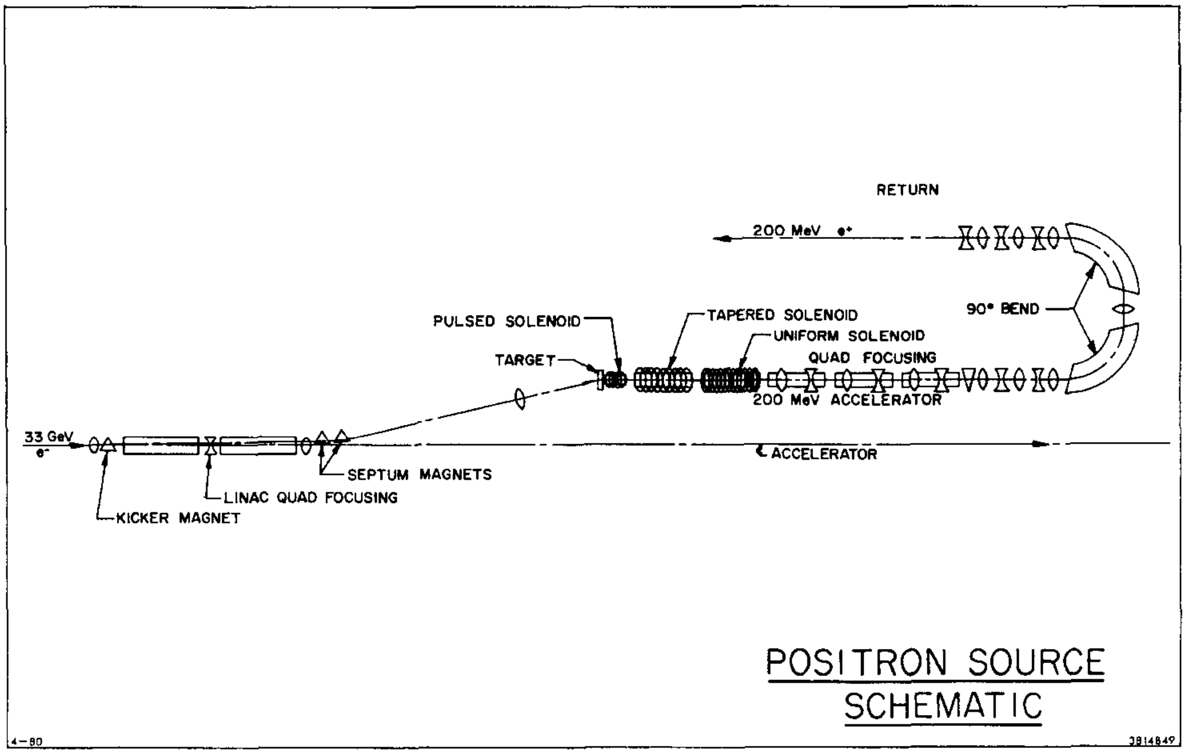

Fig. 16. A schematic representation of the positron-source components. These components are located at the 2/3 point along the linac.

TABLE 6

Positron Source Specifications

A. EXTRACTION SYSTEM

Beam:	Electron energy	33 GeV
	Pulse energy	194 Joules
	Power	35 KW
	Intensity	3.7×10^{10} electrons/pulse
	Pulse rate	180 Hz
	Size	0.4 to 1.0 mm (standard deviation)

Magnets:	Bend Angle (mr)	Field (KG)	Length (m)	Rise Time (μsec)
Fast kicker	0.5	0.5	1	< .05
Thin septum	9	5	2	140
Lambertson septum	20	8	3	DC

B. TARGET SYSTEM

Material	74%W - 26%Re
Energy deposition	39 Joules/pulse
Pulse temperature rise	200 - 480°C
Maximum compressive stress	60,000 - 140,000 psi
Length	6 radiation lengths = 21 m
Power deposition	7 KW
Maximum pulse temperature	800 - 1100°C
Steady-state temperature	600°C

C. COLLECTION SYSTEM

Beam:	Energy range at target	2 - 20 MeV
	Emittance	2 mm × 2.5 MeV = 5 MeV-mm
	Yield	$e^+/e^-_{in} = 4.8$

Magnetic Focusing:	Length (m)	Field Range (KG)
Pulsed tapered solenoid	0.15	100 - 15
DC tapered solenoid	0.40	15 - 5
DC uniform solenoid	6	5

Quadrupole Array:	Spacing	0.2 - 0.75 m
	Number	28
	Length	0.1 m
	Gradient	0.125 KG/mm
	Aperture	± 60 mm

TABLE 6 (Cont.)

D. TRANSPORT SYSTEM

Turn-Around Dipoles:	Field	18 KG
	Bend angle	90°
	Radius of curvature	0.37 m
	Pole-face rotation	22°
Quadrupole Array:	Total length	2.1 Km
	Spacing	12.7 m
	Length	0.25 m
	Gradient	3 KG/m
	Aperture	± 60 mm
Correction Dipoles:	Spacing	25 m
	Length	0.5 m
	Field	106 G

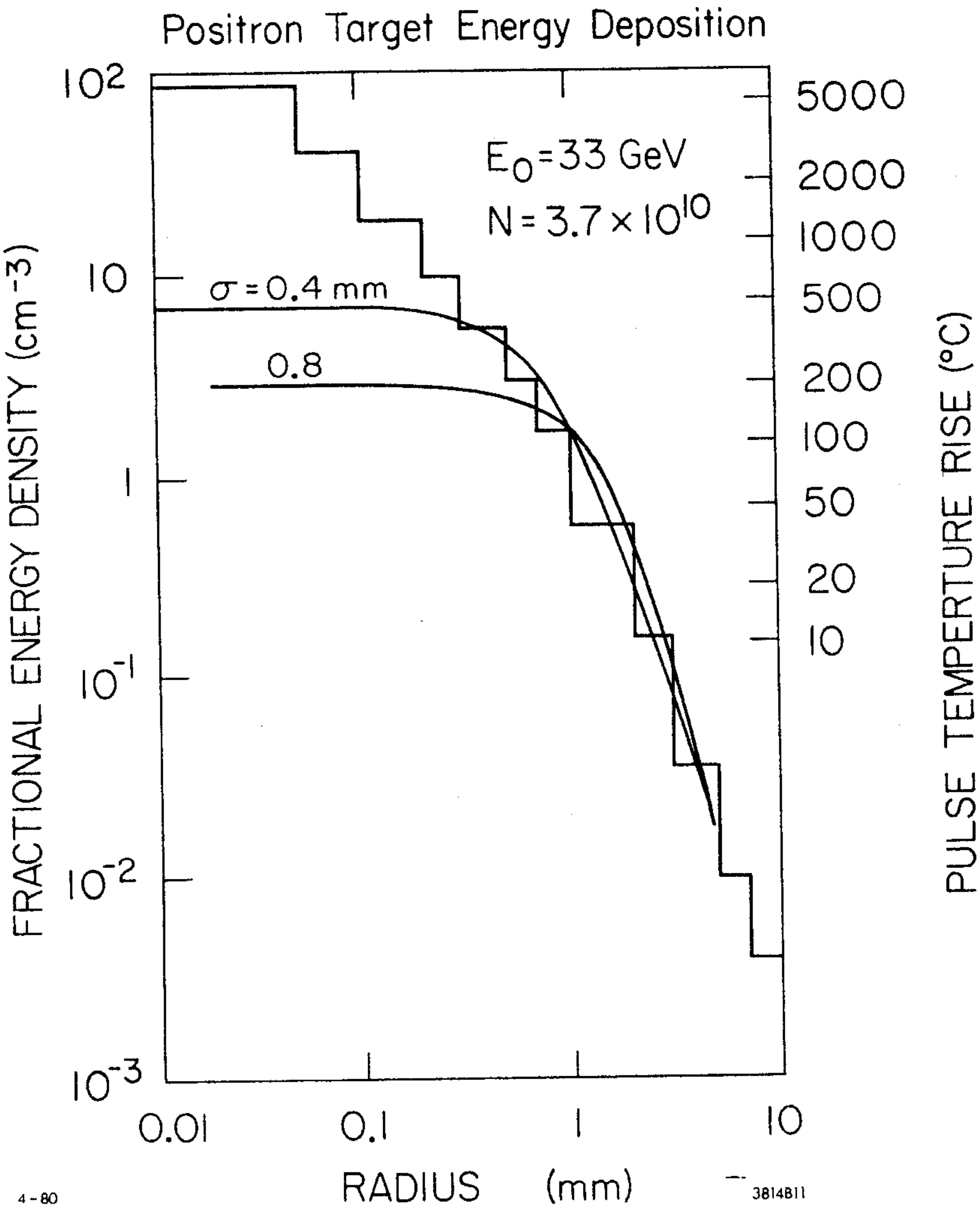

Fig. 17. Positron target energy deposition. The radial distribution of energy deposition from an electromagnetic shower cascade is shown at 6 radiation lengths in tungsten for 33 GeV incident electrons. The left-hand scale is the energy density normalized to the incident beam energy. The right-hand scale shows the pulse temperature rise for 3.7×10^{10} incident electrons, corresponding to 194 joules of beam energy. The histogram is the Monte Carlo calculation for a point incident beam. The curves are for Gaussian incident beams with $\sigma = 0.4$ and 0.8 mm.

than but approach the magnitude of the compressive stress. The endurance limit of the W-Re material is about 65,000 psi. For an 0.8 mm beam, the target will probably last indefinitely; for 0.4 mm it may have a limited life expectancy. To reduce the steady-state temperature, the target will be rotated, thus distributing the deposited power into an annulus. A reasonable geometry would have the beam impinge at a radius of 25 mm. The W-Re portion of the target would extend out to 28 mm and be brazed into a water-cooled copper annulus, with the water interface at 40 mm.

3. Focusing

The positron beam emerging from the target will enter a focusing solenoid system. The goal is to transform a 2 mm by 2.5 MeV transverse emittance into a 9 mm by 0.7 MeV emittance, which corresponds to the accelerator aperture with a superimposed 5 KG solenoidal field. This is accomplished with an adiabatically changing solenoidal field where the initial-to-final field ratio is the square of the radii ratio.[17] Thus a 100 KG initial field is needed. This is accomplished with a pulsed magnetic field utilizing a flux concentrator.[18] The flux concentrator can conveniently be made to produce the desired field taper; it produces field only where needed for the particle orbits, and automatically provides the correctly shaped collimator for unwanted shower particles.

4. Longitudinal Collection

The positrons produced in the shower emerge with a large spread in transverse and longitudinal momentum. The momentum spread causes the positrons to debunch. The design goal is to capture a large fraction of the positrons in the energy range from 2 MeV to 20 MeV. The design of the RF accelerating structure in the capture region must minimize the debunching that occurs due to this momentum spread. The high magnetic field required for broad-band matching of the transverse emittance of the shower to the acceptance of the 5 KG uniform solenoid precludes introduction of RF fields closer to the target than about 20 centimeters. By this point the low-energy particles have fallen behind the high-energy particles. This, it turns out, is advantageous for matching to the admittance of the linear accelerator section.[19] Figure 18 shows the longitudinal emittance for positrons between 2 and 20 MeV for various values of transverse momenta after 15 meters of acceleration. In this capture process the

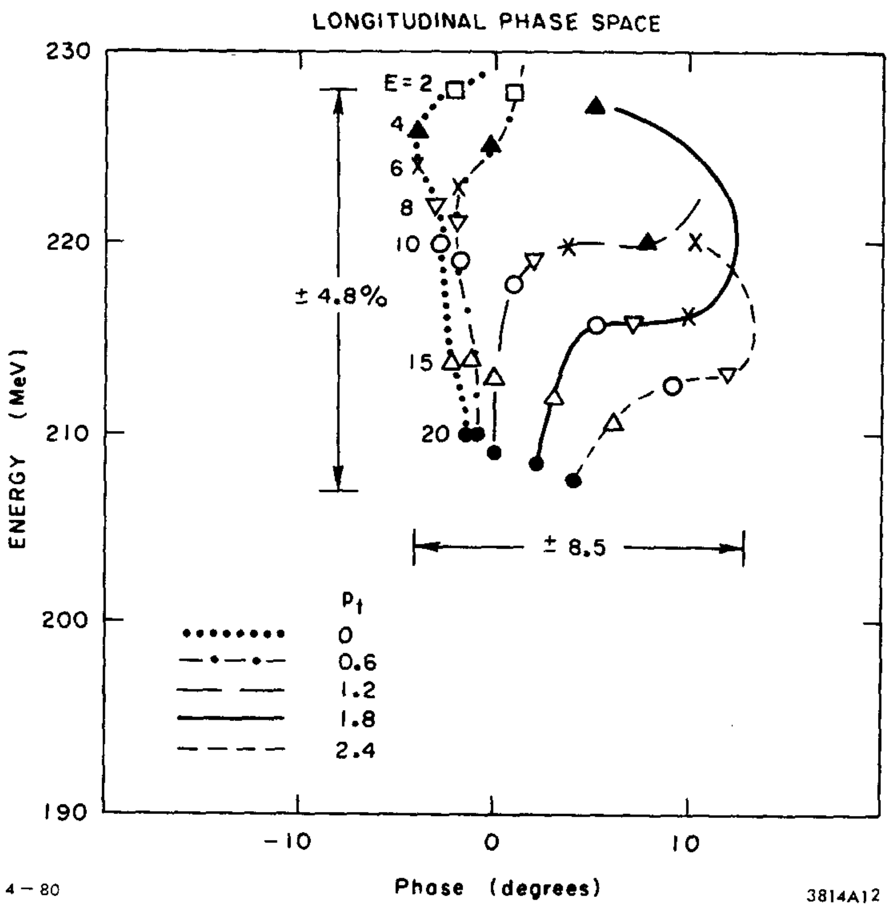

Fig. 18. Longitudinal phase space. Positron energy is plotted vs relative particle RF phase at the exit of the 200 MeV accelerator. The accelerator consists of a 10-ft linac section, starting 8 inches from the positron target, followed by a 6-inch space and a standard 40-ft girder. The phases of the RF in the 10- and 40-ft sections were individually adjusted to minimize the phase-space area. The points are labeled according to positron total energy and positron transverse momentum emerging from the target.

initial energy spread is almost exactly retained. An independent phase control on the first three-meter section of accelerator permits an optimum match of the shower positrons into the longitudinal space. A second phase control on the next twelve meters allows the positrons to be accelerated near the crest of the wave for maximum energy gain and best spectrum. The calculation assumes that all positrons leave the radiator together, so the actual bunch will be longer due to the bunch length of the incident electrons, which is about 1 mm or 3° of accelerator RF phase.

5. Transport Systems

After 20 ft of accelerator the positrons will have an energy range of 35-65 MeV, and a tightly packed quadrupole array will constrain the beam within the accelerator aperture. Short quadrupoles with large aperture will be built to fit around the accelerator structure. These magnets will have an aperture equal to their length. Field quality would normally be a problem with a magnet with this aspect ratio; however, only the central 20% of the aperture is used, and field distortions are not significant. The quadrupole spacing is increased over the remaining 30 ft of accelerator, in proportion to energy, thereby keeping the maximum beam size constant. At the end of the 50 ft accelerator the beam is at an energy of 200 MeV with an energy spread of ±5%.

Acceleration to 1.2 GeV for injection into the damper ring requires 240 ft or 6 girders of SLAC SLED II Linac. The first 50 ft are devoted uniquely to positron focusing and acceleration to 200 MeV. The remaining 1 GeV of acceleration is done in the same accelerator sections as the electron beams, thus saving the cost of 5 additional girders. The positron beam will therefore be turned through 180°, transported back to the beginning of the linac, turned around again and deflected into the linac for acceleration to 1.2 GeV.

The turn-around is easily accomplished with two 18 KG, 90° bend dipoles. The desired optical properties, however, require some special considerations in the design. In order not to increase the size of the beam, the turn-around must be achromatic. Also, since the beam will be reinjected into the linac, it must remain bunched. Any significant amount of debunching will result in an undesirably large energy spread at 1.2 GeV. The turn-around must therefore be isochronous as well as achromatic. The desired first-order optical properties are achieved by wedge-focusing with 22° pole-face rotations on the 90° bend magnets and a single quadrupole between the bend magnets. A quadrupole array is matched at each end, and a pair of 5° opposing bends provides a convenient dog leg to fit the turn-around into the 10 ft accelerator tunnel. The symmetry of the turn-around results in the cancellation of the second-order geometric terms. Second-order chromatics will be corrected with a slight curvature of the bend pole-face and a pair of sextupoles. The transformation matrix is a unity matrix in both the bend plane and the non-bend plane. The turn-arounds at each end of the transport system are essentially identical.

The transport system is a simple quadrupole array with 90° betatron phase-shift per cell. With quadrupole spacings of 12.7 m, the maximum beam radius is 33 mm. Dipole corrections every 25.4 m in both the horizontal and vertical planes correct for the earth's magnetic field and alignment errors. Computer calculations to second order show negligible beam-size increase after 2 km of transport.

After reinjection into the linac, the positrons are accelerated along with the electron bunches to the 1.2 GeV damper energy. Since the positron emittance is over 100 times the electron beam emittance, the linac focusing requirements are determined by the positrons. The quadrupole array used on the positron acceleration to 200 MeV is continued with spacings increasing in proportion to energy (this system obviously also works for the electrons).

F. Beam Damping and Compression

The purpose of the damping rings is to reduce the emittances of both e^+ and e^- beams to values suitable for the attainment of high luminosity. The e^+ emittance will be reduced by a factor up to 1000. This is done using the radiation damping process in two small high-field storage rings. The compressors' function is to reduce the bunch lengths of the beams emerging from the dampers to sufficiently small values ($\sigma_z \simeq 1$ mm) so that an acceptably small energy spread (±0.5%) will result after final acceleration. This energy spread must be made small to minimize chromatic aberrations in both the Collider arc and final transport systems. Such a maneuver is performed by exchanging $\Delta\phi$ with ΔE in longitudinal phase space.

1. Damping Rings

(a) Parameters

The rational of parameter choice is described in Ref. 20, where it is noted that realizable magnet strengths and the rise-times of injection and extraction kickers will determine the scale of parameters. Using a maximum field of 20 KG in the bends, the optimum resulting parameters are listed in Table 7. The ring energy is 1.21 GeV. Two bunches circulate in each ring; hence by extracting alternate bunches the effective cooling period ($T_c = 4\tau$) is made twice the demand interpulse period of 1/180 sec. In order not to disturb the "half-damped" bunch, the sum of the rise and fall times of either injection or extraction kicker is one revolution period, or a realizable 100 nanoseconds.

(b) Lattice

The separated-function structure of each ring is shown in Fig. 19. In the arcs, the magnet-filling factor is only about 50% to allow room for the coil ends of the magnets. For such a small ring the tunes $\nu_x = 7.106$, $\nu_y = 3.125$ are relatively high. Both positive and negative *sextupole fields, necessary for the control of the head-tail instability,* are introduced at each end of the bends by pole-end shaping. The aperture is set by the phase-space of the injected beam, with allowance for orbit distortions. The energy acceptance $\Delta E/E$ is ±1%. Kickers are located in two of the 0.4-meter straight sections, with vertically deflecting Lambertson septa in the long straight sections, as shown.

(c) RF and vacuum

As noted in the parameter table, the requirements of the radio-frequency and vacuum systems are quite modest. The RF system provides 16 KW to compensate for the synchrotron radiation and cavity losses. An average pressure of only about 10^{-6} Torr is required, since storage times are in the tens of milliseconds. This is fortunate because the small-aperture vacuum chamber will be conductance-limited.

TABLE 7

Damping Ring Parameters

Energy	1.21 GeV
Number of bunches	2
Circumference	34.01 m
Bending radius	2.049 m
Damping times	$\tau_x = 2.821$ ms; $\tau_y = 2.959$ ms; $\tau_z = 1.517$ ms

<u>Magnets</u>

Bends (40/ring):	$B_o = 19.7$ KG, length = 32.1 cm
Quads (48/ring):	g = 6.45 KG/cm, length = 10.2 cm
Beam stay-clear:	x = ±5 mm, y = ±6 mm

Tunes $\nu_x = 7.106$, $\nu_y = 3.125$

<u>Input phase space for positrons</u>

$\varepsilon = 4.1 \times 10^{-6}\ \pi$ rad-meters at 1.21 GeV

$\Delta E/E = 1\%$

(phase space for electrons is much smaller)

<u>Output phase space</u>

For coupling $K = 1$, $\varepsilon = 8.5 \times 10^{-9}\ \pi$ radian-meters

$\Delta E/E = 0.073\%$

<u>Radiofrequency system</u>

Revolution frequency:	8.814 MHz
U/turn:	0.093 MeV
RF frequency (example only):	969.57 MHz, h = 110
RF voltage:	0.220 MV
Current (2 bunches):	141 ma
Synchrotron radiation power:	13.1 KW; Cavity power: 3.0 KW
Synchrotron tune:	$\nu_z = 0.0073$
Bunch length:	$\sigma_z = 1.0$ cm

Vacuum P less than 10^{-6} Torr

Polarization time $\tau_p = 11$ minutes (too long to be useful)

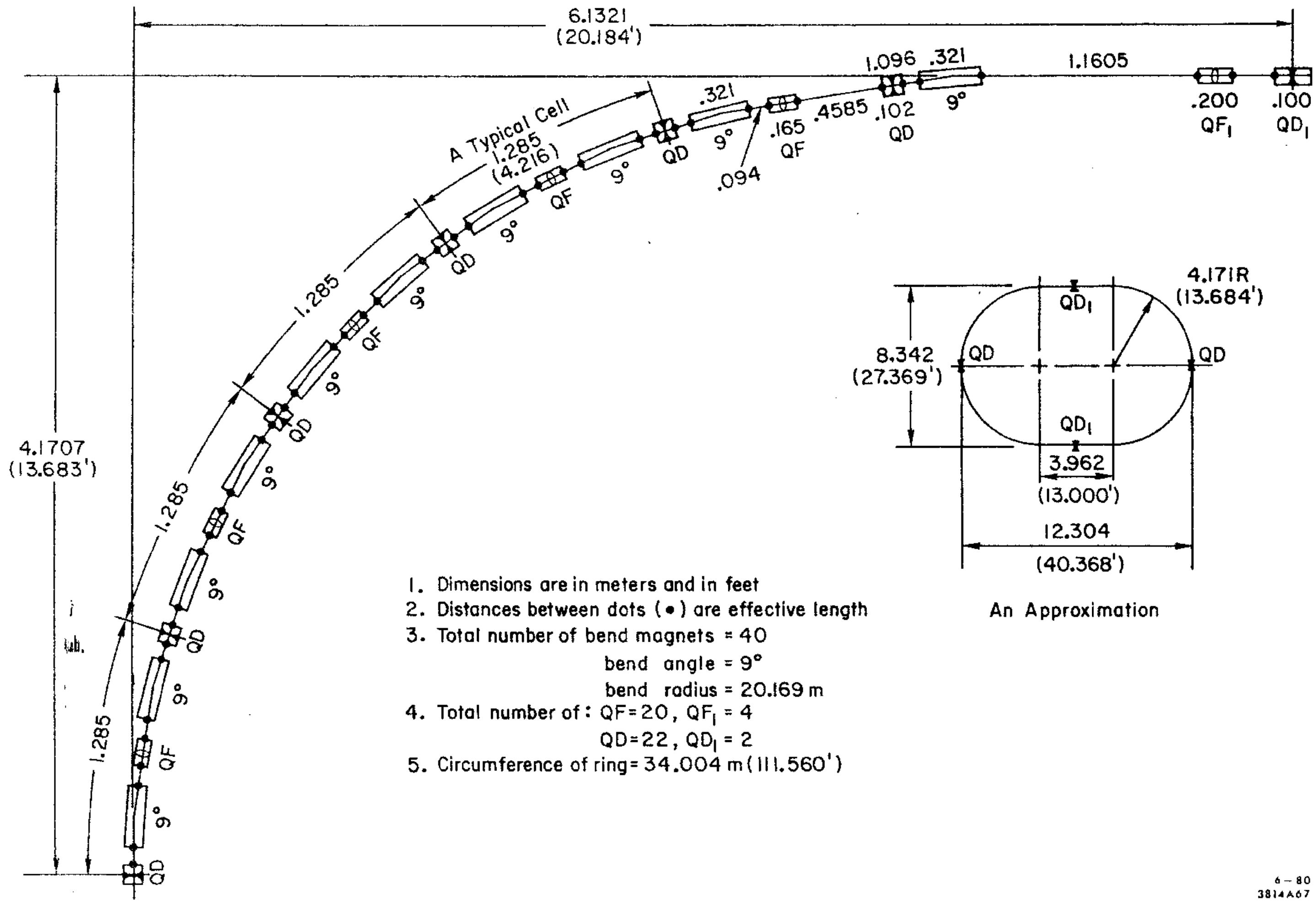

Fig. 19. A typical quadrant of the lattice of the damping rings.

(d) Location

Pre-acceleration to the operating energy of 1.21 GeV is required. It has been found convenient to locate the rings between Sectors 1 and 2 of the SLAC linac, using the first linac sector as the booster. The site is shown in Fig. 20. One ring is mounted directly above the other to conserve space in the underground vault. Transport to and from the rings is discussed below.

(e) Extraction Tolerance

In order to launch the damped and phase-compressed beams back onto the linac axis with the tolerances required by dilution (see Appendix A), one must hold the pulse-to-pulse jitter in position and angle of the extracted beam to $\Delta x_o \simeq 20$ microns, $\Delta\theta_o \simeq 0.5$ microradians. The only time-dependent magnets in this process are the extraction kickers. Assuming a kicker deflection angle of, say, 1 milliradian, this implies an amplitude stability of $\simeq$.05%. It is believed that holding this difficult tolerance is feasible by using feedback de-Qing circuits in the modulators and by other methods.

2. Compressor

The scheme for bunch-length compression is described in Ref. 21. The object is to reduce σ_z of the bunches as they leave the damping rings from $\simeq$1 cm to $\simeq$1 mm. This is done by "accelerating" the particles of the bunch at 0^o central phase, thus introducing a strong correlation between their time of arrival on the wave and their energy, and subsequently passing them through a non-isochronous transport system such that the higher energy particles travel a longer path and hence arrive at the linac entrance at almost the same time as all others.

(a) RF acceleration

Thirty megavolts are required, a demand that can easily be met by a standard SLAC 10-ft linac section driven by a klystron. This equipment is already on hand, since a 40-ft girder will be removed from the linac between Sectors 1 and 2 to make room for the compressor bend.

(b) Compressor arc

Transport to the linac is via a smooth 90^o arc of average radius 19 meters containing some ten bends and approximately fifteen quadrupoles.

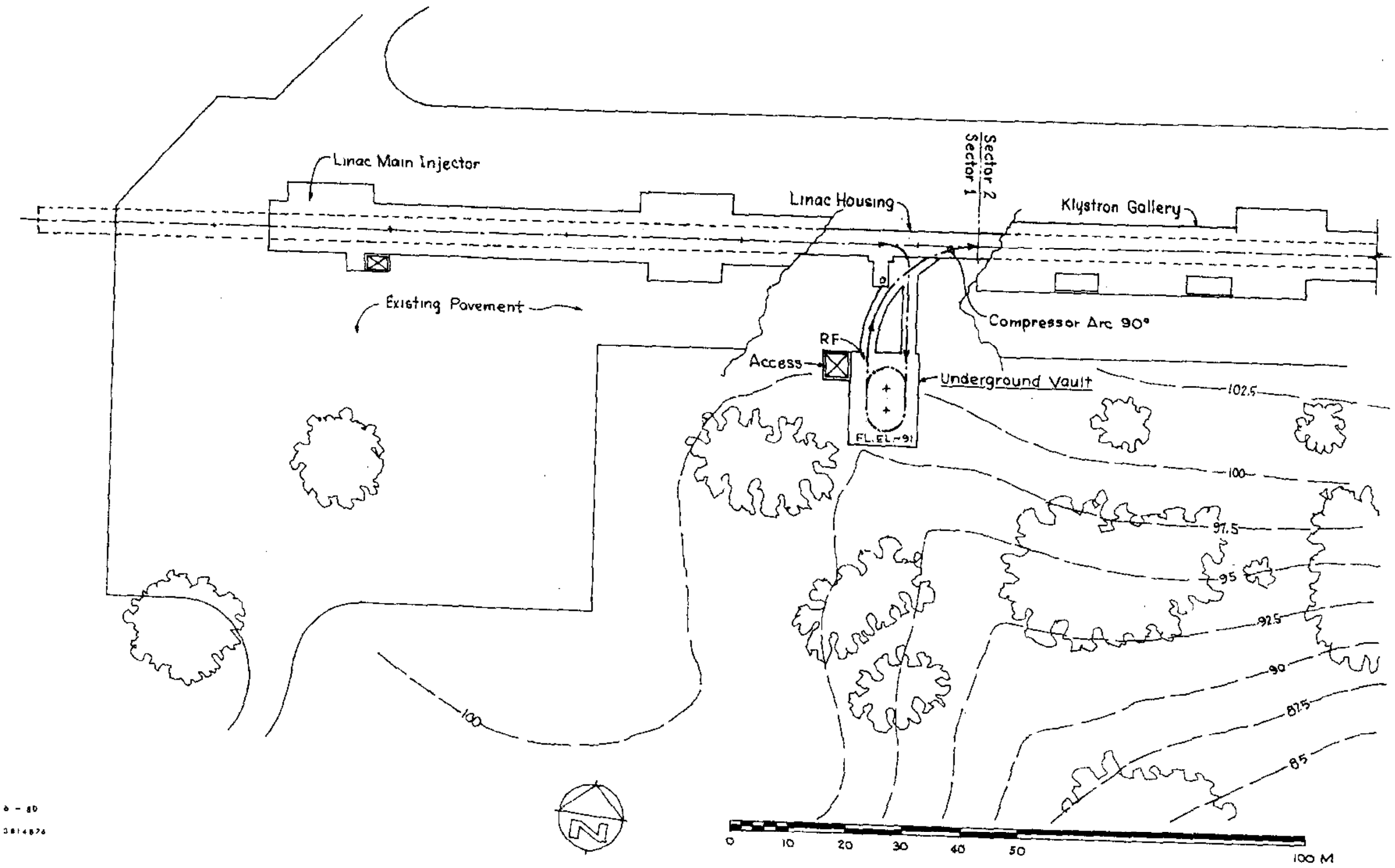

Fig. 20. Location of the damping ring/compressor system.

A horizontal aperture of 5 cm is enough to accommodate the path-length difference required. The required bending fields of 8 KG and quadrupole gradients of 1 KG/cm are modest. Emittance growth in this arc has been found to be negligible.

3. Transport: Linac to Damping Rings

Figure 21 shows the paths to and from the damping rings in plan view. Since one ring is mounted directly above the other, the transport and compressor bend lines are also double and of opposite polarities to accommodate electrons and positrons. An elevation is shown in Fig. 22. At the end of Sector 1 and the beginning of Sector 2 the beams are split, then merged along the axis of the linac by DC magnets. The tight 90° input arc is achieved by the use of a double-channel sector magnet in which the upper and lower channels have opposing fields. The central hole is fieldless, permitting a non-deflecting straight-through path, as shown in Fig. 23. Should one wish to bypass the damping rings completely, the splitting magnets can simply be turned off. Should one wish to bypass the rings for other than Collider physics on a pulse-to-pulse basis, pulsed "antisplitter" magnets are envisioned. In this way the critical steering required for Collider work can be maintained.

G. <u>High Current Electron Source</u>

The electron source for the Collider must produce two intense electron pulses for each cycle of operation: one for the actual collisions, and one to produce positrons for later collisions. Each of these electron pulses must result in 5×10^{10} electrons being captured and transported to the electron damper ring. The emittance of these pulses must be small enough to be damped to the value required for Collider operation during two betatron damping times of the damper ring.

1. The Electron Gun

The electrons will be generated by photoemission from semiconductor cathodes. SLAC has experience in operating such electron guns on the linac. They were used to provide the polarized electron beam for the recent inelastic scattering parity-violation experiment. Development work has continued since that experiment, and currently we have been

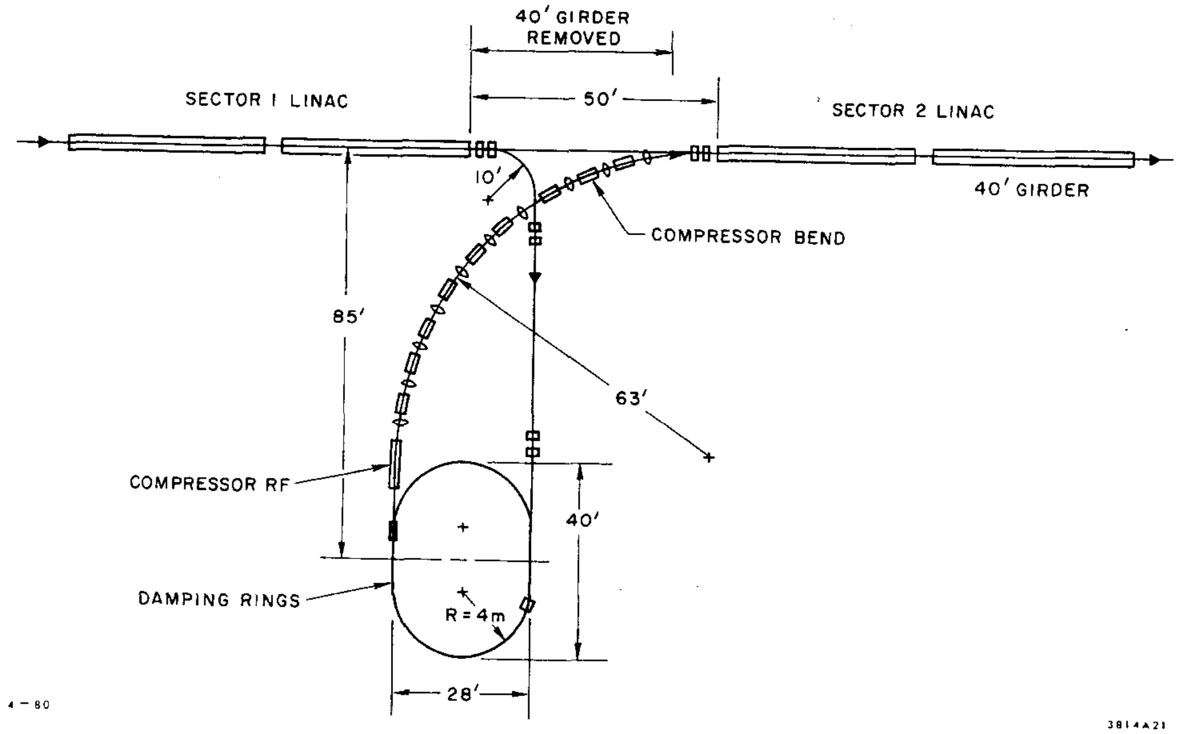

Fig. 21. Beam paths to and from the damping rings.

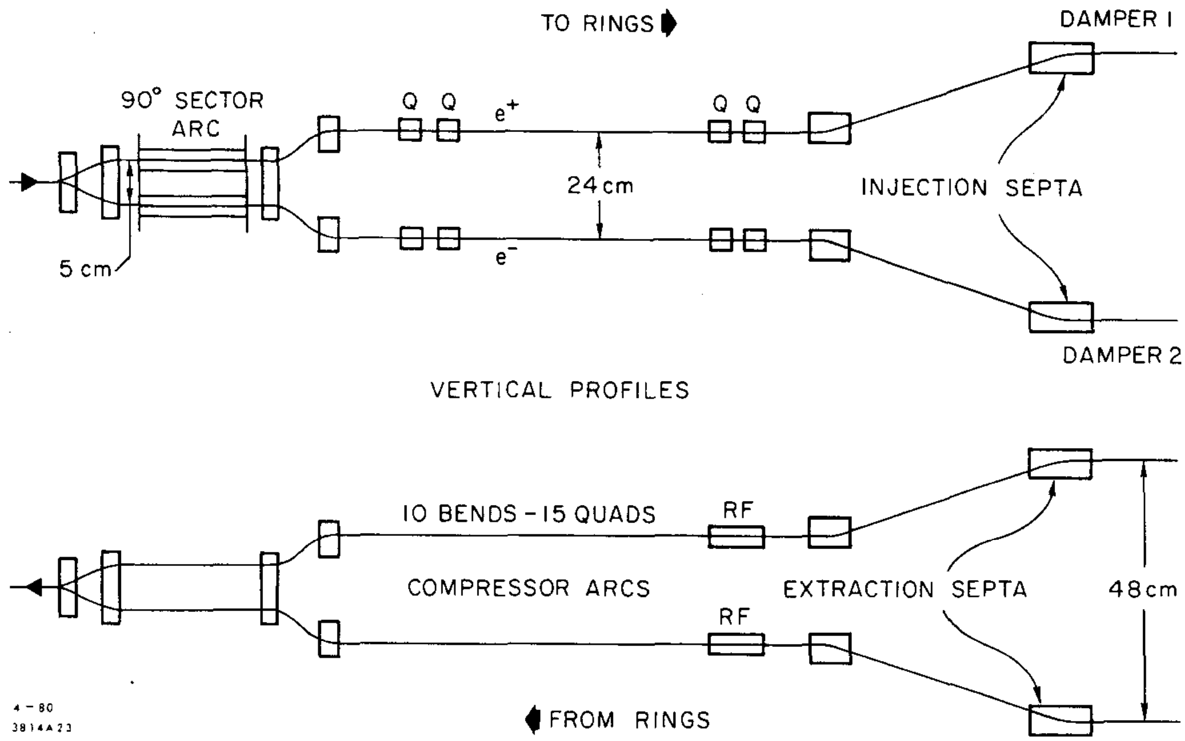

Fig. 22. Schematic vertical profiles of the beam paths to and from the damping rings.

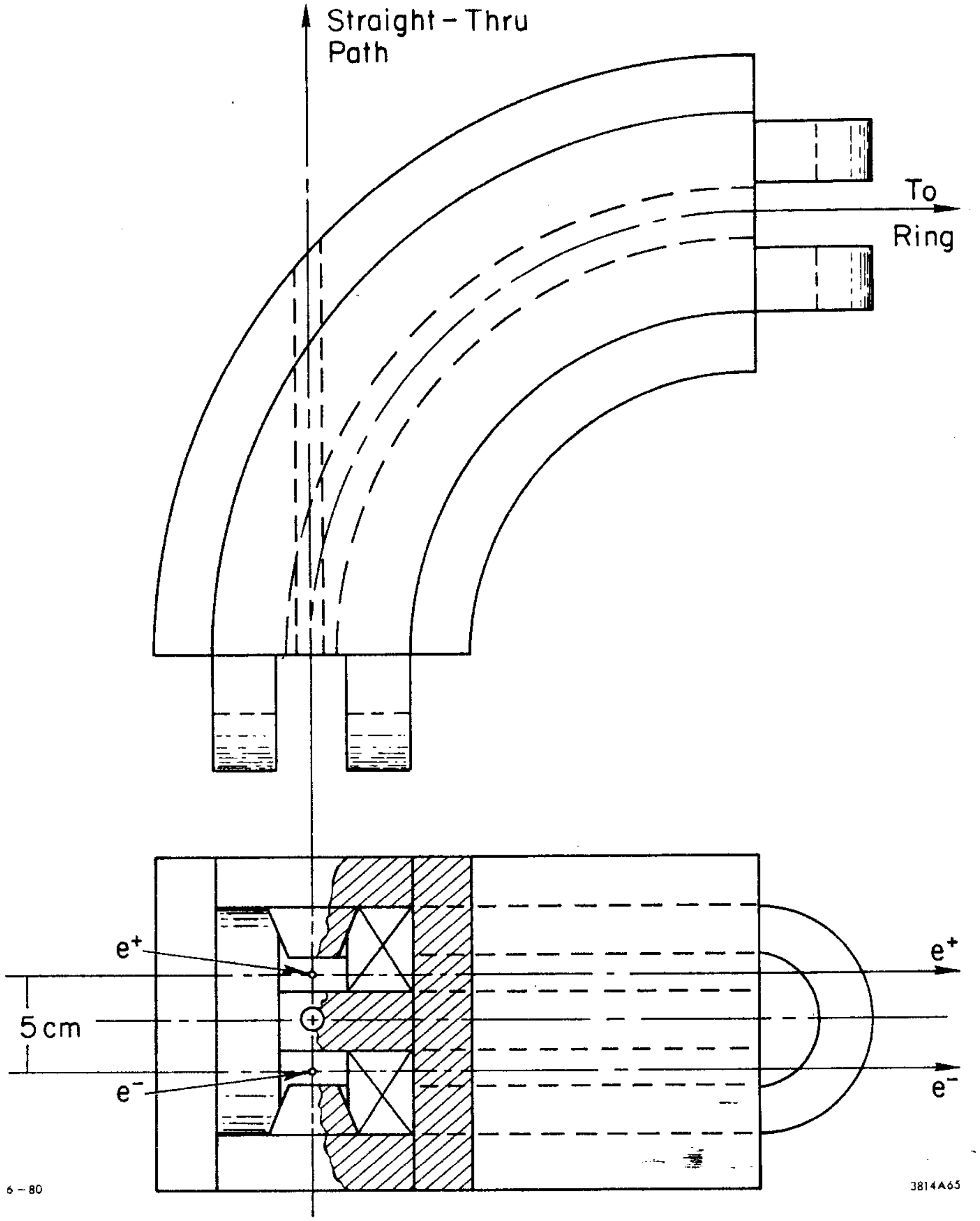

Fig. 23. The 90° double-channel bending magnet.

able to produce cathodes which exhibit the following characteristics:

(a) Emission current densities of 180 A/cm^2 (space-charge limited), a number well in excess of anything that is feasible with thermionic emitters.

(b) Constant quantum efficiencies over a range of 4×10^7 in optical illumination power, from 2 mW to 80 KW.

(c) Photoemission currents which follow the incident optical pulse shape into the nanosecond region.

(d) Operation in electric fields of 80 KV/cm without apparent degradation.

(e) Emission of beams with longitudinal polarizations in excess of 50% when the cathode is illuminated with circularly polarized light of the proper wavelength.

Continuing developmental work will further explore and improve upon several of these features of photoemission cathodes. In particular, it is expected that photoemission currents should follow the incident optical pulse shape well into the subnanosecond region, and that the longitudinal polarization can be increased to values on the order of 90%. The availability of a polarized beam may be important for experimental studies at Collider energies.

2. The Buncher

While it appears likely that photoemission cathodes could directly generate an electron pulse containing 5×10^{10} electrons and lasting only 100 to 150 psec, computer simulations indicate that the transient and space-charge phenomena associated with such a bunch are so severe that it might not be possible to bunch and capture all of this charge into a single S-band bunch in the linac. Since these problems decrease significantly as the electron bunch becomes longer, we have decided to employ a subharmonic buncher between the electron gun and the S-band linac. In this scheme, initial bunching will be accomplished at the 16th subharmonic (178 MHz) of the linac RF frequency. This will allow the electron pulse from the gun to be up to 1.5 nsec long, thus eliminating most of the ill effects associated with the higher charge density of the 100 psec bunch. The subharmonic buncher planned will deliver an electron pulse of approximately 100 psec length at 200 KV to a standard SLAC injector section. The subharmonic buncher itself will consist of a single cavity and a drift section. Subharmonic bunching has been used to achieve single bunches containing more than 5×10^{10} electrons in an L-band linac at Argonne.

3. The Injector

The bunch from the subharmonic bunching section will enter a standard SLAC injector section, exactly like that used presently on the linac. This section is composed of a standard 10-ft accelerator section with an attached 10-cm traveling-wave buncher section. At the output of this section, the beam will be fully bunched and will have an energy of about 50 MeV. Solenoidal focusing will be used along the entire length of the subharmonic buncher and the injector section. The cathode itself will be in a magnetic-field-free region, in order to avoid emittance degradation. A 6-foot-long instrumentation section will follow this single-bunch injector, before the beam enters the conventional linac.

4. The Laser

The necessary optical pulses for the photoemission cathodes will be provided by a frequency-doubled, actively mode-locked, Q-switched Nd:YAG laser oscillator. The design of this laser is based very closely upon the laser oscillator that is now in use at Lawrence Livermore Laboratory as the first element in the large SHIVA and ARGUS laser chains. The major difference between the two systems is the higher repetition rate that is required for our application. The energy in a single optical pulse necessary to produce the required number of electrons (even from a cathode of very poor quantum efficiency) is much smaller than that produced by the LLL laser, so it is expected that the higher repetition rate will be achieved without undue difficulty, and without the necessity of using multiple lasers. The active mode-locking of the laser will be done at 59.5 MHz, which is the 48th subharmonic of the linac RF frequency. The phase stability of the optical pulses so produced with respect to the linac RF should be more than adequate ($\simeq 10$ psec). This laser normally produces a train of pulses extending over a fraction of a micro-second, so the generation of two electron pulses is simply a matter of selecting out two optical pulses from the train.

The 532 nm wavelength of the frequency-doubled Nd:YAG laser will not, in general, be exactly that required for the production of maximum electron polarization. The cathodes currently under consideration as highly polarized electron emitters require significantly longer wavelengths for optimum polarization. For these cases, the 532 nm optical pulse may readily be used as a pump pulse for a secondary dye laser operating at the desired wavelength.

5. The Complete System

A complete single-bunch injection system, composed of the photoemission cathode and its associated laser, the subharmonic buncher, the standard injection section, and the instrumentation section, is presently being designed and constructed. The high-power RF for this injector will come from the second of the two existing injector klystrons, so it is only necessary to add some further RF "plumbing" in the injector area. The entire injection system will be mounted on the linac axis directly behind a heavy shielding wall at the end of the present SLAC injection area. In addition to the photoemission gun, a thermionic gun is being designed to serve as a backup. We anticipate that the final design of an intense single-bunch injector can be made with the information learned on this developmental system, and that the final design will make use of many, if not all, of the subsystems presently being developed. The complete developmental system is expected to begin operating in the latter part of 1980, both for the study of intense single-bunch generation and for experiments on the behavior of such bunches in the linac.

H. Instrumentation and Control

1. General Description

The existing SLAC Main Control Center (MCC) will be expanded to accommodate the new SLC computer system and four new control consoles. The computer control system will contain up to 150 remote data-acquisition and control clusters linked to large central processors located in MCC. The remote clusters will be located along the linac in the 30 existing sector instrumentation alcoves and in 75 to 100 alcoves distributed along the beam-injection lines and the Collider arms. Clusters will also be located at the injector, damping rings, and positron source. The system will be linked to existing beam-switchyard computers to provide control and monitoring functions for PEP, SPEAR, and other experimental beams.

In addition to the computer instrumentation that will provided for the new beam-transport components of the SLC, new instrumentation will also be provided along the linac for klystron and power-supply monitoring and control, and for other systems such as vacuum and cooling water. Particular attention will be given to precise computerized measurement of beam position of the entire SLC system.

A new integrated timing system will provide exact timing information for all SLC components. Existing personnel protection, beam containment and machine protection systems will be expanded to support the needs of the SLC.

2. Computer System

The computer system will provide an integrated data-acquisition and control system for all elements necessary to provide SLC beams. The system will also provide monitoring and control functions for the existing SLAC beam switchyard through a link to existing control computers.

In addition to performing responsive and flexible "look-and-adjust" functions, the system will execute on-line mathematical machine-modeling programs in order to perform automated control algorithms on the beam parameters. Examples of these algorithms include automated configuration setup and change, automated orbit correction, and klystron replacement for the linac. In order to maximize experimental luminosity, the computer system will be required to produce updated control parameters within a second or two.

In order to provide responsive and flexible controls for beam operations and to support the complex mathematical modeling necessary for automated algorithms, the computer system contains a combination of large 32-bit Fortran-oriented processors and a highly distributed network of 16-bit microprocessors which will be integrated into a control cluster. The block diagram in Fig. 24 shows a proposed configuration.

Several commercial or standarized options are available for the remote data-acquisition and control clusters which will directly interconnect to the apparatus to be monitored and/or controlled. The hardware

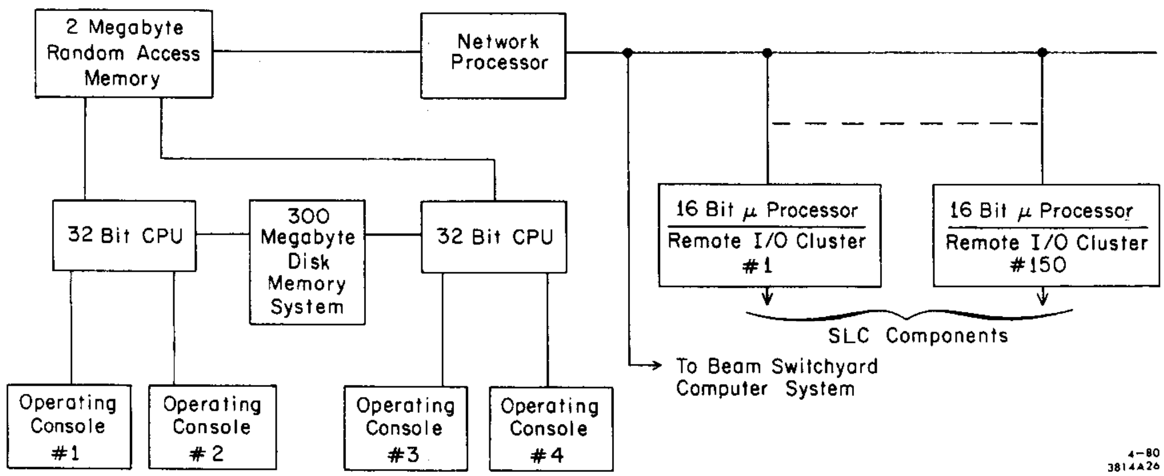

Fig. 24. Schematic representation of the SLC control system.

must be capable of economically supporting a flexible configuration of microprocessors and related input-output modules. Although the detailed configuration of a cluster will vary with the particular application, they will be similar in function in that they will monitor and control power supplies, beam-position monitors, vacuum pumps, valves, etc. The cluster for the linac sectors will also monitor and control the modulator/ klystron system.

A typical cluster will handle up to 300 input or output signals. The local control response time of a cluster will be on the order of milliseconds, with an analog measuring and control accuracy better than 0.1%. The clusters will be connected to the central computers via high speed ($\simeq 1$ megabaud) links.

3. Timing

The SLC will require precise, low-jitter timing for many of its components. In addition, more or less standard timing signals will be required for beam-position monitors, modulators and like systems. The precise signals will be required for the laser-gun pump signal, the RF drive line, and the damping rings and compressor. The precise timing stability and accuracy will be of the order of 5 picoseconds. The other signals may be relaxed to the order of 1 nanosecond.

It is essential that the RF frequency of the damping rings be subharmonically related to the 2856 MHz linac frequency. This, along with the 5 picosecond (or approximately 1 degree @ 2856 MHz) stability and accuracy criterion, will ensure precise injection into the linac from the damping rings and, somewhat less critically, from the gun into the linac and thence into the damping rings for the scavenger bunches.

4. Position Monitors

The monitoring of the beams' trajectory along the linac and around the two Collider arms will require a large number of position detectors. A typical position-monitor station will be made of four coaxial feedthroughs mounted at 90° intervals around the vacuum chamber. If the pick-up element, whether a loop or a button-like electrode, is physically longer than the length of the bunch, the beam-induced signals will exhibit a time length comparable to the bunch length. The signal produced by the short, intense bunches as they travel past small pick-up electrodes will assume the shape of a pair of impulses with several kilovolts of amplitude. Yet there is a clear advantage in obtaining single impulses as opposed to doublets, i.e., pairs of impulses, one positive and one negative. Fortunately, the second impulse of the doublet can be greatly attenuated by using a small, longitudinal strip-line that has been loaded with a lossy dielectric such as ferrite. Alternatively, the pick-up element can be made up of four coaxial cables connected to a small gap in the beam chamber. In this case, the second impulse can be eliminated by enclosing the gap with a ferrite-filled enclosure.

The four detected impulses will be "smoothed" with a length of ordinary cable and will then be processed in a conventional manner (Fig. 25). The complete processing of each set of four signals will be completed in less than 5 milliseconds (which is shorter than the inter-pulse period), using low-cost analog-to-digital converters. The data will be stored locally, then delivered upon command to the data-acquisition system for calculation of the bunch position. Since each button electrode in the SLC system will have its own processing channel, a complete SLC trajectory will be measured for each individual beam pulse.

Given two signals, V_1 and V_2, obtained from opposite electrodes mounted on a beam pipe of radius R, the beam position in the direction defined by the two electrodes is simply given by $R(V_1 - V_2)/(V_1 + V_2)$. For the linac chamber, $R = 10$ mm; a measurement of V_1 and V_2 to 0.5% will therefore permit a beam-position detection to 0.05 mm. On the Collider, R is even smaller, so the tolerance on the measurement of V_1 and V_2 can be somewhat relaxed to obtain a detection with a precision of 0.1 mm. Each set of four processing channels will be calibrated by routinely applying the same 1 nsec pulse to each input in order to record the variations and dissimilarities that might occur in the electronics. During tune-up and initial orbit corrections, digital averaging of data can be used to yield an even finer beam-position measurement.

5. Protection Systems

(a) The personnel protection system

The Personnel Protection System for the SLC will be consistent with the PPS philosophy and design incorporated in the existing linac, and

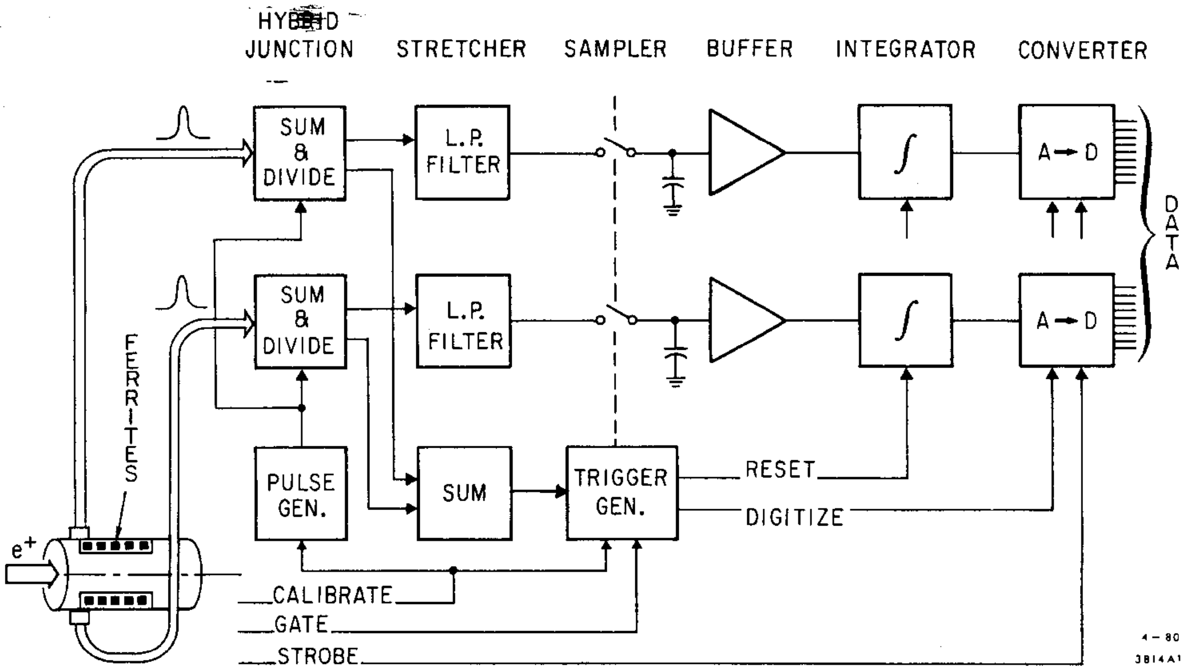

Fig. 25. Schematic representation of the beam-position-monitoring system.

will provide access monitoring and control with "Access Modules" at the beam target area. These Access Modules will include keybanks, closed circuit TV, badge-reading, intercom and telephone capability. Access to the linac will be through the existing system with the addition of one or more controlled access points at the injector and damping ring areas. The Collider will be divided into two PPS zones (one for each arm) with a third zone at the target area. These zones will include PA system and emergency beam-shut-off facilities and will be separated by remotely locked gates. Control and monitoring will be located at the SLC/linac Main Control Center. In addition, the system will include beam-shut-off ion chambers located at potentially hazardous radiation areas.

(b) The beam containment system

The Beam Containment System for the SLC will be designed to monitor and detect high-power beams of sufficient power density to be destructive to the beam-line components and which could present potential hazards to personnel occupying areas downstream of the beam path. It will consist of three beam-sensing current pick-ups in each leg of the Collider, with distribution and processing electronics to perform average-current monitoring to limit maximum power, and with pulse comparison at upstream and downstream locations to insure correct beam transport to regions where beam power may be safely absorbed and dissipated. "Disaster monitors" will be provided at suitable locations for back-up protection at sensitive areas of the beam-transport system where potentially hazardous beam-burn-through could in principle occur. In addition, ion chambers (five in each arm) will be located at key areas along the transport system. The system will be integrated into the existing Beam Containment system used with the linac.

6. Broadband Communications

In order to minimize the need for a large, expensive cable plant, multiplexed methods for transmitting analog, digital, video, and voice information over the SLC site are being investigated. The use of frequency-division and time-division multiplexing techniques for SLC requirements is being investigated in order to determine economic and operational feasibility.

A most promising approach seems to be the use of commerically available cable television (CATV) systems and equipment to frequency multiplex many channels of information. With this system one 3/4-inch cable, used with appropriate amplifiers, taps, modulation and demodulation, could support 17 TV channels. In turn, each of the TV channels could support a 2 megabaud digital channel, or two hundred 9600-baud digital channels, or 500 voice channels.

A competing technology, the use of fibre optics combined with time-division multiplexing of the signals, will be studied in the near future.

I. Luminosity

The luminosity that can be attained by the SLC is determined by a combination of effects which occur in the major subsystems of the object. In this section we discuss these effects and their energy dependence, give the design luminosity as a function of energy, and set forth some possibilities for future developments which would increase the luminosity.

1. Initial Design Luminosity

The luminosity of the SLC is given by

$$\mathscr{L} = \frac{N^2 f \gamma}{4\pi\beta^* (\varepsilon_{nx}\, \varepsilon_{ny})^{\frac{1}{2}}}$$

where N is the number of particles in a bunch, f is the accelerator repetition rate (180 Hz), γ is the energy at the collision point in rest-mass units, β^* is the β function at the collision point, and ε_{nx} and ε_{ny} are respectively the horizontal and vertical invariant emittances of the bunches $(\sigma_x \sigma_{x'} \gamma)$ at the collision point. The final emittance of each bunch is determined by (1) its emittance as it leaves the damping ring, which is increased by the effects of transverse wake-fields in the linac; and (2) quantum fluctuations in the synchrotron radiation emitted in the Collider arcs as affected by the orbit distortions in the arcs and also by the bending required for chromatic corrections in the final-focusing system.

The damping rings operate at a fixed energy and thus always launch a bunch with the same emittance, independent of the final linac energy.

The emittance growth caused by transverse wake-fields (see Appendix A) is a complex phenomenon, since it depends on the linac alignment tolerances, on the charge per bunch, and on the accelerating gradient in the linac. For a given linac alignment tolerance (0.1 mm in our case), the emittance growth from the transverse-wake effect is a constant if

$$\frac{N \ln(E_f/E_o)}{G} = \text{constant}$$

where G is the accelerating gradient, E_f is the final energy, E_o is the damping ring energy, and N is 5×10^{10} at 50 GeV. In determining the Collider luminosity as a function of energy, we include a fixed invariant emittance growth and constrain N as a function of E_f by the above equation.

The contributions to the emittance from quantum fluctuations in the synchrotron radiation emitted in the Collider arcs and in the final-focus system are each proportional to the fifth power of the final energy (see Appendix B). The individual contributions to the emittance are given below.

Invariant Emittance (m-rad)

Source	ε_{nx}	ε_{ny}
Damping Ring	2×10^{-5}	2×10^{-5}
Linac Transverse Wake	0.34×10^{-5}	0.34×10^{-5}
Collider Arc	$0.94 \times 10^{-5}(E/50)^5$	
Orbit Distortion in Arcs	$0.58 \times 10^{-5}(E/50)^5$	$0.26 \times 10^{-5}(E/50)^5$
Final Focus	$0.28 \times 10^{-5}(E/50)^5$	

The luminosity as a function of energy is shown in Fig. 26 for a β^* of 1 cm. At low energy, the quantum effects are negligible, and the luminosity increase is slightly faster than linear from the increase in γ and from the increase in N allowed by the transverse-wake effect. The effects of the synchrotron radiation have become significant at 100 GeV, and if we were to increase the linac energy, these effects would make the luminosity peak at 120 GeV and then decrease.

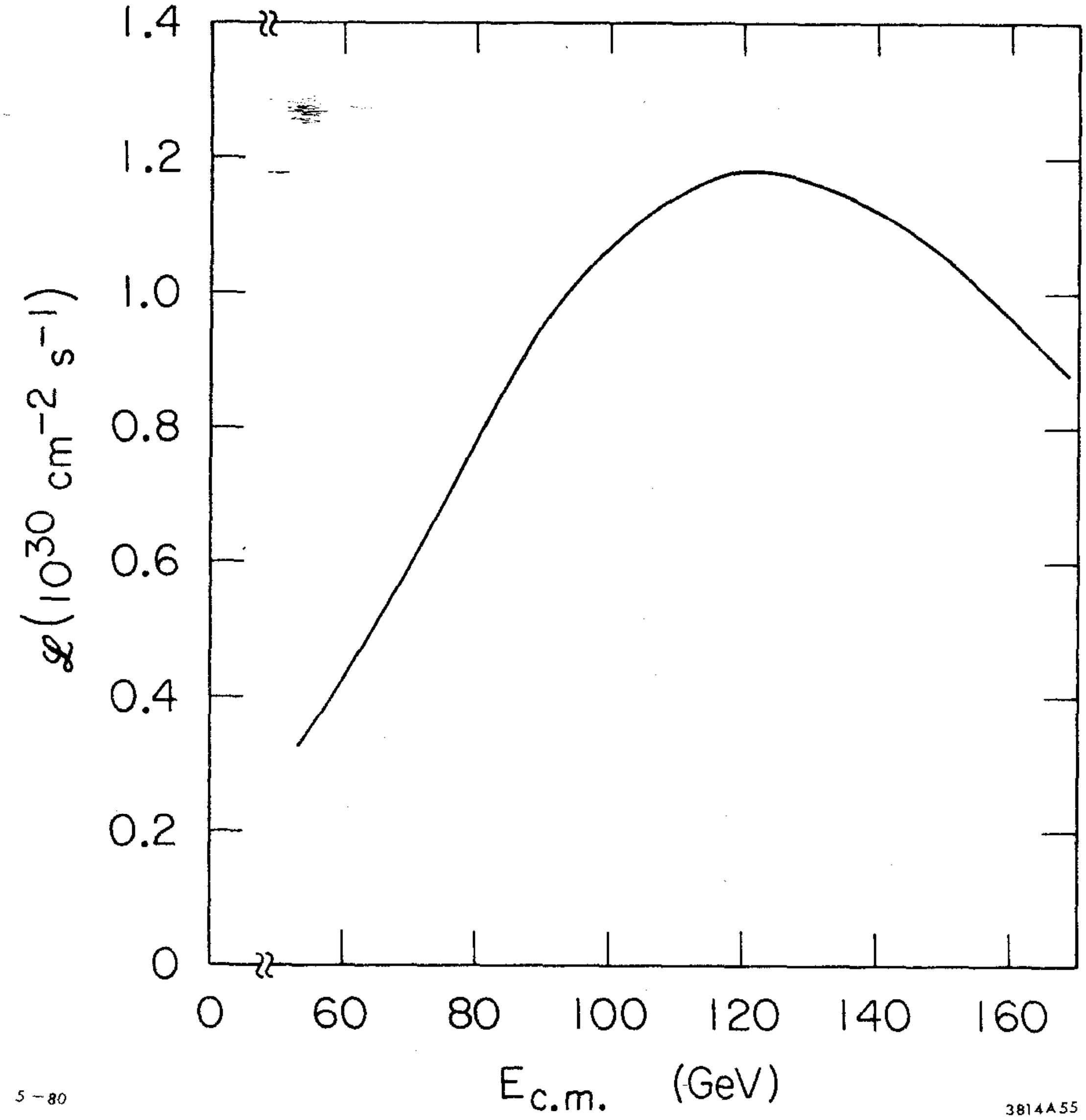

Fig. 26. Luminosity vs center-of-mass energy in the SLC.

2. Possibilities for Luminosity Improvement

The luminosity shown in Fig. 26 is different in character from the limiting luminosity that can be attained in storage rings. In storage rings the limit is believed to be fundamental (the limiting tune-shift effect), while in the Collider the limit is imposed by various technical factors. There are significant possibilities for improvement, some of which are discussed briefly below.

One possibility, which is evolutionary, is to attain more precise control of the trajectory in the linac. This would allow an increase in the number of particles per bunch before exciting serious emittance growth from the transverse wake-fields. A reduction of a factor of 2 in the trajectory errors would allow an increase of approximately 2 in the luminosity.

Another improvement would arise from a decrease in the β function at the collision point from 1 cm to 1/2 cm, which would increase the luminosity by a factor of 2. A modified final-focusing system, which has a lower value of β^*, is under design.

The beam-beam pinch effect described in Appendix D will also increase the luminosity. With $\beta^* = 1$ cm, the disruption parameter D is approximately 0.4, and the pinch effect increases the luminosity by approximately 30%. However, with $\beta^* = 1/2$ cm, D is increased to 0.8, which greatly strengthens the pinch and gives a luminosity enhancement of a factor of 3 over that obtained with the reduced β^* alone.

From a combination of all these effects we believe that the ultimate luminosity of the SLC may lie between 5×10^{30} and 10^{31} $cm^{-2}sec^{-1}$.

References for Section II

1. Z. D. Farkas, H. A. Hogg, G. A. Loew and P. B. Wilson, Proc. IXth Int. Conf. on High Energy Accel., SLAC (1974), p. 576.
2. Z. D. Farkas, H. A. Hogg, G. A. Loew and P. B. Wilson, IEEE Trans. Nucl. Sci. NS-22, No. 3, 1299 (1975).
3. Z. D. Farkas, H. A. Hogg, G. A. Loew and A. R. Wilmunder, IEEE Trans. Nucl. Sci. NS-24, No. 3, 1827
4. G. A. Loew, Proc. Xth Int. Conf. on High Energy Accel., Serpukhov, USSR (1977), Vol. 1, p. 58.
5. G. A. Loew, "Ideas on Linacs for Colliding Beams," AATF/79/4.
6. H. Wiedemann, AATF/79/7, AATF/79/9, AATF/79/12, Sept. 1979.
7. E. D. Courant, M. S. Livingston, H. Snyder, Phys. Rev. 88, 1190 (1952).
8. G. E. Fischer, AATF/79/5, Aug. 1979.
9. R. Steining, Collider Note CN-14, Feb. 1980.
10. G. E. Fischer, AATF/80/18, March 1980.
11. H. Wiedemann, AATF/79/7, Sept. 1979.
12. See Appendix D; also R. Sah, AATF/80/14; J. Jaros, AATF/80/22.
13. J. E. Augustin et al., Proc. of the Workshop in Possibilities and Limitations of Accelerators and Detectors, p. 89, FNAL, Oct. 1978.
14. K. Halbach, LBL Report 9604, Aug. 1979.
15. R. F. Holsinger, 1979 Proton Linear Accelerator Conf.
16. R. L. Ford and W. R. Nelson, SLAC Report No. 210.
17. R. B. Neal, ed., The Stanford Two-Mile Accelerator, W. A. Benjamin, Inc., New York (1968), pp. 551-560; R. Helm, SLAC Report No. 4 (1962).
18. Y. B. Kim and E. D. Platner, Rev. Sci. Instrum. 30, 524 (1959); M. N. Wilson and K. D. Srivasta, Rev. Sci. Instrum. 36, 1096 (1965).
19. B. Aune and R. H. Miller, SLAC-PUB-2393.
20. H. Wiedemann, AATF/79/8, Sept. 1979.
21. H. Wiedemann, AATF/79/11, Sept. 1979.

III. EXPERIMENTAL USE

A. General

In this section we shall discuss the design specifications for the experimental hall, and also the backgrounds which will be experienced by detectors at the Collider. We begin with a review of the physics environment to be expected at energies of 100 GeV, the physics opportunities which we hope to encounter, and the specifications for some typical detectors that might be used at the SLC. We then discuss the size and layout of the interaction hall, the assembly and support areas, and the counting houses for the Collider. Finally, we review the various sources of backgrounds that will be encountered at the SLC, discuss how they might be reduced, and evaluate the irreducible counting rates that must be tolerated by a detector working at 100 GeV.

B. The Environment

In order to explore the characteristics of the physics environment at 100 GeV, we have performed Monte Carlo studies using the simplest version of the Weinberg-Salam model with three generations of leptons and quarks, and with $\sin^2\theta_W = 0.23$. This represents our best guess as to what to expect at these new high energies. The Z^0 formed in e^+e^- collisions around 90 GeV is expected to decay into pairs of primary fermions with the following probabilities: 18% into neutrino pairs, 9% into charged lepton pairs, and 73% into quark pairs of various flavors. The quarks can radiate a gluon according to the standard QCD formalism. The fragmentation of the quarks and gluons to form jets of hadrons is described by the Field-Feynman recursive procedure, which is a reasonable first approximation for the expected hadronization. Several interesting "fingerprints" of the multihadron events likely to be encountered are shown in the following figures.

The average charged multiplicity is displayed in Fig. 27, together with the predicted multiplicity distributions for Z^0 decays. One must expect events with an average charged multiplicity of 20, and about ten percent of the time there will be events with total multiplicity as large as ≈ 80.

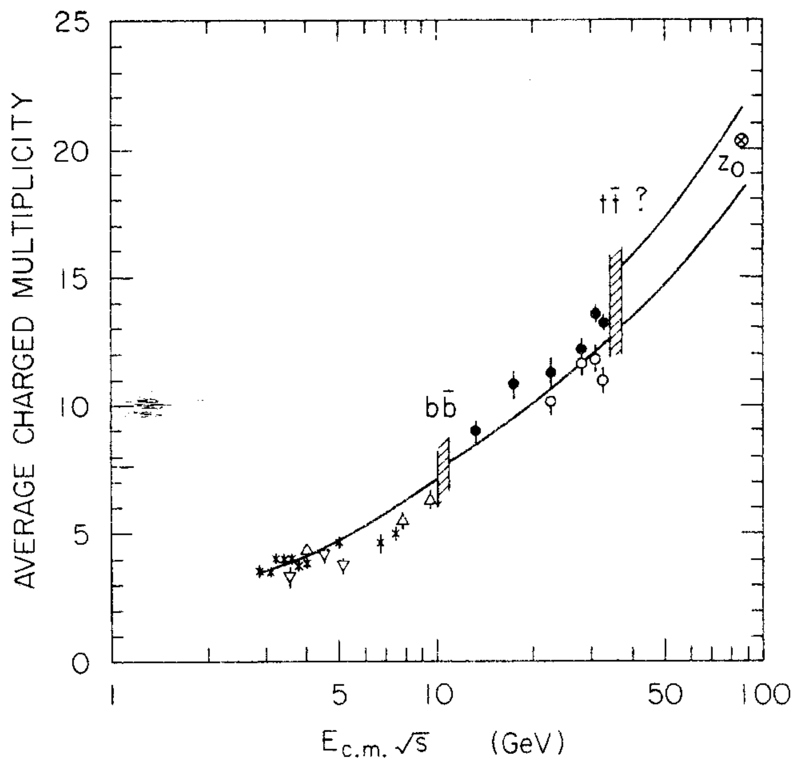

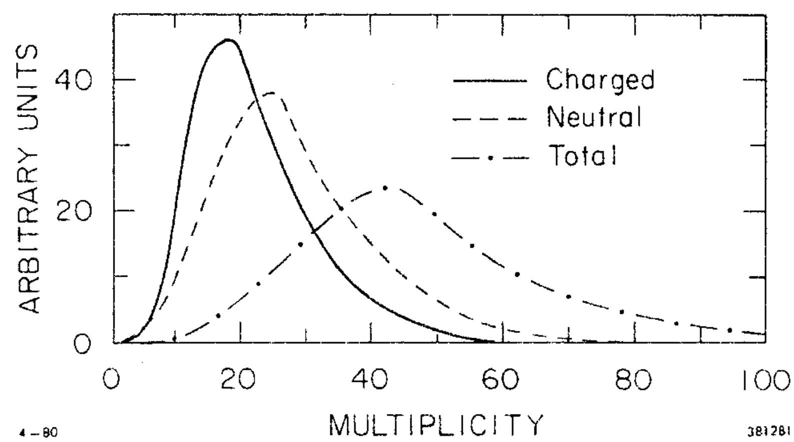

Fig. 27. (a) The average charge multiplicity as a function of the center-of-mass energy $\sqrt{s}$. Representative data points from SPEAR, DORIS and PETRA are shown, together with the expectations from the model of $e^+e^- \to \gamma \to$ hadrons (with and without t quark production) and $e^+e^- \to Z^0 \to$ hadrons. Higher order QCD corrections are expected to increase the average multiplicity for $\sqrt{s} \geq 40$ GeV. (b) The distribution of charged, neutral and total multiplicity expected from the decay $Z^0 \to q\bar{q}$, with the mass of the Z^0 taken as 90 GeV. About 84% of the neutral particles are photons, and about 89% of the photons come from π^0 decays.

The characteristics of the momentum spectrum of the hadrons from Z^0 decays are summarized in Figs. 28 and 29. The inclusive momentum distribution for all charged hadrons, displayed as a function of $x = (p/p_{beam})$, is shown in Fig. 28. Data from lower energies are shown together with a prediction of 90 GeV $Z^0 \to q\bar{q} \to$ hadrons. Notice the build-up of low-momentum hadrons as the energy of the e^+e^- collision increases. Figure 29 displays the momentum spectrum for only the fastest charged hadron or fastest neutral particle in a given event. Clearly, any detector working in this energy range (about the Z^0) must be capable of detecting and measuring charged and neutral hadrons over a broad range of momenta.

Finally, the spatial distribution of the decays may be characterized by a parameter called sphericity, which describes the "jettiness" of an event: 0.5 is a phase-space-like spherical event, while a sphericity of 0 is a pencil-like, back-to-back jet. Figure 30 shows the average sphericity as a function of center-of-mass energy. At 100 GeV, the final-state hadrons from Z^0 decays are expected to be strongly collimated in well-defined back-to-back jet structures, with frequent appearance of a third and even a fourth jet corresponding to the radiation of gluons by the primary quarks.

In summary, a detailed study of the multihadron events will present a substantial challenge for a detector. These events will have large multiplicity and will be highly collimated into jets, which in turn will decay into hadrons with a very broad momentum spectrum. In addition to these one-photon and Z^0-formation processes, there will be a background from the two-photon process. These events are discussed with other sources of background in Section F below, and in more detail in Appendix E.

C. Physics Opportunities

The main physics goals of experiments at 100 GeV center-of-mass energies and beyond are briefly summarized below.

1. The Z^0

The observation of the neutral vector boson, a carrier of the weak interaction, is clearly the main prize. The standard model of electroweak

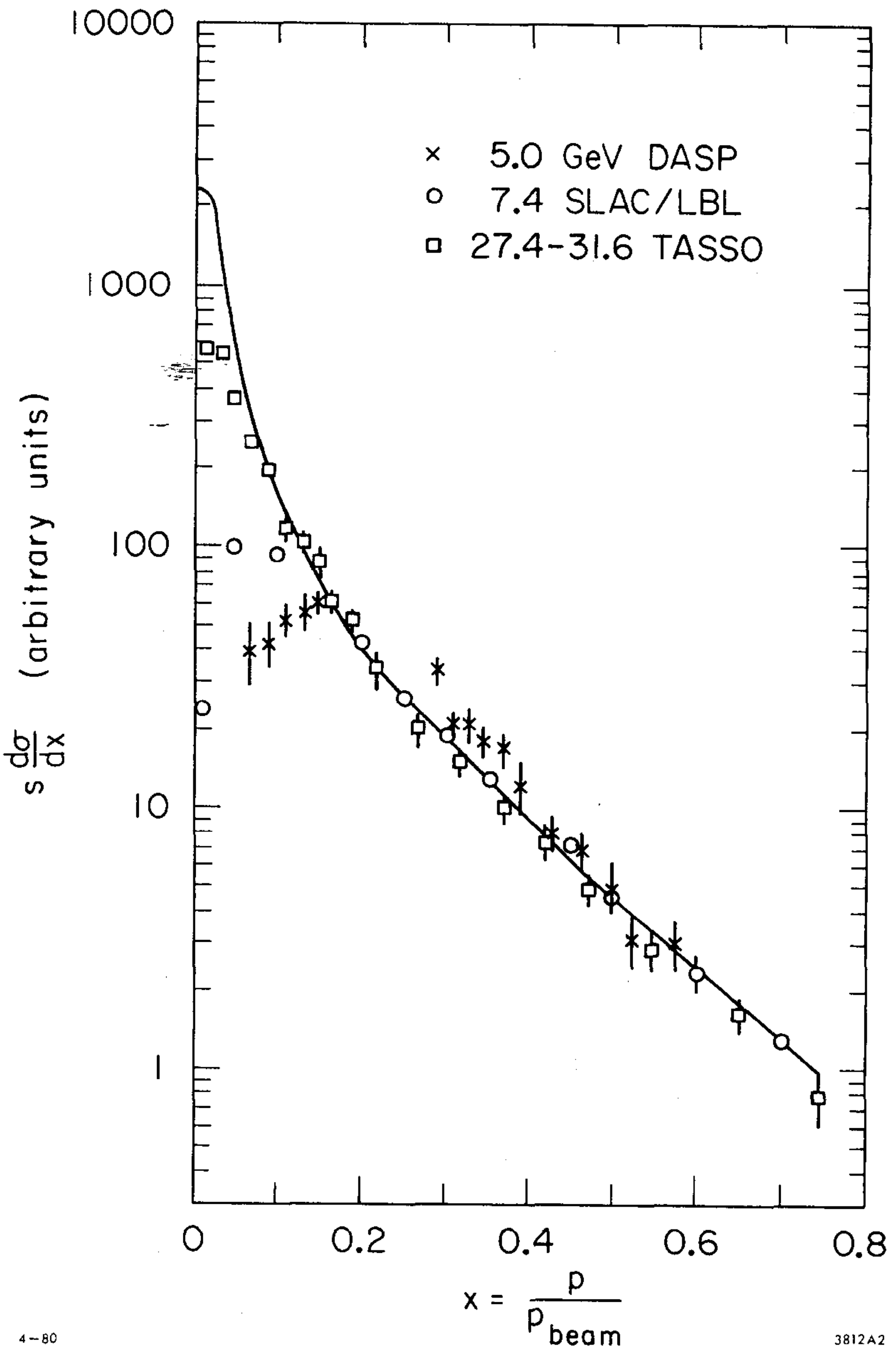

Fig. 28. The inclusive distribution of the quantity $x = p/p_{beam}$ of charged hadrons from the decays $Z^0 \to q\bar{q}$. Representative data from lower energies are shown for comparison. The normalization of the predicted curve is arbitrary.

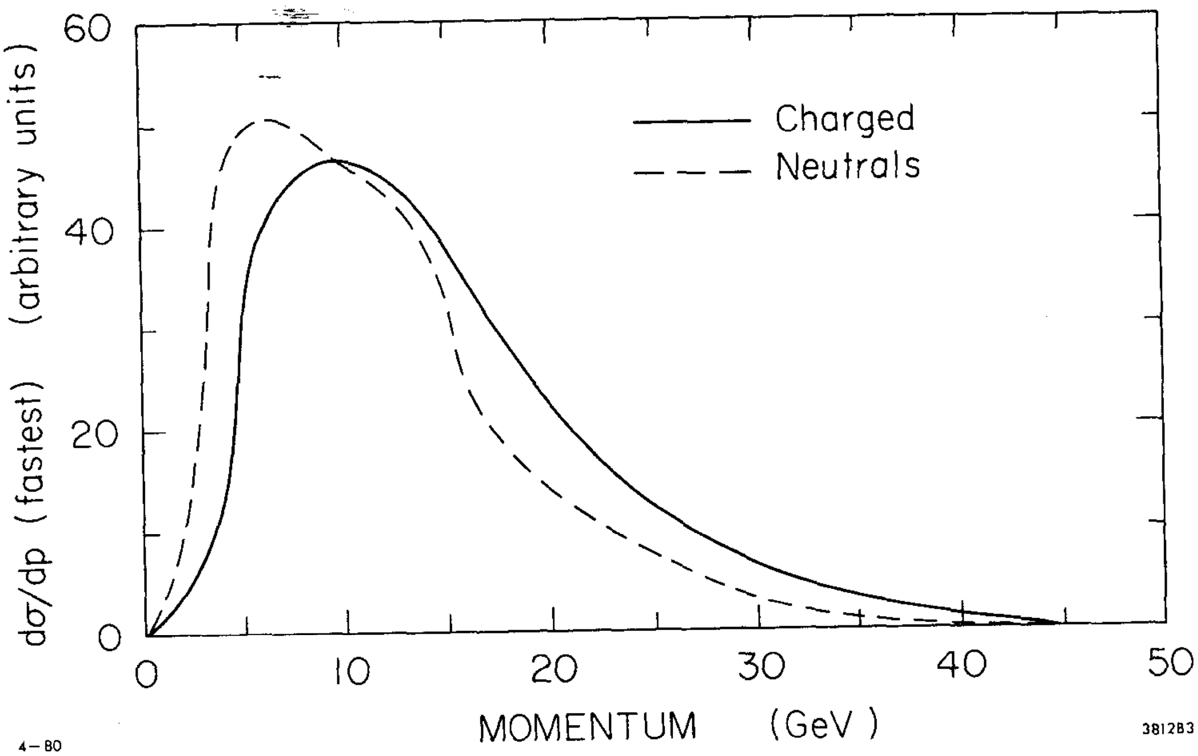

Fig. 29. The momentum distribution of the fastest charged hadron and the fastest neutral particle expected for the decays $Z^0 \rightarrow q\bar{q}$.

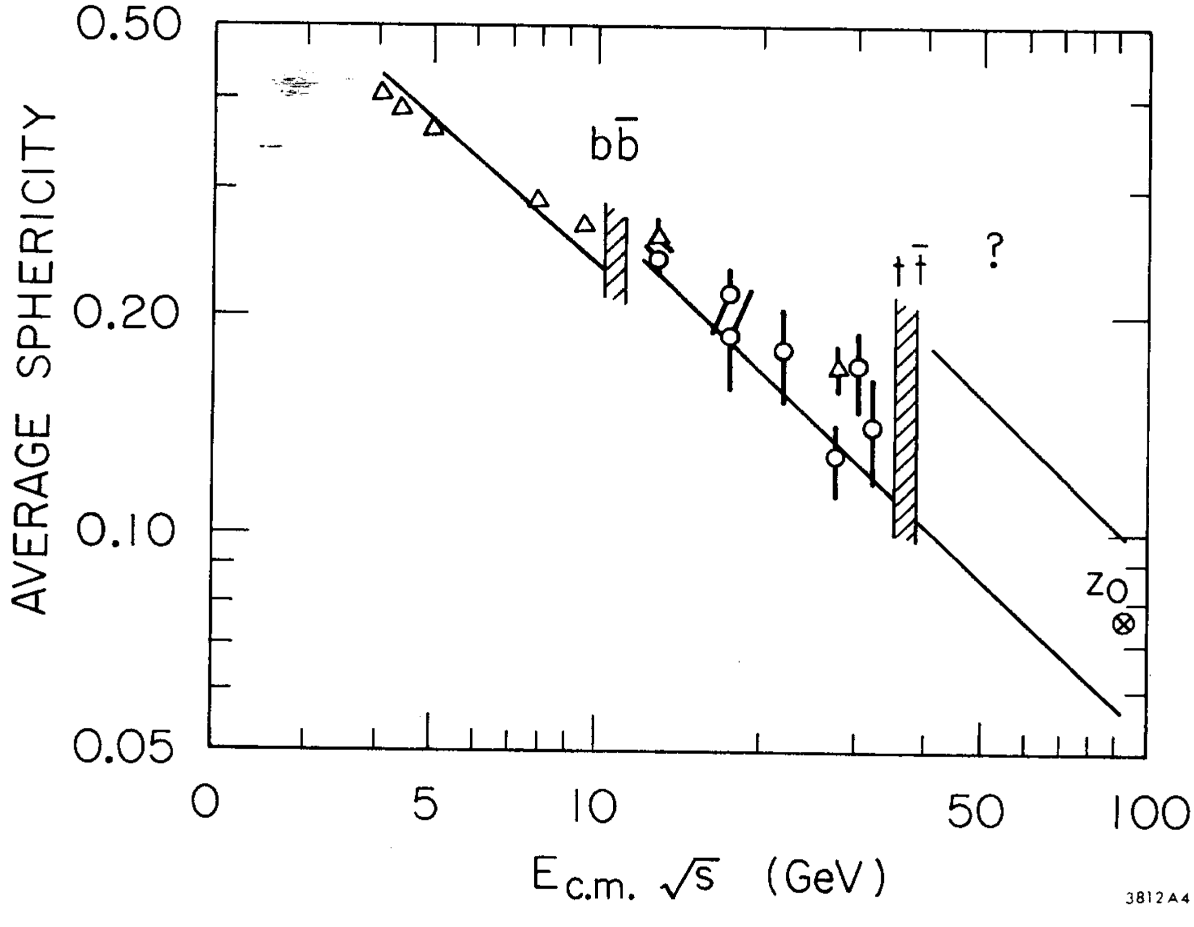

Fig. 30. The average sphericity of multi-hadron events in e^+e^- collisions as a function of center-of-mass energy. Higher order QCD corrections are expected to increase the average sphericity for $\sqrt{s} \geq 40$ GeV.

interactions predicts the Z^0 mass to be in the neighborhood of 90 GeV, and to be copiously produced in e^+e^- annihilation. Indeed, the yield of multihadron events should exhibit an enormous bump at the Z^0. The ratio, R, of the cross-section for such multihadron events divided by the electromagnetic production $e^+e^- \rightarrow \mu^+\mu^-$ is expected to increase from a value of around 5 at present energies to about 5000 at the Z^0 mass. Measurements of the Z^0 width, expected to be about 2.5 GeV in the standard model, can be related to the number of neutrino types that exist, and thus to the number of generations of heavy leptons and quarks beyond the presently known three, up to the Z^0 mass.

The discovery of the Z^0 would motivate studies of its various decay modes. Within the standard model it is expected to decay into lepton pairs and quark-antiquark pairs, as discussed above. Each lepton and quark type has a vector coupling (g_V) and axial-vector coupling (g_A) to the Z^0. Measurement of branching fractions, angular distributions of the charge asymmetry, and polarization-related parameters will serve to separate these coupling parameters. The standard model predicts a universality among the three lepton-quark generations which can best be tested in the Z^0 decays.

2. Electroweak Interactions at Energies Beyond the Z^0

In spite of the dramatic successes of SU(2) × U(1) in predicting electroweak effects, all evidence available to date is consistent with a phenomenological point-like weak interaction which includes a neutral-current piece. The rising cross section resulting from this phenomenological model must be damped, and such damping is contained in the standard model. The behavior of cross sections and the measurements of weak-electromagnetic interference in the interesting regions beyond the Z^0 will be an important test of the ideas which predict unification of these two forces. In addition, the energies above the Z^0 may offer the best promise for studying new phenomena not seen in Z^0 decays.

3. Hadronic Processes

The Z^0 is a prolific source of quarks of all flavors that are not too massive to be energetically excluded. Decays of the Z^0 into quark-antiquark pairs of different flavors will be seen through fragmentation into collimated jets of hadrons. The multihadron decays should be a particularly good source of gluon jets radiated from the primary quarks, and should allow a thorough study of the QCD properties of quarks and gluons. Although many of the QCD predictions will be tested at lower energy machines, extension of these measurements to higher energies will be an important test of QCD ideas. For example, scaling violations in fragmentation functions and broadening in 3-jet events should be pronounced at these higher energies. Identification of jet flavor is a most interesting, challenging, and difficult experimental problem. Improving the techniques of flavor discrimination will contribute greatly to the understanding of quark properties.

4. New Phenomena

The more speculative possibilities of e^+e^- annihilation at 100 GeV energies may also turn out to be the most important. For example, an often considered and most controversial aspect of $SU(2) \times U(1)$ is the Higgs boson. This conjectured boson (or bosons) is responsible for the origin of mass in the standard model, and understanding its properties could lead to a fundamentally important understanding of the mass spectrum of particles. If light enough, Higgs bosons could be seen in the decays of the Z^0.

Evidence of more than one Z^0 would indicate a different structure of the weak interaction than that given by the standard $SU(2) \times U(1)$ model. Alternative models, which are compatible with the existing data, generally predict two Z^0's, one lighter and the other heavier than the conventional Z^0. The standard model may fail in other ways. For example, present assignments place fermions in right-handed singlets, but evidence for right-handed doublets could emerge from further refinement of the neutral-current parameters.

Free quarks are often discussed as a possible final state at the higher energies. Heavy leptons, neutral as well as charged, or any new particles which carry weak charge, may also exist in the final states. Electron-positron annihilation is the most promising place to search for such dramatic events. The most important discoveries may well come from a list of effects which today are only speculations.

5. Polarization Studies

Neutral-current processes are expected to exhibit large polarization-dependent effects. Annihilation of longitudinally polarized electrons on unpolarized positrons in the Collider will permit the investigation of the full set of spin-dependent effects and allow very accurate measurements of many neutral-current parameters.

Intense beams of longitudinally polarized electrons are readily available at SLAC. Polarizations of 50% are now available, and higher polarization beams are a good future prospect. Reversal of polarization is achieved at the source, between beam pulses, and without influence on other beam parameters, thus offering promise of eliminating nearly all systematic effects arising from drifts in accelerator and detector efficiencies and asymmetries in the measurements of neutral-current parameters.

Figure 31 shows a model calculation of the vertical and longitudinal projections of spin in the interaction region for a 50% polarized linac beam and a beam-transport system which approximates the north transport arm of the Collider. Depolarizing effects in the beam-transport system come primarily from the finite energy spread in the beam and from synchrotron radiation, but are expected to be small at the interaction point of the Collider. The rapid oscillations show that useful polarization will occur through all ranges of energies. At the Z^0 mass, the expected width of approximately 2.5 GeV will be sufficiently large to contain several maxima of the g-2 oscillations inside the Z^0 resonance. Present studies to increase beam polarization are underway, and if successful will yield higher polarizations than those shown here.

Polarization asymmetries complement the branching ratios and charge-asymmetry measurements for the different lepton and quark types. The accuracy of $\sin^2\theta_W$ will immediately improve an order-of-magnitude over present low-energy measurements in the first data taken, and the polarization information will contribute significantly to this improvement. As data accumulate and specific decays of the Z^0 can be isolated, measurement of g_A and g_V for the different quarks and leptons should provide a most stringent test of $SU(2) \times U(1)$ ideas.

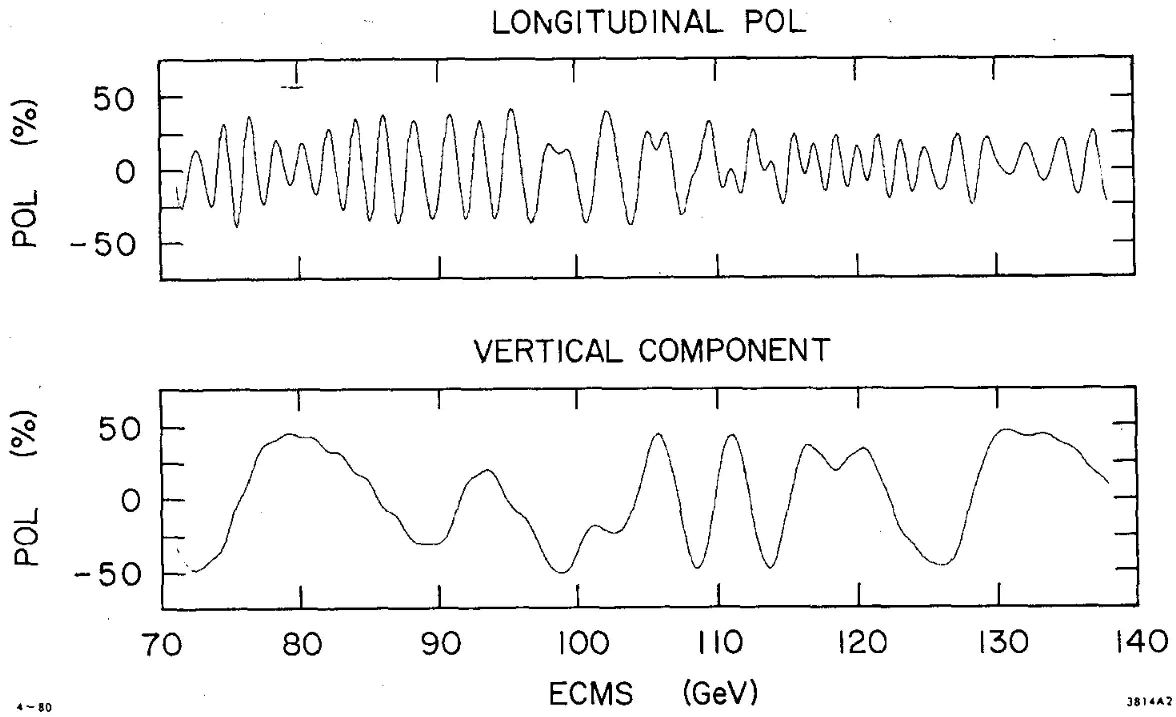

Fig. 31. A model calculation of spin projections in the interaction region as a function of center-of-mass energy, for 50% polarization leaving the linac. The g-2 precession of the electron spin results in rapid oscillations of the longitudinal component and rather slower oscillations of the vertical component from a beam-transport system that approximates the north arc of the Collider ring.

D. The Detectors

We have considered four possible large detector systems that could be used at the SLC, in order to set the scale for detector space and service requirements. Three of these detectors are current experiments at PEP: the High Resolution Spectrometer, the Mark II, and the Time Projection Chamber. The fourth is a "gedanken" detector configured specifically to study multihadron final states at 100 GeV. Table 8 lists some of the characteristics of these "typical" detectors. The so-called Very Large Detector has a large-bore superconducting solenoid of 10 KG field with a high-resolution charged-particle tracking system that is surrounded by electromagnetic and hadron calorimeters and with reasonable muon-detector coverage. It is slightly larger than the existing PEP detectors and about 2-3 times the overall weight.

The existing PEP experiments have their associated electronics in one of three areas: (a) local mounting on the detector, (b) in an intermediate electronics trailer, or (c) in an interaction-area counting house. At PEP the largest use is made of method (b), and the trailers are rather large, occupying 60-70 square meters of the floor area. In order to minimize the size of the SLC assembly halls and at the same time to allow several experiments to prepare for running, we have assumed that the dependence on the intermediate electronics trailers will be reduced for experiments at the SLC. More electronics can be mounted directly on the experiment, and more use will be made of the very conveniently situated counting houses. We have assumed that the SLC experiments can be adequately supported by smaller trailers of about 40 square meters in size.

E. Interaction Hall, Assembly Building and Support Areas

1. General Principles

The experimental hall and the support and assembly building are shown in Fig. 32. The following general principles have been followed in the design and specification of these buildings, in order to obtain maximum use and flexibility of the single interaction point:

(a) The size and facilities of the experimental building allow the simultaneous construction, testing, and maintenance of two large and complex detectors (Fig. 33).

Table 8

Physical Properties of Four Potential SLC Detectors

Name	High Resolution Spectrometer (HRS)	Mark II	Time Projection Chamber (TPC)	Very Large Detector
Length along beam line (m)	7.6	7.5	6.7	13.0
Width (m)	9.8	9.2	7.3	10.0
Total height (m) (corrected for SLC beam height)	10.2	9.0	9.0	10.0
Minimum height required from apparatus bottom to beam (m)	4.0	4.0	4.0	5.0
Weight including muon detector (metric tons)	2000	1800	1000	4000
Size of associated electronics trailer (m^2)	$6.1 \times 11 = 67$	$6.3 \times 11.2 = 71$	$6.4 \times 8.6 = 55$	$10 \times 4 = 40$

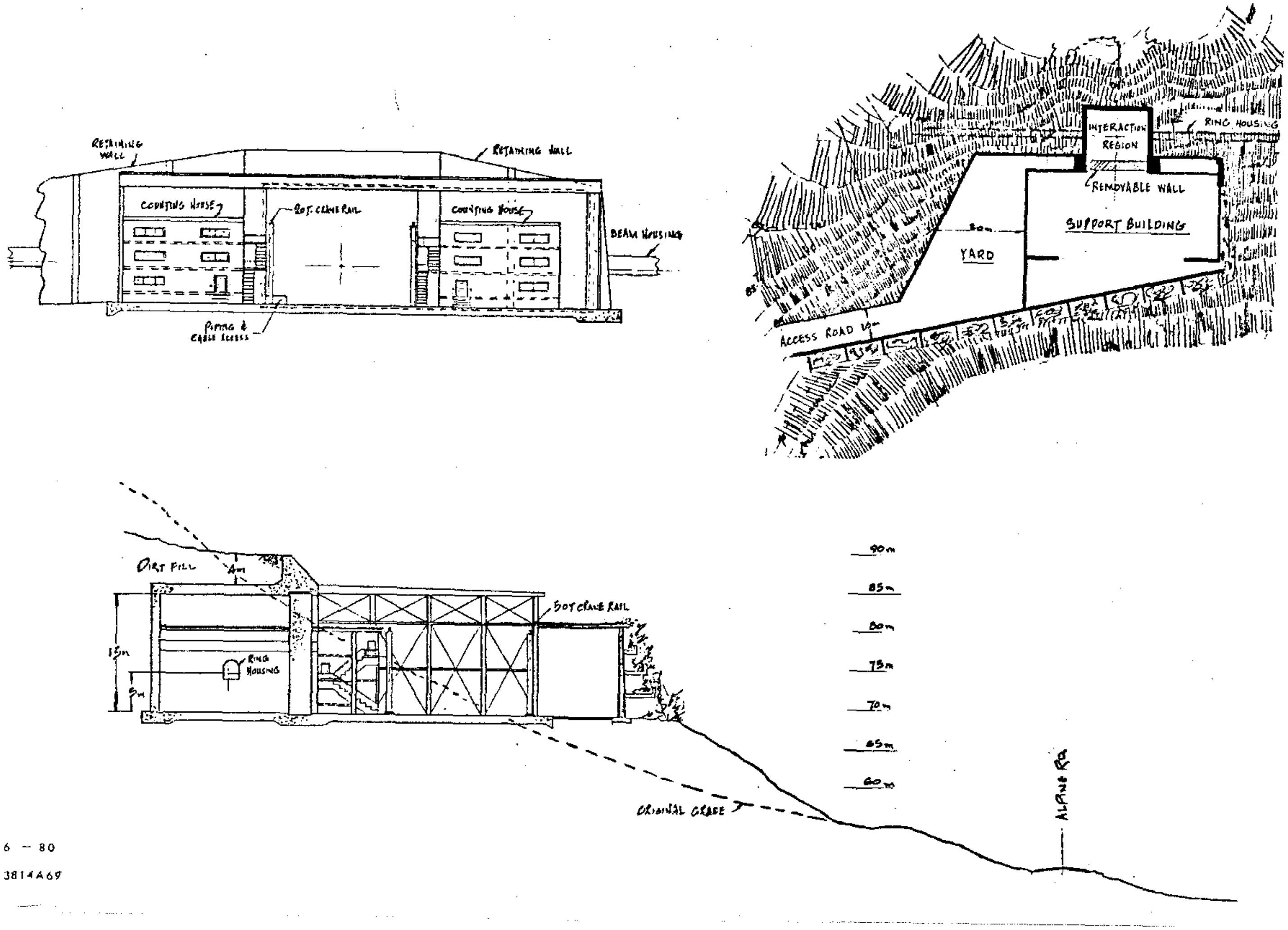

6 - 80
3814A69

Fig. 32. Schematic layout of the experimental hall and assembly building.

(b) While one detector is taking data in the interaction hall, the other detector can be fully tested and kept fully operational in the staging hall. This includes keeping all electronic and cryogenic systems operational. This capability is obtained by having two separate and complete counting houses, and having sufficiently large areas for conventional and cryogenic utilities.

(c) To minimize beam down-time it is intended that a detector can be moved out of the interaction hall in a week, and that the other detector can be moved in and made operational within an additional two to three weeks. This short down-time is obtained by bringing a detector to its fully operational state in the staging hall. It is then transported as a unit into the interaction hall with all electronic cables and most power cables intact. It should only be necessary to disconnect and reconnect major power, cooling, cryogenic, and vacuum lines.

(d) The staging hall is sufficiently large to allow staging of a third small special-purpose detector.

(e) The experimental building is large enough to contain the service and support facilities inside the building.

2. Interaction Hall

(a) Space Layout

Figure 33 shows a detailed layout of the interaction hall. The length along the beam line of 20 m can accommodate the Very Large Detector listed in Table 8 and still allow room for monitoring devices along the beam line outside the detector. The width similarly can accommodate all the detectors discussed above. The beam height of 5 m means that detectors of the type illustrated in Table 8 do <u>not</u> require a pit in the interaction hall, which simplifies their installation and removal. There is also room in the interaction hall for a substantial amount of electronics to be placed close to, or mounted on, the detector. Space will be available along the beam lines to add additional heavy concrete shielding for detectors that are sensitive to slow-neutron backgrounds.

(b) Crane Capability

The interaction hall crane has a 20-25 ton lifting capability which extends 15 m along the beam line. The transverse coverage is ±6 m when

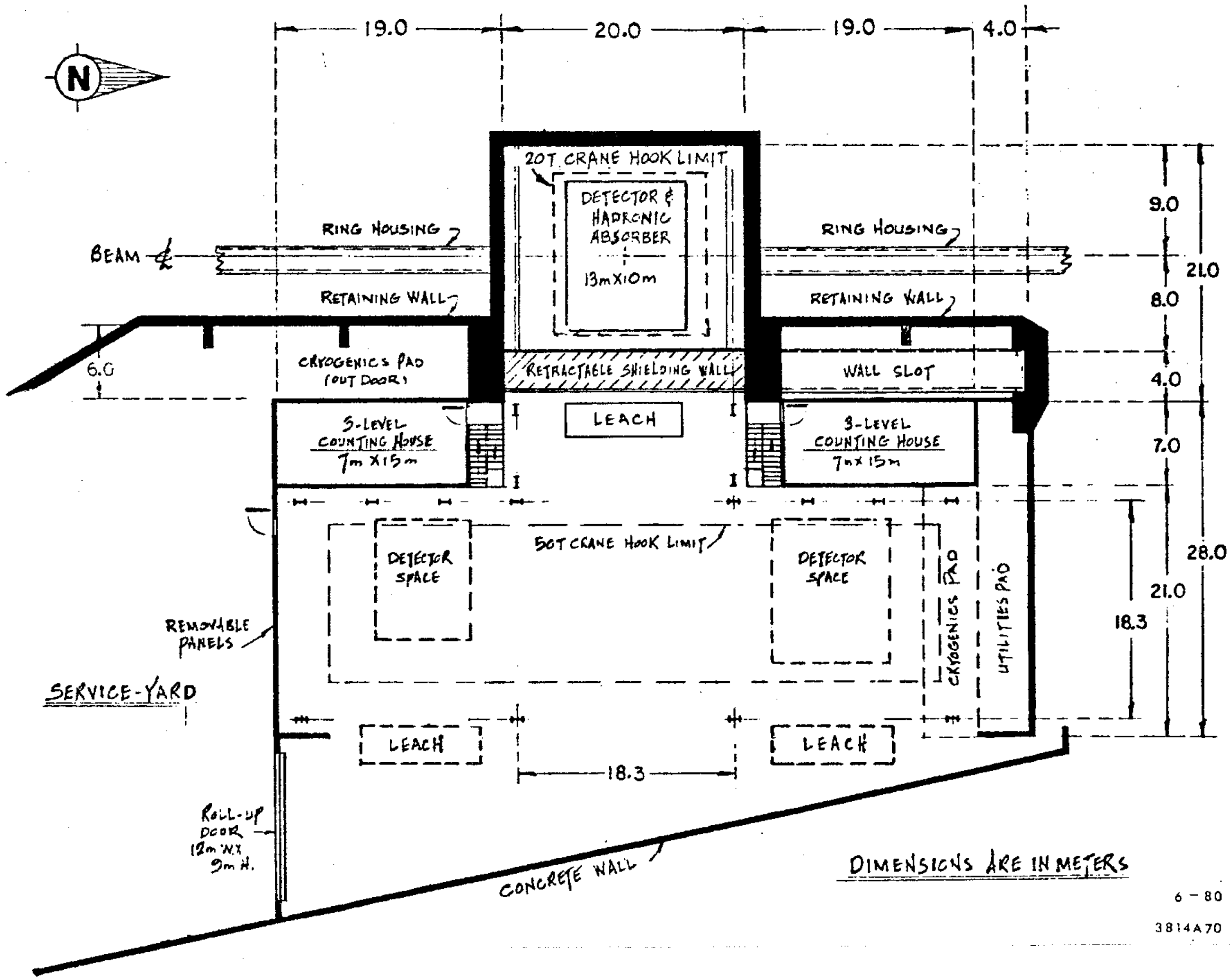

Fig. 33. Plan view of the experimental hall and assembly building.

the shield wall is closed. With the shield wall open, the coverage extends into the staging hall. The purpose of the crane is to allow in-situ repairs of the detectors, which may require, for example, removal of the end-cap doors, removal of a shower detector or calorimeter module, or removal of part of the muon detector. The crane is not intended for complete disassembly of the detectors, which will be accomplished by transporting the whole detector back to the staging hall.

(c) Shield wall

The interaction hall is separated from the staging area by a movable shielding wall, made of concrete 3-4 m thick. The wall can be fully opened or closed in a few hours, and is parked in an enclosure in the retaining wall of the experimental hall (see Fig. 33). This easy access to the interaction hall allows convenient crane support from the staging area for minor repair and maintenance work, and also facilitates rapid installation and removal of the entire detector.

3. Staging Hall

(a) Space layout

Figure 33 shows the staging hall with two detectors being assembled; one is a typical size for a current PEP detector, and the other is the Very Large Detector of Table 8. The staging hall is sufficiently large to allow both detectors to be assembled and operated with their electronic trailers attached.

(b) Crane capability

Most of the staging hall is covered by a 50-ton crane. If the initial assembly of a detector requires greater lifting capacity, this can be done by a portable crane in the apron outside the experimental building, and the detector can then move into the staging hall.

(c) Access

The overhead door at the south wall of the building allows access for loads up to 12 m wide. Hence, detectors of the type illustrated in Table 8 can be moved into the staging hall, as well as around the staging hall, as a unit.

4. Counting Houses

The experimental building contains <u>two</u> complete counting houses (Fig. 33). Each has at least two floors, and perhaps a third floor, with an area per floor of $7 \times 15\ m^2$. The two lower floors of each house are intended for the electronics and control systems. The remoteness of the experimental building from the main SLAC work areas may make a third floor particularly useful.

Each counting house is large enough for the operation of a very large and complex experiment. A counting house will be assigned to an experiment when the assembly of that experiment begins in the staging hall, and throughout the life of the experiment. Thus, all cabling from the counting house to the detector or the electronic trailer is arranged so that the detector can be moved into and out of the interaction hall without disconnecting the cables.

5. Utility and Cryogenic Area

Each experiment has its own utility and cryogenic service area. These areas contain local refrigerators, liquefiers, and storage tanks for cryogenic fluids, chillers for air conditioning, and emergency power generators. The main AC switchgear and power supplies for room-temperature detector magnets will not be installed in these utility areas but will be in the main SLAC experimental areas, the current being brought to the SLC experimental building through water-cooled cables. Similarly, the compressors for the liquid-helium cryogenic system will be remote, the high pressure gaseous helium being piped to the liquefiers in the experimental building.

F. Backgrounds at the SLC

There are significant differences in the backgrounds for the SLC and a conventional storage ring. On the one hand, the SLC has a much smaller average current, by a factor of about 10^5, and a larger signal-to-noise ratio as measured by luminosity per current. The particle density, however, is about 10^4 higher in the SLC.

The lower current means that single-beam effects tend to be much less of a problem at the SLC. Thus, the degraded electrons from beam-gas bremsstrahlung upstream of the interaction region are negligible, and the troublesome masks used at PEP between the quadrupoles and the detector can be left out.

The higher electron densities result in a strongly disrupted beam after the collision, and the transport system for the SLC must have sufficient aperture to transmit the blown-up beams. In addition, the strong fields at the collision point produce a prodigious flux of high-energy photons which must also clear local apertures. The photons from the overlapping bunches interact to produce a detectable background of electron pairs.

The most difficult background is one common to both machines: the synchrotron radiation from the upstream bending magnets. A distributed low-field bending magnet is essential, and a mask against its radiation is also required.

The resulting total background at the SLC should be a few hundred low-energy photons entering the detector per crossing, less than 1000 slow neutrons per crossing, and a slight increase in the coplanar electron-pair background beyond the unavoidable rate from QED effects. These backgrounds should present little difficulty with either the trigger or the clutter in an SLC detector.

The local and remote background sources are described in Appendix E. Rates are estimated, and it is noted where these will have an impact on design parameters.

IV. CONVENTIONAL FACILITIES

A. Site

As with all SLAC projects, the Collider will be situated in a terrain of rolling hills, with low-density residential areas in more-or-less close proximity to the boundaries. The experimental hall will be situated on a steep sidehill a few hundred feet from a well-traveled road and residences; its site preparation will require the excavation of a rather large volume of earth and construction of high retaining walls for both the hall and its adjoining yard.

The project's site work includes provisions for earthquake protection, and for disposition of excavated material from hall and beam housings. It also includes landscaping, roads, fencing, drainage systems, permanent and temporary construction yards and parking areas. There will be an underground duct bank for 12 KV power and a sanitary sewer to serve the experimental hall. (Other utilities will be transported in beam housings).

1. Earthwork

About 75,000 cubic yards of earth will be excavated from the site of the experimental hall. Only 15,000 cubic yards will be replaced as backfill. The balance will be used for construction of shielding fills or shaped into stockpiles contoured to blend into the landscape. Including beam-housing excavations, a total of 78,000 cubic yards will be disposed of in this way. All new earthwork surfaces will receive erosion control treatment.

2. Road

Only one permanent road, providing access to the experimental hall, will be required by this project. It will run from an intersection with the Alpine access road southeast of PEP's Region 4 buildings to the experimental hall and will be designed for heavy loads. The Alpine access road will have to be relocated around or over a new shielding fill.

3. Fences

It will be necessary to include the experimental hall within SLAC's radiation security boundary. Therefore, a standard radiation fence will be constructed to enclose the hall and its access road. Materials from existing fences to be made unnecessary by this new enclosure will be used as much as possible.

4. Yards and Parking

A yard will be provided at the experimental hall. It will have to remain clear at most times as it will be used primarily as a turnaround for vehicles. Because of the steep hillside site it will not be possible to provide parking at the building. Either a shuttle-bus system or a parking area on the broad ridge south of the hall, with a connecting foot path to the hall, is planned. A contractor's construction yard will be provided, probably near the intersection of SLAC's access road with San Mateo County's Alpine Road. Small yards may prove to be necessary at drainage shafts.

5. Landscaping

The hall site, road and new land surfaces resulting from the construction will be suitably landscaped. Oaktree plantings to match the natural landscape will predominate.

6. Utilities

A concrete-encased duct bank for permanent 12.47 KV power and temporary 480 V construction power will be provided, running cross-country from sources in the research yard to the hall. Construction power on temporary poles will be provided to drainage shafts, working tunnel portals and the construction yard. This overhead system will be removed as soon as permanent power distributed underground is functioning. Magnet power and research power to the hall will be transported in the beam housings, as will cooling water.

7. Sanitary Sewer

A sanitary sewer to serve the experimental hall will require an annexation to the Menlo Park Sanitary District. The sewer will run down a steep hillside to the existing sewer along Alpine Road.

B. Tunnels (Beam Housings)

From the point where the Collider's two beam runs depart from SLAC's central beam, the two limbs comprise runs of about 1348 m (north) and 1379 m (south) to the interaction point at the eastern side of the SLAC site (see Fig. 34). Each limb must follow a path through the Beam

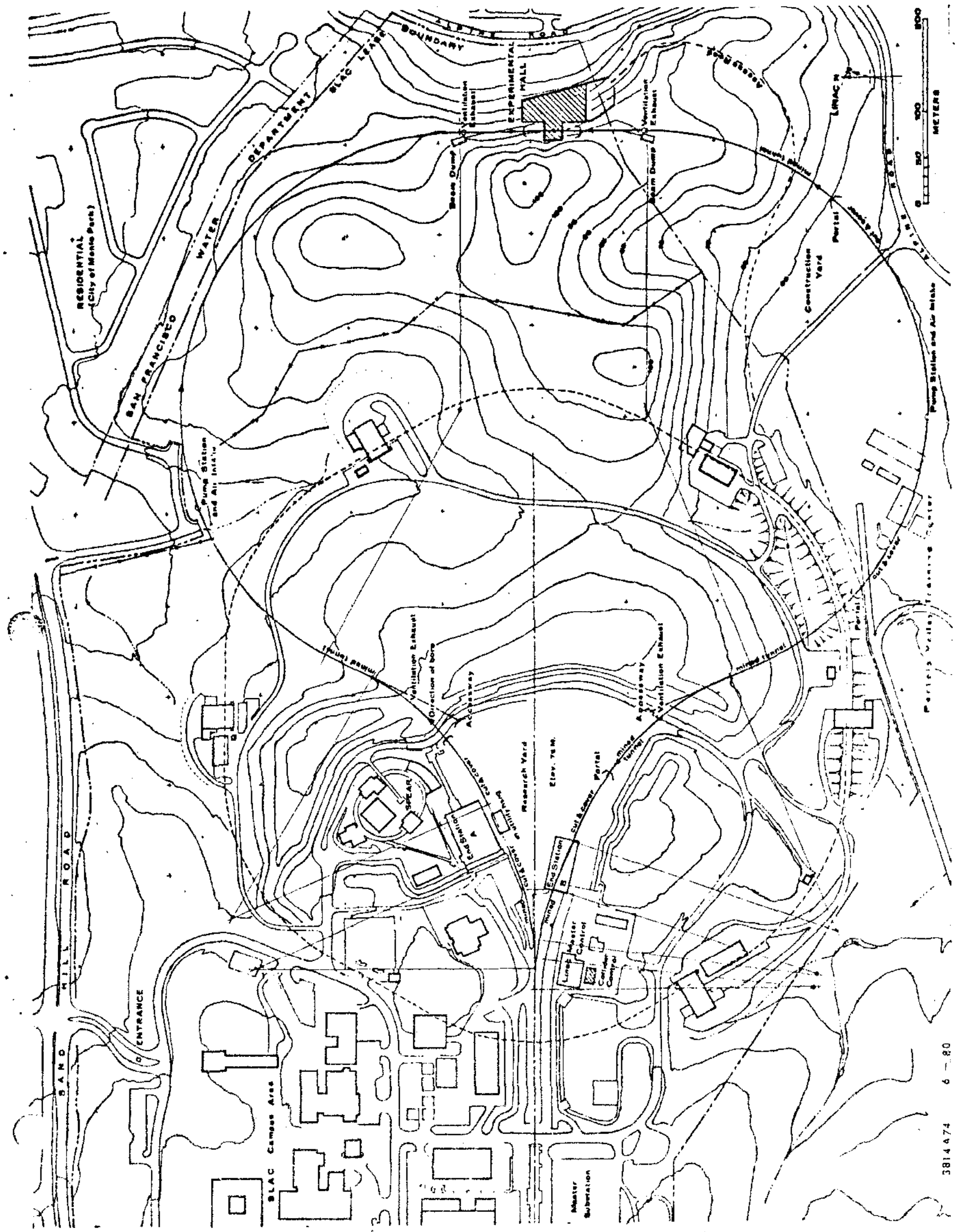

Fig. 34. Contour map of the SLC site.

Switchyard involving both cut-and-cover and mined tunnel construction methods. They must then traverse the research yard, by cut-and-cover methods, and enter mined tunnels. The north run will be entirely through mined tunnels to the interaction area. The south run will traverse the low-elevation area at its southern extremity by cut-and-cover methods. Alluvial deposits and poor ground water conditions make mined tunneling inadvisable, if not infeasible, in this area.

The size and orientation of the ring layout are guided by the following considerations:

1. Minimum radii of arcs consistent with good beam quality.
2. Site-boundary limitations.
3. Need for a difference of at least 20 m in the lengths of the beam paths to the interaction point.
4. Terrain, particularly in regard to the experimental hall site.
5. Distance on each side of the interaction point necessary for final focusing.

Lengths of beam-runs and types of construction are shown on the profiles of the runs (Fig. 35). The various types of housings are summarized as follows:

In existing structures	182 m
Associated with the hall	40 m
In hall beam alcove	20 m
Cut-and-cover construction	809 m
Mined tunnel construction	1676 m
Total	2727 m

It is intended that the beam housings be subcontracted separately from the hall. Tunnel constructors prefer to contract in this fashion rather than as part of a general construction contract. A precise design or cross-section would not be specified in the mined-tunnel parts, although reasonable dryness, durability, strength and construction sequencing will be required. A minimal cross-sectional space need will be delineated into which the tunnel structure cannot intrude. In this way each bidder will be able to offer a shape and size which he believes he can provide at lowest cost. This method will allow use of various

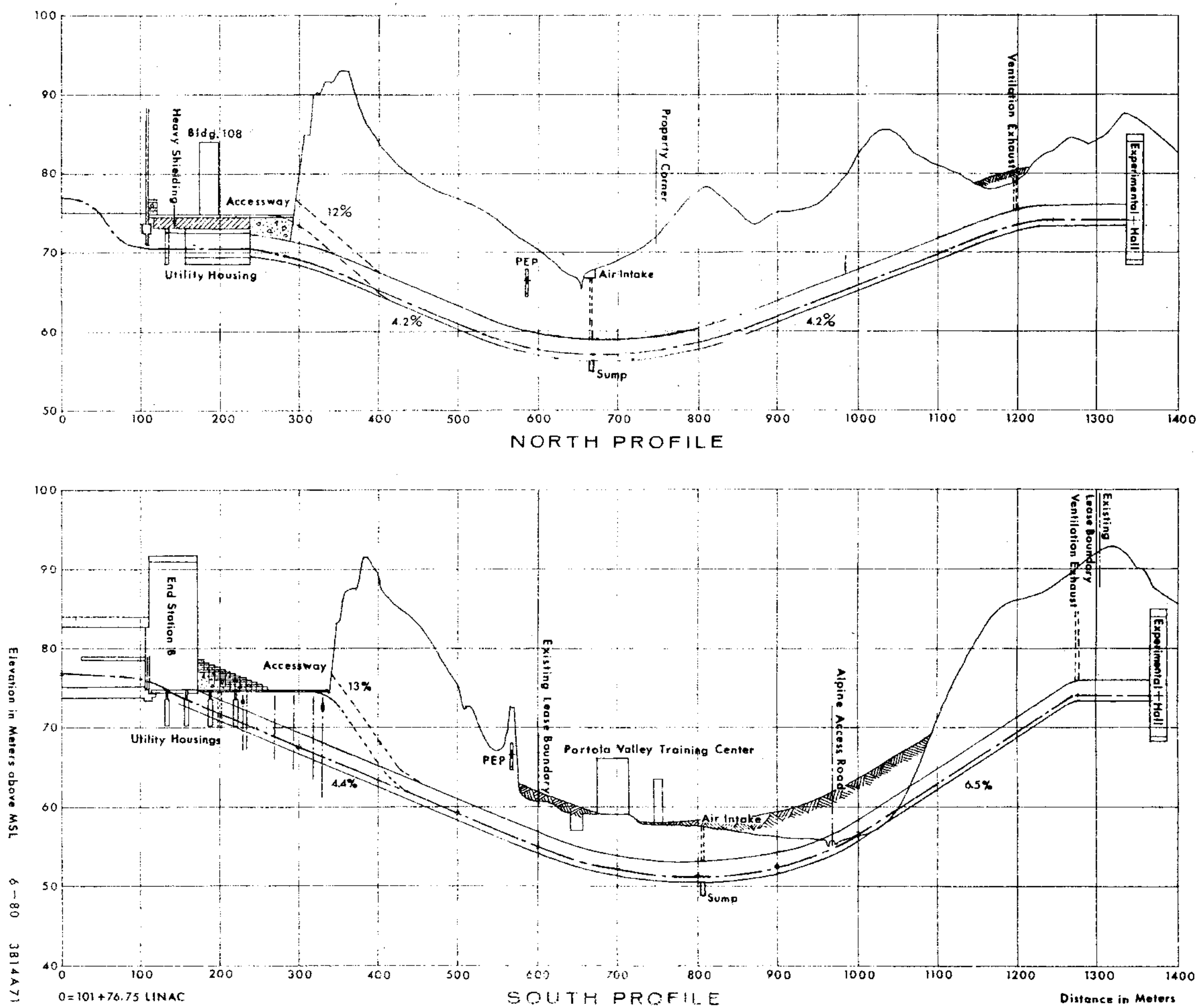

Fig. 35. Profile views of the SLC site.

construction methods, types of equipment, and tunnel-lining methods. It will also permit flexibility to meet various underground conditions as they are encountered.

Certain portions of the work, particularly those in the Beam Switchyard and Research Yard, will have to be scheduled to fit SLAC's operations programs. The paths through the BSY have been chosen to cause the least disruption of existing beam runs and to provide the best Collider beam alignments.

As a design policy it has been decided to mount most of the services associated with the beam components directly on the support elements of the prefabricated magnet-lattice assemblies, with connection features between assemblies. This will limit the amount of services to be supported by the structure of the tunnel itself to cooling-water piping, telephone conduit, etc. At intervals throughout the beam housings, alcoves will be constructed to contain power and I&C panels, so that field connections between tunnel-supported services and beam components will be held to a minimum. This should result in simplified tunnel construction and rapid component-installation work.

Access to the beam housings will be made via two tunnels with portals in the research yard, descending at grades of 12%-13% to meet the housings, as shown in Fig. 35. Their positions dictate that the aisles shall be at the inner sides of the housings.

Drainage water from the low points will be pumped up shafts. There will be two such facilities, at the north and south sides of the ring.

As there are considerable elevation differences in the housings, convection forces should ordinarily suffice to provide ventilation, with exhaust shafts at high points and intakes at the low. However, exhaust fans will be provided at high points to reduce heat problems. Ventilation control for fighting fires may be necessary.

Housings for underground beam dumps will be constructed as parts of the tunnel work at points 100 to 120 m north and south of the experimental hall. Diverging Y's will be built into the tunnels, continuing until the separations between the legs of the Y's are about six meters. Space necessary for the mechanical equipment will be provided. Pumps and controls will be located in separate housings accessible to operating personnel.

C. Control Room

The Collider will operate as an extension of the existing SLAC linac, and its functional integrity is vitally dependent on the operating characteristics of the entire length of the accelerator. Its control facilities must therefore be very closely linked with SLAC's Main Control Center. The control room building will be constructed adjacent to MCC. The addition will be similar to the MCC building, with a floor area of 2,500 sq. ft. The entire area will be devoted to control equipment and operating personnel space. Communications links with the Collider's experimental hall will be made via the Collider's beam housings.

D. Damping Ring Vault

The damping rings (described in Section II.F) will be assembled in a reinforced concrete underground vault near the end of the linac's Sector 1. A site immediately south of the roadway paralleling the south side of the Klystron Gallery has been chosen to provide the simplest beam runs between the linac and the damping rings. The southern location may cause some obstruction of the aisle in the accelerator housing by beam-transport apparatus. However, it was selected rather than a northern site owing to high ground-water levels north of the accelerator.

The vault must house the rings and the necessary RF equipment for the facility. A floor area of 12 by 16 m has been chosen, with an equipment access shaft to be located adjacent to it of a size adequate to accommodate the components to be installed in the vault. At present two tunnels are planned to connect the accelerator housing and the vault.

The vault itself will be shielded by earth overlying it. The shaft will be shielded by concrete blocks. Since the beam-run tunnels will intersect an existing accelerator housing man-access shaft, the latter can be used for quick access when the linac is not operating. If ready access during linac operation is required, it can be provided by a mazed man-entry into the access shaft when the damping rings are not operating. Forced ventilation can be provided via the accelerator housing. Power and mechanical services are available from the Klystron Gallery. Concrete pylons (or a section of wall) will be located inside the ring position, to serve as roof support and to provide features on which two jib cranes may be mounted to facilitate component handling in the vault.

E. Experimental Support Building

The criteria used in sizing the experimental and staging areas at the SLC interaction region were discussed in Section III.E of this report. In this section we describe the resulting structures from the point of view of their conventional engineering design. Figure 36 is a plan view of the experimental support facilities, and Figure 37 shows these facilities in several cross-sectional views.

An initial cut will be made and concrete retaining walls constructed to provide an interaction region with the following approximate dimensions: width 20 meters, length 21 meters, and height 15 meters. The roof will be of concrete construction designed to withstand a 4-meter-thick earth back-fill over its surface. Back-fill and compaction behind the retaining walls will then provide radiation protection on all but one surface. The one exception will be the side between the interaction region and the assembly building. This is a 3-4 meter thick concrete wall, retractable for easy access to the detectors.

At right angles to the interaction region is the material handling and general assembly area. This building is a conventional metal buildgin having the following general dimensions: length 63 meters, width 28 meters, and height 25 meters.

The floors of both areas will be 1/2-meter-thick reinforced concrete to handle the large detector loads of 2,000 tons or more. Material handling is accomplished with a 20-25 ton crane over the interaction region, and a 50-ton crane over the assembly area.

The assembly building contains two counting houses and provides utility pads for power supplies and cryogenic equipment. A complete detector can be built in the assembly building, checked out, and interchanged with the on-line detector. This interchange involves purely orthogonal moves and can be accomplished on rollers (this has been demonstrated at PEP), making for great flexibility of experimental equipment layout. A further feature of the building is a removable section of the South Wall, which will permit moving a complete detector into and out of the assembly building.

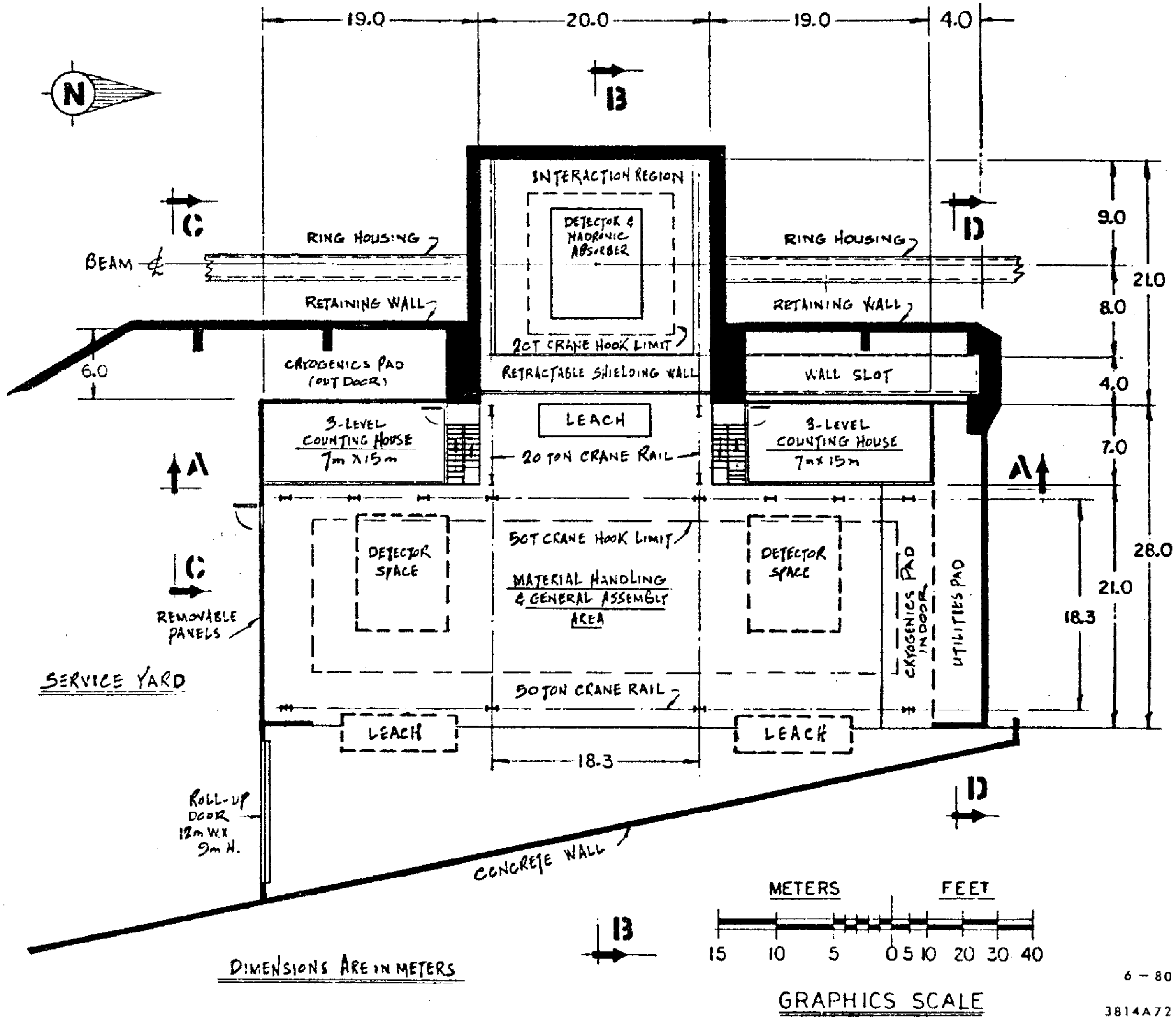

Fig. 36. General layout of the experimental hall and assembly building.

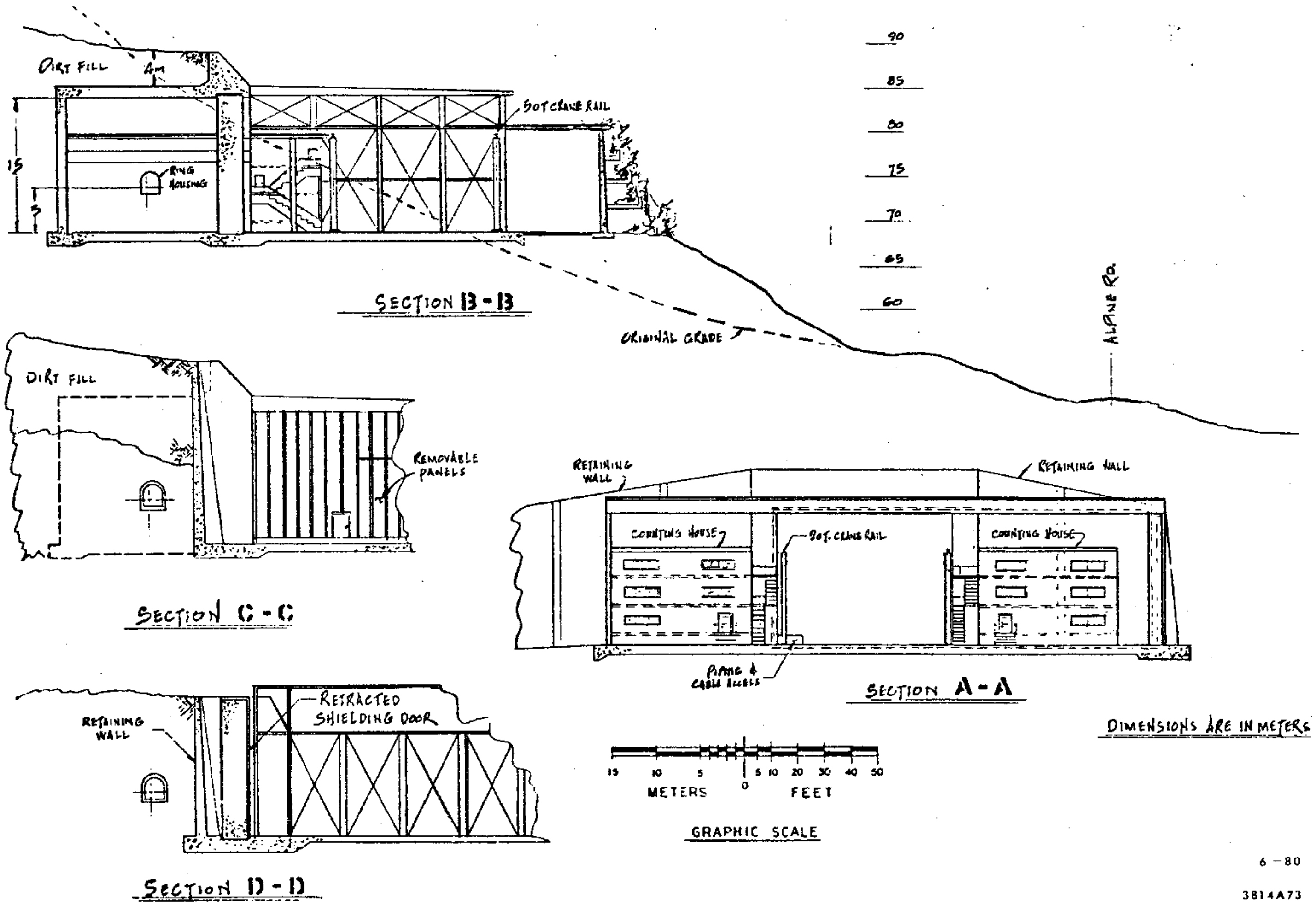

Fig. 37. Cross-sectional views of the experimental hall and assembly building.

The triangular area to the East of the assembly building serves three important functions. First, it provides an entry point which permits placement of loads underneath either crane. This avoids the costly requirement of two-level cranes, which, to maintain the hook height at 11 meters (found to be desirable at PEP) would necessitate increasing the height of one of the buildings. Second, the assembly building presents a barn-like structure to the neighborhood, which is deemed unacceptable. Consequently, the East wall is of concrete, architecturally designed and landscaped to blend into the surroundings and to obscure the building from surrounding communities. Third, the areas will be covered and a roll-up door installed in the South wall to provide general access to the main building and additional valuable machine shop and storage space. This is an important factor because of the remote location of the building from the rest of SLAC.

V. COST ESTIMATES AND SCHEDULE

The estimated cost of the SLAC Linear Collider project, stated in 1980 dollars, is $63.4 million, of which $37 million is for technical components and $26.4 million is for conventional facilities. An additional allowance of $26.4 million is made for labor and cost escalation (1% per month based on the cost schedule shown below) over the three-year construction period. The total estimated cost is thus $89.8 million.

Contingencies have been applied at 15% of conventional construction and 20% of technical components. These rates are believed to be appropriate in view of recent experience in the construction of PEP.

The construction schedule for the SLC project is shown in Fig. 37. This schedule is based on the following increments of new obligational authority ($ million):

FY80	FY81	FY82	FY83	FY84	TOTAL
0.3	1.5	35	38	15	89.8

This schedule would permit beam tests at the beginning of FY85.

The tables following Fig. 38 (Schedules 1-5) give the estimated costs for the SLC project in some detail.

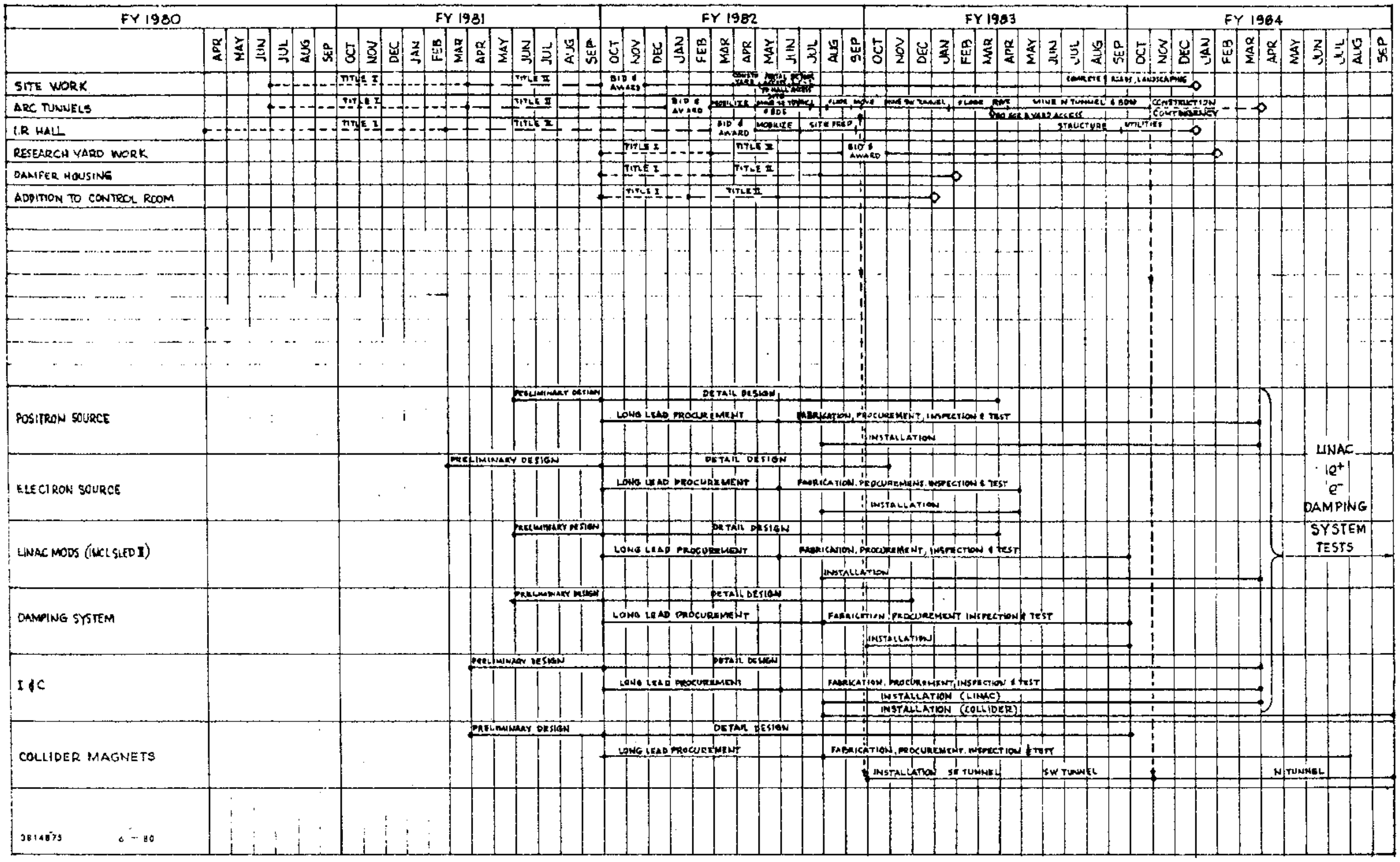

Fig. 38. SLC construction schedule.

Schedule 1: ED & I

		($ Thousands)	
		Item Cost	Total Cost
1-A:	Conventional @ 15% of const	$2,900	
1-B:	Technical components @ 25% of hardware	6,200	
1-C:	PE&D, FY1980	300	
			$9,400

Schedule 2: TECHNICAL COMPONENTS

		Item Cost	Total Cost
2-A:	Positron source		
	Extraction	$ 230	
	Target	210	
	Collection	480	
	Pre-booster	340	
	Turn around	460	
	Transport back	600	
	Booster focusing	60	
	AC power	120	
			$2,500
2-B:	Electron source		
	Buncher and injector	$ 110	
	RF system	90	
	Gun power supply and SF_6 system	30	
	Laser and components	180	
	Vacuum system and components	70	
	Gun structure	30	
	Magnet and power supply	90	
			$ 600
2-C:	Accelerator modifications		
	Steering and focus	$1,540	
	Modulators-klystron mods	90	
	Injection	70	
			$1,700

		($ Thousands)	
		Item Cost	Total Cost
2-D:	SLED-II		
	Modulators	$2,140	
	Klystrons	160	
			$2,300
2-E:	Collider Arcs		
	Collider ring magnets	$4,020	
	Power supplies	370	
	LCW system	730	
	Collider arc vacuum	360	
	Position monitors	100	
	Beam instruments	150	
	Linac to collider magnets	70	
			$5,800
2-F:	Final Focus		
	Magnets, power supplies, steering, utilities	$1,290	
	Vacuum system; position monitors	360	
	Beam extraction; beam dumps and associated utilities	750	
			$2,400
2-G:	Damping rings		
	Mags for rings, injection, steering, and pwr supplies	$1,310	
	RF cavities, klystron, power supplies, electronics		
	Vac sys; position & light monit; toroid	480	
	Transport to damp ring mags and pwr sup	140	
	Vacuum system transport to rings and pos mon	60	
	Compressor magnets, power supplies, steering	480	
	Compressor RF, waveguide	70	
	Compressor vacuum system	80	
			$2,900

		Item Cost	Total Cost
		($ Thousands)	
2-H:	Instrumentation and control		
	Basic instrumentation	$4,200	
	Positron source and return line	100	
	Electron source	30	
	Damping rings	150	
	Linac	1,140	
	Switch yard	140	
	Main ring	800	
	Final transport	140	
			$6,700
	GRAND TOTAL TECHNICAL COMPONENTS		$24,900

Schedule 3: CONVENTIONAL FACILITIES

		Item Cost	Total Cost
3-A:	Site		
	Road work	$ 105	
	Hardstand yards and parking	50	
	Drainage facilities (lump sum)	60	
	Fencing (840 m @ $30)	25	
	Misc. earthwork (handling) (78000 m^3 @ $2)	155	
	Landscaping (lump sum)	30	
	Temporary power for construction	30	
	Sanitary sewer connection	15	
	Relocate existing facilities; clear obstructions in research yard	330	
			$ 800
3-B:	Utilities		
	Electric		
	Duct bank-12.47 Kv (600 m @ $160)	$ 96	
	Hall substation	104	
			$ 200

	($ Thousands)	
	Item Cost	Total Cost
3-C: Structures		
(i) Beam housings in open areas		
Mined tunnel (158 m @ $4700)	$7,426	
Cut & cover (500 m @ $3000)	1,500	
Adjacent to hall (60 m @ $3300)	198	
Shafts, vents, portals (lump sum)	776	
		$9,900
(ii) Linac-collider connection		
In existing structures (145 m @ $0)	--	
Cut & cover (350 m @ $3000)	$1,050	
Mined tunnel (93 m @ $4900)	450	
		$1,500
(iii) Beam dump (including shielding) (2 @ $250)		$ 500
(iv) Experimental hall		
(a) Site development		
Clear and grub (lump sum)	$ 20	
Excavation (74000 m^3 @ $8.40)	620	
Misc (security, fencing, etc.)	40	
	$ 680	
(b) Building		
Beam alcove (462 m^2 @ $2040)	$ 943	
Shielding chamber (104 m^2 @ $3060)	318	
Assembly areas (1323 m^2 @ $540)	714	
Access and storage (561 m^2 @ $1210)	679	
Counting areas (630 m^2 @ $603)	380	
	$3,034	
(c) Shielding wall		
Concrete (1013 m^3 @ $400)	$ 405	
Hardware	50	
	$ 455	
(d) Utilities		
Electrical (3080 m^2 @ $80)	$ 246	
Mechanical (3080 m^2 @ $65)	200	
Utilities pad L.S.	70	
	$ 516	

	($ Thousands)	
	Item Cost	Total Cost
3-C: Structures (cont'd.)		
(iv) Experimental hall (cont'd.)		
(e) Cryogenics space (108 m^2 @ $2130)	$ 230	
(f) Retaining walls	$ 585	
Total Exp hall		$5,500
(v) Control room addition (2500 ft^2 @ $80)	$ 200	$ 200
(vi) Damping ring vault		
Excavation (4900 m^3 @ $20)	$ 98	
Connecting tunnels (118 l.f. @ $2000)	236	
Concrete (653 m^3 @ $320)	209	
Jib cranes & support structure	26	
Mech/Elec	31	
		$ 600
GRAND TOTAL CONVENTIONAL FACILITIES		$19,200

Schedule 4: OTHER

4-A: Standard equipment		
Bridge cranes (2)	$ 400	$ 400
4-B: Contingency		
(i) 20% of technical components	$6,200	
(ii) 15% of conventional construction	3,300	
		$9,500

Schedule 5: RECAPITULATION

ED&I	$9,400	
Technical components	24,900	
Conventional facilities	19,200	
Other	9,900	
	GRAND TOTAL (FY1980 dollars)	$63,400

APPENDIX A

SPACE CHARGE EFFECTS IN THE LINEAR ACCELERATOR

1. Introduction

Space-charge forces cause the effective emittance and energy spread of particle bunches which pass through the linear accelerator to grow. This growth must be limited because the bunches must be focused to a two-micron-radius spot at the collision point. The properties of the ion-optics which focus the bunches have been chosen on the assumption that the energy spread of the particle bunches leaving the linear accelerator is ±0.5% and that the effective emittance of the bunches is 3×10^{-10} radian-meters.

It is a simple matter to produce a low-intensity beam exceeding this specification. As the current is increased, however, the emittance and energy spread of the beam will grow. The maximum current which can be accelerated subject to the conditions on maximum usable emittance and energy spread is determined by the space-charge-control measures which are adopted.

The space-charge effects which are important here are the head-to-tail type which are common in particle accelerators. The leading particles at the head of the bunch leave behind fields in the linac RF structure which act on particles which follow in the tail of the bunch. Once the distribution of fields which a single particle leaves behind is known, it is a straightforward matter to compute the space-charge disruption of the ensemble of particles which constitute a bunch.

Two types of wake field trail behind a particle passing through the linac RF structure. There is a longitudinal wake which decelerates and a transverse wake which deflects particles that follow. The longitudinal wake field depends only on the distance between the particle generating the wake field and the particle upon which the wake field acts. The transverse wake field is more complicated. Like the longitudinal wake this wake depends on the distance between the particle which generates it and the particle on which it acts. It is also proportional to the distance between the path of the generating particle and the geometrical center line of the linac RF cavities, but is independent of the transverse position of the particle on which it acts. There are other higher order wake fields which depend on higher powers of the distance between the path of the generating and following particle and the axis of the RF cavities. These fields are unimportant in the present application.

The transverse wake field that causes growth in the effective transverse emittance of the bunches and the longitudinal wake field that causes growth in energy spread differ in their dependence on the distance between the leading particle that generates the wake and the following particle that is acted on by the fields. For the range of bunch lengths appropriate to the Collider, the transverse wake increases with increasing separation between the particles, while the longitudinal wake decreases. For this reason, the energy spread increases when the bunch is made shorter, while the transverse emittance growth decreases. The bunch length, which is a controllable parameter, must be chosen to best balance these two space-charge effects. For the present Collider parameters, a Gaussian bunch with a rms length of 1.0 millimeter is consistent with the acceleration of 5×10^{10} particles/bunch with the required limits on energy spread and transverse emittance.

The effects of the longitudinal wake field are partially controlled by placing the bunch ahead of the crest of the RF wave in the linac and thus compensating the energy loss due to the wake. This procedure will be discussed in Part 3.

The effects of the transverse wake field are controlled by making a precise trajectory correction for the beams so that they pass very close to the center of the RF structure. This procedure minimizes the wake field. The effect of the residual wake field is minimized by the choice of a very tightly focused linac quadrupole lattice. There is one more condition which can only be satisfied by a tuning procedure. It is necessary to inject the beam into the linac with a very small component of free betatron motion. This will be accomplished by empirical tuning of injection conditions using emittance detectors at the end of the linac as monitors. This procedure has been tried successfully with short trains of bunches during accelerator physics experiments. The theory of transverse emittance growth will be discussed in Part 4.

In the following sections of this Appendix the calculation of the wake fields in the linac RF structure, the effects of these fields, and the control measures which we propose to adopt will be described.

SUMMARY

To meet the Collider specification on energy spread, we shall require that the bunch be placed 3.5 mm ahead of the crest of the RF wave in the accelerator. The unloaded energy of the accelerator must be 52.7 GeV if the average energy of the bunches is to be 50 GeV. To meet the Collider specification on emittance, we shall require that the trajectory of the bunches in the accelerator be kept within 0.1 mm rms of the axis of the RF structure. The injection conditions into the accelerator must be tuned empirically.

2. Calculation of Longitudinal and Transverse Wake Fields

We consider an axisymmetric periodic structure having a geometry as shown in Fig. A-1. It can be shown[1] that for this structure a synchronous mode (traveling-wave mode with phase velocity equal to c) has an axial electric field that varies with radial position and azimuthal angle ϕ as

$$E_z = E_o \left(\frac{r}{a}\right)^m \cos m\phi \quad , \tag{1}$$

where a is the beam-hole radius, and m is an integer. In terms of the "cold" (no charges present) electromagnetic properties of the structure, we can define a loss parameter k_n for each mode by

$$k_n = \frac{(E_{on} d)^2}{4W_n} \quad , \tag{2}$$

where d is the periodic length, and W_n is the energy stored per period. For a point charge q traveling parallel to the axis of the structure at $r = r_e$ and $\phi = 0$, the beam-induced energy deposited in the nth mode per period is[2]

$$W_n = k_n \, q^2 \left(\frac{r_e}{a}\right)^{2m} \quad .$$

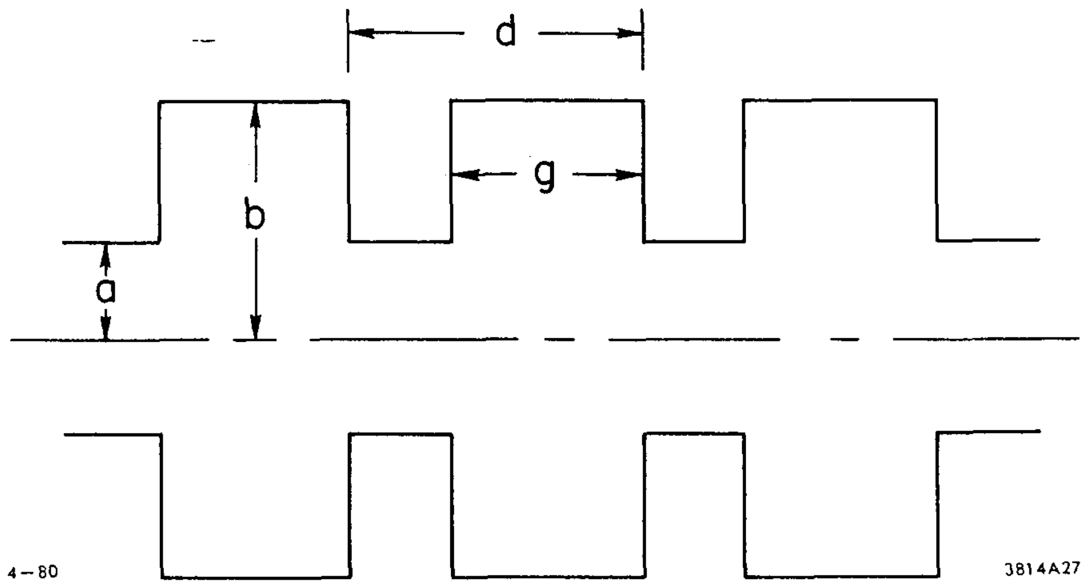

Fig. A-1. Structure geometry analyzed by the program TRANS.

Eliminating W_n using the preceding two expressions, we have

$$E_{on} d = -2 \left(\frac{r_e}{a}\right)^m k_n q \quad . \tag{3}$$

The minus sign indicates that the phase of the induced field is such as to oppose the motion of the charge. As a function of distance $\Delta z = c\tau$ behind the exciting charge, the field varies as $E_z \sim \cos \omega_n \tau$. Using this, together with Eq. (3) in Eq. (1), we obtain

$$E_{zn} (r,\phi,\tau)d = -2 k_n q \left(\frac{r}{a}\right)^m \left(\frac{r_e}{a}\right)^m \cos m\phi \cos \omega_n \tau \quad . \tag{4}$$

For longitudinal modes ($m = 0$), we define the wake potential for the nth mode as the voltage per period per unit exciting charge,

$$w(\tau) \equiv E_{zn} d/q = -2 k_n \cos \omega_n \tau \quad .$$

By superposition, the total wake potential for N modes is

$$w(\tau) = -2 \sum_{n=1}^{N} k_n \cos \omega_n \tau \quad . \tag{5}$$

For defecting modes ($m > 0$), we define the wake potential seen by a relativistic ($v = c$) particle with charge e, following at a distance $c\tau$ behind a unit point charge, by

$$w(\tau) = (c/e) \vec{\Delta} p_\perp = (\vec{E}_\perp + c\vec{B}_\perp)^{(f)} d \quad ,$$

where $\Delta p_\perp$ is the transverse momentum kick per period. The superscript (f) indicates that the electric and magnetic fields are evaluated in a frame moving with the particle. It can be shown[3] that, for a synchronous particle, the momentum kick can be expressed in terms of the E_z field component alone:

$$(\vec{E}_\perp + c\vec{B}_\perp)^{(f)} = j \, (c/\omega) \vec{\Delta}_\perp E_z^{(f)} \quad .$$

Assuming $E_z = -|E_z| \, e^{j\omega\tau}$, the preceding two relations give

$$\vec{W} (\tau) = d(c/\omega) \sin \omega\tau \left(\hat{r} \frac{\partial |E_z|}{\partial r} + \hat{\phi} \frac{1}{r} \frac{\partial |E_z|}{\partial \phi}\right) \quad ,$$

where $\hat{r}$ and $\hat{\phi}$ are unit vectors. From Eq. (4) we now obtain

$$\hat{r}: \quad W_n(r,\phi,\tau) = 2m \left(\frac{k_n}{\omega_n a/c}\right) \left(\frac{r}{a}\right)^{m-1} \left(\frac{r_e}{a}\right)^m \cos m\phi \sin \omega_n \tau$$

$$\hat{\phi}: \quad W_n(r,\phi,\tau) = -2m \left(\frac{k_n}{\omega_n a/c}\right) \left(\frac{r}{a}\right)^{m-1} \left(\frac{r_e}{a}\right)^m \sin m\phi \sin \omega_n \tau \qquad (6)$$

for the components of the wake in the $\hat{r}$ and $\hat{\phi}$ directions. The $\hat{r}$ component of the wake at $\phi = 0$ for dipole ($m = 1$) modes is of most interest:

$$w_n(\tau) = 2\left(\frac{k_n}{\omega_n a/c}\right) \left(\frac{r_e}{a}\right) \sin \omega_n \tau \quad . \qquad (7)$$

Analogous to Eq. (5), the total wake for N modes is the sum of the individual wakes.

Two computer programs are available for finding the values of ω_n and k_n required in Eqs. (5) and (6). The program KN7C[4] can be used for longitudinal modes ($m = 0$). More recently, a program TRANS has been developed[1] which can find the modes in the structure shown in Fig. A-1 for any value of m. The real SLAC structure is a constant-gradient structure. The beam-hole size varies from 1.31 cm to 0.96 cm along the length of the structure. For the computer runs, the dimensions of an average cavity (cavity No. 45 in the middle of the structure) were used:

$$a = 1.163 \text{ cm}$$
$$b = 4.134 \text{ cm}$$
$$g = 2.915 \text{ cm}$$
$$h = 3.499 \text{ cm} \quad .$$

Because of the varying beam-hole size, the wake for the actual structure is estimated to be about 5% larger than the wake computed using the average cell. There will also be a small error due to the fact that in the real structure the disks are rounded, as opposed to right-angled as assumed in Fig. A-1.

Both programs have been checked for agreement with the analytic modes for a pillbox cavity in the limit of vanishing beam aperture. In addition, TRANS gives agreement with the measured frequency and k for the lowest frequency deflection mode in the SLAC structure. TRANS also gives the same result (Brillouin diagram, stored energy per period) for an RF-separator structure analyzed previously by Hereward and Bell.[5]

If an accurate knowledge of the wake is required down to times on the order of τ_o, then modes to frequencies on the order of $\omega_o \simeq 1/\tau_o$ must be known. The bunch length for the Collider will be on the order $\sigma_z \simeq 1$ mm, or $\sigma_t \simeq 3$ ps. The wake should be accurate to at least $\tau_o \simeq 0.1\,\sigma_t \simeq 0.3$ ps. Thus modes with angular frequencies up to about 3×10^{12} ought to be computed. Because the density of modes increases in proportion to frequency, there is a practical limit on the frequency that can be reached with reasonable computation time. As an example, 450 modes have been computed for the SLAC structure for m = 1, up to a maximum frequency $\omega_o = 4.8 \times 10^{11}$. Since this is considerably lower than the desired frequency of about 3×10^{12}, there appears to be a problem. Fortunately, the situation is saved by the fact that at higher frequencies the statistical properties of the modes follow simple scaling laws. For example, by summing the k_n's within bins of equal width in frequency and making a log-log plot of the result as a function of frequency, it is found that

$$\Delta k = \frac{A_m}{\omega^{3/2}}\, \Delta\omega \quad . \tag{8}$$

This result is, in fact, predicted analytically by the optical resonator model[6] of a disk-loaded structure. Using this frequency variation for $dk/d\omega$, analytic expressions can be found for the wake due to frequencies greater than ω_o. For the case m = 0, we obtain

$$w_o(t) = \frac{4A_o}{\omega_o^{1/2}} \left\{ \cos x - \sqrt{\pi x/2}\; [1 - 2S\;(\sqrt{2x/\pi})] \right\} \tag{9}$$

where $x = \omega_o \tau$ and S is the Fresnel integral. A similar expression is obtained for m = 1:

$$\frac{w_1(\tau)}{(r_e/a)} = \frac{4A_1 c}{a\omega_o^{3/2}} \left\{ \frac{x}{3}\, [2\cos x + \frac{\sin x}{x} - \sqrt{2\pi x}\left(1 - 2S\;(\sqrt{2x/\pi})\right)] \right\} \quad . \tag{10}$$

The constants A_0 and A_1 are found by fitting a line with slope -3/2 on a log-log plot to the binned mode results versus frequency. The total wake is then obtained by adding the analytic extension, as given by Eqs. (9) and (10), to the computation of discrete modes up to ω_o. It is found that the total wake using 50 modes plus analytic extensions agrees well with the total wake using 450 modes plus analytic extension. The relative contribution of the analytic extension is, of course, much larger in the 50-mode case.

Figure A-2 shows how, for the m = 0 case, the wake from the analytic extension adds to the wake from discrete modes to give the total wake for the SLAC structure. Note that the slope of the analytic extension, and hence the slope of the total wake, becomes infinite as $\tau \to 0$. The intercept, however, is finite and from Eq. (5) is equal to twice the average loss per particle per period per picocoulomb of total charge. The validity of this wake for the SLAC linac has been checked experimentally in single-bunch beam-loading experiments.[7] The model predicts, first of all, the average energy loss per particle:

$$\Delta U = eq \left[\sum_{n=1}^{N} k_n \, e^{-\omega_n^2 \sigma_t^2} + \int_{\omega_o}^{\infty} \frac{A_a e^{-\omega^2 \sigma_t^2}}{\omega^{3/2}} \, d\omega \right] \tag{11}$$

where σ_t is the bunch length. For 10^9 electrons, the measured[7] average energy loss per electron for the total length of the SLAC structure (≈81500 cells) was 50 MeV. The loss computed from Eq. (1) is 40 MeV, about 20% lower. A more detailed test of the wake function is obtained by examining the shapes of the single-bunch energy spectra. In Ref. 7 the measured and computed spectra are plotted for three phase angles of the bunch center with respect to the crest of the accelerating wave, and for four values of bunch charge. Very good agreement is obtained between the calculated and measured shapes. Again, the computed values give lower total energy widths for the spectra as compared to the measured widths. The computed widths are lower by about 25%. Since the length of the bunch used in these experiments was three times shorter than the Collider design length (σ_z = 1 mm) we expect that this discrepancy will be less when the experiment is repeated with a Collider-type bunch.

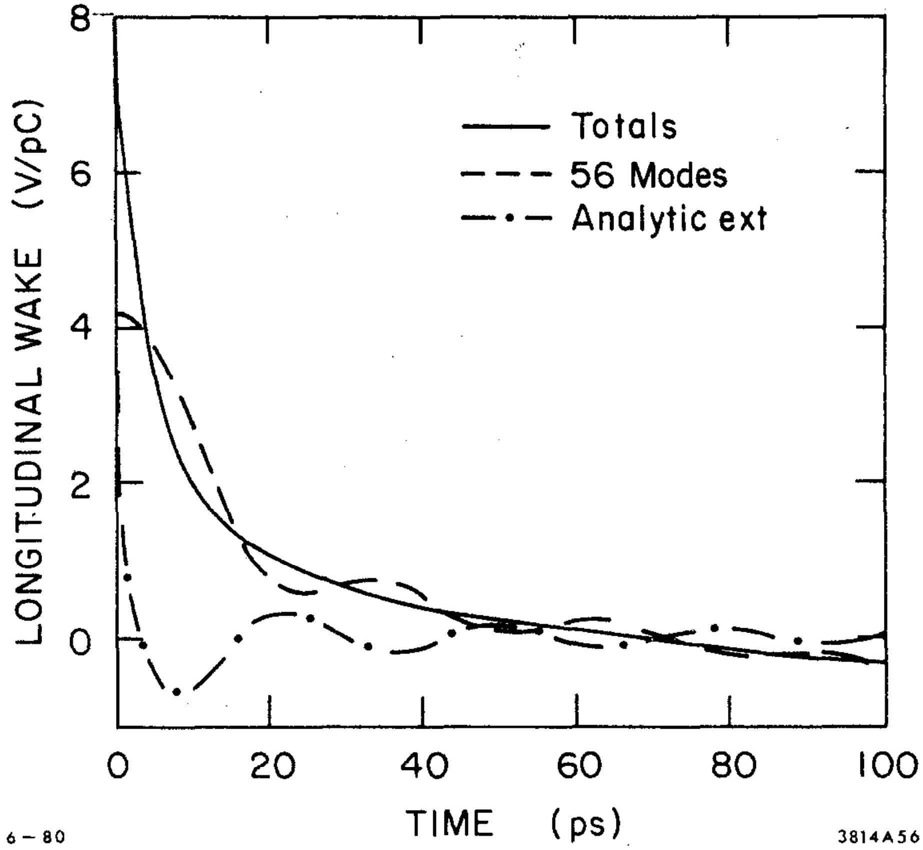

Fig. A-2. Contributions from the analytic extension and wake from discrete modes to the total longitudinal wake per cell for the SLAC linac structure.

Figures A-3 and A-4 show the total SLAC wake per cell for dipole ($m = 1$) modes for τ = 0-10 ps and τ = 0-100 ps. An important parameter for the dipole case is the slope of the wake as τ approaches zero. From Eq. (10), we see that this slope is finite, even taking into account modes to infinite frequency. From Fig. A-3 the slope for small τ is about 0.33 V per picosecond per picocoulomb per cell.

3. Longitudinal Wake-Field Effects and Control Measures

The effect of the longitudinal wake is to increase the energy spread of the beam by decelerating particles at the tail of the bunch. The control measure we have adopted is to place the bunch ahead of the crest of the accelerating RF wave in order to achieve a partial compensation of this effect of the wake field.

There is an analytic expression which closely approximates the longitudinal wake field calculated in Section 2. Let z be the distance between an electron that generates the wake and the point at which the wake is measured. Then:

$$W(z) = -0.115e^{-\sqrt{z/1.62}} \text{ volts} \quad . \tag{12}$$

In this expression z is measured in millimeters. The minus sign signifies deceleration. This expression is a good approximation for the wake field only over the range of z from 0 to 10 mm. In Fig. A-5 we have shown the convolution of the total wake given in expression (12) with a Gaussian bunch with an rms length of 1 millimeter. The bunch contains 5×10^{10} electrons. The maximum energy loss caused by wake-field deceleration in this bunch takes place at a point 1 millimeter behind the bunch centroid. The loss in energy at this point is 2.2 GeV.

The complete wake approximated in (12) is made up of the contributions of many modes in the RF structure. It is useful to give a separate (and exact) expression for the lowest frequency mode. This is the mode which is also excited by the external RF power sources.

$$W(z) = -0.0177 \cos (0.0598 z) \text{ volts} \quad . \tag{13}$$

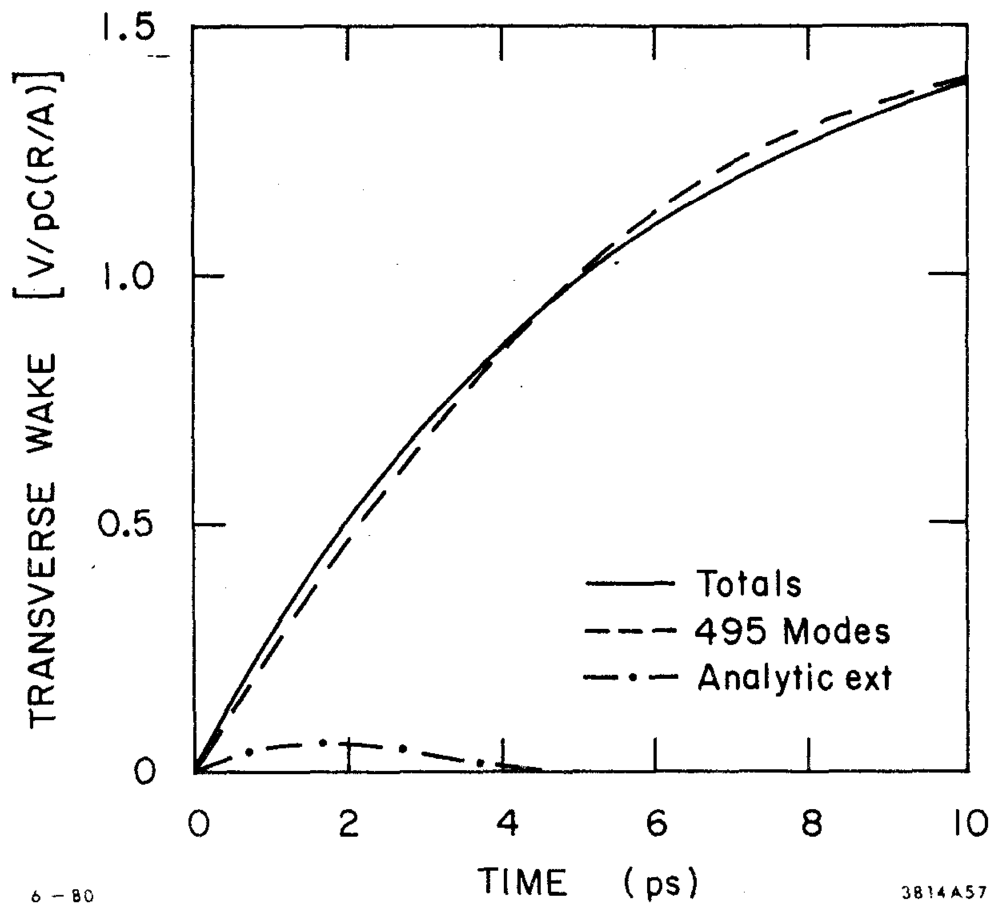

Fig. A-3. Dipole (m = 1) wake per cell for the SLAC linac structure for τ = 0 to τ = 10 ps.

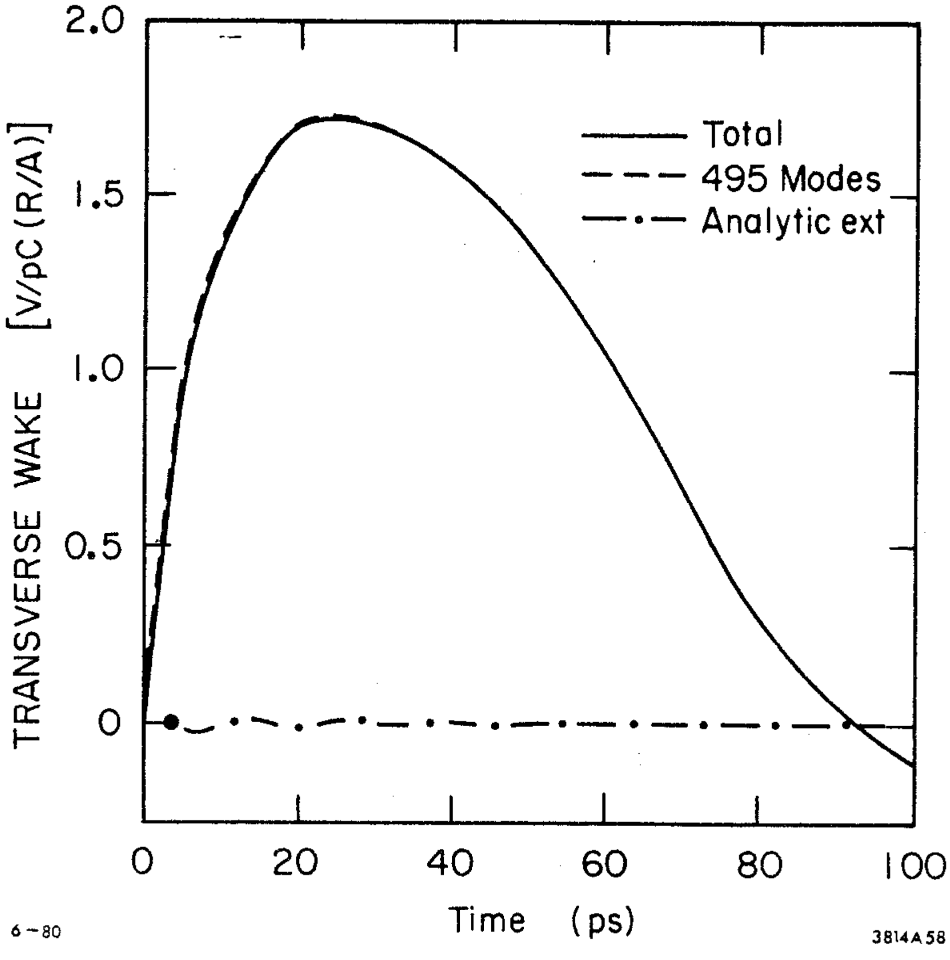

Fig. A-4. Dipole wake per cell for the SLAC linac structure for $\tau = 0$ to $\tau = 100$ ps.

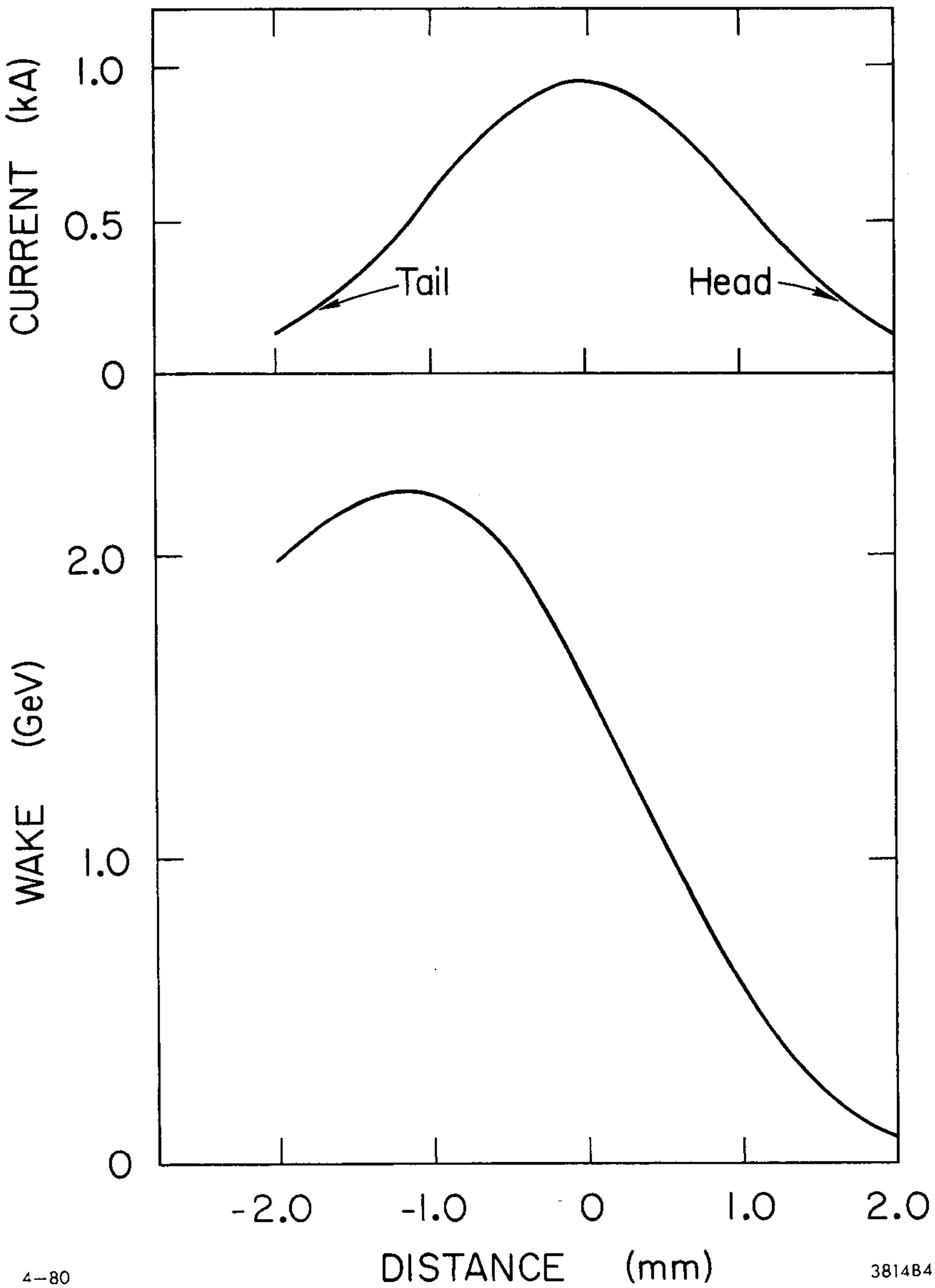

Fig. A-5. The longitudinal wake for the design intensity of 5×10^{10} particles/bunch and the design bunch shape, a Gaussian with δ = 1.0 mm. The current in the bunch is 950 amperes.

The total field which acts on an electron in the linac is the linear sum of the wake field and the field that has been stored in the RF structure before the bunch enters. The energy gain from this latter field is:

$$E(z) = E_o \cos (0.0598\ z + \delta) \text{ volts} \quad . \tag{14}$$

The greatest energy can be extracted from the stored energy in the RF structure if the phase δ between the stored field and the bunch centroid is chosen to be such that the fundamental part of the wake field given by the convolution of (13) with the bunch distribution interferes destructively with the stored field. Unfortunately, the energy spread within the bunch would be too large if this choice of phase were made. In order to make a partial compensation for the wake-field-induced energy spread, the phase of the stored field is chosen such that the centroid of the bunch is located 3.5 mm ahead of the crest of the stored field. To accelerate the centroid of the bunch to 50 GeV, the parameter E_o in (14) must be 52.73 GeV. For this choice of parameters the energy distribution of the particles within the buch is shown in Fig. A-6.

It is interesting to note that of the 12,500 joules stored in the fundamental RF mode in the linac structure, 415 joules have been converted into bunch kinetic energy, and 7.8 joules have been left behind in the structure in the form of higher order modes.

If we wished to accelerate more charge in a bunch of the same length and if we wished to maintain the same limit on energy spread, it would be necessary to add compensating sections to the linac which operate at a higher frequency than the 2856 MHz fundamental. This option is not considered to be practical at the present time.

4. Transverse Wake Fields and Control Measures

When a point charge travels off-axis down a linac structure it interacts with the walls of the structure and leaves behind a transverse wake field which will deflect particles traveling behind the point charge. If an intense bunch of particles travels through a structure whose transverse dimensions are large compared to the length of the bunch, the transverse wake field will be such that all particles behind the head of the bunch are deflected further away from the axis of the structure.

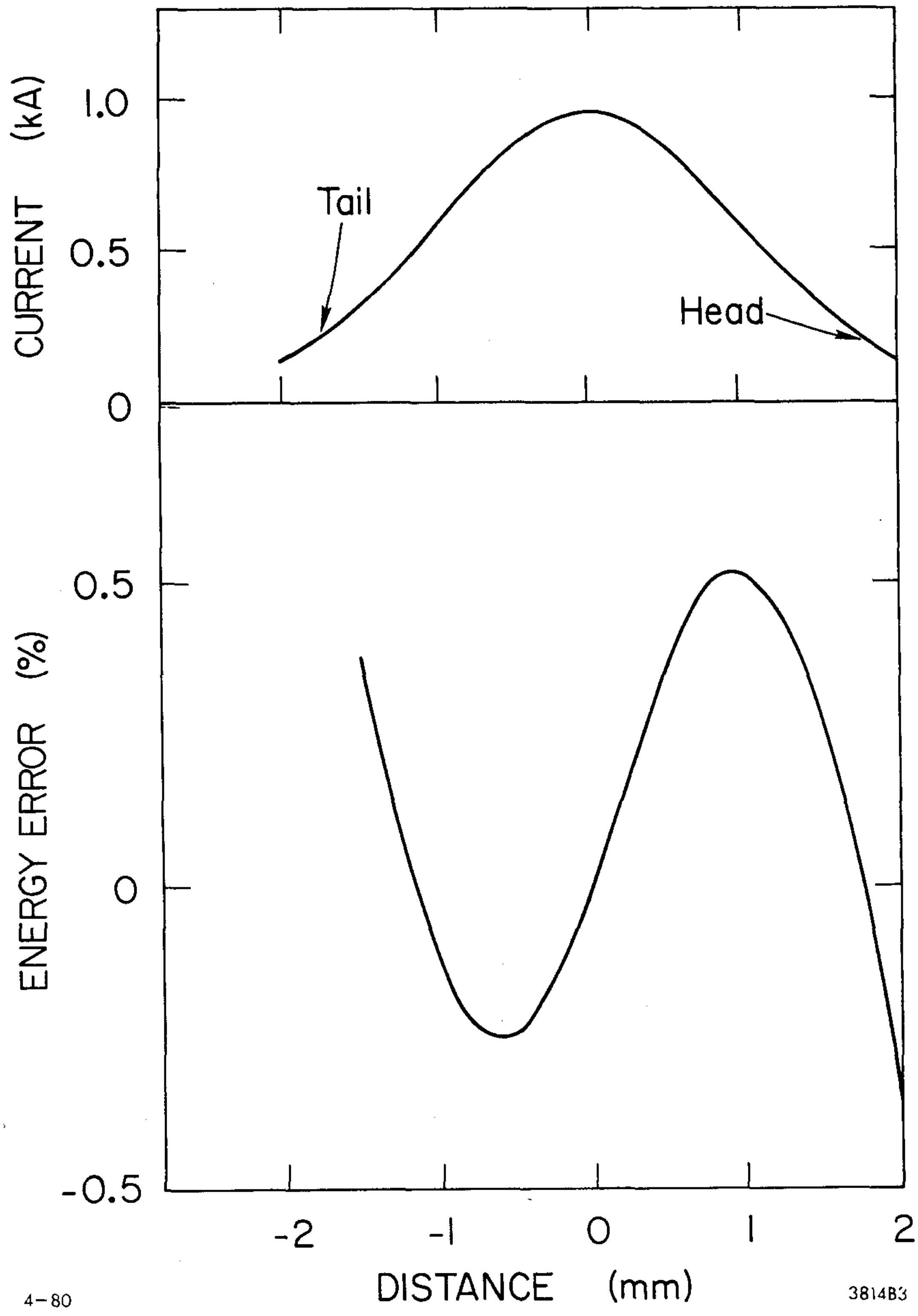

Fig. A-6. The fractional energy error as a function of position within the bunch after partial compensation has been made by placing the bunch-center 3.5 mm ahead of the crest of the RF wave.

Thus, as the bunch travels down along the linac, the projected area in transverse phase space occupied by all the particles in the bunch will increase.

To estimate the magnitude of these effects we shall first derive the equation of motion for particles in the bunch and then solve this equation by a perturbation method. The results of this analysis will then be applied to the SLAC linac for bunches of 5×10^{10} electrons, the design specification.

Equation of Motion

In what follows we treat the bunch as if its transverse dimensions were zero. We calculate the displacement of a particle in the bunch, $x(z,s)$, as a function of z, the longitudinal position relative to the center of the bunch. z is positive toward the head of the bunch, and s is the distance from the beginning of the linac. The approximation of zero transverse dimensions for the bunch is a good one for the Collider, since the transverse dimension of the bunch is very much less than the diameter of the linac irises. Thus, the transverse wake field is uniform across the bunch. In effect, $x(z,s)$ is the displacement of the center of a slice through the bunch at the position z.

The transverse force at z depends on the displacement of all charges with $z' > z$ and is given by

$$F_x(z,s) = e^2 \int_z^{\infty} dz' \rho(z') \, W(z'-z) \; x(z',s) \tag{15}$$

where ρ is the line density of particles in the bunch ($\int \rho \, dz$ is normalized to the total number of particles in the bunch), and $e \cdot W \cdot x$ is the transverse field produced by a point charge displaced from the axis by x at a distance $z'-z$ behind the point charge. All of the properties of the linac structure are contained in W. We have assumed that the displacement of a particle changes sufficiently slowly with s so that the average W of the structure can be used. We also assume that the bunch length is much shorter than the betatron wavelength so that the retardation in the transverse field from the head to the tail of the bunch can be ignored.

The equation of motion for x(z,s) can be written as

$$\frac{d}{ds}\left\{\gamma(s)\frac{d}{ds}\,x(z,s)\right\} + \left(\frac{2\pi}{\lambda(s)}\right)^2 \gamma(s)\,x(s,z) = r_o \int_z^\infty dz'\,\rho(z')\,\cdot \qquad (16)$$

$$W(z'-z)\;x(z',s) \quad .$$

where $\gamma(s)$ is the energy of the beam at position s in units of mc^2, m being the rest mass of the particle, $\lambda(s)$ is the instantaneous wavelength of betatron focusing at position s, and $r_o = e^2/mc^2$ is the classical radius of the particle. We have assumed that the betatron focusing is provided by a smooth function rather than coming from a series of discrete quadrupoles.

We assume that the energy of the beam increases linearly with s as a result of acceleration in such a way that $\gamma(s) = \gamma_o(1+Gs)$ with $\gamma_o mc^2$ the beam energy at injection and G the acceleration gradient. We assume that the strength of the focusing force in the linac scales with beam energy so that the instantaneous betatron wavelength remains constant $\lambda(s) = \lambda_o$.

We first make a change of variable in the equation of motion (16) from s to a new variable $u = 1 + Gs$. Eq. (16) then becomes

$$\frac{d^2x}{du^2} + \frac{1}{u}\frac{dx}{du} + \left(\frac{k_o}{G}\right)^2 x = \frac{r_o}{\gamma_o G^2 u}\int_z^\infty dz'\,\rho(z')\;W(z'-z)\;x(z',u) \quad , \qquad (17)$$

where we have defined $k_o = 2\pi/\lambda_o$. This equation will be solved by an iteration procedure. The solution x(z,s) is expanded in a series of powers in terms of the wake field

$$x(z,s) = \sum_{n=0}^{\infty} x^{(n)}\,(z,s) \quad . \qquad (18)$$

The zeroth order solution $x^{(o)}$ is first obtained by setting the wake field W equal to 0 in Eq. (17) and demanding the initial conditions $x(z,u) = x_o$ and $dx(z,u)/du = 0$ at $s = 0$ or $u = 1$. The n-th order term $x^{(n)}$ is then obtained from the $(n-1)^{th}$ order term $x^{(n-1)}$ by solving Eq. (17) with the x's on the left-hand side replaced by $x^{(n)}$ and the x on the right-hand side replaced by $x^{(n-1)}$. The solution can be obtained using a Green's function.

$$x^{(n)}(z,u) = \int_1^u du'\ G(u,u')\ \frac{r_o}{\gamma_o G^2 u'} \int_z^\infty dz'\ \rho(z') \cdot$$

$$W(z'-z)\ x^{(n-1)}\ (z',u') \tag{19}$$

with G(u,u') the Green's function. For the Collider, the betatron oscillation wavelength is much shorter than the distance required to double the energy, i.e., $k_o >> G$. The acceleration is then adiabatic, and we have

$$x^{(o)}(z,s) \simeq \frac{x_o}{\sqrt{u}} \cos\left[\frac{k_o}{G}\ (u-1)\right] = \frac{x_o}{\sqrt{1+Gs}} \cos k_o s \quad , \tag{20}$$

and

$$G(u,u') \simeq \frac{G}{k_o} \sqrt{\frac{u'}{u}} \sin\left[\frac{k_o}{G}\ (u-u')\right] \quad . \tag{21}$$

The factor $\sqrt{1+Gs}$ in Eq. (20) is the usual adiabatic damping factor.

Substituting Eqs. (20) and (21) into Eq. (19), we find that the terms in the series solution (18) are

$$x^{(n)}(z,s) = \frac{x_o}{\sqrt{1+Gs}} \left(\frac{r_o}{\gamma_o k_o}\right)^n I_n(s)\ R_n(z) \quad , \tag{22}$$

where we have defined

$$R_n(z) = \int_z^\infty dz_1\, \rho(z_1)\ W(z_1-z) \int_{z_1}^\infty dz_2\, \rho(z_2)\ W(z_2-z_1)\ \ldots.$$

$$\int_{z_{n-1}}^\infty dz_n\, \rho(z_n)\ W(z_n-z_{n-1}) \quad , \tag{23}$$

and

$$I_n(s) \simeq \frac{1}{n!}\ e^{ik_o s} \left[\frac{1}{2iG}\ \ell n(1+Gs)\right]^n \quad . \tag{24}$$

In the derivation, we have assumed that the beam energy at the end of acceleration is much higher than the beam energy at injection, and taking the real part is understood in Eq. (24).

A closed form can be obtained for R_n if we approximate ρ by a rectangular distribution and W by a linear function, i.e.,

$$\rho = \begin{cases} N/\ell & \text{for } |z| < \ell/2 \\ 0 & \text{for } |z| \geq \ell/2 \end{cases} \tag{25}$$

$$W = W_o \frac{z}{\ell} \quad . \tag{26}$$

Both approximations are close enough for the Collider to allow a good assessment to be made of the importance of higher order terms. We find

$$R_n(z) = \frac{1}{(2n)!} \left[NW_o \left(\frac{1}{2} - \frac{z}{\ell}\right)^2 \right]^n \quad . \tag{27}$$

Knowing $R_n(z)$ and $I_n(s)$, we can substitute Eq. (22) into Eq. (18) to obtain

$$x(z,L) = \frac{x_o}{\sqrt{1+GL}} e^{ik_oL} \sum_{n=0}^{\infty} \frac{1}{n!(2n)!} \left(\frac{\eta}{2i}\right)^n \quad , \tag{28}$$

where we have evaluated x at the end of linac s = L and have defined

$$\eta = \frac{L\ r_o NW_o}{k_o(\gamma_f - \gamma_o)} \ln \frac{\gamma_f}{\gamma_o} \cdot \left(\frac{1}{2} - \frac{z}{\ell}\right)^2 \quad . \tag{29}$$

There is no closed form for Eq. (28), but one can find an asymptotic expression in the strong-wake-field limit $|\eta| >> 1$. This asymptotic expression is

$$x(z,L) \simeq \frac{x_o}{\sqrt{6\pi}\ (1+GL)} |\eta|^{-1/6} \exp\left(\frac{3\sqrt{3}}{4} |\eta|^{-1/3}\right) \cos\left[k_oL - \frac{\eta}{|\eta|} \cdot \left(\frac{3}{4} |\eta|^{1/3} - \frac{\pi}{12}\right)\right] \quad . \tag{30}$$

In Fig. A-7, we have plotted x(z,L) across the bunch for values of $k_oL = 0, \pi/2, \pi$ and $3\pi/2$ (Modulus 2π). The wake field strength is such that the value of η at the very tail of the bunch is equal to 150. The vertical scale is in units of $\sqrt{\gamma_o/\gamma_f}\ x_o$. It is clear from Fig. A-7 that the distortion of the bunch can be very large.

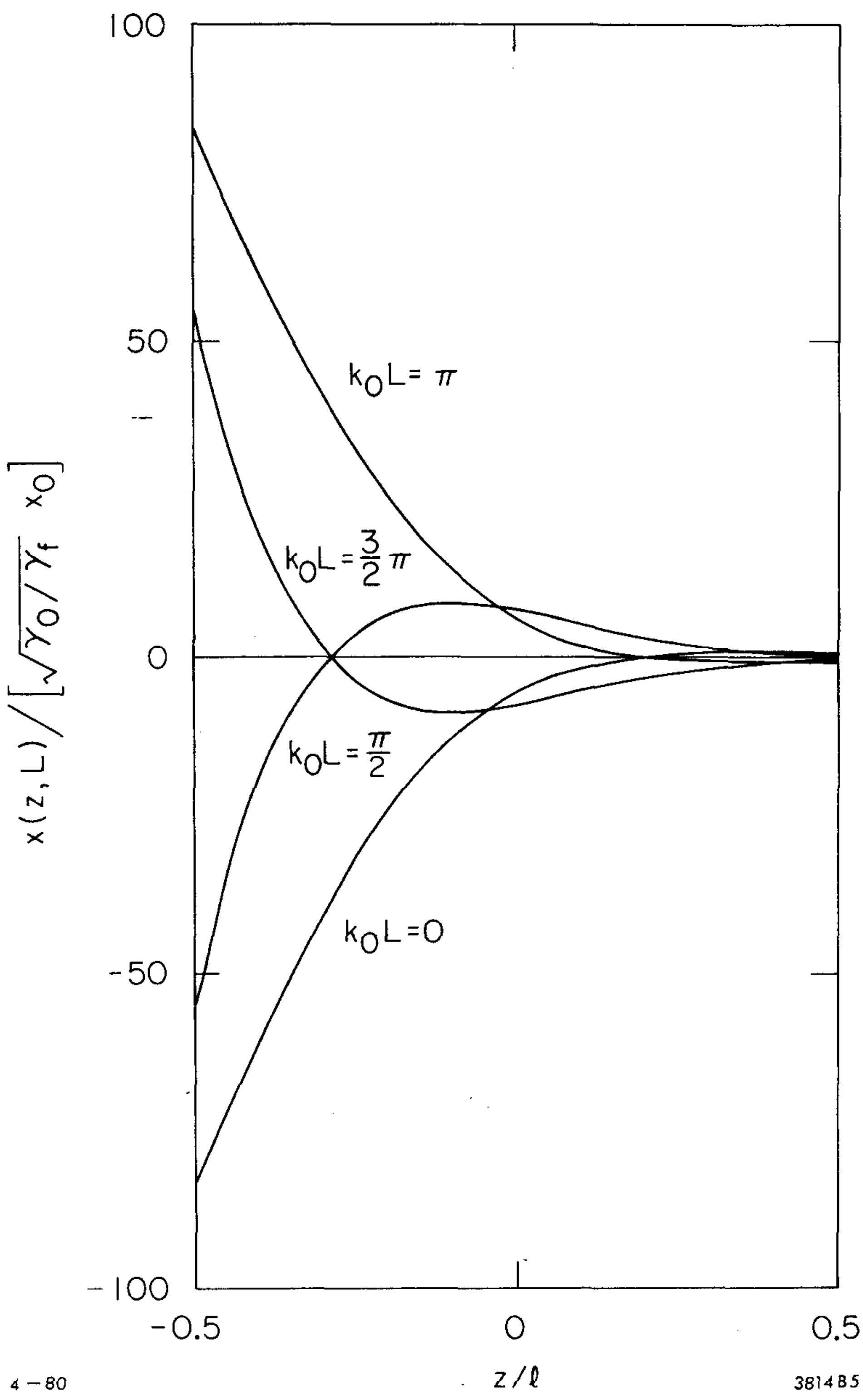

Fig. A-7. The transverse bunch shape at the end of acceleration for four different values of total betatron phase: 0, $\pi/2$, π, and $3\pi/2$. The wake-field strength parameter $\eta = 150$ at the tail of the bunch.

Misalignment Effects

In the previous analysis, we have assumed that the accelerator structure is perfectly aligned, and the wake field is produced as a consequence of beam injection with a displacement error. In this section, we will study the effect caused by misalignment of the accelerator pipe. We assume the beam is injected into the linac with perfect precision and it travels down the linac in a straight line in the limit of weak beam intensity. We will study the case with acceleration under the approximation that the acceleration is adiabatic.

The equation of motion can be written as:

$$\frac{d^2x}{du^2} + \frac{1}{u}\frac{dx}{du} + \left(\frac{k_o}{G}\right)^2 x = \frac{r_o}{\gamma_o G^2 u} \int_z^\infty dz' \; \rho(z') \; W(z'-z) \cdot \left[x(z',u) - d(s)\right] \quad . \tag{31}$$

where d(s) is the transverse position error of the linac structure at position s. If there are N_c sections with the i-th section misaligned by a distance d_i, one has

$$d(s) = \sum_{i=1}^{N_c} d_i \, \ell_i \, \delta(s-s_i) \quad ,$$

where ℓ_i and s_i are the length and the position of the i-th section respectively. Compared with Eq. (17), Eq. (31) contains an additional force term on the right-hand side that comes from the pipe misalignment.

The zero-th order solution to Eq. (31) is $x^{(o)} = 0$, instead of Eq. (20) since the beam is assumed to be injected without error. The trajectory of the head of the bunch strictly follows $x^{(o)}$ and is, therefore, a perfect straight line. The first-order perturbation term comes solely from the linac structure misalignment d_i:

$$x^{(1)}(z,s) = \sum_{\substack{i \\ (s>s_i)}} \frac{r_o d_i \ell_i}{\gamma_o k_o} \cdot \frac{1}{(1+Gs)^{1/2}(1+Gs_i)^{1/2}} \cdot \sin\left[k_o(s-s_i)\right] \cdot R_1(z) \quad , \tag{32}$$

where the quantity $R_n(z)$ has been defined in Eq. (23).

In order to apply this to the Collider, it is necessary to carry out the perturbation calculation up to the second order in the wake field. The second-order term can be obtained through the use of Eq. (19). Substituting Eq. (32) in Eq. (19) we find

$$x^{(2)}(z,s) = \sum_{\substack{i \\ (s>s_i)}} \frac{r_o{}^2 d_i \ell_i}{2\gamma_o{}^2 k_o{}^2 G} \cdot \frac{\ell n[(1+Gs)/(1+Gs_i)]}{(1+Gs)^{1/2}(1+Gs_i)^{1/2}} \cdot \cos\left[k_o(s-s_i)\right] \cdot R_2(z) \quad . \tag{33}$$

If we assume the misalignment errors d_i are uncorrelated from one linac section to the next, we can make an rms estimate to obtain

$$\langle x^{(1)^2} \rangle = \frac{1}{2N_c} \langle d^2 \rangle \left(\frac{r_o L}{\gamma_f k_o}\right)^2 \ell n \frac{\gamma_f}{\gamma_o} \cdot R_1{}^2(z)$$

$$\langle x^{(2)^2} \rangle = \frac{1}{24N_c} \langle d^2 \rangle \left(\frac{r_o L}{\gamma_f k_o}\right)^4 \ell n^3 \left(\frac{\gamma_f}{\gamma_o}\right) \cdot R_2{}^2(z) \quad , \tag{34}$$

where $\langle d^2 \rangle^{1/2}$ is the rms value of the misalignment and we have assumed that all linac sections have the same length $\ell_i = L/N_c$. We have also made the approximation that $\gamma_f \gg \gamma_o$.

If we assume a square distribution (25) and a linear wake field (26), we can use Eq. (27) to obtain the quantities $R_n(z)$. The ratio of $\langle x^{(2)^2} \rangle$ to $\langle x^{(1)^2} \rangle$ under these assumptions is $\eta^2/1728$.

The emittance growth due to misalignment can be substantially reduced by empirically controlling the injection offset x_o and angle x_o' at the beginning of the linac. The corresponding first and second order contributions have been obtained in Eq. (22):

$$x^{(1)}(z,L) = \frac{1}{\sqrt{1+GL}} \frac{r_o}{\gamma_o k_o} R_1(z) \frac{\ell n(1+GL)}{2G} \left(x_o \sin k_o L - \frac{x_o'}{k_o} \cos k_o L\right) \quad ,$$

$$x^{(2)}(z,L) = \frac{-1}{\sqrt{1+GL}} \left(\frac{r_o}{\gamma_o k_o}\right)^2 R_2(z) \frac{\ell n^2(1+GL)}{8G^2} \left(x_o \cos k_o L + \frac{x_o'}{k_o} \sin k_o L\right) \quad . \tag{35}$$

By choosing proper values of x_o and x_o', it is possible to cancel either the first-order misalignment contribution, Eq. (32), or the second-order misalignment contribution, Eq. (33), by a corresponding contribution from (35). For example if the second-order misalignment term dominates, one might choose

$$\begin{pmatrix} x_o \\ x_o' \end{pmatrix} = \frac{4G}{\ell n^2(1+GL)} \sum_i d_i \ell_i \frac{\ell n[(1+GL)/(1+Gs_i)]}{(1+Gs_i)^{1/2}} \begin{pmatrix} \cos k_o s_i \\ k_o \sin k_o s_i \end{pmatrix} . \quad (36)$$

so that the second-order contribution from the injection offset and angle cancels the second-order contribution from the misalignments. The required x_o and x_o' have rms values given by

$$\langle x_o^2 \rangle = \frac{8}{3N_c} \frac{\gamma_f/\gamma_o}{\ell n(\gamma_f/\gamma_o)} \langle d^2 \rangle = \frac{1}{k_o^2} \langle x_o'^2 \rangle \quad . \quad (37)$$

With x_o and x_o' given by Eq. (36), the first-order term obtained by the sum of misalignment and injection contributions is

$$x^{(1)} = \frac{1}{\sqrt{1+GL}} \left(\frac{r_o}{\gamma_o k_o}\right) R_1(z) \sum_i \frac{d_i \ell_i}{\sqrt{1+Gs_i}} \left[1-2\,\frac{\ell n(1+Gs_i)}{\ell n(1+GL)}\right] \sin\,[k_o(L-s_i)] \quad . \quad (38)$$

The rms value of this $x^{(1)}$ is given by

$$\langle x^{(1)2} \rangle = \frac{1}{6N_c} \langle d^2 \rangle \left(\frac{r_o L}{\gamma_f k_o}\right)^2 \ell n \frac{\gamma_f}{\gamma_o} \cdot R_1^2(z) \quad , \quad (39)$$

which is 1/3 of that for the case with no injection cancellation effort. Thus this scheme of minimizing the emittance growth due to misalignment by controlling the injection conditions not only cancels the second-order misalignment contribution but also significantly reduces the first-order contribution.

Collider Linac Tolerances

The design parameters for the Collider mode of operation are:

$$
\begin{array}{ll}
N = 5 \times 10^{10} & \sigma_x = 70\ \mu\mathrm{m} \\
\gamma_o = 2.4 \times 10^3\ (1.2\ \mathrm{GeV}) & \ell = 3.5\ \mathrm{mm} \\
\gamma_f = 10^5\ (50\ \mathrm{GeV}) & W_o = 5.9 \times 10^5\ \mathrm{m}^{-3} \\
L = 3 \times 10^3\ \mathrm{m} & N_c = 240 \\
\gamma_o = 100\ \mathrm{m} &
\end{array} \tag{40}
$$

Under these conditions, the asymptotic experssion must be used in order to find the proper tolerance criterion.

The value of η, according to Eq. (29), is 37 at $z = 0$, 94 at $z = -\sigma_z = -\ell/2\sqrt{3}$, and 150 at $z = -\ell/2$. The bunch shape for this case has been shown in Fig. A-7. The corresponding values of the magnitude of $x(z,L)$ are $1.5x_o$ for $z = 0$ and $6.1x_o$ for $z = -\sigma_z$. If we choose $z = -\sigma_z$ for our beam-quality requirements, we obtain the tolerance on the injection displacement $|x_o| < \sigma_x/6.1 = 11\ \mu\mathrm{m}$. This tolerance on injection error x_o is a criterion on the injection jittering since a static injection error can always be compensated by a set of trajectory kickers before injection. The corresponding tolerance on the jittering of the injection angle is $\pm 1\ \mu\mathrm{rad}$.

Substituting the SLAC linac data into Eq. (34), it turns out that the misalignment effect is dominated by the second-order perturbation rather than the first-order perturbation. For a particle at $z = -\sigma_z$ the ratio $x^{(2)}_{rms}$ to $x^{(1)}_{rms}$ is about 2.2.

The misalignment effect can be minimized by injecting the beam with empirically determined offset x_o and angle x_o'. Since the second-order contribution dominates, the optimum choice of x_o and x_o' is given by Eq. (36). The expected rms value of the required injection offset, given by Eq. (37), is $\langle x_o^2 \rangle^{1/2} = 0.35\ \langle d^2 \rangle^{1/2}$. After optimizing by controlling the injection conditions, the resultant beam-size growth, $\langle x^{(1)2} \rangle^{1/2}$, is given by Eq. (39), which is found to be $0.25\ \langle d^2 \rangle^{1/2}$ at the bunch center and $0.62\ \langle d^2 \rangle^{1/2}$ at σ_z behind the bunch center. For this beam-size growth at $z = -\sigma_z$ to be less than the transverse beam size σ_x at the end of the linac, we demand a misalignment tolerance of $\langle d^2 \rangle^{1/2} = 0.11$ mm.

The effect of misalignment is determined by examining the reduction in luminosity arising from the emittance growth. Since the luminosity is inversely proportional to the emittance, the reduction factor R is approximately given by

$$R = \int_{-\ell/2}^{\ell/2} \frac{dz/\ell}{1 + \langle x^{(1)^2} \rangle / \sigma_x^2} \tag{41}$$

with $\langle x^{(1)^2} \rangle$ given by Eq. (39). In Fig. A-8 we have plotted R versus $\langle d^2 \rangle^{1/2}$. For $\langle d^2 \rangle^{1/2} = 0.1$ mm, the reduction in luminosity is about 20%. The third-order term is appreciable only at the very tail of the bunch and thus does not affect the luminosity noticeably.

Another mechanism that relaxes both the injection and the misalignment tolerances is the following: Different particles have slightly different energies and thus different betatron frequencies. The resonant driving situation is therefore pessimistic. This Landau damping effect will become significant if $\Delta k_o L > \pi$, where Δk_o is the spread in the betatron wave number in the bunch.

5. The Linac Lattice

The main consideration that influenced our choice of linac lattice has been the need to minimize the beta function in order to reduce the disruption caused by transverse wake fields. Another important consideration has been that the trajectories of simultaneous beams of electrons and positrons passing through the lattice must be well-centered on the linac axis to suppress the generation of transverse wake fields.

The lattice we have adopted is a 90 degrees/cell FODO array with a quadrupole at the end of each 12.5-meter linac girder. At the end of each linac sector there is a 3-meter-long drift section in which a quadrupole doublet has been placed. The nature of this matching scheme is such that if one sector begins with an F quadrupole, the next sector begins with a D quadrupole. A sketch of the elements in two adjacent sectors is shown in Fig. A-9. The betatron functions for this lattice are shown in Fig. A-10. It can be seen that the betatron functions are no larger in the matching cells than they are in the standard cells.

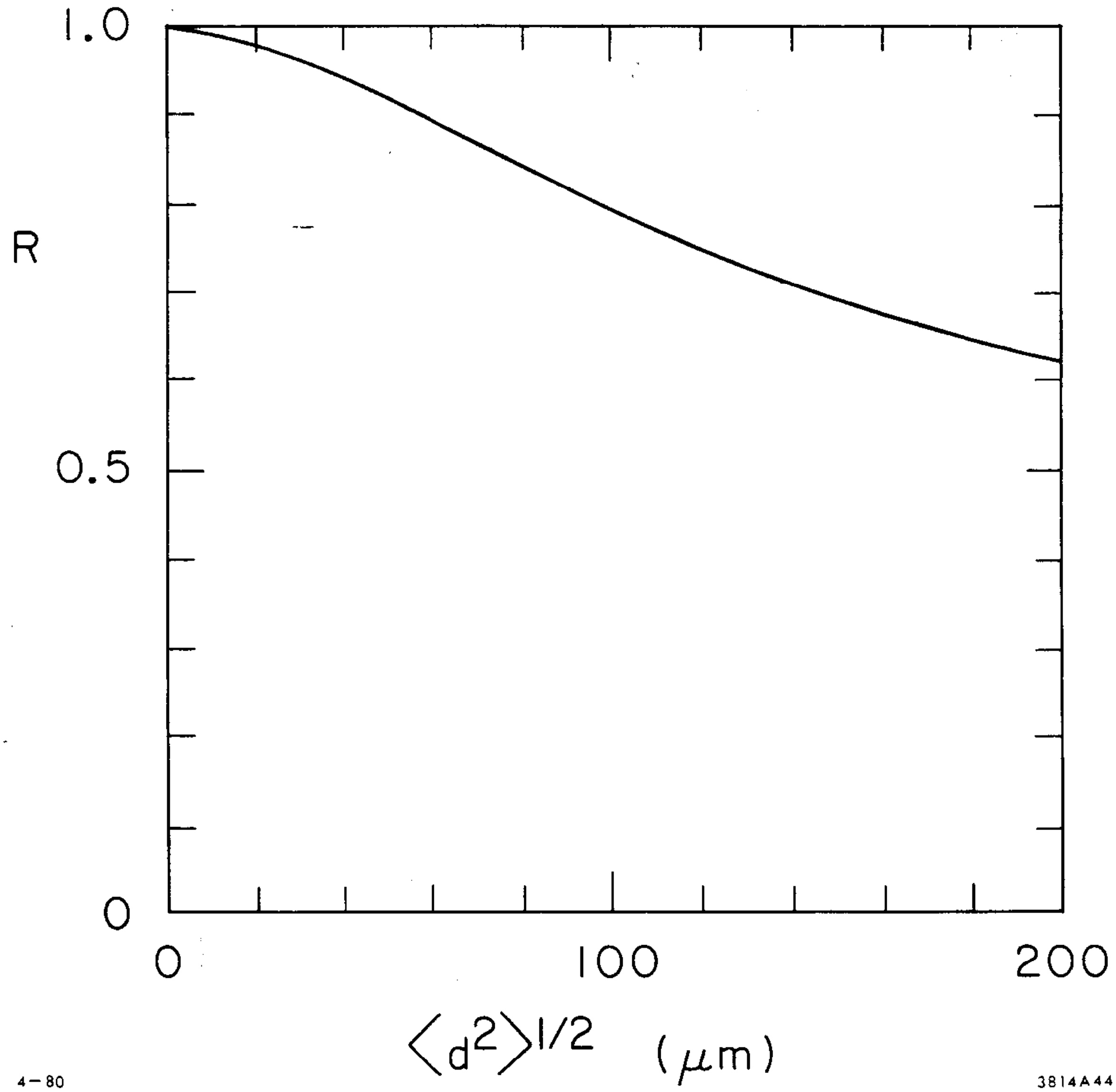

Fig. A-8. The luminosity reduction factor R vs the misalignment tolerance of the accelerator pipe $\langle d^2 \rangle^{\frac{1}{2}}$.

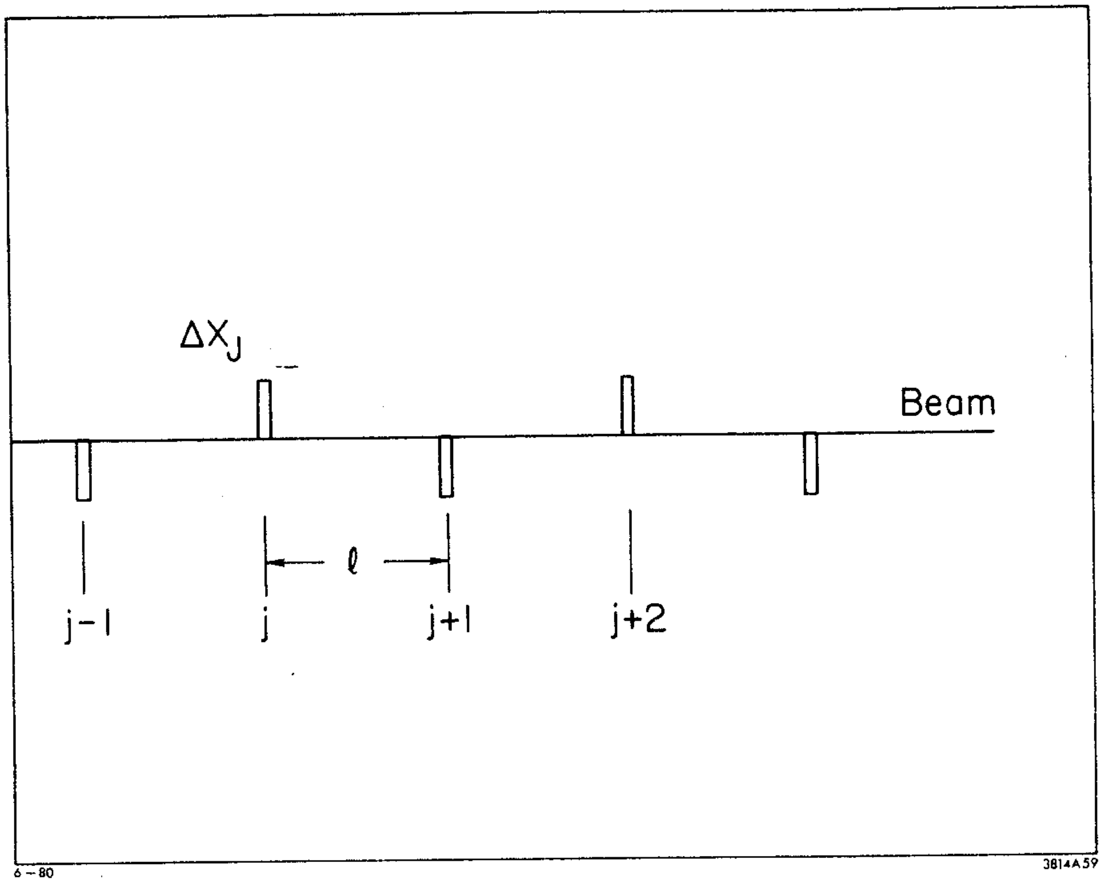

Fig. A-9. The linac quadrupole lattice. A matching doublet is placed in the 3-m drift section between linac sectors.

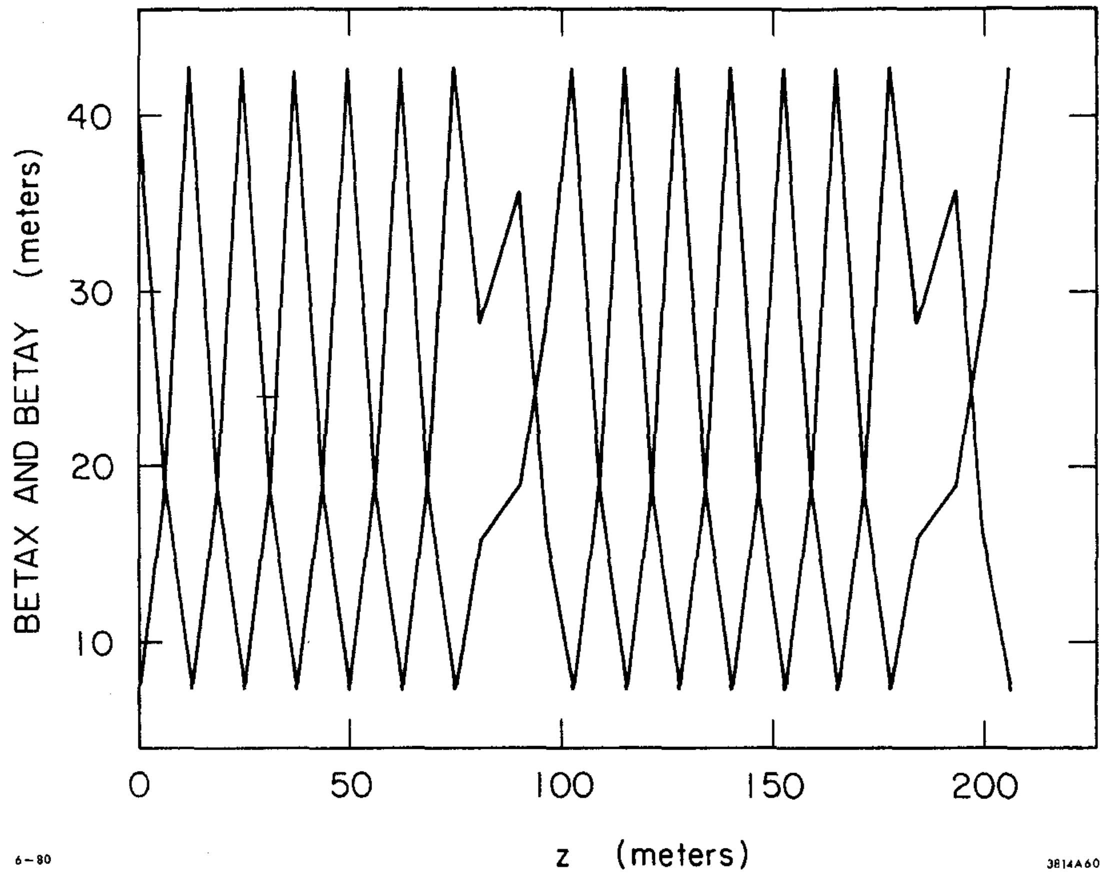

Fig. A-10. The betatron functions for the linac lattice. Note that these functions are no larger in the matching cells than in the normal lattice.

The phase advance of 90 degrees/cell is maintained up to a beam energy of 26 GeV by scaling the quadrupole strength appropriately. Between 26 GeV and 50 GeV the quadrupole strength is held constant (because of a power limitation on the quadrupole), and the phase advance/cell decreases to 42 degrees/cell at the end of the linac.

Within each quadrupole there is a beam-position monitor (a set of four strip-lines) which is electrically gated so that the position (in two dimensions) of the electron and the positron beams can be measured separately. Each quadrupole has trim windings that can be used to make a magnetic dipole correction field in any direction perpendicular to the linac axis.

There are two kinds of forces that cause trajectory errors: static fields (such as those caused by quadrupole misalignments) deflect positrons and electrons in opposite directions, while RF fields (such as those caused by a tilted linac girder or by waveguide-end couplers) deflect positrons and electrons in the same direction. We shall show that it is possible to simultaneously correct the trajectory distortions caused by both sources of error with the static dipole windings on the quadrupoles.

We have made a computer model of the linac lattice in order to study the trajectory-correction problem. We model the RF error deflections by giving the beam a single random kick at the center of each 12.5-meter girder, the same point at which the acceleration has been introduced. The static error problem has been modeled by introducing a random displacement of each quadrupole, and another random displacement of each position monitor.

We have chosen the following distributions for random errors for our study. Quadrupole displacements and beam-position-monitor errors have been uniformly distributed between -.1 and +.1 mm. The RF kicks are uniformly distributed between -3×10^{-5} and $+3 \times 10^{-5}$ GeV/c and are assumed to be centered in each 12.5-meter girder. This distribution is consistent with measurements which have been made on the SLAC linac.

Our correction scheme is as follows. Let the correctors be specified by index j (j = 1, 2, ...N) and the monitors by index i (i = 1, 2, ...M). Let x_i^+ and x_i^- be the measured positions of the e^+ and e^- at the i-th monitor before corrections are applied. If we turn on the j-th corrector the orbit at the i-th monitor will change by $C_{ij}^+ \theta_j$ for the

e^+ beam and $-C^-_{ij}\ \theta_j$ for the e^- beam. $\pm\theta_j$ are the kicking angles for the e^+ and e^- beams. $C^{\pm}_{ij}$ are the response matrices determined by the linac lattice. $C^{\pm}_{ij}$ will be zero if the j-th corrector is downstream of the i-th monitor.

We wish to find a solution (j = 1, 2, ...N) which minimizes the rms value (S) of the orbit after correction:

$$S = \sum_{i=1}^{n} \left(x_i^+ + \sum_{j=1}^{n} C^+_{ij}\ \theta_j\right)^2 + \left(x_i^- - \sum_{i=1}^{n} C^-_{ij}\ \theta_j\right)^2 \tag{42}$$

If we group the constants C^+_{ij} and C^-_{ij} to form two MxN matrices C^+ and C^-, and group x_i^+ and x_i^- to form two M-dimensional vectors $\vec{x}^+$ and $\vec{x}^-$, the solution for $\vec{\theta}$ which minimizes S is given by the following expression:

$$\vec{\theta} = -\left(\tilde{C}^+C^+ + \tilde{C}^-C^-\right)^{-1} \left(\tilde{C}^+\vec{x}^+ - \tilde{C}^-\vec{x}^-\right) \quad . \tag{43}$$

$\tilde{C}$ is the transpose of C. Thus a solution can be easily determined.

The trajectories of the electron and positron beams before and after correction are shown in Figs. A-11 through A-14. After correction the rms displacement error for each beam is typically <0.05 mm.

Trajectory distortions will tend to disperse the beam as a function of energy and thereby increase the effective transverse emittance. The cumulative effect of the random dispersions caused by trajectory errors δx_i may be found by an adiabatic perturbation method. Under the assumptions that the acceleration, the phase advance/cell and the energy deviation are all constant, we find that the expectation value for the emittance increase is

$$\overline{\Delta\epsilon} = \frac{2n(\delta x_{rms})^2}{\ell^2} \left[\left(\sqrt{\beta_F} - \sqrt{\beta_D}\cos\frac{\mu}{2}\right)^2 + \left(\sqrt{\beta_D} - \sqrt{\beta_F}\cos\frac{\mu}{2}\right)^2\right] \times \left(\delta^2 + \frac{n^2}{6}x^2\delta^4\right) \quad . \tag{44}$$

where n is the number of FODO cells, δx_{rms} is the rms trajectory error, ℓ is the half-cell length, β_F and β_D are the betatron functions at the F and D quadrupoles, μ is the phase advance/cell, and x is the betatron chromaticity per cell.

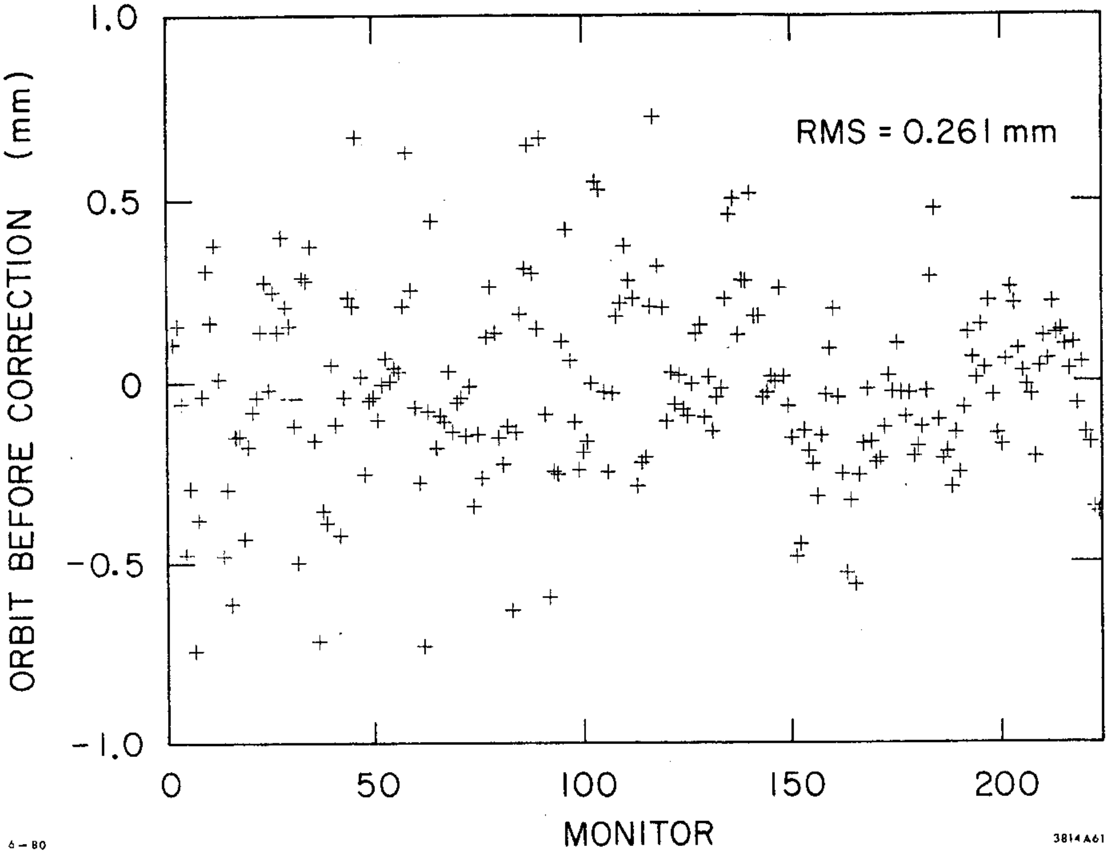

Fig. A-11. Positron beam position before correction.

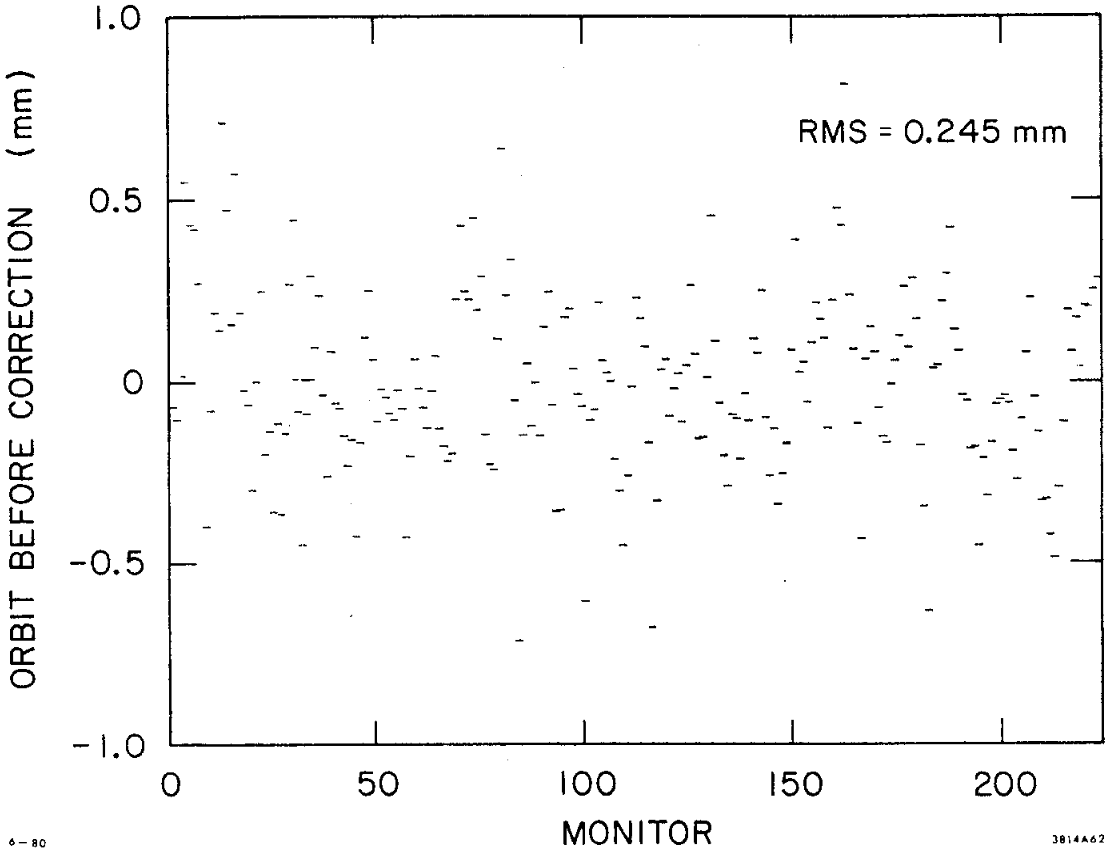

Fig. A-12. Electron beam position before correction.

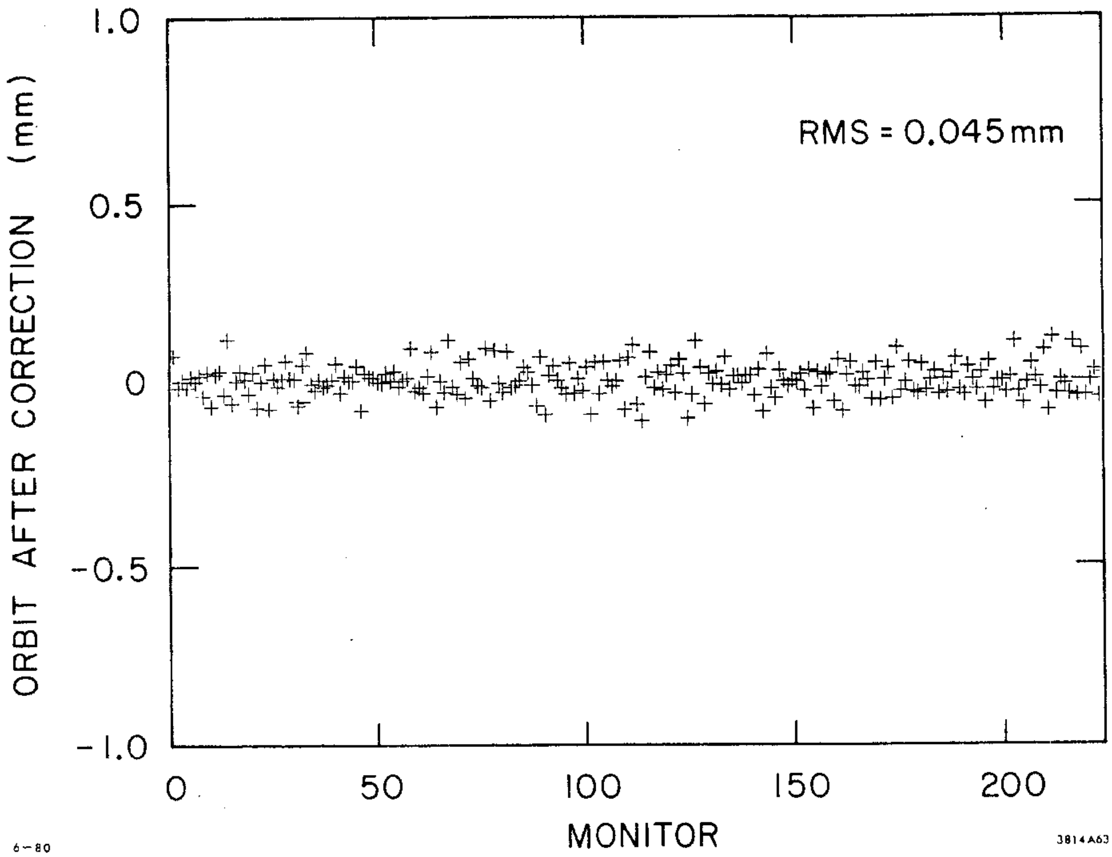

Fig. A-13. Positron beam position after correction. The rms position error is less than 0.05 mm.

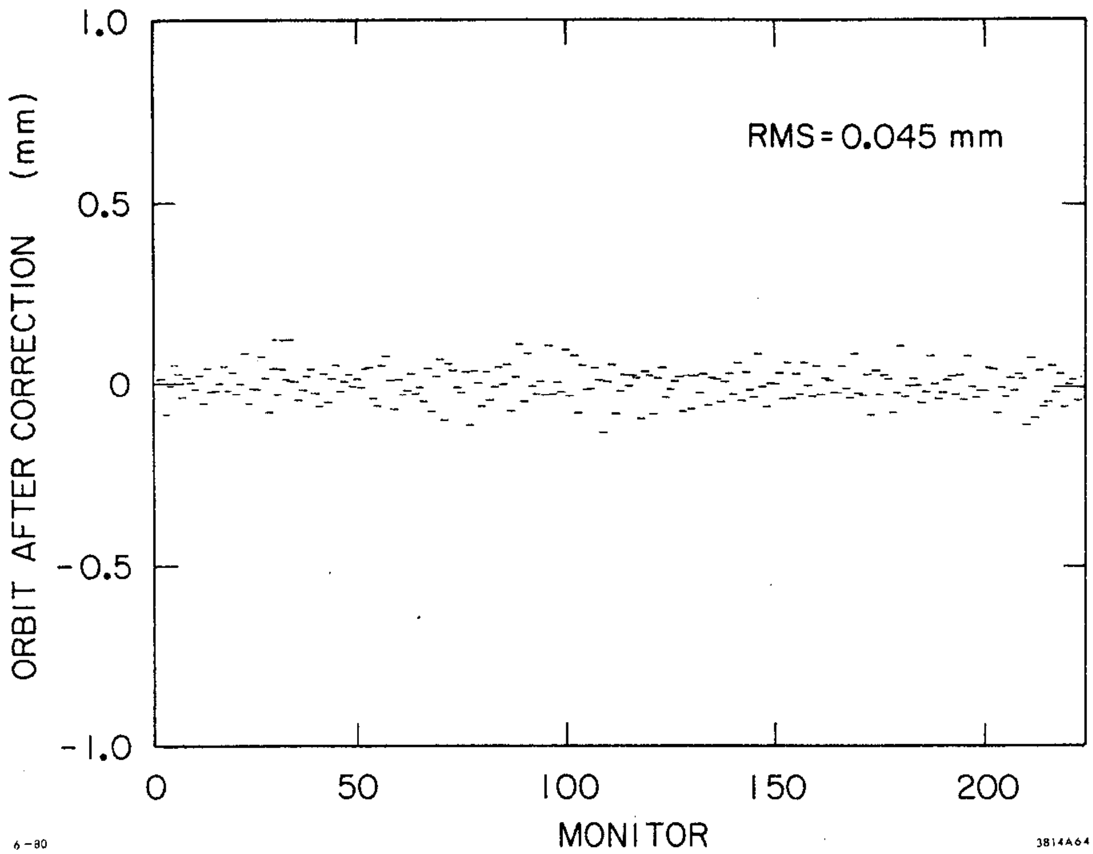

Fig. A-14. Electron beam position after correction. The rms position error is less than 0.05 mm.

For the linac lattice we have described in this Appendix we find

$$\overline{\Delta\varepsilon} = 79(\delta x_{rms})^2 \; (\delta^2 + 9600\ \delta^4) \quad . \tag{45}$$

With $\delta = 0.005$ and $\delta x_{rms} = 10^{-4}$ meters, we find an emittance growth of 2.2×10^{-11} radian-meters, which is small compared to our design value of 3×10^{-10} radian-meters.

6. Computer Simulation

We have made a computer model of the accelerator in order to study transverse wake-field effects. From our study we have concluded that the most critical parameters are the position and angle of the 1.2 GeV bunches injected into the linac. These parameters must be very stable from pulse to pulse.

Our model contains the following features. The linac lattice (a FODO array with 12.4 meters between quadrupoles) is divided into 480 sections or 4 sections per lattice cell. The quadrupoles are adjusted so that the betatron phase advance per cell is 90° in the energy range from 1.2 to 26 GeV. From the 26 GeV point to the end of the linac the quadrupole strength is constant (100 KG is the maximum value consistent with the design of the quadrupole). At the end of the linac the phase advance has dropped to 44 degrees per cell.

Moving along with the bunch is a grid of 61 slices, each 0.1 mm long. The bunch is simulated by populating slices with electrons according to the desired distribution. The results described here were obtained with Gaussian bunches cut off at $\pm 2\sigma$.

We denote the position along the linac by index j (section number), and the position in the grid moving with the bunch by index m (slice number). The state vector which describes the position of slice m in transverse phase space at location j in the linac is defined as follows:

$$\begin{aligned} \mathrm{Re}(x_j^m) &= \text{position at point } j/\sqrt{\beta_j} \\ \mathrm{Im}(x_j^m) &= \text{angle at point } j \times \sqrt{\beta_j} \quad . \end{aligned} \tag{46}$$

If the slice is perturbed by an angular deflection at point j, the state vector at point j+1 is given as follows:

$$x^m_{j+1} = \left\{ x^m_j + \delta x^m_j \right\} \sqrt{\frac{E_j}{E_{j+1}}}\; e^{-i(\phi_{j+1} - \phi_j)} \quad . \tag{47}$$

In this expression ϕ_j and E_j are the betatron phase and particle energy. The angular deflection of slice m at position j is determined by the position relative to the axis of the waveguide of all slices ahead of slice m. The wake deflection that is generated by these slices is

$$\delta x^m_j \equiv i \sum_{k>m}^{61} n_k \frac{W(k-m)}{E_j} \left\{ \beta_j \mathrm{Re}(x^k_j) - \sqrt{\beta_j}\, d_j \right\} \quad . \tag{48}$$

In this expression d_j is the displacement of the RF structure relative to the axis of the accelerator, and n_k is the number of electrons in slice k. W(k−m) is the wake field per electron at a distance of 0.1 × (k−m) millimeters. The displacement errors d_j can be controlled by accurate alignment. The wake field is fixed by the linac structure.

There are two effects we have studied. The first is the effect of an error in injection position or angle on the final emittance of the bunch. The second effect is that of the random misalignment of the linac sections. We shall show that the former effect is the most important and that the effects of random section misalignment are removed by the empirical tuning procedure used to optimize the injection angle and position.

We describe the injection error in a phase-independent manner by giving the corresponding value of the Courant and Snyder invariant. Figure A-15 shows the evolution of the Courant and Snyder parameter for the central slice of the bunch as it passes through the linac. When the bunch has few electrons in it, the parameter damps as 1/energy. When the bunch is well populated, the injection error is no longer damped. It should be noted that the various cases shown in Fig. A-15 differ in bunch length as well as in the number of electrons per bunch. The bunch has been shortened as the current is reduced in order to maintain a constant energy spread. This reduction in length reduces the transverse wake field while maintaining constant the longitudinal wake field.

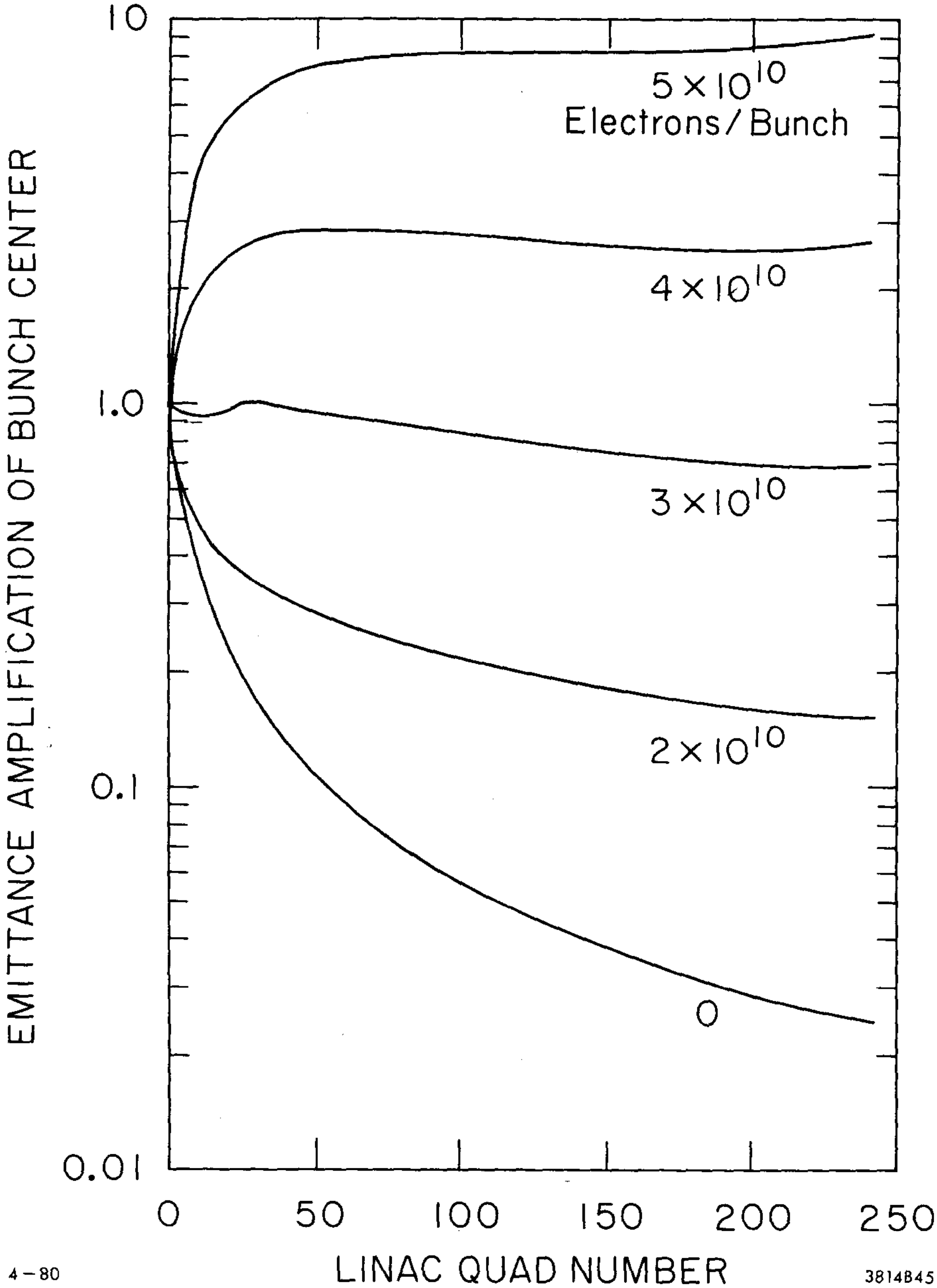

Fig. A-15. The curves show the evolution of an injection error for the central slice of the bunch. When the number of electrons in the bunch is small, the Courant and Snyder invariant damps as 1/E.

The injection error must be tuned empirically through the use of emittance monitors at the end of the linac. For the tuning to be successful the jitter in the injection conditions must be limited. If we require that the jitter in injection conditions have no more effect than to displace the slice of the bunch 0.5 σ behind the center to 3×10^{-10} radian-meters, the following tolerance must be maintained (a beta of 42 meters is assumed):

Tolerance on Injection Stability

NUMBER --	POSITION ERROR	ANGLE ERROR
5×10^{10}/bunch	13 microns	0.3 microradians
4×10^{10}/bunch	30 microns	0.7 microradians
3×10^{10}/bunch	57 microns	1.6 microradians

The 50 GeV phase-plane distribution of a bunch of 5×10^{10} electrons injected into the linac with a position error of 13 microns is shown in Fig. A-16. The figure shows that the disruption of the bunch increases rapidly as the point of observation is moved back from the head of the bunch.

Random misalignment of the linac sections can cause the bunch to be disrupted even if it is injected without error. In our model we have assumed that the waveguide at each quadrupole has been randomly misaligned in the range -0.2 to +0.2 mm relative to the axis of the linac. In Fig. A-17 the curve marked "no correction" shows the evolution of the Courant and Snyder invariant for the central slice of the bunch. The final position of 10^{-9} radian-meters is greater than our design emittance. To correct for the misalignment, the injection conditions have been empirically tuned (by a computer operator in this case). The procedure was terminated when the curve marked "with correction" was obtained. In Fig. A-18 we show the phase-plane distribution of the bunch after the tuning correction was made.

If the injection jitter is held to the tolerance shown above, the effects of the linac waveguide random misalignment should not be important.

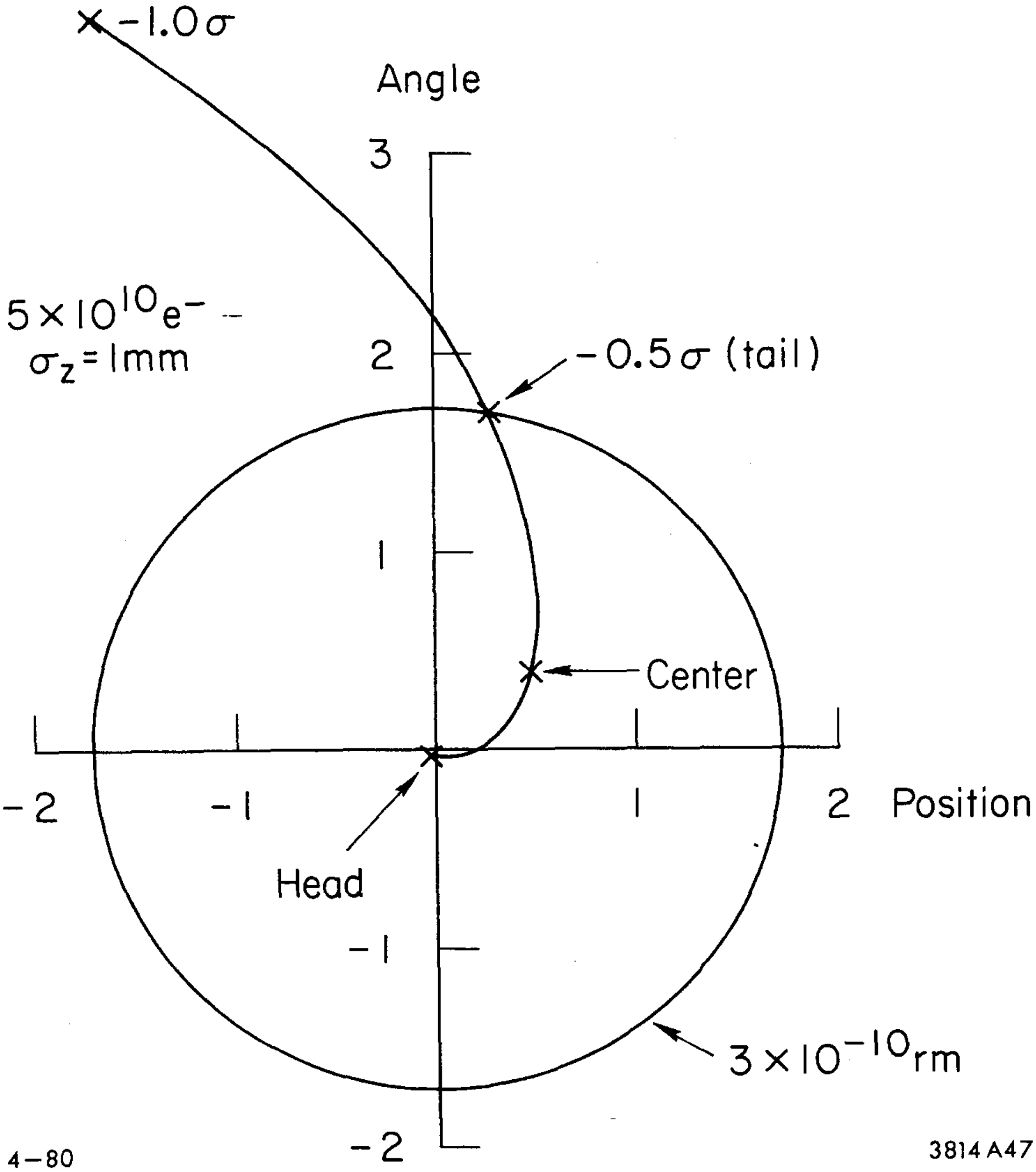

Fig. A-16. The transverse phase space at 50 GeV of a bunch of electrons injected into the linac with a position error of 14 microns.

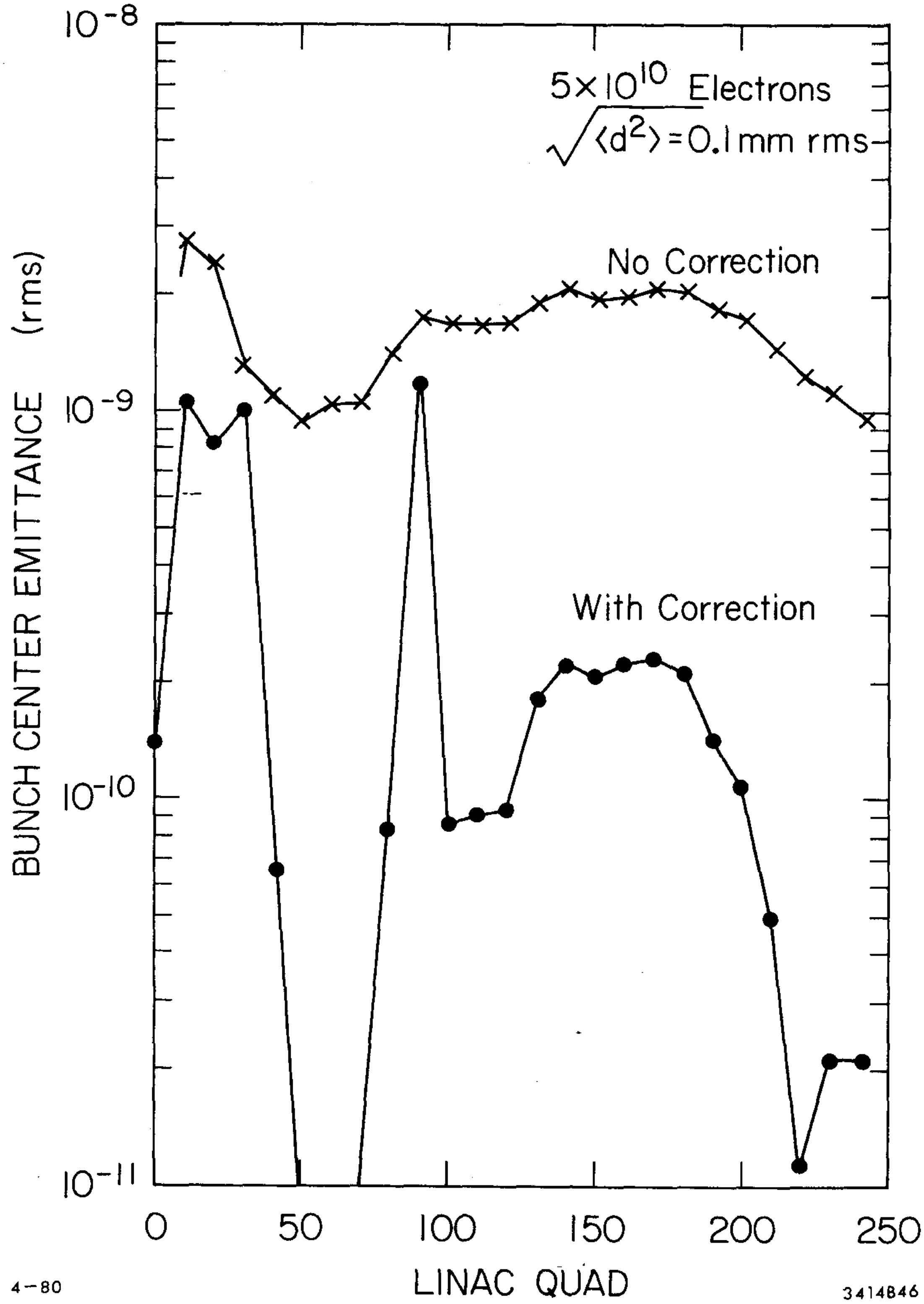

Fig. A-17. The curve marked "no correction" shows the Courant and Snyder invariant of the center of a bunch that has been injected without error into a misaligned linac. The misalignment of the linac sections has been uniformly distributed between -0.2 and +0.2 mm. The "with correction" curve shows the improvement made by empirical tuning of the injection conditions to compensate for the misalignment.

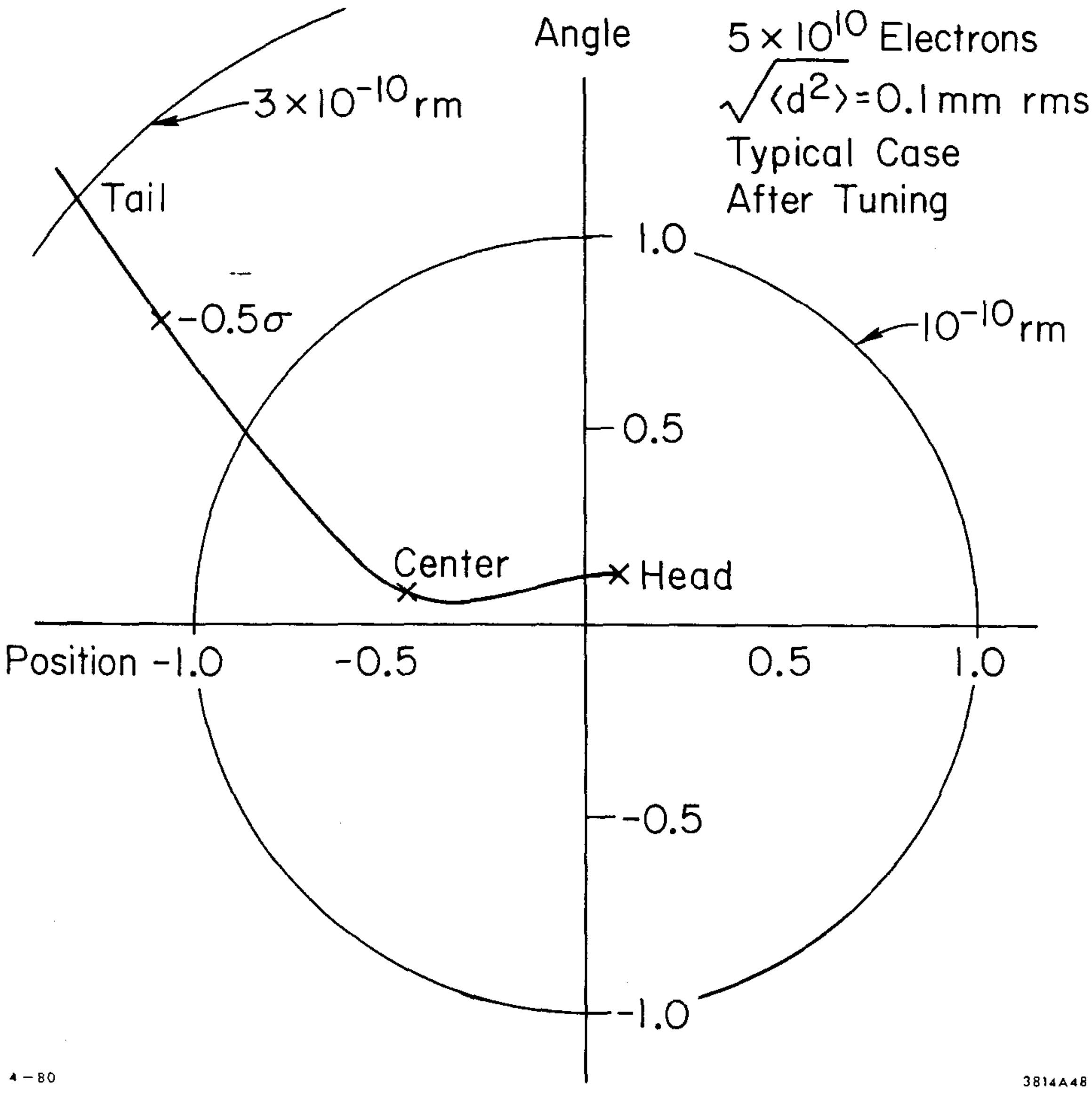

Fig. A-18. The transverse phase space of the bunch shown in Fig. A-17 at 50 GeV after empirical tuning of the injection conditions.

References

1. B. Zotter and K. Bane, PEP Note-308 (1979)
2. See for example P. Wilson, PEP Note-276 (1978)
3. W.K.H. Panofsky and W. A. Wenzel, Rev. Sci. Instr. 27, 967 (1956)
4. E. Keil, Nucl. Instr. Methods 100, 419 (1972)
5. M. Bell and H. G. Hereward, AR Division Report 65-37, CERN (1965)
6. Reported in E. Keil, Nucl. Instr. Methods 100, 419 (1972), Sec. 4.3
7. R. F. Koontz, G. A. Loew, R. A. Miller and P. B. Wilson, IEEE Trans. Nucl. Sci. NS-24, 1493 (1977)

APPENDIX B

EMITTANCE GROWTH IN THE COLLIDER

1. Quantum Fluctuations

As the particles travel along the Collider arms, they lose energy in the form of synchrotron radiation. The emission of light quanta causes a perturbation of the betatron oscillation. This in turn leads to an increase of the beam emittance which is undesirable for good luminosity.

The emittance is given by[1]

$$\frac{d\varepsilon}{ds} = \frac{\langle N\langle u^2\rangle\mathscr{H}\rangle_s}{2cE_o^2} \tag{1}$$

where the emittance is defined as the area of the phase space divided by π. Since we assume a Gaussian beam, we define the emittance for a standard deviation $\varepsilon = \sigma^2/\beta$. N is the number of photons emitted per second, $\langle u^2\rangle$ is the average photon energy squared, c is the speed of light, E_o is the beam energy, and $\mathscr{H}$ is a lattice function defined as

$$\mathscr{H} = 1/\beta[\eta^2 + (\beta\eta' - 1/2\beta'\eta)^2]$$

Here β is the horizontal betatron function, and η is the horizontal dispersion function. The average $\langle\rangle_s$ is taken along the beam line. For $N\langle u^2\rangle$ we find

$$N\langle u^2\rangle = \frac{55}{24\sqrt{3}}\, r_e\, \hbar mc^4\, \frac{\gamma^7}{\rho^3}$$

If the total length is $\Delta s = \phi\rho$, with ϕ the total deflection in one arc, then from Eq. (1) we now get

$$\Delta\varepsilon\ (\text{rad-m}) = 2.1 \times 10^{-11}\ \phi E^5\ (\text{GeV}^5)\ \rho\ \langle\mathscr{H}/\rho^3\rangle_s$$

In order to minimize the emittance growth we have to choose a lattice that minimizes $\rho\langle\mathscr{H}/\rho^3\rangle$. Obviously this demands the maximum possible bending radius ρ. This we have done as permitted by the available site. The quantity $\mathscr{H}$ depends strongly on the parameters chosen for the lattice. For a simple FODO cell this quantity reaches a minimum for a phase advance per cell of $\psi^o = 140^o$. (See Fig. B-1 and Reference 2.)

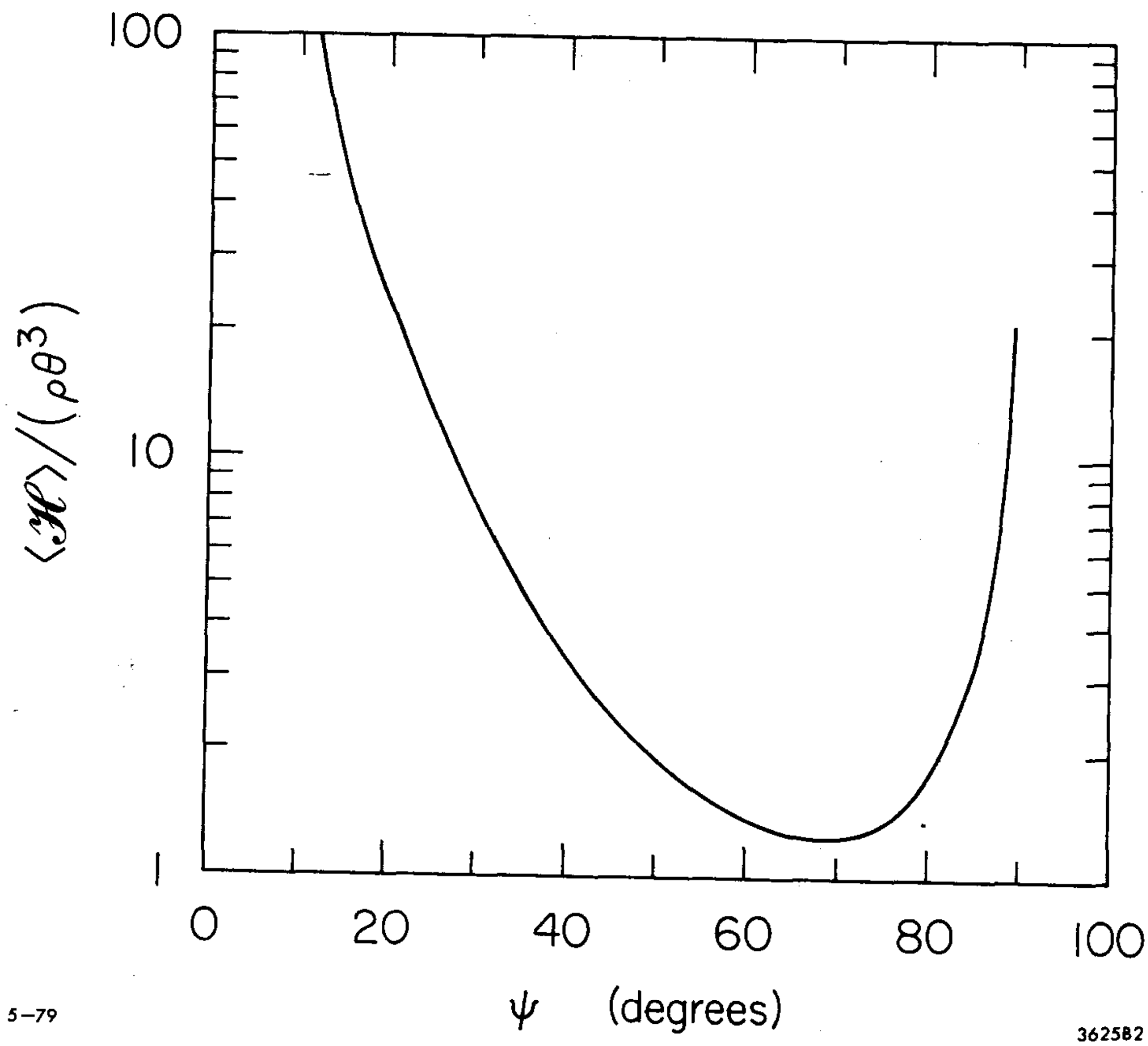
100
10
1
0
20
40
60
80
100
$\langle \mathcal{H} \rangle / (\rho\theta^3)$
ψ (degrees)
5-79
3625B2

Fig. B-1

Calculations show that it is impossible to provide the necessary focusing for small emittance growth in a separated-function lattice design. We have decided, therefore, to use a combined-function lattice. Since the beam travels through this lattice only once, we do not have to worry about the antidamping that is inherent in such a lattice.

Although the minimum emittance growth is achieved for a phase advance per cell of 140°, we have chosen to use a phase advance per cell of only about 110° in order to be at safe distance from the lattice stop band at 180° per cell. For technical reasons we have also chosen a field gradient of not more than

$$g = 7 \text{ KG/cm} \quad \text{(at 50 GeV)}$$

The optimum cell parameters are then

cell length:	5.20 m
magnet length:	2.55 m
bending radius:	292.8 m

For this lattice we obtain

$$\langle \mathcal{H}/\rho^3 \rangle_s = 1.37 \times 10^{-11} \text{ m}^{-2}$$

The total bending angle is $\phi = 211^{\circ}$, and the emittance blowup is then

$$\Delta\varepsilon = 0.94 \times 10^{-10} \text{ rad-m (at 50 GeV)}$$
$$\Delta\varepsilon = 5.2 \times 10^{-10} \text{ rad-m (at 70 GeV)}$$

The emission of synchrotron radiation also increases the energy spread of the beam. For the chosen lattice we obtain

$$\Delta(\sigma_\varepsilon/E) = 1.6 \times 10^{-5} \text{ (at 50 GeV)}$$

$$\Delta(\sigma_\varepsilon/E) = 8.6 \times 10^{-5} \text{ (at 70 GeV)}$$

This is much smaller than the ±0.5% energy spread of the beam coming from the linear accelerator.

2. Orbit Distortions

Because of the large field gradients in the magnets, the aperture in the Collider arcs is only a few millimeters. This requires a very good correction of the central beam path. Accurate correction is also required because distortion of the central path would cause an additional growth in beam emittance which should be minimized. Several correction schemes have been studied, and from this work we have concluded that both the beam center and slope will have to be corrected at frequent intervals along the beam line.

The following correction scheme has been adopted. There will be beam-position monitors located on either side of every fourth magnet in the Collider lattice. The second monitor will be used to calculate the slope of the beam path in the first monitor. Beam displacement and slope will then be corrected through the use of two correction coils. We assume the following alignment errors for the magnets,

transverse displacement	rms	0.10 mm
rotation about beam line	rms	0.17 mrad
yaw and pitch	rms	0.15 mrad

and for the beam-position monitors:

transverse displacement	rms	0.10 mm

After correction, the beam-path distortions are then typically

horizontal	rms	$\delta x \simeq 0.5$ mm
vertical	rms	$\delta y \simeq 0.4$ mm

The associated increase in beam emittance due to beam-path errors alone is, at 50 GeV,

$$\delta\varepsilon_x = 0.58 \times 10^{-10} \text{ rad-m}$$

$$\delta\varepsilon_y = 0.26 \times 10^{-10} \text{ rad-m}$$

The path distortions also create horizontal and vertical dispersion functions that must be corrected to zero at the interaction point. It can be shown, however, that this perturbation of the dispersion functions is just equal but opposite in sign to the path distortion that is corrected to zero at the interaction point.

Calculations[3] indicate that chromaticity correction is required in the Collider arcs to minimize the linear terms in $\Delta p/p$ of the dispersion functions at the interaction point. If this were not done, the chromatic effects at the interaction point would greatly increase the beam spot size.

A more detailed calculation shows that higher order terms contribute less than 10% to the beam size if the path distortions are kept within the tolerances specified above.

References

1. M. Sands, Physics With Intersecting Storage Rings, Academic Press, New York (1971).

2. R. H. Helm, H. Wiedemann, PEP Note 303 (SLAC).

3. D. Ritson, AATF/80/17 (SLAC).

APPENDIX C

FINAL FOCUS SYSTEM

1. Function of the Final Focus System

The purpose of the FFS is to demagnify the beam envelope in the Collider arc lattice to a size suitable for beam collisions at the interaction region. The final spot size will be determined by the beam emittance, the beta function β^* at the I.R., the momentum spread in the beam, and the quality of the FFS optics. In particular, if the focusing system is not chromatically corrected, the momentum dispersion in the beam can lead to a substantial degradation in the quality of the final focus.

The objective is to design a FFS for 70 GeV/c within ~ 100 meters having a I.R. spot size $\sigma_{xy} = \sqrt{\beta_{x,y}\varepsilon}$ of approximately 2 μm for a beam emittance of $\varepsilon = 3 \times 10^{-10}$ m-rad and a momentum spread of $\delta = \pm 0.5\%$. This requires a $\beta_{x,y}$ equal to or less than 1 cm.

2. Conceptual Layout

Figure C-1 shows a simple one-dimensional thin lens analogue for one stage of the FFS. It has the property of point-to-point and parallel-to-parallel imaging. Thus an upright ellipse at position 1 will be transformed into another upright ellipse at position 2 with the spot size magnified by the ratio $M = f_2/f_1$ where f_1 and f_2 are the focal lengths of the two thin lenses comprising the half-wave transformer. The distance of separation between lenses $\ell_2 = f_1 + f_2$ assures parallel-to-parallel imaging. The total transformation matrix R for the system is shown in Fig. C-1 in three equivalent forms. $\beta_{I.R.}$ and $\beta_{Lattice}$ are the beta functions at the beginning and end of the system.

The minimum spot size is achieved by equating the "chromatic" broadening to the monoenergetic beam size at the I.R. This corresponds for the simple conceptual scheme shown in Fig. C-1 to a $\beta^* = \beta_{I.R.}$ of

$$\beta^* = \ell_1 \left[1 + \frac{\ell_1}{\ell_2}\right] \delta = \ell_1 (1 + \frac{1}{M}) \delta \qquad (1)$$

or

$$\beta^* \geq \ell_1 \delta \quad \text{for} \quad M >> 1$$

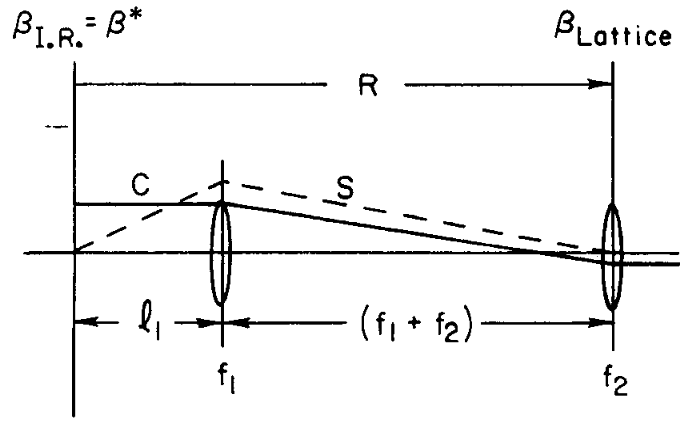

$$R = \begin{bmatrix} -M & 0 \\ 0 & -\frac{1}{M} \end{bmatrix} = \begin{bmatrix} -\frac{f_2}{f_1} & 0 \\ 0 & -\frac{f_1}{f_2} \end{bmatrix} = \begin{bmatrix} -\sqrt{\beta_L/\beta^*} & 0 \\ 0 & -\sqrt{\beta^*/\beta_L} \end{bmatrix}$$

4 - 80 3814A39

Fig. C-1. A thin-lens analogue of a $\lambda/2$ optical transformer.

where ℓ_1 is the distance from the I.R. point to the center of the first lens, ℓ_2 is the distance from the first lens to the second lens, and $\delta = \pm(\Delta p/p)$ is the momentum spread in the beam. As an example, if $\ell_1 = 4$ meters and $\delta = \pm 0.5\%$, then $\beta^* \geqq 2$ cm. This is not an unreasonable result for the Collider, but we require a simultaneous solution for both the transverse planes x and y.

For a quadrupole focusing system the simple one-dimensional result shown in Fig. C-1 may be extended to two dimensions by the use of four quadrupole lenses as illustrated in Fig. C-2. This system is a "half-wave transformer" in both the x and y planes as is evident from the total transfer matrix R. The result for the β_x^* and β_y^* corresponding to the minimum spot size at the I.R. is

$$\frac{\beta_x^*}{2\delta} \geqq (\ell_1 + \ell_2) - \sqrt{\ell_2(\ell_1 + \ell_2)}$$

$$\frac{\beta_y^*}{2\delta} \geqq (\ell_1 + \ell_2) + \sqrt{\ell_2(\ell_1 + \ell_2)}$$

or

$$\sqrt{\beta_x^* \beta_y^*} \geqq 2\delta\sqrt{\ell_1(\ell_1 + \ell_2)} \qquad (2)$$

This inequality has been compared with an exact evaluation using the programs TRANSPORT and TURTLE. It was found that the exact results were typically 30-50% higher than the lower limits given by Eq. (2).

As an example, let $\ell_1 = 4$ meters, $\ell_2 = 2.5$ meters and $\delta = \pm 0.5\%$. Then Eq. (2) yields

$$\sqrt{\beta_x^* \beta_y^*} \geqq 5 \text{ cm} \quad .$$

This implies the need for a chromatic correction system for the above design parameters.

3. Chromatic Correction System

The chromatic broadening of the beam spot at the I.R. can in principle be reduced by introducing sextupoles in the FFS in a region where the beam is momentum dispersed. However the sextupoles will,

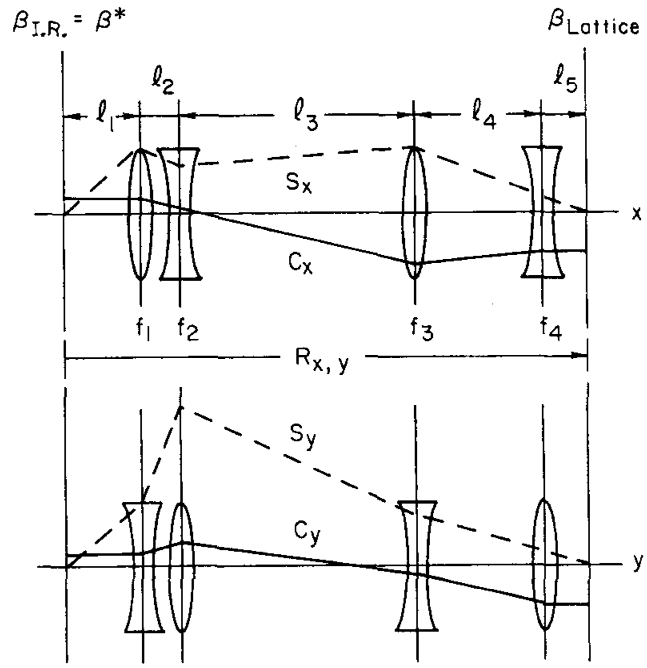

$$R_{x,y} = \begin{bmatrix} -M_x & 0 & 0 & 0 \\ 0 & -\frac{1}{M_x} & 0 & 0 \\ 0 & 0 & -M_y & 0 \\ 0 & 0 & 0 & -\frac{1}{M_y} \end{bmatrix} = \begin{bmatrix} -\sqrt{\beta_x^L/\beta_x^*} & 0 & 0 & 0 \\ 0 & -\sqrt{\beta_x^*/\beta_x^L} & 0 & 0 \\ 0 & 0 & -\sqrt{\beta_y^L/\beta_y^*} & 0 \\ 0 & 0 & 0 & -\sqrt{\beta_y^*/\beta_y^L} \end{bmatrix}$$

4-80
3814B40

Fig. C-2. A two-dimensional λ/2 transformer using quadrupole lenses.

themselves, introduce higher-order geometric and chromatic aberrations. These higher-order aberrations must then be minimized in order to achieve the smallest possible beta function at the I.R. This is accomplished by the following techniques. The correcting sextupoles in each plane are introduced as pairs separated by a π phase shift. This makes it possible to correct the final focusing to second-order leaving residual third and higher-order aberrations as the limiting factors. These residual aberrations are minimized by placing the sextupoles in regions of high beta and by choosing the momentum dispersion at the correcting elements such that the residual geometric and chromatic aberrations are approximately equal. It can be shown analytically or by numerical evaluation that for the optimum correction, the dispersed beam size should approximately be equal to the geometric beam size at the correcting elements. This has been achieved in the FFS shown in Fig. C-3. For the system illustrated, the above conditions are satisfied by introducing a dipole bend magnet B_3 midway between the paired sextupoles with a bend angle α_3 of

$$\alpha_3 \sim \frac{2}{\delta} \sqrt{\frac{\varepsilon}{\beta_3(x)}} = \frac{2}{M_3(x)\delta} \sqrt{\frac{\varepsilon}{\beta^*}} \qquad (3)$$

The final parameters for the matching and correction system for the FFS is accomplished in 114 meters. This is achieved with four half-wave transformers. The first two transformers match the monoenergetic beta functions at the arc lattice to an I.R. beta function of 1 cm in both the x and y planes. The last two transformers are used to make the chromatic correction. They are identical but placed in mirror symmetry about the center of the B_3 bend magnet. Contained within each of the last two half-wave transformers are two sextupoles, one for the x plane and one for the y plane, which correct the principal second-order chromatic aberrations. Dipoles B_3, B_2, and B_1 are inserted; B_1 at the end of the arc lattice, B_2 between transformers 1 and 2, and B_3 between transformers 3 and 4. B_3 is chosen to introduce the appropriate eta function (dispersion) into the system as per Eq. (3). Dipoles B_2 and B_1 are then chosen so as to make the dispersion at the final focus achromatic to second-order in δ.

The beta functions at the position of the dipoles are chosen so as to restrict the emittance growth caused by synchrotron radiation to an

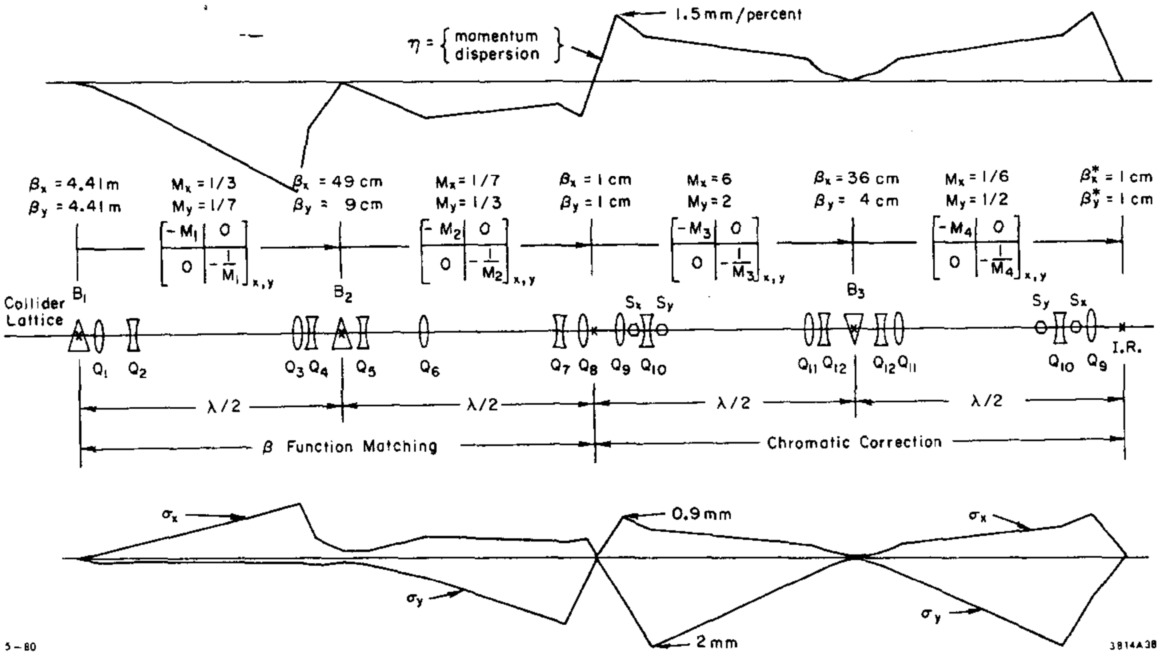

Fig. C-3. The optical layout of the SLC final focus system.

acceptable value. The emittance ε introduced by each magnet is a function of the beam energy E and some lattice functions (see Appendix B). For example, at 5^{0} GeV, $\varepsilon = .28 \times 10^{-11}$ m-rad for the combined three dipoles. The optics for the final focus system requires approximately twice the length of a system without a correction. (This is due to the additional length of the correcting region.) The detailed scheme given in Fig. C-3 has been designed to minimize the total length required.

4. TRANSPORT and Ray Tracing Calculations

A detailed TRANSPORT listing of the proposed FFS is given in Table C-1 showing the lengths and strengths of all optical elements. The first- and second-order transform matrices from the Collider lattice to the I.R. are given at the end. The demagnification between the lattice and I.R. is $M_{x,y}{}^{*} = 1/21$. There is a residual eta prime (angular dispersion) of -0.48 mr/percent at the I.R., but since the bunch length is small, the luminosity is not seriously affected. The sextupoles are adjusted to make the (1 26) and (3 46) chromatic aberration coefficients (underlined in Table C-1) vanish, since they are the principal contributors to the second-order chromatic distortion of the final spot.

The basic design was evolved using the TRANSPORT program with the guidelines dictated by the above equations for the bend angles and emittance growth. The TRANSPORT design was then evaluated using the TURTLE second-order matrix ray-trace program, and finally by a differential ray-tracing program valid to all orders. The resulting beam distribution at the I.R. point from tracing 3000 rays with the latter program is shown in Fig. C-4 and Fig. C-5. The assumed beam at the beginning of the FFS was a Gaussian truncated at 2σ for the positions and angles of the rays and a rectangular distribution for the momentum spread. The assumed 1σ input phase space is shown at the beginning of the TRANSPORT listing in Table C-1. The optics of the system is designed for a monoenergetic $\beta_{x,y}{}^{*} = 1$ cm at the I.R. for a system having no aberrations. This would yield a $\sigma_{x,y}{}^{*} = \sqrt{\beta_{x,y}{}^{*}\varepsilon} = \sqrt{3}$ μm. Figure C-4 shows the cross section of the beam with aberrations. The two circles indicate the one and two σ radii containing 50% and 90% of the particles respectively. Figure C-5 gives the size of the I.R. as a function of

```
C3*3 ///FINAL FOCUS SYSTEM FOR COLLIDER *** K L BROWN *** 3/3/80

INPUT BEAM        .           P = 70.00000 GEV/C
                                                                    X        0.036 MM
                                                                    THETA    0.008 MR
(ASSUMED INPUT FROM SLC LATTICE    BETA X = BETA Y = 4.41 M)        Y        0.036 MM
                                                                    PHI      0.008 MR
(EMITTANCE = 0.0003 MM MR   DP/P = 0.5 PERCENT   )                  DP/P     0.500 PC

*2ND ORDER*    17.
*DRIFT*         3.                 -0.50000 M       POLE          APERTURE       BEND
   -0.500 M                                         FIELD         RADIUS         ANGLE
*Z RO*         20.                180.00000 DEG
   -0.500 M
*BEND*          4.   "BEND LEFT"    1.00000 M    18.46344 KG                   0.453 DEG
    0.500 M
*Z RO*         20.               -180.00000 DEG
    0.500 M
*DRIFT*         3.                  0.50000 M
    1.000 M
*QUAD*          5.     Q1           1.00000 M     3.09335 KG   10.00000 MM
    2.000 M
*DRIFT*         3.                  3.95809 M
    5.958 M
*QUAD*          5.     Q2           1.00000 M    -3.28872 KG   10.00000 MM
    6.958 M
*DRIFT*         3.                 16.15607 M
   23.114 M
*QUAD*          5.     Q3           1.00000 M     8.76634 KG   10.00000 MM
   24.114 M
*DRIFT*         3.                  1.00000 M
   25.114 M
*QUAD*          5.     Q4           2.00000 M    -7.61645 KG   10.00000 MM
   27.114 M
*Z RO*         20.                180.00000 DEG
   27.114 M
*BEND*          4.   "BEND LEFT"    4.00000 M    17.84997 KG                   1.752 DEG
   31.114 M
*Z RO*         20.               -180.00000 DEG
   31.114 M
*QUAD*          5.     Q5           1.00000 M    -3.15978 KG   10.00000 MM
   32.114 M
*DRIFT*         3.                  5.56604 M
   37.680 M
*QUAD*          5.     Q6           1.00000 M     3.52093 KG   10.00000 MM
   38.680 M
*DRIFT*         3.                 11.67978 M
   50.360 M
*QUAD*          5.     Q7           1.00000 M    -9.96210 KG   10.00000 MM
   51.360 M
*DRIFT*         3.                  1.00000 M
   52.360 M
*QUAD*          5.     Q8           2.00000 M    10.53973 KG   10.00000 MM
   54.360 M
```

Table C-1. A TRANSPORT listing of the SLC final focus system.

DRIFT	3.		4.00000 M			
58.360 M						
QUAD	5.	Q9	2.00000 M	11.98426 KG	20.00000 MM	
60.360 M						
SEXT	18.	X SEXTUPOLE	0.25000 M	10.21638 KG	20.00000 MM	
60.610 M						
DRIFT	3.		0.75000 M			
61.360 M						
QUAD	5.	Q10	1.50000 M	-10.39800 KG	20.00000 MM	
62.860 M						
SEXT	18.	Y SEXTUPOLE	0.50000 M	-6.37721 KG	20.00000 MM	
63.360 M						
DRIFT	3.		16.08054 M			
79.440 M						
QUAD	5.	Q11	1.00000 M	9.76822 KG	20.00000 MM	
80.440 M						
DRIFT	3.		1.37589 M			
81.816 M						
QUAD	5.	Q12	1.00000 M	-10.18461 KG	20.00000 MM	
82.816 M						
DRIFT	3.		1.00000 M			
83.816 M						
BEND	4.	"BEND TO RIGHT"	2.00000 M	18.66667 KG		0.916 DEG
85.816 M						
DRIFT	3.		1.00000 M			
86.816 M						
QUAD	5.	Q13 = Q12	1.00000 M	-10.18461 KG	20.00000 MM	
87.816 M						
DRIFT	3.		1.37589 M			
89.192 M						
QUAD	5.	Q14 = Q11	1.00000 M	9.76822 KG	20.00000 MM	
90.192 M						
DRIFT	3.		16.08054 M			
106.272 M						
SEXT	18.	Y SEXTUPOLE	0.50000 M	-6.37721 KG	20.00000 MM	
106.772 M						
QUAD	5.	Q15 = Q10	1.50000 M	-10.39800 KG	20.00000 MM	
108.272 M						
DRIFT	3.		0.75000 M			
109.022 M						
SEXT	18.	X SEXTUPOLE	0.25000 M	10.21638 KG	20.00000 MM	
109.272 M						
QUAD	5.	Q16 = Q9	2.00000 M	11.98426 KG	20.00000 MM	
111.272 M						
DRIFT	3.		3.00000 M			
114.272 M						

X	0.002 MM
THETA	0.302 MR
Y	0.002 MM
PHI	0.174 MR
DP/P	0.500 PC

(INTERACTION REGION   BETA X = BETA Y = 1 CM)

Table C-1 (cont.). A TRANSPORT listing of the SLC final focus system.

Table C-1 (cont.). A TRANSPORT listing of the SLC final focus system.

```
*TRANSFORM 1*
              0.04762  -0.00000  -0.00000  -0.00000   0.0      -0.00000
             -0.00000  21.00000   0.00000   0.00000   0.0      -0.47962
             -0.00000  -0.00000   0.04762  -0.00000   0.0      -0.00000
              0.00000  -0.00000   0.00000  21.00000   0.0       0.00000
              0.00023  -0.00000  -0.00000  -0.00000   1.00000  -0.00072
              0.0       0.0       0.0       0.0       0.0       1.00000
*2ND ORDER TRANSFORM*
  1 11 -8.106E-06
  1 12  8.759E-02   1 22 -1.303E-04
  1 13  2.076E-11   1 23 -9.295E-13   1 33  2.184E-07
  1 14 -4.366E-13   1 24 -1.853E-09   1 34  3.612E-01   1 44 -5.082E-03
  1 15  0.0         1 25  0.0         1 35  0.0         1 45  0.0         1 55  0.0
  1 16  3.041E-03   1 26 -6.362E-07   1 36  8.028E-09   1 46 -1.942E-10   1 56  0.0         1 66  1.193E-06

  2 11 -6.972E-06
  2 12  3.376E-03   2 22 -1.931E+01
  2 13  1.398E-13   2 23 -1.787E-09   2 33  7.940E-05
  2 14  3.580E-08   2 24 -2.008E-11   2 34 -3.549E-04   2 44  3.870E+02
  2 15  0.0         2 25  0.0         2 35  0.0         2 45  0.0         2 55  0.0
  2 16  8.308E-02   2 26 -1.341E+00   2 36 -6.801E-11   2 46  1.720E-05   2 56  0.0         2 66  1.337E-01

  3 11 -8.117E-11
  3 12 -1.692E-13   3 22 -1.491E-09
  3 13 -3.449E-05   3 23  3.612E-01   3 33  1.670E-11
  3 14 -1.755E+00   3 24  3.127E-03   3 34 -5.875E-12   3 44  7.257E-09
  3 15  0.0         3 25  0.0         3 35  0.0         3 45  0.0         3 55  0.0
  3 16 -3.901E-08   3 26 -9.708E-12   3 36  4.937E-03   3 46 -6.617E-05   3 56  0.0         3 66 -2.081E-09

  4 11  6.814E-13
  4 12 -7.367E-09   4 22  2.071E-10
  4 13  1.588E-04   4 23 -9.579E-05   4 33 -4.434E-15
  4 14  1.473E-02   4 24 -1.593E+02   4 34 -7.367E-09   4 44  1.259E-09
  4 15  0.0         4 25  0.0         4 35  0.0         4 45  0.0         4 55  0.0
  4 16  2.284E-10   4 26 -3.541E-06   4 36  5.406E-02   4 46 -2.179E+00   4 56  0.0         4 66 -5.328E-08

*LENGTH*        114.27229 M
```

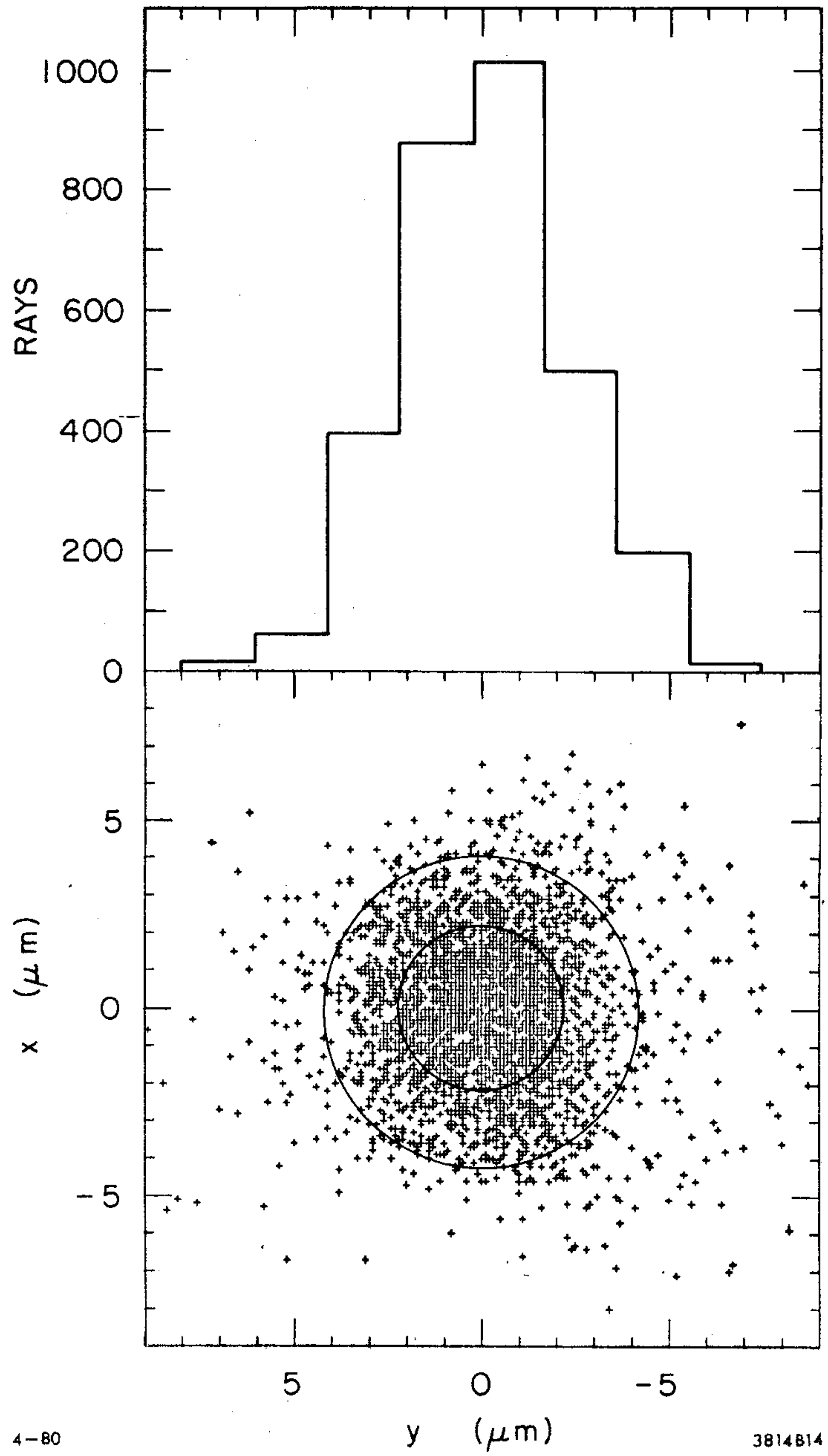

Fig. C-4. A scatter plot of 3000 rays traced through the final focus system. The two circles enclose 50% and 90% of the transmitted particles.

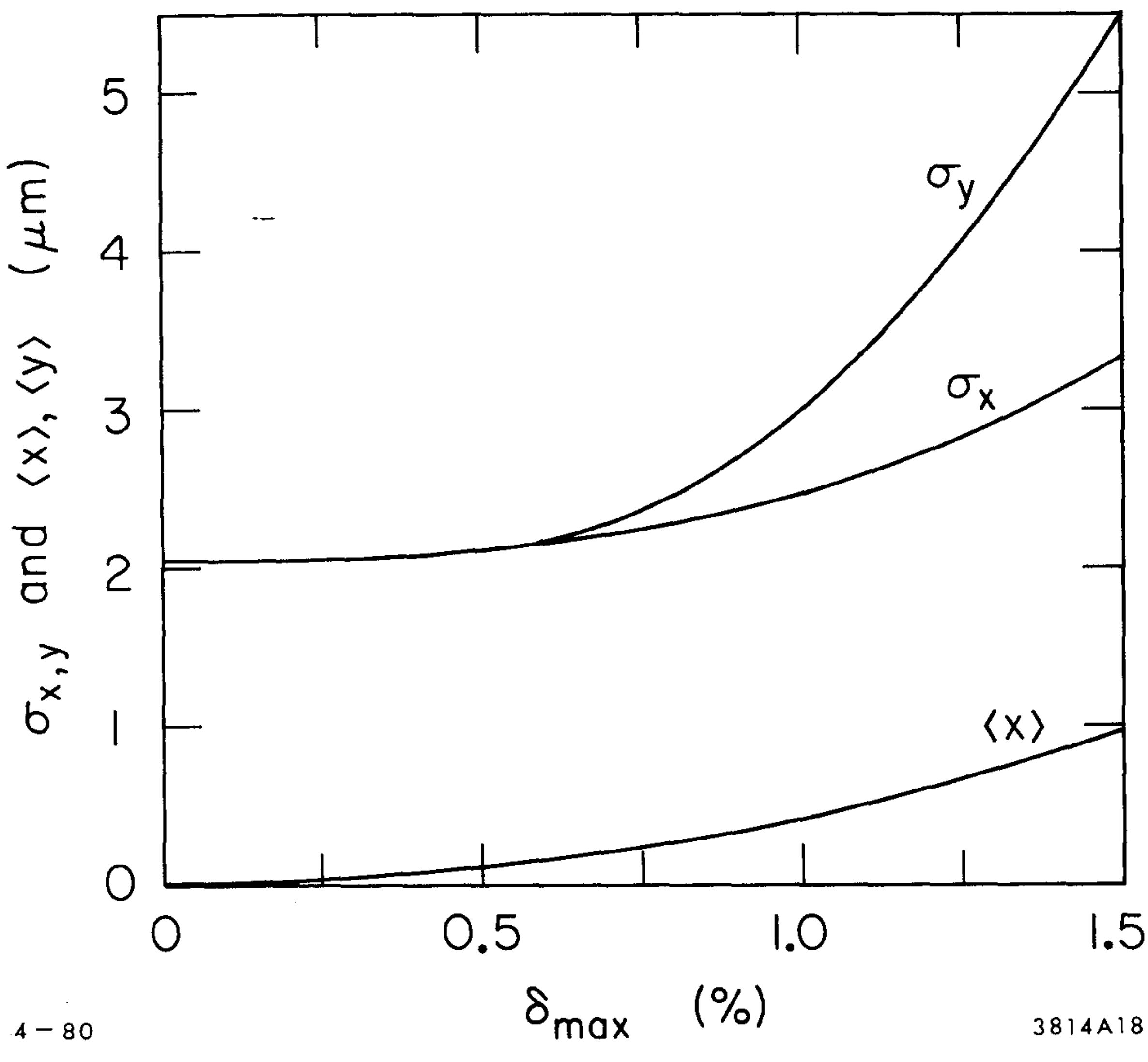

Fig. C-5. The one-sigma size of the beam at the interaction region as a function of the input momentum spread.

the input momentum spread of the beam. To all orders in the optics $\sigma_{x,y}^{*} = 2.1\ \mu m$ for the design value of $\delta = \pm 0.5\%$ and $\varepsilon = 3 \times 10^{-10}$ m-rad.

The dominant higher-order aberrations limiting the effective β^{*} of this system are the following third-order terms:

$$(x|\phi^2\delta)\phi^2\delta \cong 1.0\ \mu m$$

$$(x|\phi^2\theta)\phi^2\theta \cong 1.0\ \mu m$$

$$(y|\theta^2\delta)\theta^2\delta \cong 1.5\ \mu m$$

$$(y|\theta^2\phi)\theta^2\phi \cong 1.3\ \mu m$$

where θ and ϕ are the one σ spread in the initial beam angles.

This is consistent with the desired SLC objectives.

APPENDIX D

BEAM-BEAM INSTABILITIES AND PINCH EFFECTS

1. Introduction

There are two questions that must be addressed in considering the beam-beam interaction for linacs: (a) How large can the transverse density of the beams be before plasma-like instabilities are generated which substantially increase the size of the beams during the collision and thereby reduce the luminosity? (b) What is the effect of the beam-beam dynamics without instabilities on the average luminosity of a collision? The beam-beam dynamics have been investigated at SLAC using a modified three-dimensional cloud-in-cells (CIC) plasma-simulation program. The results of these calculations have been verified by a Lawrence Livermore Lab plasma-simulation program of the particle-in-cells (PIC) type for the axial-symmetric case.[1]

These studies indicate that the nubmer of plasma oscillations during beam passage is of order

$$n \simeq 1/3 \sqrt{D}$$

where D is the dimensionless disruption factor that will be discussed later. For the Collider design, the beams execute approximately 1/5 of a plasma oscillation, so there is not enough time for instabilities to grow. Typical instability growths correspond to n values of one or two, which allow quite large values of D.

The second result of these studies is that the oppositely charged beams attract each other and yield a pinch effect which enhances the luminosity, as shown in Fig. D-1. The enhancement grows proportional to D^2 and reaches a maximum value when the focal spots of the two beams overlap most completely ($D \simeq 2.5$). For Gaussian bunches, the enhancement remains constant to large values of D ($D \simeq 20$). For less stable shapes it drops more rapidly. The value of the enhancement is approximately 6 for a beam that is mismatched at insertion, and 2.5 for a matched beam (i.e., emittance-dominated minimum waist.)

2. Definition of the Disruption Factor

Consider a test particle with displacement δr from the collision axis which is incident on an opposing charge distribution. For the

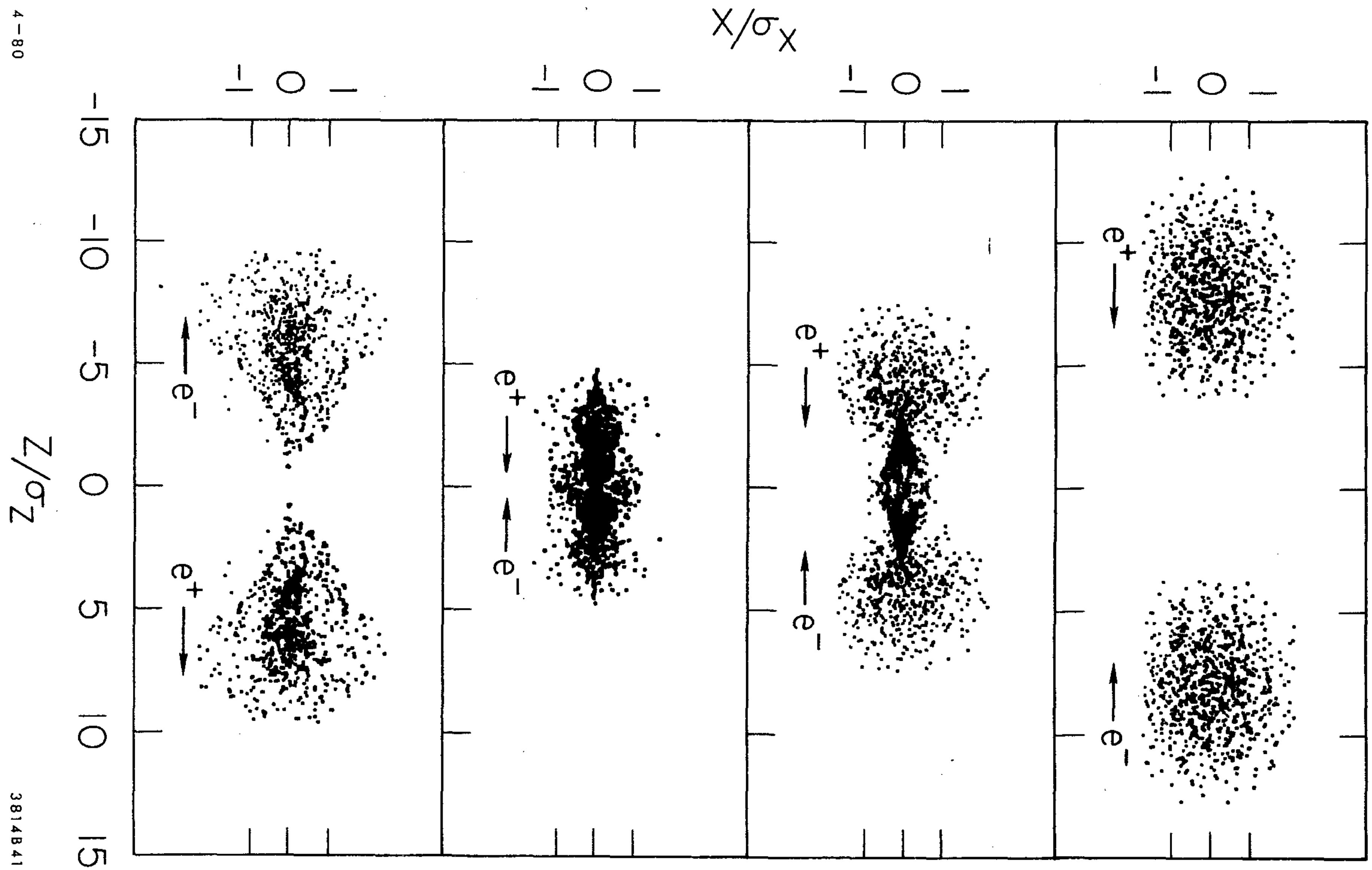

4-80

3814B41

Fig. D-1. Side view of the collision of oppositely charged beams, showing the pinch effect for Gaussian profiles and a disruption factor D = 14.4.

simple case of a uniform cylindrical beam, the total deflection of the test charge is given by

$$\Delta r' = \frac{-2\ Nr_e\ r}{\gamma R^2}$$

where N is the number of particles in the bunch, and R is the bunch radius. A similar analysis applied to a bi-Gaussian distribution gives

$$\Delta x' = -\frac{2Nr_e x}{\gamma\sigma_x(\sigma_x + \sigma_y)}$$

$$\Delta y' = -\frac{2Nr_e y}{\gamma\sigma_y(\sigma_x + \sigma_y)}$$

for $x << \sigma_x$ and $y << \sigma_y$.

Comparing the effect of the beam to a thin lens, the focal length is just given by

$$\Delta x' = -(1/f)x$$

and one can define a dimensionless parameter called the disruption factor by relating the focal length to the length of the bunch:

$$D = \sigma_z/f \quad .$$

If σ_x is not equal to σ_y, the focal lengths in the x and y directions are not equal, and one must define two such parameters D_x and D_y. When the charge distribution is uniform, the focal length f is well-defined. However, for a non-uniform bunch, the focal length is not constant. In this case, it is useful to use the focal length for small offsets (or equivalently the focal length calculated from the central density) to define the collision strength. Thus, for the Gaussian case with aspect ratio $\sigma_x/\sigma_y = 1$, the disruption parameter is

$$D = \frac{Nr_e\sigma_z}{\gamma\sigma_x^2} \quad .$$

For an arbitrary charge distribution characterized by the scale parameters λ_x, λ_y and λ_z, the variables in the problem can be scaled since we are dealing essentially with a collisionless plasma (point-like scattering). Defining the scaled variables

$$\xi_x = x/\xi_x, \ \xi_y = y/\xi_y, \ \xi_z = z/\xi_z \quad ,$$

and a shape distribution such that

$$\int \rho_\xi d\xi_x d\xi_y d\xi_z = 1$$

the luminosity becomes

$$L = \frac{f\ N_1 N_2}{\lambda_x \lambda_x} I_o \quad ,$$

where I_o is the overlap integral in x and y and the convolution in z of ρ_ξ with itself.

For a Gaussian distribution

$$\rho_\xi = \frac{1}{(2\pi)^{3/2}} e^{-(\xi_x^2/2+\xi_y^2/2+\xi_z^2/2)}$$

and $\lambda_x = \lambda_x$, $I_o = 1/4$. Using the scaled variables, the equation of motion for a test charge reduces to the simple relation

$$\frac{d^2\xi_x}{d\xi_z^2} = -D\xi_x$$

for $\xi_x \ll 1$ and $\xi_y \ll 1$. For the Gaussian example, the value of the disruption parameter is

$$D = \frac{14.4\ N\sigma_z}{E\sigma_x\sigma_y}$$

where N is the number of particles in units of 10^{10}, σ_z is the bunch length in mm, E is the beam energy in GeV, and $\sigma_x\sigma_y$ is the transverse dimensions in microns.

3. Relation of D to the Plasma Frequency and Instabilities

It is also interesting to compare D to the relativistic transverse plasma frequency of the bunch ω_p which is defined as

$$\omega_p^2 = 4\pi\rho r_e c^2/\gamma$$

For a three-dimensional Gaussian distribution with charge Ne, ρ varies with position and so does ω_p. Using ρ_{max} and comparing with D defined in terms of the central density (for simplicity $\sigma_x = \sigma_y$),

$$\rho_{max} = N/(2\pi)^{3/2}\ \sigma_x \sigma_y \sigma_z$$

$$\omega^2_{pmax} = 4\pi \rho_{max} r_e c^2/\gamma$$

one finds

$$D = \frac{N r_e \sigma_z}{\gamma \sigma_x^2} = \frac{\omega_p^2 \sigma_z^2}{c^2} \sqrt{\pi/2} \quad .$$

Instabilities tend to grow as e^{L/λ_p}; taking $n = L/\lambda_p$ and $L \simeq \sqrt{2\pi}\sigma_z$ yields $D \simeq 8n^2$. Thus $\sqrt{D}$ is a measure of the number of plasma oscillations which occur during the collision. This conclusion could also have been reached from the form of the scaled equation of motion.

The results of the full simulation indicate that the effective phase-shift for particles near the axis of a Gaussian beam is actually related to D by

$$D = 10.4\ n^2$$

The value of the numerical coefficient is not very informative since it is shape-dependent. Nevertheless, it points out that there is little chance for an instability to grow unless there are several plasma oscillations within the collision. Two oscillations would limit D to approximately 32.

4. Beam Dynamics and the Luminosity

In the leading and trailing parts of a Gaussian beam and in the transverse tails, the charge density is less than the density in the central part of the beam. Since the plasma frequency squared is proportional to the density, this means that the corresponding plasma wavelength ω_p is longer in the tails and that the tails are then more stable than the beam core. When beam dynamics are neglected, the tails of the beam contribute little to the luminosity of the collision. This is because the luminosity is related to the integral of the density squared over the transverse cross section of the beam, which in the Gaussian case, for example, receives little contribution from those parts of the beam which are more than one sigma from the center.

When beam dynamics are included, one expects that the cumulative focusing effect of the head of the beam on the central core will be important in determining the approximate transverse dimensions of the beam core when it overlaps with the core of the other beam. Thus, the charge distribution in the head of the beam is an important factor in determining the enhancement factor or ratio of the actual luminosity to the luminosity expected for undisturbed beam profiles. A non-uniform density distribution leads to a spread in the plasma frequencies, and this together with the longer plasma wavelength in the tails helps stabilize the enhancement factor. This effect is illustrated in Figs. D-2 and D-3, which compare the enhancement factor for beams with Gaussian and uniform transverse profiles, respectively. The longitudinal profile is Gaussian in both cases.

References:

1. William M. Fawley and Edward P. Lee, "Modeling of Beam Focusing and Kink Instability for Colliding Relativistic Electron and Positron Beams," UCID-18584.

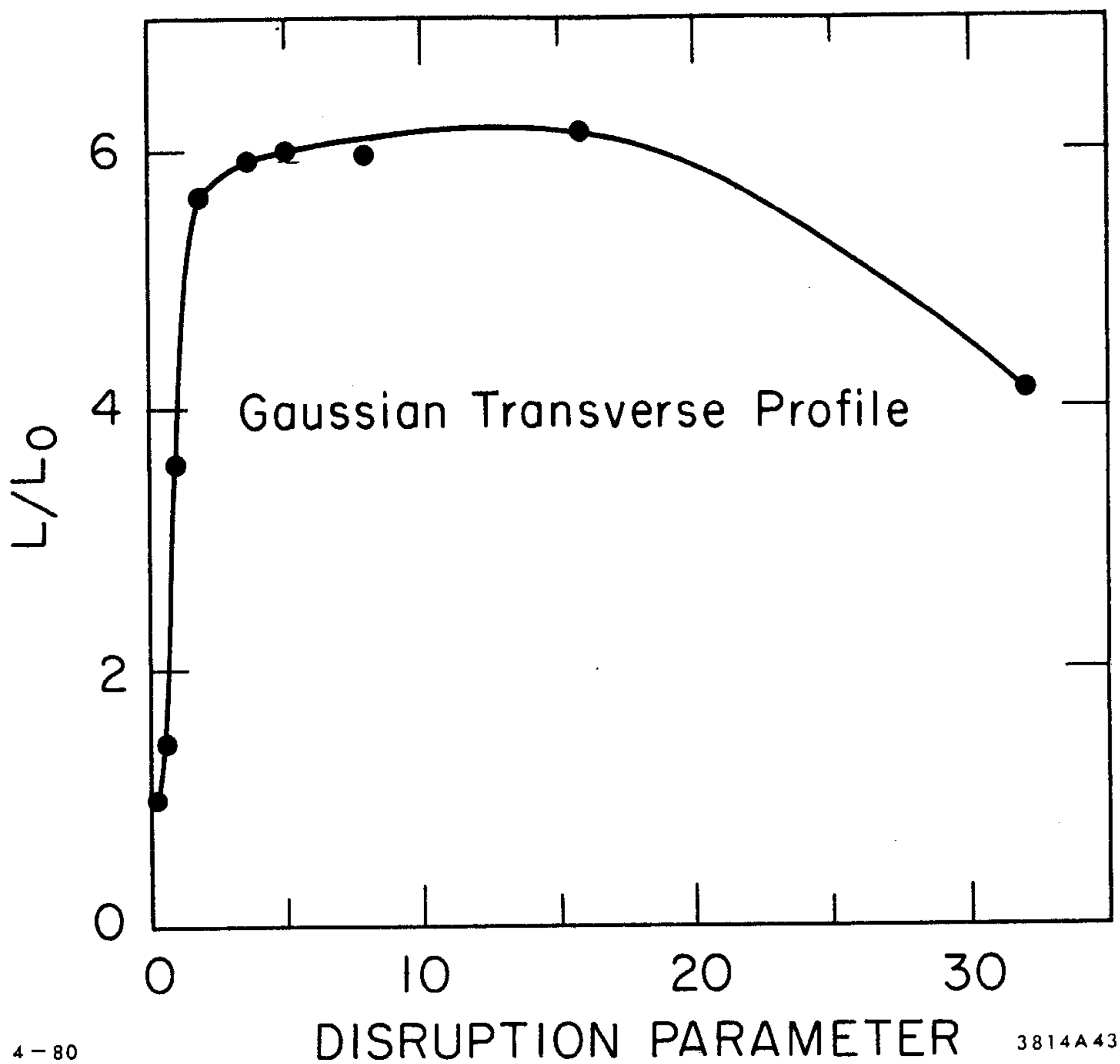

Fig. D-2. The ratio of the actual luminosity, including beam-beam pinch, to the unperturbed luminosity as a function of the disruption factor for two beams with Gaussian transverse and longitudinal profiles.

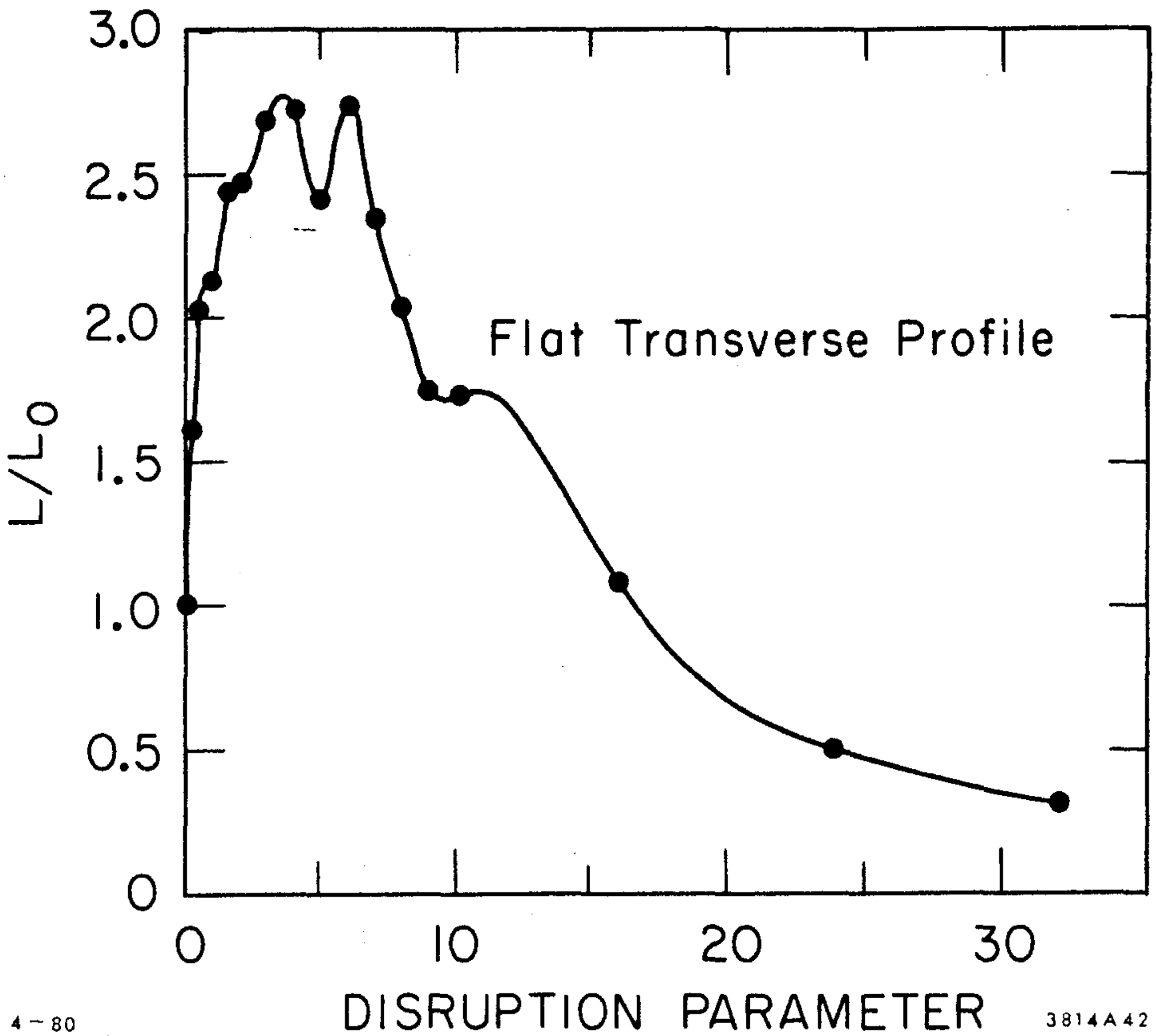

Fig. D-3. The ratio of the actual luminosity, including beam-beam pinch, to the unperturbed luminosity as a function of the disruption factor for two beams with uniform transverse and Gaussian longitudinal profiles.

APPENDIX E

DETECTOR BACKGROUNDS AT THE SLC

Because of the lower average current, the higher bunch density and the higher energy, the background environment of the SLC will be significantly different from that of existing electron-positron storage rings. The schematic of Fig. E-1 illustrates the sources of the particle backgrounds for the SLC by process and location. The six categories cover the situation for any colliding-beam machine, storage-ring or single-pass, although the emphasis will be different in each case.

The actual effects of these background sources depend on secondary processes, such as back-scattering from a mask, and these are presented in Table E-1. Also included here are the design measures to protect against an effect, if necessary, and the description of the final background in the detector. The individual effects outlined in the Table are discussed in detail in the following sections.

The nominal SLC parameters which figure in background calculations are:

$N = 5 \times 10^{10}$ electrons per beam

$E = 50$ GeV each beam

$\sigma_z = 1$ mm

$\sigma_x = \sigma_y = 2$ microns, beam size at collision

Total energy in beams = 800 Joules

1. Synchrotron Radiation from the Bends

The location of the bending magnets, quadrupoles and masks is shown in Fig. E-2, along with the trajectory of the disrupted beam. The resulting synchrotron radiation is characterized by:

	Hard Bend	Soft Bend
Photons per electron	15.5	1.4
Critical energy (MeV)	1.0	0.025

The mask has been placed at approximately 8 meters and is laterally positioned so as to shield the downstream quadrupoles from the soft-bend radiation without intercepting any of the disrupted electron beam.

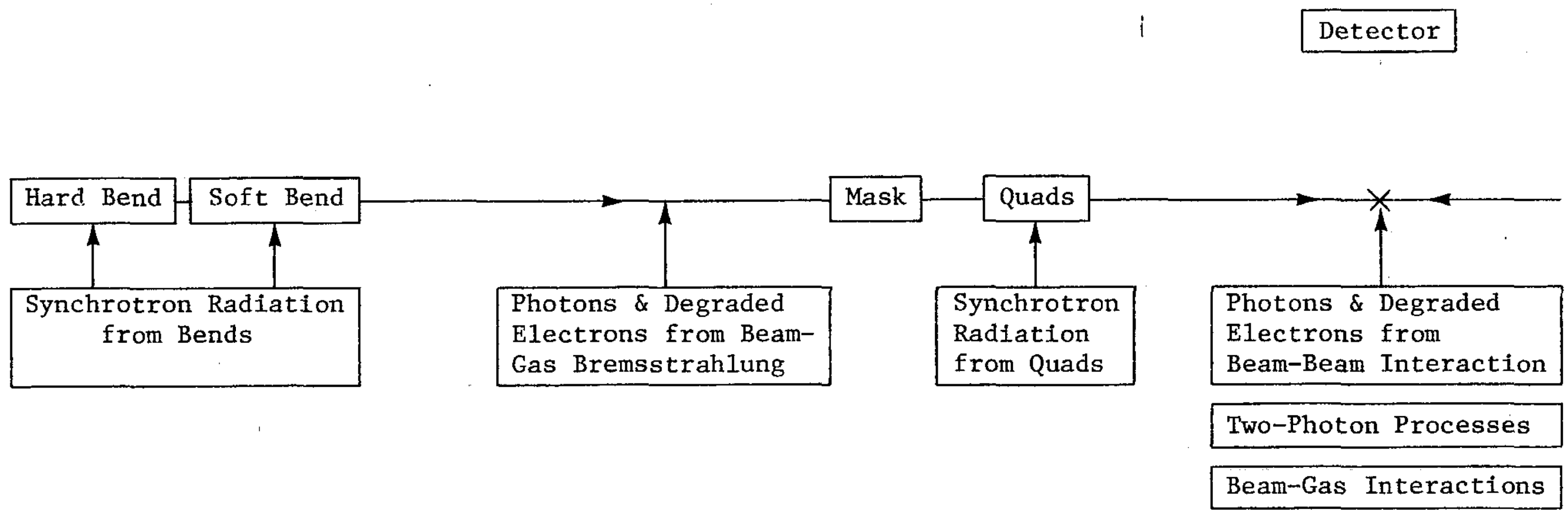

Figure E-1: Six background sources at the SLC are shown on a schematic view of the interaction region. The two most troublesome sources are the synchrotron radiation from the bends, and the photons and degraded electrons from the beam-beam interaction. A conventional storage ring suffers most from beam-gas bremsstrahlung effects and quadrupole synchrotron radiation.

Table E-1

Background Effects at the SLC

Sources	Effect on Design	Secondary Process	Effect on Detector
1. Synchrotron Radiation from bending magnets.	Heavy mask at 8 meters with local neutron shielding. Flared pipe between mask and bend magnet.	Scattering of soft-bend photons on down-stream mask and mask edges.	Low-energy photons into central detector.
		Neutrons production by hard-bend photons in mask	Neutrons over full detector.
2. Photons and degraded electrons from beam-beam interaction.	Maintain clear quadrupole and mask apertures for disrupted beam envelope of 0.7 mrad. Locally shield pipe with 1½ meters of concrete at 22 meters scraping region	Disrupted electron beam transported to distant dump.	
		Photons backscatter on downstream pipe.	Low-energy photons and neutrons into detector
		Photons interact with beam	Electron pairs and photons into central detector.
3. Two-photon annihilation	-	Electron, muon pair production	Electron and muon pairs into detector.
		Hadron production.	Background events.
4. Synchrotron radiation from quadrupoles	-	Photons backscatter on quadrupoles.	Low-energy photons.
		Photons interact with beam.	Electron pairs and photons
5. Photons and degraded electrons from upstream bremsstrahlung	-	Degraded, hard electrons overfocused by quads	Hard electrons and shower debris.
		Hard photons on beam pipe.	Shower debris.
6. Local beam-gas interactions	-	Low-energy electroproduction.	Protons and pions.

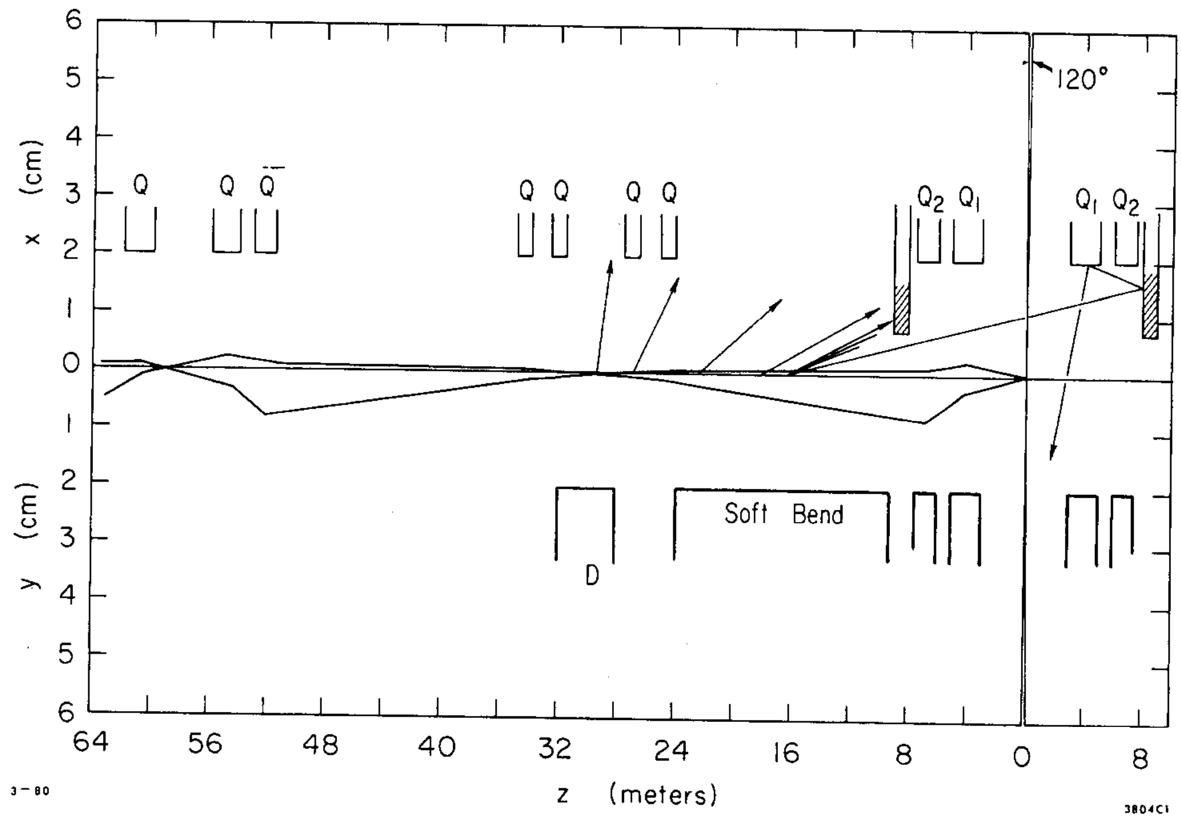

Fig. E-2. SLC trajectories, masks and magnets. The vertical and horizontal trajectories for the disrupted beam of 0.7 mrad are displayed on an exaggerated sketch of the SLC lattice near the interaction region. The sources of synchrotron radiation at the soft and hard bends are shown, although the bend itself is suppressed. This radiation is fully stopped in the hard-bend case, and the fraction of the soft-bend radiation that is intercepted by the downstream mask must scatter twice to enter the detector.

As shown in the figure, the soft-bend radiation may backscatter into the detector region from the edge of the upstream mask or interior face of the downstream mask. A second scatter is still required for the radiation to reach the detector itself. This required plural scattering, with attendant absorption, reduces the flux reaching the detector to an acceptable level.

The calculation of background from the soft-bend synchrotron radiation has been made assuming the geometry of Fig. E-2, lead masks, and the Mark II drift chamber.[1] Tabulated values of the photon scattering and absorption coefficients were used,[2] and the integrations over synchrotron radiation spectra were performed numerically. Several kinds of path are possible, and coherent Rayleigh and incoherent Compton scattering are involved. In certain regimes, fluorescent radiation plays a role.

For a 50 GeV beam, approximately 40 photons with energies from 30 to 100 KeV enter the drift chamber per crossing. These fluxes are tolerable and should be considered upper limits because of conservative assumptions in the calculations and the assumed absence of any additional shielding around the beam pipe.

The interaction region is fully shielded from the hard-bend radiation provided there is no opportunity for coherent scattering from the beam pipe before the mask is reached. Thus the pipe (not shown in Fig. E-2) will flare in the horizontal plane from a few centimeters at the bend to 30 cm at the mask.

There will be some production of neutrons by the high-energy photons at this mask, however. The neutron yield from photonuclear processes in various materials is approximately 10^9 neutrons/joule, with the neutrons being slow (a few MeV) and coming predominantly from the giant dipole resonance.[3] Threshold for production in copper is about 10 MeV.

The hard-bend photon flux contains about 10^{-4} of the total beam energy. Only 10^{-4} of this energy, however, is in photons above the neutron production threshold in this copper-backed section of the mask. The resulting production rate is

$$10^{-4} \times 10^{-4} \times 800 \left(\frac{\text{Joules}}{\text{crossing}}\right) \times 10^{9} \left(\frac{\text{neutrons}}{\text{Joules}}\right) \lesssim 10^{4}\ \frac{\text{neutrons}}{\text{crossing}}$$

Accounting for the solid angle of the detector, as seen from this mask, there will be fewer than 1000 neutrons per crossing entering the detector. Concrete shielding near the mask or the detector can provide additional attenuation by a factor of 100 to 1000 if required.

2. Photons and Disrupted Electrons from the Beam-Beam Interaction

The beam-beam interaction is considerably stronger for the SLC than for a conventional storage ring. One measure of the strength is the magnetic field produced by one beam and felt by the other. At the SLC, this field is a few megagauss. Over the one millimeter of interaction length, this field produces a maximum deflection angle of approximately 0.7 mrad. The radius of curvature during the deflection is of order one meter, leading to substantial synchrotron radiation within the cone of the degraded beam. The flux is roughly one photon for each beam electron and the critical energy is about 100 MeV. The details of this "beamsstrahlung" process are described in Reference 6.

(a) Disrupted Electrons

As shown in Fig. E-2, the disrupted electron or positron beam is transported by the optics of the machine through the same elements with an envelope four times larger than that of the incident beams. It is absolutely essential that none of this beam scrape on any of the elements close to the interaction region, and the ample clearance is shown in the figure. The disrupted beam is safely conducted to the ejection system and beam dump some 200 meters away.

(b) Photon Spray

Approximately 0.03% of the beam energy is radiated during the collision, and these photons are contained within the cone of the disruption angle of 0.7 mrad. These photons will ultimately scrape along the beam pipe starting at about 22 meters. (This effect is not clearly shown in Fig. E-2, as the curvature of the beam line, starting at the low-field bend, has been suppressed.) The most serious consequence of this dumping will be the production of slow neutrons and backscattered photons. The production rate of neutrons along the pipe will be:

$$3 \times 10^{-4} \times 800 \left(\frac{\text{Joules}}{\text{crossing}}\right) \times 10^{9} \left(\frac{\text{n}}{\text{Joule}}\right) \simeq 2.4 \times 10^{8} \left(\frac{\text{neutrons}}{\text{crossing}}\right)$$

The solid-angle of the detector viewed from this region is about $0.005 \times 4\pi$. One and one-half meters of the concrete shielding gives an attenuation of about 10^3. The net flux of neutrons entering the detector is thus

$$0.005 \times 10^{-3} \times 3 \times 10^8 \simeq 10^3$$

which is easily tolerated.

Photons produced by this scraping are a smaller problem than the neutrons. Normal, external shielding allows photons to enter the detector only by multiple-reflection paths within the beam pipe, and the net flux is very small.

(c) Photon Interactions

The photons from the beam-beam interaction are a beam in themselves of intensity comparable to that of the primary particle beams. There are, then, large numbers of collisions involving these photons and the particles (or photons) in the opposing beam. Three reactions are significant:

$$\gamma + e^{\pm} \rightarrow \gamma + e^{\pm}$$

$$\gamma + e^{\pm} \rightarrow e^{\pm} + e^{+} + e^{-}$$

$$\gamma + \gamma \rightarrow e^{+} + e^{-}$$

The total rates for these processes are calculated in Reference 6 and come to about 10 Compton scatters, 50 photon conversions, and 10 two-photon annihilations per beam crossing. In general, these electromagnetic processes are characterized by low-momentum transfers and small angles. Hence, most of the produced particles travel down the beam pipe to the interaction quadrupoles, where they are swept out.

The detailed properties of these reactions are essentially the same as those of the QED processes:

$$e^{+} + e^{-} \rightarrow e^{+} + e^{-} + \gamma$$

$$e^{+} + e^{-} \rightarrow e^{+} + e^{-} + e^{+} + e^{-}$$

where the photon is provided by the internal bremsstrahlung of the beam electron. A quantitative comparison of the two can be made by plotting the photon spectra for the beam-beam interaction photons (essentially a synchrotron radiation spectrum with a 100 MeV critical energy) and for the virtual photons associated with a beam electron (essentially the bremsstrahlung spectrum for an equivalent radiator of a few percent). As shown in Fig. E-3, the two spectra are comparable, and the effect of the beam-beam photons will be an increase in the same kinds of backgrounds coming from the QED processes by less than a factor of two. These rates are not a problem.

3. Two-Photon Annihilation

The higher energy of the SLC compared to PEP and PETRA does not bring dramatic new possibilities to the study of two-photon physics, and the decreased luminosity is a disadvantage to the serious study of this process, per se. However, the conventional one-photon-annihilation cross section is about 10 times smaller at the SLC than at PEP or PETRA, while the two-photon cross section has somewhat increased, so this process must be considered as a potential background.

The hadron background events from the two-photon process proceed as[4,5]

$$e^+ + e^- \to e^+ + e^- + \gamma_v + \gamma_v \text{ with } \gamma_v + \gamma_v \to \text{hadrons.}$$

A simplified formula for this cross section follows from dividing the process up into a photon flux and a cross section for the production of hadrons by a two-photon collision. The detected cross section is then obtained by integrating this equation over the range of total photon energy, and by accounting for the acceptance of the detector and the trigger requirements.

The photon-photon cross section can be estimated using an approximation to the vector-dominance Regge trajectory prediction, yielding the following effective cross sections at a beam energy corresponding to a total energy of 90 GeV:

Assuming full efficiency and solid angle and a minimum $E_{\gamma\gamma}$ of 1 GeV:	$\sigma(ee\to eeX) \simeq 27$ nb
Adding a trigger requirement of at least two charged particles with $P_t > 200$ MeV, and $\lvert\cos\theta\rvert < 0.7$:	$\sigma_{det}(ee\to eeX) \simeq 2$ nb

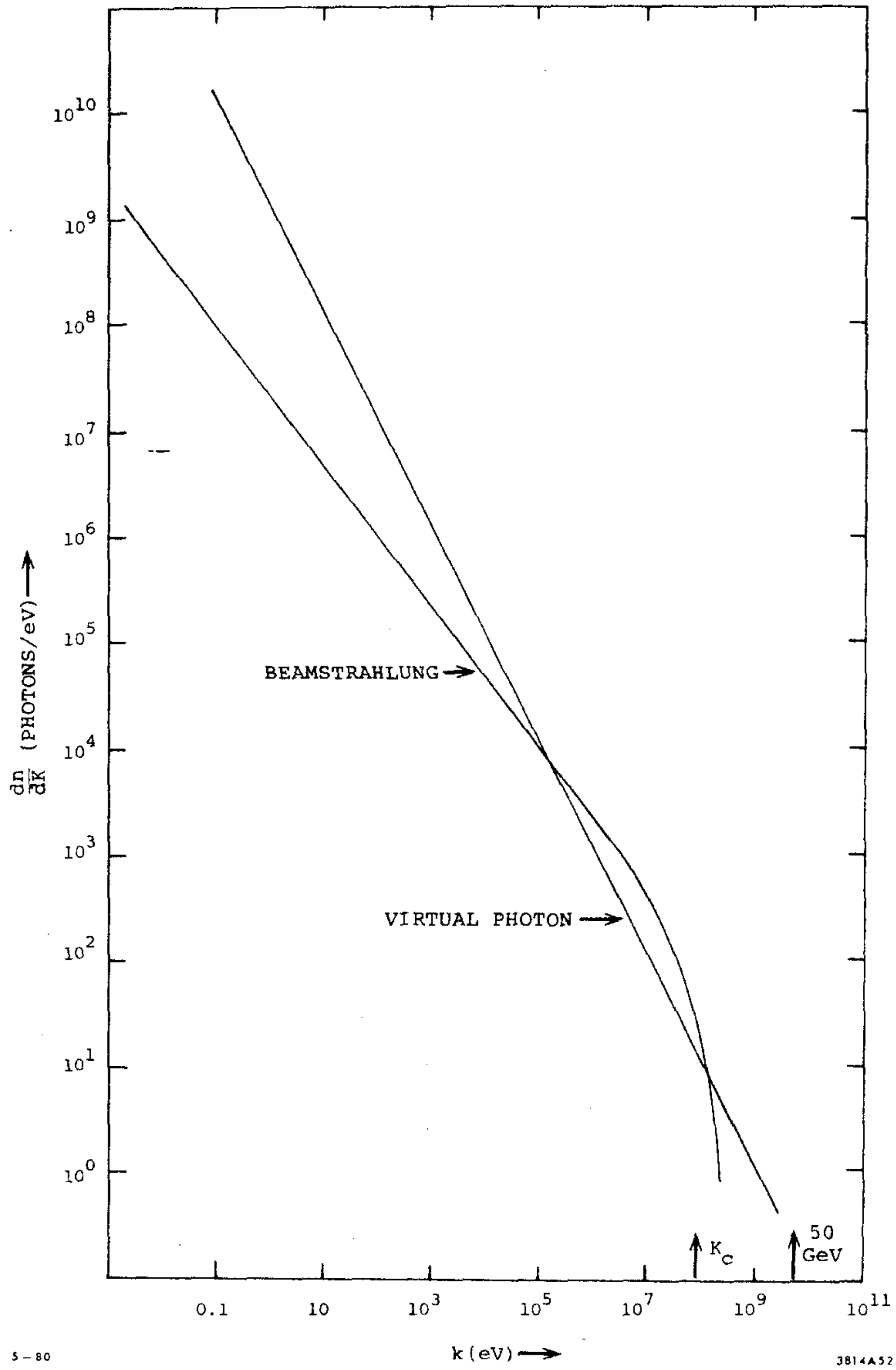

Fig. E-3. Beam-beam and virtual-photon spectra. The photons from the beam-beam interaction are distributed in a synchrotron-radiation spectrum with a critical energy of about 100 MeV. The virtual photons correspond to 50 GeV bremsstrahlung in a few-percent radiator. The two spectra are comparable for the QED processes of interest.

Requiring as well $E_{visible} > 30$ GeV: $\sigma_{det}(ee \to eeX) \simeq 0.5$ nb

Compared to the Z^o production cross section of 30 nb, this two-photon to hadron background should not be a problem. However, for the special cases of decay of the Z^o to exclusive channels with very small visible energy, there may be a problem. In these cases, the small P_t of the two-photon events may be helpful in separating these events out. It is also possible to tag one of the final-state electrons using conventional electron tagging systems just outside the radius of the close quadrupoles. The total efficiency for a single-electron tagging could be about 12%.

The production of muon pairs at the resonance may also be evaluated with these formulae, using QED to compute the two-photon to two-muon cross section. The acceptance is a strong function of the $P_{t,min}$ and polar angle of the muon pair, leading to effective cross sections:

$P_{t,min}$ (MeV/c)	θ range = 15^o to 165^o	θ range = 45^o to 135^o
100	σ_{det} = 31 nb	7.0 nb
300	6.0	1.5
500	2.1	0.51
700	1.0	0.27
1000	0.45	0.15

Even with relatively modest cuts on the transverse momentum, this effect is very small compared to the production of the Z^o.

The <u>detected</u> cross section for $e^+e^- \to e^+e^-e^+e^-$ is about the same as the detected cross section for $e^+e^- \to e^+e^-\mu^+\mu^-$, although the <u>total</u> cross section for the former process is orders of magnitude larger than that for the latter process. This is because only 10^{-6} of the e^+e^- pairs from $e^+e^- \to e^+e^-e^+e^-$ have sufficient transverse momenta to enter a conventional detector. For example, a trigger requiring 2 charged particles with $P_t > 0.3$ GeV/c and $15^o < \theta < 165^o$ gives $\sigma_{det}(eeee) = 10$ nb; which is a little larger than $\sigma_{det}(ee\mu\mu)$. When $P_t > 0.5$ GeV/c, $\sigma_{det}(eeee) \simeq \sigma_{det}(ee\mu\mu)$.

4. Synchrotron Radiation from Quadrupoles

The strong quadrupoles at the interaction region bend the electrons in arcs with radii of curvature from 1500 to 4000 meters, resulting in synchrotron radiation with about 10^{11} photons per crossing at a critical energy of a few hundred KeV.

(a) Photon Spray

These photons have a divergence characteristic of the undisrupted electron beam in the insertion quadrupoles, or about 0.4 mrad, and appear to come from the quadrupoles. This leads to a distribution at the downstream quadrupole face of about 3 or 4 mm characteristic radius, a fact confirmed by a computer program which computes the radiation in each of the quadrupoles for typical trajectories. The downstream quadrupole face, which is designed to clear the disrupted beam, has a bore of about 4 cm and intercepts less than 10^5 photons per crossing. The number reflected back into the small solid angle of the central detector through the unshielded beam pipe is negligible.

The mask at 8 meters will intercept some of the spray. The mask is in the plane in which the synchrotron radiation from the quadrupoles is least strong and least divergent, however, and the flux intercepted will be small as well as much farther from the detector.

The exiting disrupted beam is focused in the quadrupoles as it leaves the interaction region, and because of the larger divergence it emits more synchrotron radiation than the entering beam. However, the resulting radiation merely adds a small amount to the photon flux from the beam-beam interaction.

(b) Photon Interactions

The incoming synchrotron radiation from the last few millimeters of the quadrupole is focused on the collision point. This is partly smeared out by the inherent spread in angles of synchrotron radiation, and the net flux focused on the region is less than 10^6 photons per crossing, which is negligible compared to the flux from beam-beam effects.

5. Photons and Degraded Electrons from Upstream Bremsstrahlung

A fraction of the electrons in the beam will scatter on the residual gas molecules in the beam pipe. This bremsstrahlung process produces a photon of some energy, and an electron reduced in energy by this amount, both traveling in essentially the same direction as the initial electron. These "degraded" electrons are overfocused by the insertion quadrupoles and strike the beam pipe near the detector. The photons maintain their original divergence and strike the beam pipe somewhere downstream.

Assuming 15 meters of bremsstrahlung opportunity between the interaction region and the beginning of the bends, and a pressure of 5 nanoTorr, the number of degraded electrons per crossing will be

$$5 \times 10^{10} \left(\frac{\text{electrons}}{\text{crossing}}\right) \times \left(\frac{15 \text{ m}}{0.5 \times 10^{14} \text{ m}}\right) \times \ell n 200 = 0.08$$

where the radiation length comes from typical gasses at the low pressure, and the cutoff is taken as 0.5% in the 1/k spectrum. Generally only about 10% of these electrons are overfocused strongly enough to strike the detector, leading to additional clutter in about one percent of the events.

6. Local Beam-Gas Interaction

Electroproduction by the beam on the residual gas at the interaction point produces background events in the detector. Distinguishable in analysis, these would be a problem only if the trigger rate were high.

The model is photoproduction off deuterons in the region of the first resonance. A pressure of 1.5×10^{-9} Torr, a production cross section of 750×10^{-30} cm^2 and 7 deuterons per residual gas atom yields 3×10^{-17} interaction/photon in a 100 cm interaction length. The number of equivalent photons in the beam comes from an equivalent radiator of a few percent, giving

$$0.05 \left(\frac{5 \times 10^{10} \text{ e}}{\text{crossing}}\right) \left(\frac{180 \text{ cross}}{\text{second}}\right) 3 \times 10^{-17} = 10^{-5} \text{ Hz} \quad ,$$

which is obviously irrelevant.

7. Effects of Backgrounds on the Detector

The backgrounds discussed in the previous sections fall into three categories:

(a) $\gtrsim 10^2$ photons per crossing, of 10 to 100 KeV.

(b) $< 10^3$ slow neutrons per crossing.

(c) Non-collinear electron and muon pairs and hadron events from the two-photon process.

A few percent of the photons will convert in a typical inner drift chamber, leading to a few extra hits over the full chamber. For an integrating detector, such as TPC, there would be ≃1 GeV/sec deposited, which is tolerable. There is no effect on calorimetric elements.

A few percent of the neutrons will interact in scintillation counters but well outside any beam gate. A few percent will also interact in drift and proportional chambers, leading to about 10 spurious hits in the several thousand electronic channels of a typical detector. For any specialized detector for which this is a problem, there will be room for additional concrete shielding around the detector itself.

The electron-pair background is not large enough to be a trigger problem, and there is little difficulty in separating the process per se.

The hadron events from the two-photon annihilation are also readily separable.

References

1. Nuclear Inst. & Meth. 160, 227-238 (1970).
2. NSRDS-NBS 29.
3. SLAC-PUB-2211, W. P. Swanson (1978).
4. LEP Summer Study, CERN 79-01, Pgs. 553-594.
5. S. Brodsky et al., Phys. Rev. D4.
6. J. Jaros, AATF/80/22.